



Universidad de Granada

Facultad de Ciencias

Departamento de Física Aplicada

Programa de doctorado de Física y
Ciencias del Espacio

TESIS DOCTORAL

**Squeeze flow and polydispersity
effects in magnetorheology**

Autor: José Antonio Ruiz López

Granada, 18 de diciembre de 2015

Directores: Juan de Vicente Álvarez-Manzaneda y
Roque Hidalgo Álvarez

Editor: Universidad de Granada. Tesis Doctorales

Autor: José Antonio Ruiz López

ISBN: 978-84-9125-256-6

URI: <http://hdl.handle.net/10481/41977>

El doctorando José Antonio Ruiz López y los directores de la tesis Juan de Vicente Álvarez-Manzaneda y Roque Hidalgo Álvarez, garantizamos, al firmar esta tesis doctoral, que el trabajo ha sido realizado por el doctorando bajo la dirección de los directores de la tesis y hasta donde nuestro conocimiento alcanza, en la realización del trabajo, se han respetado los derechos de otros autores a ser citados, cuando se han utilizado sus resultados o publicaciones.

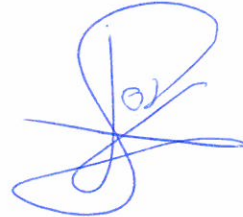
Granada, a 23 de octubre de 2015.

Director/es de la Tesis



Fdo.: Juan de Vicente Álvarez-Manzaneda

Doctorando



Fdo.: José Antonio Ruiz López



Fdo.: Roque Hidalgo Álvarez

A mi familia y a mis amigos

*“La ciencia se compone
de errores, que a su
vez, son los pasos hacia
la verdad”*

Julio Verne

Agradecimientos

En estas páginas quiero expresar mi agradecimiento a todas las personas que me han ayudado a afrontar un reto tan apasionante como escribir una tesis doctoral. En primer lugar, me gustaría agradecer a mis directores de tesis, Juan de Vicente Álvarez-Manzaneda y Roque Hidalgo Álvarez por todo su apoyo, desde que empezaron a confiar en mi para poder realizar esta tesis, pasando por todos los momentos, fáciles y difíciles, que conlleva este trabajo. Con vosotros he aprendido a andar este camino de la mejor forma posible.

Gracias también al Ministerio de Educación por la ayuda FPU (AP2010-2144), al proyecto del Ministerio de Investigación, Ciencia e Innovación, MAT 2010-15101; al proyecto del Ministerio de Economía y Competitividad, MAT 2013-44429-R; y a los proyectos de la Junta de Andalucía P10-RNM-6630, P10-FQM-5977 y P11-FQM-7074 por su financiación, sin la cuál la investigación en una universidad pública no sería posible.

No puedo olvidarme de mis queridos compañeros de la sala de becarios con los que tantos momentos hemos pasado. Desde los primeros compañeros que me encontré cuando llegué: Efrén, con el que aprendí a usar el reómetro y con el que escribíamos ecuaciones en las pizarras; Miriam, por esos ratos de baloncesto; Miguel Alberto Peláez, con el que redescubrí la filosofía en una librería

nocturna de Oporto a los que he pasado gran tiempo con ellos: Pablo Moreno, por ser tantas veces presidente; Amelia, por inculcarnos esa capacidad de trabajo y por bailar las grecas. A todo esto, ya se me olvidaba mi Paoliña, con la que he bailado y cantado tanto. César, por hacernos ver que todo era grasiento. A Carmen, por su fortaleza física y mental, a Felipe, por esos días en los que se ve a un padre salir de fiesta, a Jesús Felipe, por enseñarnos la canción de “El diablo está enfadado”, a Azahara. A Miguel Ángel y a Germán, por ser el triángulo de las Bermudas desde que empezamos en esta aventura. A Juan Pablo, por todos esos cafés, cervezas, y momentos que hacen que los compañeros merezcan la pena. A Juan Carlos, del que he aprendido mucho en simulaciones. A Miguel Wulf, por sus mochilas multicolores, que alegran la mañana a cualquiera. A Diego, por esos momentos de guitarra. A Álvaro, por estar siempre ahí aunque ya no esté en la sala. A Teresa, por nuestros momentos organizando el JICI-II. A Leonor, porque es una persona que siempre te hace feliz aunque seas cascarón de huevo. A los que nos visitaron alguna vez en la sala, sobre todo a Luisma por su gracia inconmensurable y a Fernando Bellesi, por ese acento argentino. Azahara, esta te la tenía que devolver, pero también es broma! Muchas gracias por estar ahí, ser tan organizadora y tan importante para todos. A Irene, por estar siempre con esa sonrisa. Y muchas gracias a las nuevas incorporaciones, por ser el testigo de una sala de becarios que sin duda vive: Elisa, Keshwad, José Rafael... A Paloma, María de Mar, Laura, Rafa, Jordi, José Alberto, Javi, Alice, Nico y a todos los que muchas

veces vamos a comedores, por hacerme sentir tan bien con vosotros, reirme y disfrutar.

A los miembros del Grupo I8 de Física aplicada, sobre todo a Miguel Cabrerizo, a María José, a Pepe, a Julia, a Alberto, con el que he compartido docencia, a Ana Belén, a Miguel Ángel, a María Tirado a Arturo Moncho, a Peula, a Juan Luis, y a todos los demás por formar un grupo en el que me he sentido muy a gusto estos años. Tampoco quiero olvidarme de José Antonio el técnico de Laboratorio ni de los secretarios, Conrado, Miguel Heredia y Belén, por facilitarnos nuestro trabajo.

No me quiero olvidar tampoco de tantas personas que han estado ahí en estos momentos y siempre. A mis compañeros de piso, Ramssel, Manu, Manolillo, Facun, Andrés, José Luis, Javi, y sobretodo a Manolete, porque fuiste un gran amigo y un gran compañero del que nunca me olvidaré. Tampoco me quiero olvidar de mis compañeros de la carrera, ya que todo su apoyo me ha hecho ser siempre mejor persona. A Carmen, Pilar, Karri, Luis y Ade.

I want to thank to all the people I met in my short stay in Reading: Zuowei, for the discussing times and for letting me go to this city and work in so beautiful environment; Jian, Jack, Dipesh, Alexei, Patrick..., for make me feel like at home. I also want to thank the people in my house in Reading, Nick, John and Joshua, for the speaking times.

Quiero también agradecer a todos los miembros de ASI-Granada y FJI/Precarios, por hacer de esta profesión una profesión digna, con la que podamos estar orgullosos de trabajar en condiciones. Por luchar por la investigación y por su futuro. También a todos los republicanos, en especial a los miembros de UCAR-Granada y de las demás plataformas republicanas granadinas, por pretender que nuestra tierra sea más próspera, más libre, más abierta y más igual.

A todos los músicos que aman ese bello arte.

A mis amigos de Rus, C+11, por ser como sois todos, nunca cambiéis, por todos los momentos que hemos vivido y por los que nos quedan por vivir, por esos ratos de la Lambra y por estar siempre ahí. Muchas gracias a Pedro, Mister, Pite, Mangas, Chenco, Melón, Guay, Juanito, Juan Be, Juan Je, Pantic, Santi, Mateo, Yoye, María, María Poza, Chela, Mari Jose, Manoli, Cristina y Noelia.

Muchas gracias a Antonio José Martos Martínez, mi novio, porque ha sido lo mejor que me ha ocurrido en mi vida y porque con él he tenido la fuerza suficiente para poder escribir esta tesis. Gracias por ser como eres y por estar ahí siempre.

A mi familia, porque sin su apoyo no habría podido estar estudiando, ni habría podido elaborar esta tesis, en especial a mi madre, Ana María López López y a mis abuelos, Antonio López García y Francisca López Raya.

Outline

ABSTRACT	15
RESUMEN	17
INTRODUCTION	19
OBJECTIVES	57
THEORY	59
METHODOLOGY	73
RESULTS	89
Part I. Magnetorheology in squeeze flow mode	91
Chapter 1.	93
Chapter 2.	115
Chapter 3.	167
Chapter 4.	189
Chapter 5.	197

Part II. Model magnetorheology: inverse ferrofluids	225
Chapter 6.	227
Chapter 7.	283
Part III. Effect of the polydispersity in particle size in magnetorheology	315
Chapter 8.	317
Chapter 9.	363
CONCLUSIONS	403
CONCLUSIONES	405

Abstract

Generally speaking, conventional magnetorheological fluids are colloidal suspensions of ferromagnetic particles in a non-magnetic continuous medium. Under the application of an external magnetic field, magnetic particles align in its direction forming aggregates. The mechanical properties of magnetorheological fluids under the presence of an external magnetic field significantly change. In particular, if the particle concentration and field strength is sufficiently large, it becomes necessary to overcome a stress threshold, the so-called yield stress for the onset of flow. Furthermore, under the presence of external fields magnetorheological fluids become highly viscoelastic. The mechanical properties of these materials can be easily and rapidly controlled by the external magnetic field.

Due to their controllable mechanical properties, magnetorheological fluids are currently used in several commercial applications concerning vibration control, shock absorbers, precision polishing and even biomedical applications. Currently, for their proper performance, commercial devices require higher yield stresses in their operating modes and the use of highly concentrated magnetorheological fluids.

A careful study of the rheological behavior of these systems under compression can be of great utility since it has been shown that the yield stresses under compression are higher than the yield stresses under shear flow mode at the same concentration. An extensive investigation of the magnetorheological properties under compression has been carried out in this dissertation from an experimental point of view, using theoretical

developments and performing particle-level simulations. Experimental results showed that both the normal force and the compressive stress increase during the compression test. The dependence with the magnetic field strength was quadratic. The normal force and the yield compressive stress depend linearly on the particle volume fraction in the dilute case and quadratic in the concentrated regime.

Due to fact that the magnetic particles employed in the formulation of commercial magnetorheological fluids are typically polydisperse in size, the investigation of the effect of polydispersity in the MR performance is also of interest. Experiments and particle-level simulations were done on particle size distributions having the same average diameters but different polydispersity indexes. The results showed that although the microscopic structure of magnetorheological fluids profoundly changes with the polydispersity, overall, the yield stress does not significantly changes in polydisperse systems.

Resumen

Los fluidos magneto-reológicos se pueden considerar generalmente como suspensiones de partículas ferromagnéticas en un medio continuo no magnético. Cuando se aplica un campo magnético externo, las partículas se alinean en la dirección del campo formando agregados. Las propiedades mecánicas de los fluidos magneto-reológicos en presencia de un campo magnético externo cambian significativamente. Particularmente, si la concentración de partículas y el campo magnético son suficientemente grandes, es necesario superar una barrera de esfuerzo, llamada esfuerzo umbral, para que el sistema fluya. Además, los fluidos magneto-reológicos se vuelven altamente viscoelásticos. Las propiedades mecánicas de estos materiales son fácil y rápidamente controlables mediante el campo magnético externo.

Debido al control de sus propiedades mecánicas, los fluidos magneto-reológicos están siendo usados en varias aplicaciones comerciales que implican el control de vibraciones, la absorción de impactos, el pulido de precisión e incluso aplicaciones biomédicas. Actualmente, para un funcionamiento adecuado de estos dispositivos, se requiere un esfuerzo umbral alto en el modo operativo y el uso de fluidos magneto-reológicos altamente concentrados.

El estudio exhaustivo del comportamiento de estos sistemas en compresión puede ser de gran utilidad ya que se ha demostrado que los esfuerzos umbrales en compresión son mayores que los esfuerzos umbrales en cizalla para la misma concentración. Una extensa investigación de las propiedades magneto-reológicas en compresión ha sido realizada en esta tesis desde el punto de vista experimental, usando

desarrollos teóricos y realizando simulaciones a nivel de partícula. Los resultados experimentales mostraron que la fuerza normal y el esfuerzo de compresión se incrementan mientras el sistema se comprime. Se encontró una dependencia cuadrática con el campo magnético aplicado y una dependencia lineal con la concentración para el régimen diluido y cuadrática para el régimen concentrado.

Debido al hecho de que las partículas magnéticas empleadas en las formulaciones comerciales de fluidos magneto-reológicos son altamente polidispersas en tamaño, la investigación del efecto de la polidispersidad en la respuesta magneto-reológica es de gran interés. Se realizaron experimentos y simulaciones a nivel de partícula para distintas distribuciones de tamaños con el mismo diámetro medio pero diferentes índices de polidispersidad. Los resultados indican que, aunque la estructura microscópica de los fluidos magneto-reológicos cambia profundamente con la polidispersidad, el esfuerzo umbral no cambia significativamente en el caso de sistemas polidispersos.

Introduction

Magnetorheology deals with the flow and deformation of magnetic field-responsive materials. It is a branch in the Colloidal Science covering many disciplines such as Physics, Chemistry, Material Science and also Biology. The whole knowledge of this matter needs deep background in all these disciplines and the use of different approaches in order to obtain a thorough understanding of that matter.

The pioneering contribution in magnetorheology can be considered the publication entitled “*The magnetic fluid clutch*” by Rabinow (1948) at the U.S. National Bureau of Standards. In his paper, the fundamentals of the Magnetorheology were presented under the perspective of its industrial applications.

The main characteristic of magnetorheology is the so-called magnetorheological (MR) effect: the property of the MR fluids to change their mechanical properties from a liquid-like to a solid-like material by simply applying an external magnetic field. Thus, under the application of an external magnetic field, it is necessary to overcome a minimum stress threshold to flow. This minimum stress is called the *yield stress*.

The tunable mechanical properties of MR fluids make them suitable in many industrial applications. Undoubtedly, the most developed application of MR fluids concerns the active vibration control and the transmission of torque [Dyke *et al.* (1996), Li and Du (2003), Kavlicoglu *et al.* (2008), Zhu *et al.* (2012)] but also, other industries use MR fluids for different purposes: thermal energy transfer [Heine *et al.* (2006), Reinecke *et al.* (2008)], precision polishing [Kordonski *et al.* (2002), Jha

and Jain (2004), Kordonski *et al.* (2006), Das *et al.* (2007)], chemical sensing applications [Read and Martin (2010)] and biomedical applications [Liu *et al.* (2001)].

Generally speaking, conventional MR fluids can be described, from the microscopic point of view, as a dispersion of solid soft-ferromagnetic particles in a Newtonian non-magnetic liquid medium. The MR effect can be explained by the formation of chain-like aggregates aligned in the magnetic field direction when the external magnetic field is applied. Magnetic particles magnetize and behave as dipolar moments leading to the formation of gap-spanning elongated structures. The application of a mechanical stress to this structure initially deforms the chains within a solid regime, and eventually breaks the structure if the stress is sufficiently large behaving now as a liquid. A small coercivity/remnant magnetization and a large saturation magnetization is typically required for the dispersed particles in a MR fluid.

MR fluids are a kind of magnetic-active fluids [de Vicente *et al.* (2011)]. The latter are generally classified in terms of the particle size as: MR fluids (from 0.2 to 10 μm of diameter) and ferrofluids (from 3 to 15 nm of diameter) [Rosensweig (1985)]. Typically, in MR fluids, the magnetic interaction predominates, the Brownian motion can be considered negligible and particles are typically magnetic multi-domains. However, in ferrofluids, the Brownian motion is not negligible and the particles are typically magnetic single-domains. The mechanical properties of a ferrofluid can be described as Newtonian whatever the field. Another difference in the properties of MR fluids and ferrofluids underlies in the saturation magnetization. While in a MR fluid, particles typically have a large saturation magnetization, in a ferrofluid, the saturation magnetization is small.

In MR fluids, other classification can be usually done in terms of the nature of the solid phase. Conventional MR fluids (CMRFs) are typically composed of solid ferromagnetic particles in a non-magnetic fluid. However, another formulation for MR fluids can be used. It is possible to obtain a MR fluid with a solid non-magnetic phase dispersed into a magnetic fluid (i.e. a ferrofluid). These MR fluids are called inverse ferrofluids or magnetic holes. Thus, the magnetic properties of an inverse ferrofluid come the magnetic properties of the liquid phase, the ferrofluid, and due to the small saturation magnetization of ferrofluids, inverse ferrofluids are not suitable for commercial applications. However, inverse ferrofluids (IFFs) are more suitable as model MR fluids because it is easier to control the size and shape of the particles.

Commonly, particles used in CMRFs are carbonyl iron powders because of their large saturation magnetization (about 1500 kA/m). Carbonyl iron is obtained from the thermal decomposition of iron pentacarbonyl. The synthesis of carbonyl iron provides highly polydisperse particles ($PDI \sim 1.6$). For this reason, the study of the polydispersity effects in magnetorheology is one of the main aims in this thesis.

Commercial applications of MR fluids require high yield stress in their operating modes. Although the yield stress under compression is higher than in other kinds of flows, relatively scarce attention has been done in literature for the rheological properties of MR fluids under compressive flows. A study of the behavior of MR fluids under compression (squeeze) flow is another aim of this thesis.

MR fluids have an electric counterpart, electrorheological (ER) fluids. ER fluids are typically composed of solid particles dispersed in a liquid phase with two different dielectric permittivities or conductivities. Most of the results of this thesis can be easily extrapolated to ER fluids.

Interactions in magnetorheology

The mechanical properties of MR fluids are governed by a wide range of particle mediated interactions: particle-particle, particle-fluid and particle-wall. The main interactions to which the particles are subjected are the interparticle magnetic interactions and the particle-fluid hydrodynamic interactions. However, Brownian motion and other forces such as body forces (i.e. gravity) must be considered for a whole understanding of the system.

Interparticle magnetic interactions

Magnetic interactions are obviously dependent on the electromagnetic field acting in the system and the electromagnetic characteristics of the materials (i.e. constitutive equations). The system is governed by the Maxwell equations in matter [Jackson (1999)]:

$$\left\{ \begin{array}{l} \nabla \cdot \vec{D} = \rho_c \\ \nabla \cdot \vec{B} = 0 \\ \nabla \times \vec{E} = -\frac{\partial \vec{B}}{\partial t} \\ \nabla \times \vec{H} = \vec{j} - \frac{\partial \vec{D}}{\partial t} \end{array} \right. \quad (\text{In1})$$

where \vec{D} is the so-called electric displacement vector, ρ_c is the charge density, \vec{B} is the magnetic-flux density or magnetic induction, \vec{E} is the electric field, \vec{H} is the magnetic field, \vec{j} is the current density and t is the time.

Typically, in MR fluids subjected to the presence of an external magnetic field, the electric contribution in the electromagnetic field can be neglected as variations of the magnetic flux-density are slow and the charge density can be considered small. It is important to note that when

the external magnetic field is not applied, electric contributions could become important. Thus, the problem can be solved in the magnetostatics case:

$$\begin{cases} \nabla \cdot \vec{B} = 0 \\ \nabla \times \vec{H} = \vec{j} \end{cases} \quad (\text{In2})$$

The magnetic field, \vec{H} , is dependent on the magnetic flux density, \vec{B} , by a constitutive relationship: each material provides a different relationship between \vec{B} and \vec{H} , related to the average of the microscopic magnetic properties of the material. In matter, the atoms have electrons that, in the presence of magnetic fields, provide effective atomic currents and *magnetic moments*. If the density of magnetic moments in the material is \vec{M} , also called the *magnetization*, the general relationship among these three vectors is:

$$\vec{H} = \frac{1}{\mu_0} \vec{B} - \vec{M} \quad (\text{In3})$$

Here, μ_0 is the magnetic permeability of the vacuum that in SI units is $\mu_0 = 4\pi \times 10^{-7} \text{ N/A}^2$.

For some materials, named *linear materials*, the relationship between \vec{H} and \vec{M} is given by a constitutive linear equation: $\vec{M} = \chi \vec{H}$ where χ is the magnetic susceptibility. Thus, the relationship of the magnetic induction and the magnetic field is: $\vec{B} = \mu_0(1 + \chi)\vec{H} = \mu \vec{H}$. Here, μ is the *magnetic permeability* of the material. In order to compare different materials, it is convenient to define a *relative magnetic permeability*, μ_r as the ratio between the magnetic permeability of the material and the magnetic permeability of the vacuum: $\mu_r = \mu/\mu_0 = 1 + \chi$.

However, the linear relationship between the magnetic field and the magnetic induction does not hold for all materials. First, some materials

are not isotropic [e.g. ferrite crystals, Artman and Tannenwald (1955)] and second, the constitutive equation can be non linear [e.g. ferromagnetic materials Rosensweig (1985)]. Thus, in general, the constitutive relationship can be written as $\vec{B} = \boldsymbol{\mu} \cdot \vec{H}$ where $\boldsymbol{\mu}$ is the *magnetic permeability tensor*, generally dependent on the magnetic field, $\boldsymbol{\mu} = \boldsymbol{\mu}(\vec{H}) = (\mathbf{I} + \boldsymbol{\chi}(\vec{H}))$, where \mathbf{I} is the second-order identity tensor and $\boldsymbol{\chi}$ is the *magnetic susceptibility tensor*. Moreover, under alternating magnetic fields, magnetic induction may be lagged, and a complex magnetic permeability can be defined [see section 9.2 in Getzlaff (2008)] to deal with magnetic constitutive equations for high-frequency fields. Magnetic permeability also depends on the temperature of the system and the history of the system (so-called hysteresis effects).

Materials can be classified as a function of their magnetic properties. Linear materials are named *diamagnetic* materials if their magnetic susceptibility is negative, $\chi^{diam} < 0$, and *paramagnetic* materials if their magnetic susceptibility is positive, $\chi^{param} > 0$. Typically, diamagnetic and paramagnetic materials have weak magnetic properties, $|\chi| \sim 10^{-5}$ [Jackson (1999)]. Magnetic properties of particles used in MR fluids are typically *ferromagnetic*. The atomistic explanation of magnetism was one of the goals of quantum mechanics [for a further explanation of the magnetic properties in matter see Getzlaff (2008)].

As an example, Figure In.1 shows a typical magnetization curve of a carbonyl iron powder (HS grade) provided by BASF-SE. Three different regions are typically identified in this curve, [see chapter 11 in Bozorth (1951)]: First, at low magnetic field strengths, magnetization linearly increases as a function of the magnetic field, $M \sim \chi_i H$, where χ_i is the initial magnetic susceptibility (note that this is only possible in the case of soft ferromagnetic materials); second, at moderate magnetic fields, the

slope of the magnetization decreases in a transition region; and third, at high magnetic fields, the magnetization saturates and is independent on the magnetic field, $M \sim M_S$, where M_S is the *saturation magnetization*. Semi-empirical equations are preferably used in order to fully describe the magnetic properties in ferromagnetic materials.

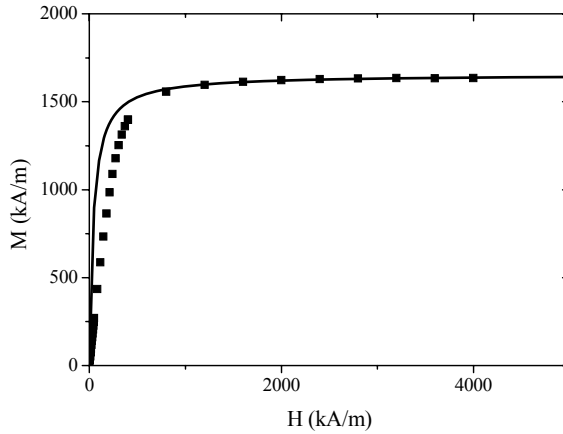


Figure In.1 Magnetization curve for carbonyl iron powder (HS grade). Solid line corresponds to the least-squared fit to the Fröhlich-Kennelly equation (Equation In4).

Among them, Fröhlich-Kennelly equation [Jiles (1991)] is a empirical equation that is wide-used in magnetorheology [i.e. Ginder *et al.* (1996), Klingenberg *et al.* (2007a)]:

$$M = \frac{\chi_i H}{1 + \frac{\chi_i H}{M_S}} \quad (\text{In4})$$

As shown in Figure In.1, Fröhlich-Kennelly model reasonably fits the experimental data at high and low magnetic fields, but at moderate magnetic fields, in the transition region, the model overestimates the experimental curve. For the case considered, initial magnetic susceptibility and saturation magnetization were found to be $\chi_i = 39 \pm 4$

and $\mu_0 M_S = 2.079 \pm 0.03 T$. Other models can be employed in order to obtain the magnetization of a ferromagnetic material such as piecewise linear models [Lee *et al.* (1991)] or other relationships [see Equation 4 in Klingenberg *et al.* (2007a)].

At this stage it is worth to point out that the magnetization of a ferromagnetic material also depends on the size of the sample. An interesting work carried out by Billas *et al.* (1993) showed that if the sample is enough small (i.e. clusters of few atoms) the magnetic moment per atom, and, hence, the magnetization, was higher about a 20% than the magnetic moment in the bulk.

Once known the particular relationship between the magnetic field and the magnetic induction, Equation In2 can be solved. In order to find the expression for the magnetic field, let us first consider the case of a single perfectly-spherical particle of diameter of σ , and a magnetic permeability, μ_p (relative permeability μ_{pr}), immersed in a continuous medium of magnetic permeability, μ_c (relative permeability μ_{cr}) and under the presence of an external magnetic field applied \vec{H}_0 . Let us consider a coordinate system in the z -direction aligned with the magnetic field and centered in the particle. If there are no free currents, magnetostatic equations are: $\nabla \cdot \vec{B} = 0$ and $\nabla \times \vec{H} = 0$. As the magnetic field is irrotational, there exists a scalar potential, Φ_M , so that the gradient of this potential is the magnetic field: $\vec{H} = -\nabla\Phi_M$. The magnetic field is now given by the expression:

$$\nabla \cdot (-\mu\nabla\Phi_M) = 0 \tag{In5}$$

If the magnetic field is small (i.e. the magnetic properties can be assumed as linear), Equation In5 leads to the Laplace's equation: $\nabla^2\Phi_M = 0$. Taking into account the boundary conditions for the magnetic field at the

interface, the magnetic field in spherical coordinates is given by Equation In6 [Jackson (1999)]:

$$\vec{H}(r, \theta) = \begin{cases} \frac{3\mu_{cr}}{\mu_{pr}+2\mu_{cr}} \vec{H}_0 & r \leq \sigma/2 \\ \vec{H}_0 + \frac{\mu_{pr}-\mu_{cr}}{\mu_{pr}+2\mu_{cr}} \left(\frac{\sigma}{2r}\right)^3 H_0 (2\cos\theta\hat{r} + \sin\theta\hat{\theta}) & r > \sigma/2 \end{cases} \quad (\text{In6})$$

Here, r and θ are the radial and polar coordinates respectively and \hat{r} is the radial unit vector and $\hat{\theta}$ is the polar unit vector.

The main fact in Equation In6 is that the magnetic field inside is constant and it provides a uniform magnetization. Moreover, outside the particle the magnetic field is the superposition of the external magnetic field and the field created by a punctual dipole moment with: $\vec{m} = \frac{\pi}{2} \frac{\mu_{pr}-\mu_{cr}}{\mu_{pr}+2\mu_{cr}} \sigma^3 \vec{H}_0$.

This moment depends on the difference of the magnetic permeabilities of the particle and the continuous medium. The factor $\frac{\mu_{pr}-\mu_{cr}}{\mu_{pr}+2\mu_{cr}}$ is called the *contrast factor* and is frequently represented by the Greek letter β . In the case of CMRFs, β must be in the interval $0 < \beta < 1$; however, for IFFs, β is negative and $-0.5 < \beta < 0$.

The magnetization of the particle is $\vec{M} = 3\beta\vec{H}_0$, and the field inside the particle can be expressed as $\vec{H} = \vec{H}_0 - \vec{M}/3$. Here, the factor 1/3 is due to the spherical shape of the particle. Generally, if a particle has an arbitrary shape and it is uniformly magnetized, the field inside can be expressed as follows: $\vec{H} = \vec{H}_0 - \mathbf{N}_D \cdot \vec{M}$ where \mathbf{N}_D is the so-called demagnetizing tensor. In the case of spherical particles, the tensor is diagonal and all its components are 1/3. In the case of other geometries, the demagnetizing tensor components can be dissimilar. For example, in the case of an infinite plate, the demagnetizing tensor is 1 in the direction normal to the plate and 0 in the other directions. In the case of an infinite cylinder the

demagnetizing tensor is 1/2 in the finite axes and 0 for the infinite axis. The calculation of the demagnetizing tensor for the general ellipsoid was given by Osborn (1945).

It is worth to note that in the derivation of the magnetic field, linearity is assumed. However, it is possible to generalize Equation In6 for ferromagnetic materials. The process consists in: first, to obtain the magnetic permeability for the external magnetic field, $\mu_{pr}(H_0)$. Then the internal magnetic field, H_1 , in the particle can be calculated by Equation In6. Once calculated the internal magnetic field, the magnetic permeability can be calculated from the magnetization curve for the new magnetic field, $\mu_{pr}(H_1)$. This is a self-consistent process that is repeated up to the convergence of the internal magnetic field and the magnetic permeability.

Unfortunately, in systems with two or more particles, the solution of the Maxwell equations complicates if compared to the case of an isolated particle, and the contribution of the magnetic field of the system is not the contribution of punctual dipoles placed at the center of any particle. However, let us first assume that other contributions can be neglected and the main contribution of the magnetic field due to the particles is dipolar in a first approximation (note that this is only possible in the dilute case). We will consider two identical particles, i and j , of the same diameter, σ , and the same magnetic permeability, μ_{pr} . The particle i is situated at the center of the coordinate system and the other particle, j , is placed at a position, \vec{r}_{ij} . An external magnetic field is applied in the z -direction, $\vec{H}_0 = H_0 \hat{z}$, where \hat{z} is the unit vector in the z -direction in a Cartesian coordinate system.

The dipolar energy of the particle i due to the field exerted by the particle j at the position of the particle i , can be calculated as follows:

$$U_{ij}^{dip} = -\vec{m}_i \cdot \vec{B}_j = \frac{\pi}{16} \pi \mu_0 \mu_{cr} \beta^2 H_0^2 \sigma^3 \left(\frac{\sigma}{r_{ij}} \right)^3 (1 - 3 \cos^2 \theta_{ij}) \quad (\text{In7})$$

Here, θ_{ij} stands for the angle between the line joining the two particles and the direction of the external magnetic field. The typical dipolar energy between two particles can be considered $U_d = \frac{\pi}{16} \mu_0 \mu_{cr} \beta^2 H_0^2 \sigma^3$. For the typical values in magnetorheology, $\sigma \sim 1 \mu m$, and $H_0 \sim 177 \text{ kA/m}$, the magnetic dipolar energy would be $U_d \sim 24 \text{ keV}$.

The force acting on the particle i due to the magnetic dipolar field created by the particle j is: $\vec{F} = \nabla(\vec{m}_i \cdot \vec{B}_j)$. Taking into account that the dipolar moment of the particle i is constant (does not depend on the position of the particle), in the point-dipole limit, after some algebra, the interacting force can be expressed as follows:

$$\vec{F}_{ij}^{dip} = \frac{3}{16} \pi \mu_0 \mu_{cr} \beta^2 H_0^2 \sigma^2 \left(\frac{\sigma}{r_{ij}} \right)^4 [(3 \cos^2 \theta_{ij} - 1) \hat{r} + \sin 2\theta_{ij} \hat{\theta}] \quad (\text{In8})$$

It is worth to note that the interaction between two particles can be attractive or repulsive depending on the angle θ_{ij} . If $3 \cos^2 \theta_{ij} - 1 > 0$ the interaction will be attractive but if $3 \cos^2 \theta_{ij} - 1 < 0$ the interaction becomes negative. The critical angle is: $\theta_c = \arccos \sqrt{1/3} \approx 54.73^\circ$.

Equation In8 provides a first approximation of the magnetostatic force between particles. This force scale is of the order: $F_0 = \frac{3}{16} \pi \mu_0 \mu_{cr} \beta^2 H_0^2 \sigma^2$. For the typical values of particle diameters in magnetorheology, $\sigma \sim 1 \mu m$, and $H_0 \sim 177 \text{ kA/m}$, the magnetic force would be in the order of $F_0 \sim 12 \text{ nN}$.

Equations In7 and In8 strongly depend on the particle size. These equations depend on the multiplication of the volumes of the particle i and j . If all the particles have not the same diameter, Equations In7 and In8 will transform to Equations In9 and In10:

$$U_{ij}^{dip} = \frac{\pi}{16} \pi \mu_0 \mu_{cr} \beta^2 H_0^2 \frac{\sigma_i^3 \sigma_j^3}{r_{ij}^3} (1 - 3 \cos^2 \theta_{ij}) \quad (\text{In9})$$

$$\vec{F}_{ij}^{dip} = \frac{3}{16} \pi \mu_0 \mu_{cr} \beta^2 H_0^2 \frac{\sigma_i^3 \sigma_j^3}{r_{ij}^4} [(3 \cos^2 \theta_{ij} - 1) \hat{r} + \sin 2\theta_{ij} \hat{\theta}] \quad (\text{In10})$$

As shown by Equations In9 and In10, the interaction between two particles in a polydisperse system will be different depending on the size of each particle.

As mentioned above, the dipolar interaction between two particles truly exists in the case of low fields and dilute suspensions. For higher fields, the magnetization of the particle cannot be longer expressed as $\vec{M} = 3\beta\vec{H}_0$ because the magnetization vector varies with position inside a particle. One possibility to solve this problem is by using the so-called Mean Magnetization Approximation. In this approximation, the mean of the magnetization of the particles is used and calculated from the magnetization of the suspension: $\langle M_p \rangle = M_{sus}/\phi$, where M_{sus} is the magnetization of the total suspension and ϕ is the volume fraction of the magnetic particles in the suspension [Klingenberg *et al.* (2007a)]. The Mean Magnetization approximation is tested in this dissertation in Chapter 7.

Local Field Theory is frequently used in order to calculate the magnetic field in a suspension of many particles. According to this, the moment of a particle i , is $\vec{m}_i = \pi\beta\sigma^3\vec{H}_{loc}(\vec{r}_i)/2$ where $\vec{H}_{loc}(\vec{r}_i)$ is the local field at the position of the particle i , \vec{r}_i . The local field is calculated by the summation

of the external magnetic field and the magnetic fields due to the magnetic dipoles of the other particles as shown in Equation In11:

$$\vec{H}_{\text{loc}}(\vec{r}_i) = \vec{H}_0 + \sum_{j \neq i} \frac{3(\vec{m}_i \cdot \hat{r})\hat{r} - \vec{m}_j}{4\pi r_{ij}^3} \quad (\text{In11})$$

The local magnetic field depends on the magnetic moments of the particles, but also the magnetic moments of the particles depend on the local magnetic field. The solution of these equations must be done in a self-consistent process. First, the moments of the particles are calculated for the external magnetic field. Then, the local field is calculated using Equation In11. Later, the magnetic moments are calculated using the local field. The process must be repeated up to obtain a desired convergence. However, Equation In11 also uses the dipolar approximation and multipolar effects are neglected. Many-body interactions were calculated, for ER fluids, for example, in Clercx and Bossis (1993).

Hydrodynamic interactions

Magnetostatic interactions are not the only interactions present in MR fluids. If the system is subjected to a flow, hydrodynamic interactions are important to describe the MR behavior of the system. Generally speaking, the mechanical behavior of MR fluids can be explained by the field-driven structuration of the suspension and the eventual breakage of the structures under the application of a strong enough flow field.

Hydrodynamic interactions considered in this work only concern the drag force exerted by the flow onto the particles. First, we assume an isolated spherical particle of diameter σ in an incompressible Newtonian fluid with viscosity η and density ρ . The coordinate system is centered at the particle and the velocity of the fluid at large distances, $r \rightarrow \infty$ is $\vec{v} = -v\hat{z}$. In the “creeping” flow limit (i.e. for very small Reynolds numbers, $Re =$

$v\sigma\rho/\eta \rightarrow 0$) the velocity field is given by Equation In12 [Bird *et al.* (1987)]:

$$\vec{v} = -v \left[1 - \frac{3\sigma}{4r} + \frac{1}{16} \left(\frac{\sigma}{r} \right)^3 \right] \cos \theta \hat{r} + v \left[1 - \frac{3\sigma}{8r} - \frac{1}{32} \left(\frac{\sigma}{r} \right)^3 \right] \sin \theta \hat{\theta} \quad (\text{In12})$$

In this case, the streamlines are shown in Figure In.2. The drag force exerted by the fluid is given by the integral of the total stress tensor at the surface of the particle, $\vec{F}_{hyd} = -3\pi\sigma\eta\vec{v}$ [Bird *et al.* (1987)]. If the particle is also moving, the hydrodynamic force will be proportional to the relative velocity as follows:

$$\vec{F}_{hyd} = -3\pi\sigma\eta \left(\frac{d\vec{r}_i}{dt} - \vec{u}_i^\infty \right) \quad (\text{In13})$$

where \vec{u}_i^∞ is the velocity of the Newtonian fluid at the position of the particle i not considering the particle distortion of the flow field.

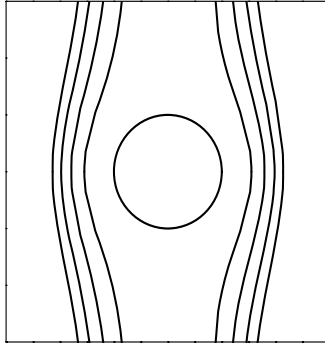


Figure In.2 Streamlines for a steady flow with a velocity $\vec{v} = -v\hat{z}$ at large distances from the sphere.

Equation In13 gives the so-called Stokesian drag force. As shown in this equation, the hydrodynamic force depends on the fluid velocity and, thus, on the kind of flow field the particle is subjected.

Let us consider now one of the simplest problems in fluid mechanics. The system consists in two parallel plates separated by a gap, h , and a Newtonian fluid of viscosity η confined within them. The upper plate is moving in the direction x as shown in Figure In.3 with a velocity $\vec{v} = v\hat{x}$. The solution of the equation of motions leads to a velocity field given by: $\vec{v} = \dot{\gamma}z\hat{x}$, where $\dot{\gamma}$ is defined as the shear rate, that, in this case is $\dot{\gamma} = v/h$.

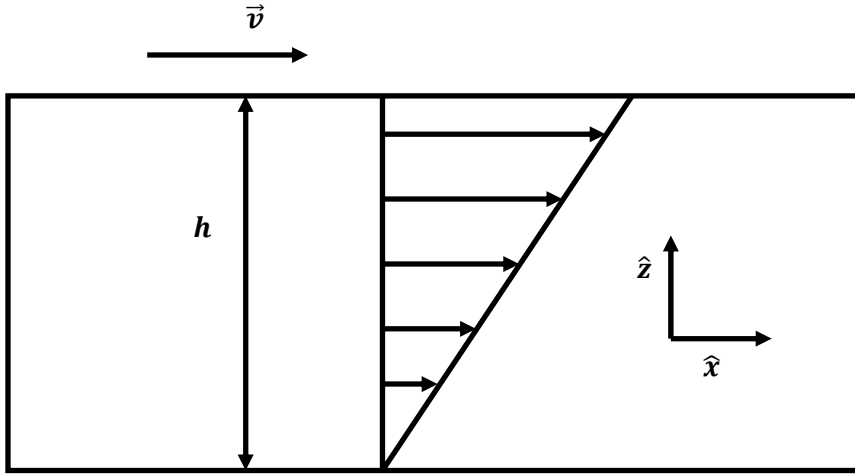


Figure In.3. Schematics of the steady shear flow between parallel-plates and fluid velocity profile.

Therefore, the drag force on a particle situated in a position z_i is: $\vec{F}_{hyd} = -3\pi\sigma\eta\left(\frac{d\vec{r}_i}{dt} - \dot{\gamma}z_i\hat{x}\right)$. The typical hydrodynamic force scale can be considered as: $F_{hyd} = 3\pi\sigma^2\eta\dot{\gamma}$ [Klingenberg *et al.* (2007a)].

The hydrodynamic force depends on the shear rate applied to the system. It is possible to define a dimensionless number as the ratio between the typical hydrodynamic force and the typical magnetostatic force. This dimensionless number is called the *Mason number*, Mn , and is expressed as follows:

$$Mn = \frac{F_{hyd}}{F_0} = \frac{8\eta\dot{\gamma}}{\mu_0\mu_{cr}\beta^2H_0^2} \quad (\text{In14})$$

The Mason number is a widely-used dimensionless number in magnetorheology [e.g. de Vicente et al. (2011), Ramos et al. (2011), Felt et al. (1996), Klingenberg *et al.* (2007a)]. It is important to note that the particular definitions for the “typical” hydrodynamic and magnetostatic forces scales may differ and thus, the definitions of the Mason number differ in the literature [Klingenberg *et al.* (2007a)]. Generally speaking, if the Mason number is small, the magnetostatic interaction predominates and the chain-like structures formed by the application of an external magnetic field remain. However, if the Mason number is large, hydrodynamic interaction predominates and the chain-like structures break. The transition between these two regimes occurs at a critical value of the Mason number, Mn^* [de Vicente et al. (2011), Berli and de Vicente (2011)].

Shear viscosity measurements are often expressed as a function of the Mason number instead of the shear rate since experimental tests at different magnetic field strengths reasonably collapse into a master curve if they are represented as a function of the Mason number [Klingenberg *et al.* (2007a)]. This fact is important for modeling the rheological behavior of MR fluids. It is also important to note that a more precise definition for the Mason number has been proposed in the literature for high magnetic fields [Klingenberg *et al.* (2007a)]. A more detailed discussion on this aspect will be the object of Chapter 7.

Micromechanical models have been proposed in the literature in order to obtain the critical Mason number, Mn^* [Martin and Anderson (1996), de Vicente *et al.* (2004), de Gans *et al.* (1999), Volkova *et al.* (2000)]. All these deterministic models (i.e. models neglecting Brownian motion)

predict a linear dependence on the particle volume fraction, ϕ , in the dilute case.

As mentioned above, Equation In13 is only valid in the case of an isolated particle. Fluid velocity and the drag force calculations in a suspension of many particles is not simple. The solution to the problem is given in the papers by Schmitz and Felderhof (1982) and Brady and Bossis (1988), for example. However, the calculation of the full hydrodynamic interaction in a general system of particles is only viable in simulations containing very few particles (approx. 100). A recent simulation study carried out by Lager et al. (2015) demonstrated that the Stokesian drag force suffices to explain the rheological behavior of MR fluids if the hydrodynamic component of the stress is not predominant over the total stress.

Brownian motion

Brownian motion is usually associated to the random movement of microscopic particles within a continuous medium fluid. The discovery of the Brownian motion is attributed to Robert Brown in 1827 while he was observing the movement of pollen grains in water.

Generally speaking, the explanation of the Brownian motion is given by the thermal fluctuation of atoms and molecules in the continuous medium and the collisions between these atoms and molecules and the colloidal particles. A continuous medium is assumed to be composed of an ensemble of atoms and molecules in thermal equilibrium (i.e. the temperature of the system is constant). This thermal equilibrium is translated, in the microscopic scale, to an average kinetic energy of the particles in the continuous medium. If a colloidal particle is immersed in the system, there will be collisions between the particles in the continuous

medium and the colloidal particle and the colloidal particle will move as a result of these collisions.

In the case of non-interacting particles, Brownian motion can be described in terms of the Stokes-Einstein relation. However, in the case of interacting particles, the probability of a system of N particles in equilibrium, at a temperature, T , initially situated in one position configuration $\alpha = (\vec{r}_1, \vec{r}_2, \dots, \vec{r}_N)$ to move to another configuration $\alpha' = (\vec{r}'_1, \vec{r}'_2, \dots, \vec{r}'_N)$ is given by:

$$P(\alpha \rightarrow \alpha') = \frac{1}{Z} e^{\frac{U(\alpha) - U(\alpha')}{k_B T}} \quad (\text{In15})$$

where $U(\alpha)$ is the potential energy of the particles at the configuration α , k_B is the Boltzmann constant and Z is the so-called partition function that is defined as the integral over all the possible configurations of the system of the Boltzmann factor: $Z = \frac{V}{\Lambda^{3N}} \int d\alpha \exp\left(-\frac{U(\alpha)}{k_B T}\right)$ where V is the volume of the system and Λ is the thermal wavelength of a particle [de Gans *et al.* (2000)]. For this particular system, the partition function was calculated in de Gans *et al.* (2000). In the case of a pair-wise potential energy the Boltzmann factor can be factorized as the interaction of each pair of particles:

$$\exp\left(-\frac{U(\alpha)}{k_B T}\right) = \exp\left[\sum_{j \neq i} \left(-\frac{U_2(r_{ij})}{k_B T}\right)\right] = \prod_{j \neq i} \exp\left(-\frac{U_2(r_{ij})}{k_B T}\right)$$

where $U_2(r_{ij})$ is the potential energy of a pair of particles.

As the magnetostatic interaction is assumed to be the main potential interaction between particles, the Brownian motion depends on the strength of the magnetic dipolar potential energy related to the thermal energy. It is possible to define a dimensionless parameter, the so-called

Lambda ratio, λ , as the “typical” magnetic dipolar energy divided by the thermal energy:

$$\lambda = \frac{U_d}{k_B T} = \frac{\pi \mu_0 \mu_{cr} \beta^2 H_0^2 \sigma^3}{16 k_B T} \quad (\text{In16})$$

Equation In16 is widely-used in the description of field-active fluids [e.g. de Gans *et al.* (2000), de Vicente *et al.* (2011), Sherman *et al.* (2015)]. As shown in Equation In16, Brownian motion depends on the particle diameter to the cube. For typical values of particle diameters and magnetic fields, Lambda ratio is usually large enough to neglect the Brownian motion of the particles in the on-state. In the case of CMRFs and IFFs, $\lambda > 100$. For these systems, the magnetostatic interaction is much higher than the thermal interaction and the Brownian motion is safely neglected, resulting in the formation of chain-like structures [de Vicente *et al.* (2011)].

However, in the case of ferrofluids, the typical particle diameters are in the range of the nanometers and therefore the Lambda ratio is $\lambda \sim 0.03$. As a result, in ferrofluids, the Brownian motion predominates and there should not occur the formation of chain-like structures under field. In fact, the rheological behavior of ferrofluids is generally described as Newtonian fluids.

It is important to note that in the case of polydisperse systems Brownian motion may be important for the smallest particles. For this reason in Chapter 8, Brownian motion will be also included in the particle-level simulations of MR fluids.

The three dimensionless parameters defined so far; the Mason number, the Lambda ratio and the particle volume fraction are of major importance

because they govern the rheological behavior of MR fluids under fields [de Vicente et al. 2011]).

Particularly, Furst and Gast (2000) demonstrated that the equilibrium structure of latex-based MR fluids, under the application of an external magnetic field and in the quiescent state, only depends on λ and ϕ . The aggregation process occurs in two steps. Firstly, the aggregation starts with the formation of chains in a very rapid process. Here, the average length of the aggregates increases as a power law following the Smoluchowski equation. Once formed the single-particle-width chains, they aggregate forming more complex clusters. These processes were experimentally observed using optical tweezers and microscopic observations [Furst and Gast (2000) and Cutillas *et al.* (1998)].

Gravity, sedimentation and other interactions

Other forces could be important to describe the performance of MR fluids. For instance, body forces, such as gravity, must be considered in some cases for a whole description of these fluids.

Usually, dispersed particles have a large density and the density mismatch between the particles and the carrier liquid can be important. Considering an spherical particle of density, ρ_p , immersed in a carried liquid of density ρ , the total body force due to the gravity exerted in the particle is the balance of the weight of the particle and the weight of the fluid displaced by the particle, \vec{F}_B . This force can be expressed as:

$$\vec{F}_B = \frac{\pi}{6} \sigma^3 (\rho_p - \rho) \vec{g} \quad (\text{In17})$$

where $g = 9.81 \text{ m/s}^2$ is the acceleration of the gravity.

Frequently, the body force due to gravity is neglected because in the on-state (i.e. when the magnetic field is applied) the magnetostatic force is higher than the gravity force [Parthasarathy *et al.* (1996)]. Klingenberg *et al.* (2007b) proposed a dimensionless number taking into account the relationship between the typical gravity force in a particle and the interparticle magnetostatic dipolar force, G :

$$G = \frac{8\sigma|\rho_p - \rho|g}{9\mu_0\mu_{cr}\beta^2 H_0^2} \quad (\text{In18})$$

where $||$ refers the absolute value in order to take into account the magnitude of the forces but not the direction.

Typical values in CMRFs give $G < 10^{-3}$. In the case of IFFs, this factor is in the order of: $G \cong 1.2 \cdot 10^{-3}$. Finally, the small particle size of ferrofluids results in a very small G : $G < 10^{-6}$. This means that in the on-state, gravity forces are generally smaller than magnetostatic forces.

The simulation work developed by Klingenberg and coworkers (2007b) demonstrated that although the value of the dimensionless number, G , is generally less than unity, gravity forces could still be important and they proposed a critical G -number, G_C , depending on the structure of the chain: $G_C = \frac{1.29\sigma}{h}$ in the case of single chains and $G_C = \frac{2.61\sigma}{h}$ in the case of double chains, where h is the gap separation between the parallel plates. For values of G higher than G_C , gravity forces must be considered but for values of G less than G_C , the effects of the gravity forces can be safely neglected. It is important to note that the critical G -number is inversely proportional to the gap between plates, so that for large gaps, the critical G -number can approach to typical values in magnetorheology. For the gaps used in this dissertation, $G_C \sim 10^{-2}$, so the gravity forces for all the systems (CMRFs, IFFs and ferrofluids) can be safely neglected.

In the durability of MR devices, it is not only important to minimize the sedimentation when the system is being used but also when the system is in its off-state. In the literature, different MR formulations have been proposed in order to avoid particle settling and agglomeration. As mentioned above, diminishing the particle size can avoid sedimentation and agglomeration. However, Brownian forces could also increase and therefore there is a compromise in the particle size.

Some of these formulations are related to modifications in the particle formulation as the addition of low-density shells covering the ferromagnetic core such as polymer coatings [Choi et al. (2006) and Wu et al. (2006)]. The use of magnetic fibers instead of spherical particles also avoids particle settling. Furthermore, the magnetic fibers exhibit a higher yield stress than spherical particles at the same concentration [Bell et al. (2008)]. This result was also reported in simulations [Kor and See (2010)] and is in agreement with results reported for ER fluids [Kanu and Shaw (1998), Otsubo (1999)]. Other approximations concern the modification of the carried medium using viscoplastic media such as greases [Rankin et al. (1999)], thixotropic networks [de Vicente et al. (2003), Chin et al. (2001)] or temperature sensitive materials [Shahrivar and de Vicente (2013)]. Recently, MR plastomers have been used in order to avoid particle sedimentation [An et al. (2010), Xu et al. (2014)]. In this dissertation, the formulation of the MR fluids was as simple as possible and contains the minimum number of ingredients. Including additives in the formulations could mask the relevant physical mechanisms under study.

Other interactions can be involved in the rheological behavior of MR fluids. Klingenberg et al. (2010) developed an experimental and simulation study of the non-magnetic interparticle forces on MR fluids. In this study, the effect of van der Waals forces was investigated in

simulations obtaining that the shear stress slightly increases as the ratio between the van der Waals and magnetostatic forces increases. The off-state stress also increases as the van der Waals forces increases. A recent simulation study developed by Fernández-Toledano *et al.* (2014) dealt with short-range repulsive and attractive forces by using R-shifted Lenard-Jones potentials or only short-range repulsive interactions. The addition of a short-range attractive interaction using R-shifted Lenard-Jones potentials leads to a two step yielding behavior also found in experiments at high concentrations [Segovia-Gutiérrez *et al.* (2012)].

Rheology

The term rheology proceeds from the Greek “rheo-” that means flow or stream. Rheology is, thus, the branch of the Science that studies the flow of the matter. It refers to the movement of the materials under a continuous medium approach.

Conservation laws

In differential form, mass and momentum conservation equations are given by [Bird *et al.* (1987)]:

Continuity equation

$$\frac{\partial \rho}{\partial t} + \nabla \cdot (\rho \vec{v}) = 0 \quad (\text{In19})$$

Equation of motion

$$\frac{\partial(\rho \vec{v})}{\partial t} + \nabla \cdot (\rho \vec{v} \vec{v}) = \nabla \cdot \mathbf{\Pi} + \rho \vec{g} \quad (\text{In20})$$

Energy conservation law

$$\frac{\partial(\rho \hat{U})}{\partial t} + \nabla \cdot (\rho \hat{U} \vec{v}) = -\nabla \cdot \vec{q} + \mathbf{\Pi} : \nabla \vec{v} \quad (\text{In21})$$

Equation In19 comes from the mass conservation and it can be simplified for *incompressible materials* to $\nabla \cdot \vec{v} = 0$. MR fluids can be safely considered as incompressible materials.

Equation In20 comes from the momentum conservation. The term $\mathbf{\Pi}$ is the so-called *total stress tensor*. The total stress components, Π_{ij} refers to the force per unit area in the positive j -direction applied on a surface normal to the i -direction [Bird *et al.* (1987)] as shown in Figure In.4.

It is important to note that in most cases the angular momentum conservation law leads to a symmetric total stress tensor. The total stress tensor can be divided in two parts as follows:

$$\mathbf{\Pi} = -\nabla p + \boldsymbol{\tau} \quad (\text{In21})$$

where p is the thermodynamic/mean pressure and $\boldsymbol{\tau}$ is called the extra or deviatoric stress tensor.

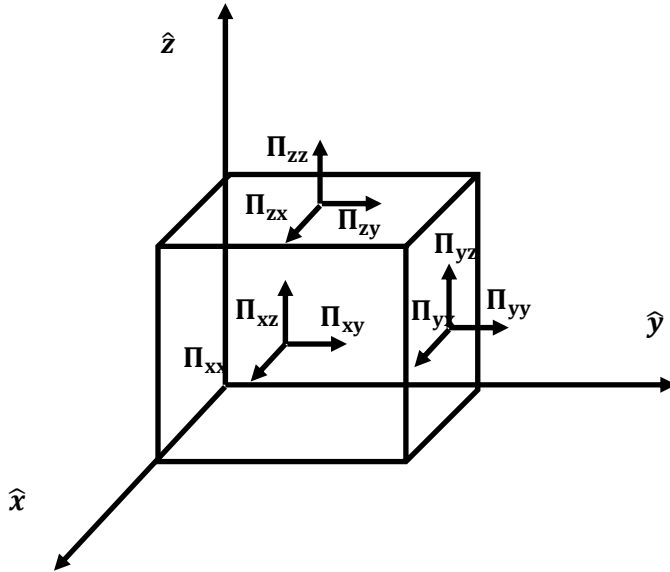


Figure In.4. Scheme of the total tensor stress components

Equation In20 comes from the energy conservation where \hat{U} is the *internal energy per unit mass* and \vec{q} is the *heat flux*.

The solution of the system requires additional information since there are more unknown quantities than equations. This fact is expected since Equations In18-20 are valid for *any* continuum media. These additional equations are called *constitutive equations* and offer relationships between the stress tensor and the kinematics in the materials. The finding of the constitutive equations for the materials is a major issue in Rheology.

Shear flow rheology

The constitutive equation of Newtonian fluids is give by [Bird *et al.* (1987)]:

$$\boldsymbol{\tau} = \eta \dot{\boldsymbol{\gamma}} - \left(\frac{2}{3} \eta - \kappa \right) \nabla \cdot \vec{v} \mathbf{I} \quad (\text{In22})$$

where $\dot{\boldsymbol{\gamma}}$ is the so-called *shear rate tensor* related to the field velocity: $\dot{\boldsymbol{\gamma}} = \nabla \vec{v} + (\nabla \vec{v})^T$. Here, the symbol T refers to the transpose of the tensor and κ is called the *dilatational viscosity*. For incompressible fluids Equation In22 reduced to: $\boldsymbol{\tau} = \eta \dot{\boldsymbol{\gamma}}$ since $\nabla \cdot \vec{v} = 0$.

Obviously, the constitutive equation of MR fluids cannot be described as Newtonian under the presence of an external magnetic field. Fluids whose behavior is not described by Equation In22 are commonly called *Non-Newtonian fluids*. Apart from memory effects, generally speaking, the properties of a Non-Newtonian fluid cannot be described with a constant viscosity but the viscosity depends on the shear rate: $\eta = \eta(\dot{\gamma})$. Here the shear rate is defined in terms of the shear rate tensor: $\dot{\gamma} = \sqrt{\frac{1}{2} \dot{\boldsymbol{\gamma}} : \dot{\boldsymbol{\gamma}}}$. If the viscosity decreases as the shear rate increases the fluid is called a *shear-thinning fluid*. If the viscosity increases as the shear rate increases, the

fluid is called a *shear-thickening fluid*. If the viscosity diverges in the zero shear-rate limit, the fluid is considered as a plastic material with a yield stress.

In order to obtain the constitutive equations of MR fluids some material functions related to specific kinematics must be defined. Here we only focus on shearing and squeeze flow fields.

Particularly, we are going to consider the flow under steady shear, the shear-stress growth, the shear stress relaxation and under oscillatory shear (small-amplitude oscillatory shear, SAOS or large-amplitude oscillatory shear, LAOS). In all these cases the velocity of the system has the general expression: $\vec{v} = (\dot{\zeta}(t)z, 0, 0)$ where $\dot{\zeta}$ is a shear rate function of time.

Steady shear flow

In the case of a steady shear flow, the shear rate function is: $\dot{\zeta}(t) = \dot{\gamma}_0$ where $\dot{\gamma}_0$ is a constant shear rate. The three material functions defined for this kind of kinematics are: $\eta(\dot{\gamma}) = \tau_{zx}/\dot{\gamma}_0$, $\psi_1(\dot{\gamma}) = (\tau_{xx} - \tau_{zz})/\dot{\gamma}_0^2$ and $\psi_2(\dot{\gamma}) = (\tau_{zz} - \tau_{yy})/\dot{\gamma}_0^2$, where $\eta(\dot{\gamma})$ is the viscosity, $\psi_1(\dot{\gamma})$ is the primary normal stress coefficient and $\psi_2(\dot{\gamma})$ is the second normal stress coefficient. For a Newtonian fluid the normal coefficients are 0, but for Non-Newtonian fluids, normal stress coefficients are not zero [e.g. Weissenberg effect, Weissenberg (1947)].

Stress growth

For stress growth tests, a constant shear rate is suddenly applied at an instant, t_0 . In this case, the shear stress function is: $\dot{\zeta}(t) = \begin{cases} 0 & t \leq t_0 \\ \dot{\gamma}_0 & t > t_0 \end{cases}$. The material functions are now, $\eta^+(t, \dot{\gamma}) = \tau_{zx}/\dot{\gamma}_0$, $\psi_1^+(t, \dot{\gamma}) = (\tau_{xx} - \tau_{zz})/\dot{\gamma}_0^2$ and $\psi_2^+(t, \dot{\gamma}) = (\tau_{zz} - \tau_{yy})/\dot{\gamma}_0^2$. It is

important to note, that the viscosity and the stress tensor is now not only a function of the shear rate but also of the time.

Generally speaking, in MR fluids subjected to a stress growth test, the shear stress, τ_{zx} starts to increase linearly in a elastic region. Later, the stress achieves a maximum and for large enough times, the stress becomes constant in a stationary plateau [see Figure 2 in de Vicente *et al.* (2011)]. So, it is possible to relate a constant shear stress associated to the shear rate as the shear stress plateau at large times.

Stress relaxation

In the case of stress relaxation tests, a constant shear rate is applied until a certain time when the shear rate becomes zero. The shear rate function is:

$\dot{\zeta}(t) = \begin{cases} \dot{\gamma}_0 & t \leq t_0 \\ 0 & t > t_0 \end{cases}$. The material functions are also dependent on the time:

$$\eta^-(t, \dot{\gamma}) = \tau_{zx}/\dot{\gamma}_0, \quad \psi_1^-(t, \dot{\gamma}) = (\tau_{xx} - \tau_{zz})/\dot{\gamma}_0^2 \quad \text{and} \quad \psi_2^-(t, \dot{\gamma}) = (\tau_{zz} - \tau_{yy})/\dot{\gamma}_0^2.$$

Creep

In creep tests, a sudden constant shear stress is applied: $\tau_{zx}(t) = \begin{cases} 0 & t \leq t_0 \\ \tau_0 & t > t_0 \end{cases}$. The main material function is called the compliance, $J(t)$, and

it is defined as: $J(t) = \gamma(t)/\tau_0$ where $\gamma(t)$ is the total strain as a function of the time. In MR fluids, creep tests start with a rapid increase in the compliance and then the compliance linearly increases as a function of the time, leading to a constant shear rate, as in the case of shear growth tests.

Usually, creep tests are performed together with a recovery test. In a recent study, Wang *et al.* (2014) investigated the creep and recovery of MR fluids using an experimental and simulation approach.

Oscillatory shear

In an oscillatory shear test, an oscillating strain is applied with a constant angular frequency, ω , and a constant amplitude, γ_0 : $\gamma(t) = \gamma_0 \sin(\omega t)$.

If the strain amplitude is sufficiently small, the stress will generally follow a sinusoidal dependence but delayed by an angle, δ : $\tau(\omega, t) = \tau_0 \sin(\omega t + \delta)$. This sinusoidal form can be also expressed as:

$$\tau(\omega, t) = \tau_0 \cos \delta \sin(\omega t) + \tau_0 \sin \delta \cos(\omega t) \quad (\text{In23})$$

It is important to note that the first term in Equation In23 is related to the shear strain and the last term is related to the shear rate. It is possible to define two magnitudes relating the stress to the shear strain and the shear rate, $G' = \frac{\tau_0 \cos \delta}{\gamma_0}$ and $G'' = \frac{\tau_0 \sin \delta}{\dot{\gamma}_0}$. These constant are called the *viscoelastic moduli*: G' is the so-called *storage modulus* and G'' is the so-called *loss modulus*.

From the definitions above, it is important to note that for a perfect elastic solid, $G' = G_e$, where G_e is the elastic modulus, related to the Young modulus and $G'' = 0$. For Newtonian fluids, the storage modulus is $G' = 0$ and $G'' = \eta\omega$. In general both storage and loss moduli are different from zero and the material is named *viscoelastic*. For convenience, it is also possible to describe the viscoelastic behavior using a complex notation, where the strain and the stress are described as: $\gamma^*(t) = \gamma_0 \exp(i\omega t)$ and $\tau^*(\omega, t) = \tau_0 \exp(i(\omega t + \delta))$. The complex viscoelastic modulus is thus defined as $G^* = \frac{\tau^*}{\gamma^*} = G' + iG''$. It is also possible to define a complex viscosity as $\eta^* = \frac{\tau^*}{\dot{\gamma}^*} = \eta' - i\eta''$ where the components of the complex viscosity are related to the components of the viscoelastic modulus: $\eta' = G''/\omega$ and $\eta'' = G'/\omega$.

Typically the rheological behavior of MR fluids under the presence of an external magnetic field is viscoelastic and the viscoelastic moduli are typically found by experiments, simulations or theoretical models [e.g. Parthasarathy and Klingenberg (1999), Ginder *et al.* (1996), Ramos *et al.* (2010)]. For small enough strain amplitudes (small amplitude oscillatory shear, SAOS), the viscoelastic moduli remain constant and do not depend on the strain amplitude. This region is called the linear viscoelastic region. The linear strain interval is generally small; from 0.01% to 0.1% [de Vicente *et al.* (2011)]. In the non-linear viscoelastic behavior (large amplitude oscillatory shear, LAOS) both viscoelastic moduli start to decrease. The storage modulus decreases with strain amplitude following a power law with slope -2 and loss modulus also decreases with strain amplitude following a power law but the slope in this case is -1. Since the storage modulus decreases more rapidly than the loss modulus, in some critical point, both becomes equal. Generally speaking, for strains higher than this critical strain, the system can be considered a fluid and for strains smaller than the critical strain, the system can be considered as a solid.

Squeeze flow rheology

In order to solve the equations of motion for squeeze flow, it is important to establish a coordinate system. The coordinate system we use here is schematized in the Figure In.5. In this section we will use cylindrical coordinates. The fluid will be placed within two parallel plates. The initial gap is considered h_0 . As a consequence of the squeeze flow the gap between plates will decrease and at a certain time. Thus, the gap will be $h(t)$.

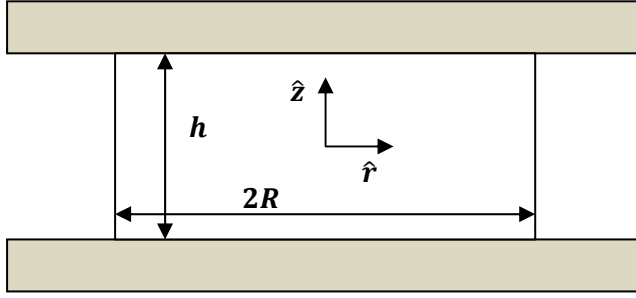


Figure In.5. Scheme of the squeeze flow coordinates system.

Squeeze flow is a kind of biaxial elongation flow. The velocity profile for a biaxial elongational flow is given by: $\vec{v} = (-\frac{\dot{\varepsilon}_H(t)}{2}x, -\frac{\dot{\varepsilon}_H(t)}{2}y, \dot{\varepsilon}_H(t)z)$, with $\dot{\varepsilon}_H(t) < 0$. Here, $\dot{\varepsilon}_H(t) = \dot{h}(t)/h(t)$ is called the *compressive strain rate* and $\dot{h}(t)$ is the approaching velocity whereby the gap decreases. By integration of the compressive strain rate over the time we can calculate the strain: $\varepsilon_H(t) = \ln \frac{h(t)}{h_0}$. This strain is called the Hencky strain [Engmann et al. (2005)]. However, for convenience, we will use another definition of the strain in this dissertation, $\varepsilon(t) = \frac{h_0 - h(t)}{h_0}$. The use of this definition leads to a different definition for the compressive strain rate, $\dot{\varepsilon}(t) = -\frac{\dot{h}(t)}{h_0} = -\dot{\varepsilon}_H(t) \frac{h(t)}{h_0}$.

The main material functions to be obtained in squeeze flow tests is the gap as a function of the time, $h(t)$, and the normal force, $F_N(h, t)$. Typical experiments in squeeze flow are: constant force experiments, constant velocity experiments and constant compressive strain rate experiments. In constant force experiments the applied force remains constant while the gap is measured as a function of the time. In constant velocity experiments, the gap moves uniformly at a constant velocity, $v = -\dot{h}$ while the force is monitored. In constant compressive strain rate experiments the Hencky compressive strain rate is constant while the

force is monitored. In this dissertation, most of the experiments are run at constant velocity.

It is also important to explicitly state the boundary conditions in the problem. In constant velocity tests, the boundary conditions depend on the particular properties of the surface. Solutions of the normal force for slipping surfaces and no-slipping surface in the case of Newtonian fluids are given by Equations In24 and In25 respectively [Engmann et al. (2005)]:

$$F_N = \frac{3\eta v}{h^2} V \quad (\text{In24})$$

$$F_N = \frac{3\eta v}{2h^5} V^2 \quad (\text{In25})$$

References

- An, H. N., S. J. Picken and E. Mendes, "Enhanced hardening of soft self-assembled copolymer gels under homogeneous magnetic fields", *Soft Matter* **6**, 4497-4503 (2010).
- Artman, J. O., and P. E. Tannenwald, "Measurement of susceptibility tensor in ferrites", *J. Appl. Phys.* **26**, 1124-1132 (1955).
- Bell, R. C., J. O. Karli, A. N. Vavreck, D. T. Zimmerman, G. T. Ngatu and N. M. Wereley, "Magnetorheology of submicron diameter iron microwires dispersed in silicon oil", *Smart. Mater. Struct.* **17**, 015028 (2008).
- Berli, C. L. A., and J. de Vicente, "A structural viscosity model for magnetorheology", *Appl. Phys. Letters* **101**, 021903 (2012).
- Billas, I. M. L., J. A. Becker, A. Châtelain and W. A. de Heer, "Magnetic Moments on Iron Clusters with 25 to 700 atoms and Their

Dependence on Temperature", *Phys. Rev. Lett.* **71(24)**, 4067-4070 (1993).

Bird, R. B., R. C. Armstrong and O. Hassager, *Dynamics of polymeric liquids* (2nd Edition) (Wiley & sons, Canada, 1987)

Bozorth, R. M., *Ferromagnetism* (van Nostrand, Toronto, 1951)

Brady, J. F., and G. Bossis, "Stokesian Dynamics", *Ann. Rev. Fluid. Mech.* **20**, 111-157 (1988).

Chin, B. D., H. P. Jong, M. H. Kwon and O. O. Park, "Rheological properties and dispersion stability of magnetorheological (MR) suspensions", *Rheol. Acta* **40**, 211-219 (2001).

Choi, J. S., B. J. Park, M. S. Cho and H. J. Choi, "Preparation and magnetorheological characteristics of polymer coated carbonyl iron suspensions", *J. Magn. Magn. Mater.* **304**, 374-376 (2006).

Clercx, H. J. H., and G. Bossis, "Many-body interactions in electrorheological fluids", *Phys. Rev. E* **48(4)**, 2721-2738 (1993).

Cutillas, S., G. Bossis and A. Cebers, "Flow-induced transition from cylindrical to layered patterns in magnetorheological suspensions", *Phys. Rev. E* **57(1)**, 804-811 (1998).

Das, M., V. K. Jain and P. S. Ghoshdastidar, "Fluid flow analysis of magnetorheological abrasive flow finishing (MRAFF) process", *Int. J. Mach. Tool Manufact.* **48**, 415-426 (2008).

de Gans, B. J., H. Hoekstra and J. Mellema, "Non-linear magnetorheological behaviour of an inverse ferrofluid", *Faraday Discuss.* **112**, 209-224 (1999).

- de Gans, B. J., N. J. Duin, D. van den Ende and J. Mellema, "The influence of particle size on the magnetorheological properties of an inverse ferrofluid", *J. Chem. Phys.* **113**, 2032-2042 (2000).
- de Vicente, J., D. J. Klingenberg and R. Hidalgo-Álvarez, "Magnetorheological fluids: a review", *Soft Matter* **7**, 3701-3710 (2011).
- de Vicente, J., M. T. López-López, J. D. G. Durán and F. González-Caballero, "Shear flow behavior of confined magnetorheological fluids at low magnetic field strengths", *Rheol. Acta* **44**, 94-103 (2004).
- de Vicente, J., M. T. López-López, F. González-Caballero and J. D. G. Durán, "Rheological Study of the Stabilization of Magnetizable Colloidal Suspensions by Addition of Silica Nanoparticles", *J. Rheol.* **47**, 1093-1109 (2003).
- Dyke, S. J., B. F. Spencer Jr., M. K. Sain and J. D. Carlson, "Experimental Verification of Semi-active Structural Control Strategies Using Acceleration Feedback" in *Proceedings of the Third International Conference on Motion and Vibration Control* (Chiba, Japan, 1996).
- Engmann, J., C. Servais and A. S. Burbidge, "Squeeze flow theory and applications to rheometry: A review", *J. Non-Newtonian Fluid Mech.* **132**, 46388 (2005).
- Felt, D. W., M. Hagenbuchle, J. Liu and J. Richard, "Rheology of a magnetorheological fluid", *J. Intell. Mater. Syst. Struct.* **7**, 589-593 (1996).

- Fernández-Toledano, J. C., J. Rodríguez-López, K. Shahrivar, R. Hidalgo-Álvarez, L. Elvira, F. M. de Espinosa and J. de Vicente, "Two-step yielding in magnetorheology", *J. Rheol.* **58(5)**, 1507-1534 (2014).
- Furst, E. M., and A. P. Gast, "Dynamic and Lateral interactions of dipolar chains", *Phys. Rev. E* **62(5)**, 6916-6925 (2000).
- Getzlaff, M., *Fundamentals of magnetism* (Springer-Verlag Heidelberg, Berlin, 2008)
- Ginder, J. M., L. C. Davis and L. D. Elie, "Rheology of magnetorheological fluids: models and measurements", *Int. J. Mod. Phys. B* **10**, 3293-3303 (1996).
- Heine, M., J. de Vicente and D. J. Klingenberg, "Thermal transport in sheared electro- and magnetorheological fluids", *Phys. Fluids* **18**, 023301 (2006).
- Jackson, J. D., *Classical Electrodynamics* (3rd edition) (Wiley & Sons, New York, 1999)
- Jha, S., and V. K. Jain, "Design and development of the magnetorheological abrasive flow finishing (MRAFF) process", *Int. J. Mach. Tool Manufact.* **44**, 1019-1029 (2004).
- Jiles, D. C., *Introduction to magnetism and magnetic materials* (Chapman & Hall, London, 1991)
- Kanu, R. C., and M. T. Shaw, "Enhanced electrorheological fluids using anisotropic particles", *J. Rheol.* **42(3)**, 657-670 (1998).
- Kavlicoglu, B. M., F. Gordaninejad, C. A. Evrensel, Y. Liu, N. C. Kavlicoglu and A. Fuchs, "Heating of a high-torque

-
- magnetorheological fluid limited slip differential clutch", *J. Intell. Mater. Syst. Struct.* **19**, 235-241 (2008).
- Klingenberg, D. J., J. C. Ulciny and M. A. Golden, "Mason numbers for magnetorheology", *J. Rheol.* **51(5)**, 883-893 (2007a).
- Klingenberg, D. J., J. C. Ulciny and A. L. Smith, "Effects of body forces on the structure and rheology of ER and MR fluids", *Int. J. Mod. Phys. B* **21(28-29)**, 4841-4848 (2007b).
- Klingenberg, D. J., C. H. Olk, M. A. Golden and J. C. Ulciny, "Effects of nonmagnetic interparticle forces on magnetorheological fluids", *J. Phys. Condens. Matter* **22**, 324101 (2010).
- Kor, Y. K., and H. See, "The electrorheological response of elongated particles", *Rheol. Acta* **49**, 741-756 (2010).
- Kordonski, W., and D. Golini, "Multiple application of magnetorheological effect in high precision finishing", *J. Intell. Mater. Syst. Struct.* **13**, 401-404 (2002).
- Kordonski, W., A. B. Shorey and M. Tricard, "Magnetorheological jet (MR Jet TM) finishing technology", *J. Fluids Eng.* **128**, 20-26 (2006).
- Lagger, H. G., T. Breinlinger, J. G. Korvink, M. Moseler, A. di Renzo, F. di Maio and C. Bierwisch, "Influence of hydrodynamic drag model on shear stress in the simulation of magnetorheological fluids", *J. Non-Newtonian Fluid Mech.* **218**, 16-26 (2015).
- Lee, C. H., F. Reitich, M. R. Jolly, H. T. Banks and K. Ito, "Piecewise Linear Model for Field-Responsive Fluids", *IEEE T Magn.* **37(1)**, 558-560 (2001).

- Li, W. H., and H. Du, "Design and experimental evaluation of a magnetorheological brake", *Int. J. Adv. Manuf. Tech.* **21**, 508-515 (2003).
- Liu, J., G. A. Flores and R. Sheng, "In vitro investigation of blood embolization in cancer treatment using magnetorheological fluids", *J. Magn. Magn. Mater.* **225**, 209-217 (2001).
- Martin, J. E., and R. A. Anderson, "Chain model of electrorheology", *J. Chem. Phys.* **104(12)**, 4814-4827 (1996).
- Osborn, J. A., "Demagnetizing factors of the general ellipsoid", *Phys. Rev.* **67(11-12)**, 351-357 (1945).
- Otsubo, Y., "Electrorheology of whisker suspensions", *Colloids Surf. A* **153**, 459-466 (1999).
- Parthasarathy, M., and D. J. Klingenberg, "Electrorheology: mechanisms and models", *Mater. Sci. Eng.* **R17**, 57-103 (1996).
- Parthasarathy, M., and D. J. Klingenberg, "Large amplitude oscillatory shear of ER suspensions", *J. Non-Newtonian Fluid Mech.* **81**, 83-104 (1999).
- Rabinow, J., "The magnetic fluid clutch", *AIEE Trans.* **67**, 1308-1315 (1946).
- Ramos, J., D. J. Klingenberg, R. Hidalgo-Álvarez and J. de Vicente, "Steady shear magnetorheology of inverse ferrofluids", *J. Rheol.* **55(1)**, 127-152 (2011).

- Ramos, J., J. de Vicente and R. Hidalgo-Álvarez, "Small-amplitude oscillatory shear magnetorheology of inverse ferrofluids", *Langmuir* **26(12)**, 9334-9341 (2010).
- Rankin, P. J., A. T. Horvath and D. J. Klingenberg, "Magnetorheology in viscoplastic media", *Rheol. Acta* **38**, 471-477 (1999).
- Read, D., and J. E. Martin, "Analyte Discrimination from Chemiresistor Response Kinetics", *Anal. Chem.* **82(16)**, 6969-6975 (2010).
- Reinecke, B. N., J. W. Shan, K. K. Suabedissen and A. S. Cherkasova, "On the anisotropic thermal conductivity of magnetorheological suspensions", *J. Appl. Phys.* **104**, 023507 (2008).
- Rosensweig, R. E., *Ferrohydrodynamics* (Dover, New York, 1997).
- Schmitz, R., and B. U. Felderhof, "Mobility matrix for two spherical particles with hydrodynamic interaction", *Physica* **A116**, 163-177 (1982).
- Segovia-Gutiérrez, J. P., C. L. A. Berli and J. de Vicente, "Nonlinear viscoelasticity and two-step yielding in magnetorheology: A colloidal gel approach to understand the effect of particle concentration", *J. Rheol.* **56(6)**, 1429-1448 (2012).
- Shahrivar, K. and J. de Vicente, "Thermoresponsive Polymer-based Magneto-rheological (MR) composites as a bridge between MR fluids and MR elastomers," *Soft Matter*, **9**, 11451 (2013).
- Sherman, S. G., L. A. Powell, A. C. Becnel and N. M. Wereley, "Scaling temperature dependent rheology of magnetorheological fluids", *J. Appl. Phys.* **117**, 17C751 (2015).

Volkova, O., G. Bossis, M. Guyot, V. Bashtovoi and A. Reks, "Magnetorheology of magnetic holes compared to magnetic particles", *J. Rheol.* **44**, 91-104 (2000).

Wang, Z., K. Shahrivar and J. de Vicente, "Creep and recovery of magnetorheological fluids: Experiments and simulations, *J. Rheol.* **58(6)**, 1725-1750 (2014).

Weissenberg, K., "A continuum theory of rheological phenomena", *Nature* **159**, 310-311 (1947).

Wu, W. P., B. Y. Zhao, Q. Wu, L. S. Chen and K. A. Hu, "The strengthening effect of guar gum on the yield stress of magnetorheological fluid", *Smart. Mater. Struct.* **15**, N94-N98 (2006).

Xu, Yangguang, X. Gong, T. Liu and S. Xuan, "Squeeze flow behaviors of magnetorheological elastomers under constant volume", *J. Rheol.* **58(3)**, 659-679 (2014).

Zhu, X., X. Jing and L. Cheng, "Magnetorheological fluid dampers: A review on structure design and analysis", *J. Intell. Mater. Syst. Struct.* **23(8)**, 839-873 (2012).

Objectives

This work aims to study the rheological properties of magnetorheological (MR) fluids under squeeze flow and the investigation of the effect of polydispersity in size. The main objectives in this work stand as follows:

Magnetorheology in squeeze flow mode

1. To obtain the yield compressive stress in squeeze flow magnetorheology as a function of the magnetic field strength, particle volume fraction, initial gap, sample volume and continuous medium viscosity.
2. To measure the normal force acting on the confining surfaces in a parallel-disk geometry as a function of the instantaneous gap in constant-velocity squeeze flow experiments in the filtration regime.
3. To study the influence of magnetic field strength, particle volume fraction, continuous medium viscosity, initial gap and sample volume in the normal force.
4. To develop a theoretical micromechanical model for squeeze flow.
5. To perform particle-level simulations in an attempt to obtain the generated normal force under squeeze motion.
6. To compare the experimental, simulated and theoretical normal force with existing continuous media theories considering MR fluids as Bingham-like plastic systems.

Model magnetorheology: inverse ferrofluids

1. To compare the rheological performance of model MR fluids under steady shear and large amplitude oscillatory shear to available continuous media theories, macroscopic models and micromechanical models as well as particle-level simulations.
2. To test the Mean Magnetization Approximation by using different dimensionless numbers and scaling numbers in magnetorheology.
3. To synthesize model MR fluids from inverse ferrofluids (IFFs) composed of monodisperse silica particles dispersed in ferrofluids.
4. To experimentally determine the rheological properties of IFFs under steady shearing flows and their dependence on magnetic field strength and particle volume fraction.

Effect of the polydispersity in particle size in magnetorheology

1. To investigate the effect of polydispersity in magnetorheology by the formulation of MR fluids with different polydispersity indexes and the same average size under steady shear tests.
2. To study the effect of polydispersity by carrying out particle-level simulations in start-up tests.
3. To quantify the effect of polydispersity in the apparent yield stress in conventional MR fluids.
4. To explore the influence of polydispersity in the microstructure of the MR fluids by particle level dynamic simulations.

Theory

MR fluids can be modeled as conventional Newtonian fluids in the absence of magnetic fields. However, non-Newtonian characteristics prevail in the presence of magnetic fields such as the presence of an apparent yield stress and viscoelasticity.

In this section, different models applied in magnetorheology will be presented. The models can be classified as follows: *continuous media theories*, wherein the whole dispersion is treated as a continuous medium with a constitutive equation; *bi-continuous* or *macroscopic models*, wherein the particle aggregates are assumed to be continuous and dispersed within a continuous liquid phase; and, finally, *micromechanical models*, wherein an ensemble of particles are distributed within the carrier fluid.

Continuous media theories

Undoubtedly, the most wide-used continuous media theory for MR fluids under the presence of an external magnetic field is the Bingham plastic model [Bossis et al. (2002), de Vicente *et al.* (2011)]. According to this model the shear rate will remain zero if the stress does not overcome a stress threshold, the so-called yield stress, τ_y . However, for shear stresses higher than the yield stress, the shear rate will increase linearly with the stress. In the flow regime (i.e. when the shear stress is higher than the yield stress), the shear stress can be expressed as a function of the shear rate as follows:

$$\tau = \tau_y + \eta_p \dot{\gamma} \quad (\text{Th1})$$

Here, η_p is called the Bingham plastic viscosity. This equation can be expressed in dimensionless quantities by the following expression [Marshall *et al.* (1989), Ramos *et al.* (2011), Berli and de Vicente (2012)]:

$$\frac{\eta}{\eta_\infty} = 1 + \frac{Mn^*}{Mn} \quad (\text{Th2})$$

where η_∞ is the high shear viscosity. The critical Mason number Mn^* can be assumed to be only dependent on the particle concentration if other colloidal interactions are neglected (compared to magnetostatic and hydrodynamic interactions): $Mn^* = Mn^*(\phi)$ [Marshall *et al.* (1989)].

As an example, in Figure Th.1, the dimensionless viscosity for IFFs at 10 vol% at different magnetic field strengths is represented as a function of the Mason number. As shown in Figure Th.1, the different experimental data collapse into a master curve suggesting that the magnetostatic and hydrodynamic interactions are the main interactions in IFFs. The Bingham model reasonably captures the general trend of the curve but there are some deviations in the low shear and transition regimes; the Bingham model does not predict the low shear viscosity plateau and anticipates a sharper transition from the magnetostatic to the hydrodynamic dominated regime.

In order to explain these deviations, an empirical equation obtained by modification of the Bingham model was proposed [de Vicente *et al.* (2011), Berli and de Vicente (2012)]:

$$\frac{\eta}{\eta_\infty} = 1 + \frac{Mn^*}{Mn^\Delta} \quad (\text{Th3})$$

Equation Th3 successfully explains the experimental results for different Δ values, generally in the range $2/3 < \Delta < 1$. For example, Felt *et al.* (1996) give $\Delta = 0.74 - 0.83$ and de Gans *et al.* (1999a) give slightly higher values, $\Delta = 0.8 - 0.9$. The model predictions improve when the

Krieger-Dougherty equation is used for the calculation of the high-shear rate viscosity [Goodwin et al. (1997)].

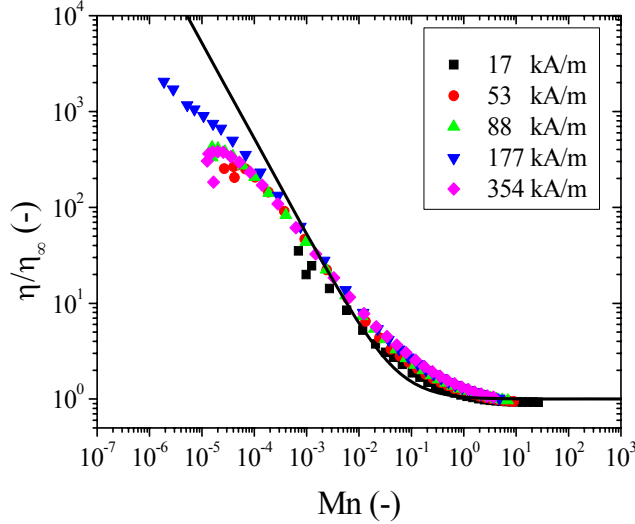


Figure Th.1 Dimensionless viscosity as a function of the Mason number for an inverse ferrofluid at a particle concentration of 10 vol% for different external magnetic field strengths. Solid line represents the best fit to the Bingham model.

Although Equation Th3 is very successful in the description of the viscosity curves, it is an empirical equation without a physical meaning for the exponent Δ .

Recently, Berli and de Vicente (2012) developed a structural viscosity model in order to explain the experimental viscosity versus Mason number curves. This model establishes a critical shear rate, related to the typical time scales used in magnetorheology, that leads to a dimensional form of the dimensionless viscosity:

$$\frac{\eta}{\eta_{\infty}} = \left[\frac{1 + (Mn/Mn^*)^{1/2}}{(\eta_{\infty}/\eta_0)^{1/2} + (Mn/Mn^*)^{1/2}} \right]^2 \quad (\text{Th4})$$

Here, η_0 is the low shear viscosity. For the case of IFFs, the low shear rate viscosity plateau is clearly observed (e.g. see Figure Th.1). However, this low shear plateau is very hard to find in the case of CMRFs. Indeed, the existence of a constant low shear rate viscosity obviously contradicts the existence of a real yield stress in MR fluids [e.g. Rankin *et al.* (1999), Berli and de Vicente (2012), de Vicente *et al.* (2011)]. Typically, the low shear viscosity is several orders of magnitude higher than the high shear viscosity, and the yield stress is defined in terms of the transition from the low shear viscosity to the high shear viscosity. This yield stress is therefore related to the critical Mason number Mn^* . In these sense, the yield stress can be still used as an *apparent yield stress*. In the limit of $\eta_\infty/\eta_0 \rightarrow 0$, Equation Th4 leads to a Casson-like equation:

$$\frac{\eta}{\eta_\infty} = 1 + \frac{Mn^*}{Mn} + 2 \left(\frac{Mn^*}{Mn} \right)^{1/2} \quad (\text{Th5})$$

Equation Th5 also provides a divergent viscosity for low Mason number and a yield stress, but the transition from the magnetostatic regime to the hydrodynamic regime is now smoother than the Bingham model and therefore in much better agreement with experiments. In Chapters 6 and 7 these theories will be tested for IFFs and CMRFs.

Continuous media theories have also been used in non-shearing flows; e.g. squeeze flow under fields. Covey and Stanmore (1981) developed a theoretical study of the squeezing behavior of a Bingham-like fluid at a constant approaching velocity, v , and considering non-slip conditions at the walls. The results obtained where a function of a new dimensionless parameter, the so-called *plasticity number*, $S = \frac{\eta_p v R}{h^2 \tau_y}$, where R is the total radius of the sample.

Later, William *et al.* (1993) solved the problem of the squeeze flow motion of a bi-viscous fluid (i.e. a fluid with two different viscosities depending on whether the shear stress is below or above to a critical shear stress, τ_y). It is important to note that in the bi-viscous model the critical shear stress does not have the same physical meaning than the yield stress in the case of the Bingham model, but in both cases they are transitional stresses. For slow enough velocities, in the so-called *filtration regime*, these two models lead to a single equation that relates the normal force F acting on the confining plates and the separation distance between them h :

$$F = \frac{2\tau_y V^{3/2}}{3\sqrt{\pi}h^{5/2}} \quad (\text{Th6})$$

In Chapters 2 and 3 of this dissertation, experiments on MR fluids in squeeze flow mode will be compared to Equation Th6.

Macroscopic models

In a macroscopic model, the MR fluid is assumed to be composed by aggregates of different shapes within a continuous medium. These models constitute a coarse-grained description of a MR fluid and take into account the shape anisotropy of the aggregates but, they do not provide information on the particle structure inside the aggregate. Aggregates are composed by particles at a (internal) volume fraction, ϕ_a . The volume fraction of particle within the aggregate can be estimated as that of a randomly closed packing fraction for monodisperse spheres, $\phi_a = 0.64$. In the case of MR fluids formulated with particles having polydispersity in size, other values for ϕ_a can be considered. The volume fraction of the aggregates in the continuous medium is calculated as, $\phi_s = \phi/\phi_a$ [Ramos *et al.* (2011)].

Bossis *et al.* (1997) developed macroscopic models for different geometries: spheroids, cylinders and layered aggregates. In their work the stress is obtained from the derivative of the magnetic energy density of an aggregate and then, multiplying this result by the number of aggregates in the system. Thus, inter-aggregate interactions are neglected and the models do only strictly apply in the dilute limit.

The shear stress, τ , is obtained as a function of the strain, γ , as follows:

$$\tau = \frac{1}{2} \mu_0 \mu_{cr} H_0^2 \phi_s \frac{\mu(\phi)}{\mu_c} \tilde{\mu}_a \frac{\partial}{\partial \gamma} \left[\frac{1}{(1+\gamma^2)(1+\tilde{\mu}_a n_{\parallel})} + \frac{\gamma^2}{(1+\gamma^2)(1+\tilde{\mu}_a n_{\perp})} \right] \quad (\text{Th7})$$

Here, $\mu(\phi)$ is the magnetic permeability of the suspension at a particle volume fraction, ϕ . Considering a Mean Field Theory, for instance, the Maxwell-Garnett theory (1904), the permeability can be written as a function of the contrast factor and the particle volume fraction:

$$\frac{\mu(\phi)}{\mu_c} = \frac{1+2\beta\phi}{1-\beta\phi} \quad (\text{Th8})$$

The term $\tilde{\mu}_a$ is given by $\tilde{\mu}_a = \mu_a/\mu_c - 1$ where μ_a is the magnetic permeability of the aggregate, which in its turn can be expressed using the Maxwell-Garnett theory for the aggregate as follows: $\frac{\mu_a}{\mu_{cr}} = \frac{1+2\beta\phi_a}{1-\beta\phi_a}$. The use of Maxwell-Garnett theory is justified in Volkova *et al.* (2000). n_{\parallel} and n_{\perp} refer to the demagnetizing factors of the aggregate in the parallel and perpendicular direction of the external magnetic field, respectively [Osborn (1949)]. These factors depend on the shape of the aggregate leading to different models depending on the aggregate shape [Bossis *et al.* (1997)].

For all the shapes considered (spheroids, cylinders and layers), the stress initially increases linearly with the strain, then reaches a maximum and eventually levels off for higher strains [see Figure 2 in Bossis *et al.*

(1997)]. These results are in agreement with experiments in start-up tests [see Figure 2b in de Vicente *et al.* (2011)]. The maximum of the stress is considered as the yield stress. For spheroids (S), the yield stress is given by [Ramos *et al.* (2011)]:

$$\tau_{y,S} = -0.325\mu_0\mu_{cr}H_0^2\phi_s\frac{1+2\beta\phi}{1-\beta\phi}\tilde{\mu}_a\left(\frac{1}{1+\tilde{\mu}_an_\perp} - \frac{1}{1+\tilde{\mu}_an_\parallel}\right) \quad (\text{Th9})$$

In the case of cylinders (C) and layers (L), Bossis *et al.* (1997) generalized a model previously presented by Rosensweig (1995) for the shear stress. The resulting yield stress is given by:

$$\tau_{y,C/L} = 0.325\mu_0\mu_{cr}H_0^2\phi_s\tilde{\mu}_a\frac{1-\phi_s}{C+\tilde{\mu}_a(1-\phi_s)} \quad (\text{Th10})$$

where C is a factor depending on the shape: $C = 2$ in the case of cylinders and $C = 1$ in a layered structure.

According to these models, the storage modulus can be calculated by taking the ratio between the stress and the strain, τ/γ in the low-strain limit [Ramos *et al.* (2010)]:

$$G'_S = -\mu_0\mu_{cr}H_0^2\phi_s\frac{1+2\beta\phi}{1-\beta\phi}\tilde{\mu}_a\left(\frac{1}{1+\tilde{\mu}_an_\perp} - \frac{1}{1+\tilde{\mu}_an_\parallel}\right) \quad (\text{Th11})$$

$$G'_{C/L} = \mu_0\mu_{cr}H_0^2\phi_s\tilde{\mu}_a\frac{1-\phi_s}{C+\tilde{\mu}_a(1-\phi_s)} \quad (\text{Th12})$$

It is important to note that the yield stress and the storage modulus do not depend linearly on the particle volume fraction. Also, they do not depend linearly on the magnetic dipolar interaction between two particles. However, in the dilute case and for enough small magnetic field strengths, the dependence becomes linear with the particle volume fraction and quadratic with the external magnetic field.

It is also important to note, that macroscopic models do not provide information concerning the loss modulus, mainly due to the difficulties of

developing a suitable hydrodynamic model in MR fluids for systems of more than one particle. Macroscopic models will be compared to experiments and particle-level simulations in Chapter 6.

Micromechanical models

In a micromechanical model, discrete particles are considered to interact through prescribed forces in a deterministic way. Generally, particles are assumed to be perfect spheres of the same size (i.e. monodisperse). Under field, single-particle-width chains are frequently assumed to form. Then, these structures deform upon the application of a shear flow and different approaches are followed to obtain the yield stress, the critical Mason number or the storage modulus.

Klingenberg and Zukoski (1990) developed a micromechanical model taking into account the multipolar magnetic interaction between only two isolated particles. They considered a balance between the magnetostatic and the hydrodynamic forces acting on the particles. Particles attracted if the shear strain remained below a critical value that they calculated as $\gamma_c = 0.389$. The yield stress was calculated as the stress corresponding to this critical strain (i.e. the maximum in the stress versus strain curve):

$$\tau_{y,KZ} = 1.026 \mu_0 \mu_{cr} \beta^2 H_0^2 \phi \quad (\text{Th13})$$

Later, de Gans et al. (1999a) included additional repulsive forces to the analysis. In this case, the critical strain obtained was the same as in Klingenberg and Zukoski (1990) but the yield stress differed as follows:

$$\tau_{y,dG1} = 1.11 \mu_0 \mu_{cr} \beta^2 H_0^2 \phi \quad (\text{Th14})$$

Similarly to Klingenberg and Zukoski (1990), the yield stress depends on the dipolar magnetostatic interaction and linearly with the particle loading.

If the particles do not move affinely with the flow and there exists a gap between the first particle (that remains attached to the plate) and the second particle in the chain ("bead-rod" model), the yield stress now depends on this gap, $\delta = (h - \sigma)/\cos \theta - (h - \sigma)$, as shown in [de Gans et al. (1999a), Ramos et al. (2011)]:

$$\tau_{dG2} = \frac{9}{8}\mu_0\mu_{cr}\beta^2H_0^2\phi \left\{ \sin \theta (5 \cos \theta - 1) \left[\left(\frac{\delta}{\sigma} + 1 \right)^{-4} + \frac{1}{3} \left(\frac{\delta}{\sigma} + \frac{3}{2} \right)^{-3} \right] \right\} \quad (\text{Th15})$$

For the typical values used in magnetorheology (i.e. $\sigma \sim 1\mu\text{m}$ and $h = 300\mu\text{m}$), the yield stress can be calculated as follows [Ramos et al. (2011)]:

$$\tau_{y,dG2} = 0.079\mu_0\mu_{cr}\beta^2H_0^2\phi \quad (\text{Th16})$$

Again, Equation Th16 also gives a linear dependence on the particle volume fraction and the dipolar magnetostatic force.

Micromechanical models predict the existence of a critical Mason number in agreement with continuous media theories. The micromechanical models lead to a Bingham-like constitutive equation and offer a physical meaning of the Bingham parameters (e.g. the critical Mason number). The relationship of the critical Mason number with the particle volume fraction, the high shear viscosity and the continuous medium viscosity can be expressed as follows [Ramos et al. (2011)]:

$$Mn^* = C\phi \frac{\eta_c}{\eta_\infty} \quad (\text{Th17})$$

The values for the constant C are different considering the approximations used in each model. Thus, $C = 8.82$ in Martin and Anderson (1996), $C = 8.485$ in de Vicente et al. (2004), $C = 5.25$ in the de Gans et al. (1999a) and $C = 1.91$ in Volkova et al. (2000). It is worth to note that the critical Mason number dependence on the particle volume fraction is theoretically linear in the case of a dilute system.

Micromechanical models have been also used to calculate the storage modulus. The model developed by Klingenberg and Zukoski (1990) gives:

$$G'_{KZ} = \frac{9}{2} \mu_0 \mu_{cr} \beta^2 H_0^2 \phi \quad (\text{Th18})$$

Martin and Anderson (1996) considered the multibody interparticle magnetic force in a free single chain and obtained:

$$G'_{MA} = \frac{9}{4} \xi(3) k_3 \mu_0 \mu_{cr} \beta^2 H_0^2 \phi \quad (\text{Th19})$$

where ξ represents the Zeta Riemann function, $\xi(3) \cong 1.20206$, and $k_3 = \left(1 - \frac{k}{4} - \frac{k}{8}\right)^{-1}$ with $k = \xi(3)\beta$.

Including repulsive interactions between particles, de Gans et al. (1999b) found:

$$G'_{dG} = \frac{3}{4} \xi(4) \mu_0 \mu_{cr} \beta^2 H_0^2 \phi \left[2 \left(1 - \frac{\beta \xi(3)}{2}\right)^{-2} + \left(1 + \frac{\beta \xi(3)}{2}\right)^{-2} \right] \quad (\text{Th20})$$

Using a balance between non-Stokesian hydrodynamic forces and magnetostatic forces, de Vicente et al. (2005) provide another expression for the storage modulus:

$$G'_{dV1} = \frac{9}{8} \mu_0 \mu_{cr} \beta^2 H_0^2 \frac{\phi}{\phi_a} \quad (\text{Th21})$$

However, by assuming the expression for the torque in a thin spheroid the storage modulus modifies as follows:

$$G'_{dV2} = \frac{1}{2} \mu_0 \mu_{cr} H_0^2 \frac{\phi}{\phi_a} \frac{(\mu_a - 1)^2}{\mu_a + 1} \quad (\text{Th21})$$

Macroscopic and micromechanical models will be used in this dissertation in Chapter 6. Neither macroscopic nor micromechanical models exist in literature in the case of the squeeze flow. A micromechanical model will be proposed for the squeeze behavior of MR fluids in Chapter 1.

References

- Berli, C. L. A., and J. de Vicente, "A structural viscosity model for magnetorheology", *Appl. Phys. Lett.* 101, 021903 (2012).
- Bossis, G., E. Lemaire and O. Volkova, "Yield stress in magnetorheological and electrorheological fluids: A comparison between microscopic and macroscopic structural models", *J. Rheol.* 41(3), 687-704 (1997).
- Bossis, G., O. Volkova, S. Lacis and A. Meunier, "Magnetorheology: Fluids, Structures and Rheology", in *Ferrofluids*, ed. S. Odenbach (Springer, Bremen, Germany, 2002), p. 202.
- Covey, G. H., and B. R. Stanmore, "Use of the parallel-plate plastometer for the characterization of viscous fluids with a yield stress", *J. Non-Newtonian Fluid Mech.* 8, 249-260 (1981).
- de Gans, B. J., H. Hoekstra and J. Mellema, "Non-linear magnetorheological behaviour of an inverse ferrofluid", *Faraday Discuss.* 112, 209-224 (1999a).
- de Gans, B. J., C. Blom, A. P. Philipse and J. Mellema, "Linear viscoelasticity of an inverse ferrofluid", *Phys. Rev. E* 60(4), 4518-4527 (1999b).
- de Vicente, J., D. J. Klingenberg and R. Hidalgo-Álvarez, "Magnetorheological fluids: a review", *Soft Matter* 7, 3701-3710 (2011).
- de Vicente, J., M. T. López-López, J. D. G. Durán and F. González-Caballero, "Shear flow behavior of confined magnetorheological

- fluids at low magnetic field strengths", *Rheol. Acta* 44, 94-103 (2004).
- de Vicente, J., M. T. López-López, J. D. G. Durán and G. Bossis, "A Slender-body Micromechanical Model for Viscoelasticity of Magnetic Colloids", *J. Colloid. Interface Sci.* 282, 193-201 (2005).
- Felt, D. W., M. Hagenbuchle, J. Liu and J. Richard, "Rheology of a magnetorheological fluid", *J. Intell. Mater. Syst. Struct.* 7, 589-593 (1996).
- Goodwin, J. W., G. M. Markham and B. Vincent, "Studies on Model Electrorheological Fluids", *J. Phys. Chem. B* 101, 1961-1967 (1997).
- Klingenberg, D. J., and C. F. Zukoski, "Studies on the steady-shear behavior of electrorheological suspensions", *Langmuir* 6, 15-24 (1990).
- Marshall, L., C. F. Zukoski and J. W. Goodwin, "Effects of Electric Fields on the Rheology of Non-aqueous Concentrated Suspensions", *J. Chem. Soc.. Faraday Trans. I* 85(9), 2785-2797 (1989).
- Martin, J. E., and R. A. Anderson, "Chain model of electrorheology", *J. Chem. Phys.* 104(12), 4814-4827 (1996).
- Maxwell-Garnett, J. C., "Colours in metal glasses and in metallic films", *Philos. Trans. R. Soc. London* 203, 385-420 (1994).
- Osborn, J. A., "Demagnetizing factors of the general ellipsoid", *Phys. Rev.* 67(11-12), 351-357 (1945).

Ramos, J., D. J. Klingenberg, R. Hidalgo-Álvarez and J. de Vicente, "Steady shear magnetorheology of inverse ferrofluids", *J. Rheol.* 55(1), 127-152 (2011).

Ramos, J., J. de Vicente and R. Hidalgo-Álvarez, "Small-amplitude oscillatory shear magnetorheology of inverse ferrofluids", *Langmuir* 26(12), 9334-9341 (2010).

Rankin, P. J., A. T. Horvath and D. J. Klingenberg, "Magnetorheology in viscoplastic media", *Rheol. Acta* 38, 471-477 (1999).

Rosensweig, R. E., "On magnetorheology and electrorheology as states of unsymmetric stress", *J. Rheol.* 39, 179-192 (1995).

Volkova, O., G. Bossis, M. Guyot, V. Bashtovoi and A. Reks, "Magnetorheology of magnetic holes compared to magnetic particles", *J. Rheol.* 44, 91-104 (2000).

Williams, E. W., S. G. Rigby, J. L. Sproston and R. Stanway, "Electrorheological fluids applied to an automotive engine mount", *J. Non-Newtonian Fluid Mech.* 49, 221-238 (1993).

Methodology

In this section, the general methodology used in this dissertation will be presented. This section is later completed with the information provided in each of the following chapters wherein the specific methodology is exposed.

Experimental procedure

Materials

Materials used in this dissertation differ accordingly to the formulation of the MR fluids: conventional MR fluids (CMRFs) or inverse ferrofluids (IFFs).

Magnetic particles used in this dissertation are composed of carbonyl iron powders provided by BASF-SE in different grades: HQ, HS and OM grades. Carbonyl iron powders are obtained by the thermal decomposition of iron pentacarbonyl. Basically, the synthesis involves a nucleation reaction that results in onion-ring-structured particles. Particles are highly pure, with more than the 97.5% of iron, and the rest are impurities of other compounds such as carbon (max. 1%), nitrogen (max. 0.9%) and oxygen (max. 0.5%). The different grades are obtained by proprietary procedures using different finishing processes such as milling. Carbonyl iron powders used in the formulation of commercial MR fluids are highly polydisperse in size and for this reason the investigation of the effect of polydispersity in magnetorheology is one of the aims of this dissertation.

In Figure Mt.1, a scanning electron microscopy (SEM) micrograph of a typical carbonyl iron powder (HS grade) is shown. The size histograms of

the carbonyl iron powders used in this dissertation are shown in Figure Mt.2. It is important to remark that the magnetic characteristics of the different carbonyl iron powders used in this work are very similar, obtaining saturation magnetization of $M_S = 1691 \text{ kA/m}$ for HQ-grade particles, $M_S = 1703 \text{ kA/m}$ for HS-grade particles and $M_S = 1550 \text{ kA/m}$ for OM-grade particles.

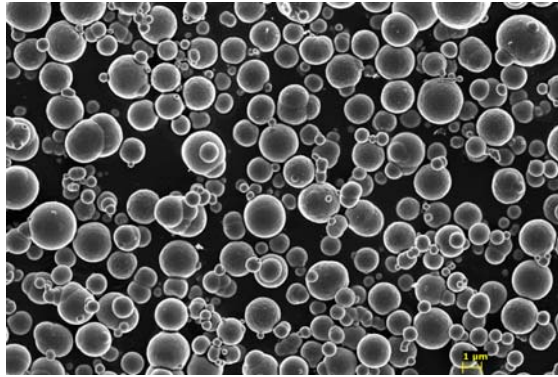


Figure Mt.1. SEM-micrograph of carbonyl iron powder (HS grade, provided by BASF-SE).

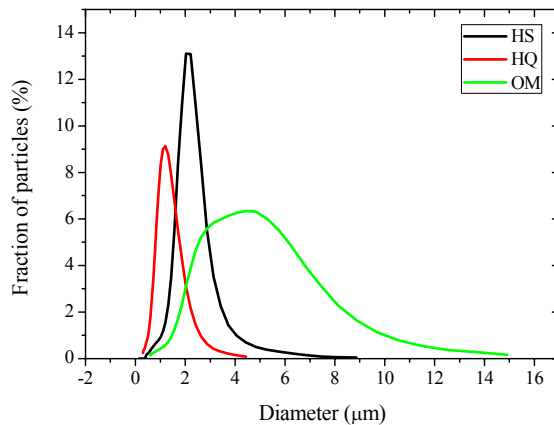


Figure Mt.2. Particle size distribution of different grades of carbonyl iron powders (black solid line, HS grade; red solid line, HQ grade and green solid line, OM grade).

As shown in Figure Mt.2, particle diameters of carbonyl iron powders are around several microns. The mean particle size, σ_m , and the polydispersity index, PDI , of the different grades are: $\sigma_m = 1.26 \mu m$, $PDI = 1.64$ for the HQ grade; $\sigma_m = 2.20 \mu m$, $PDI = 1.63$ for the HS grade and $\sigma_m = 4.30 \mu m$, $PDI = 1.85$ for the OM grade. The main characteristics of the different grades of carbonyl iron powders are summarized in Bombard *et al.* (2002).

It is definitely possible to obtain more polydisperse systems by mixing these different grades. However, obtaining more monodisperse systems is clearly a more difficult challenge; Chiriac and Stonian (2009) obtained narrow particle size distributions by sieving commercial micrometric iron particles.

IFFs were formulated in this work to improve the monodispersity of MR fluids. Silica particles were synthesized using the Stöber's method [Stöber *et al.* (1968)]. The reagents used in the synthesis process are typically low molar-mass alcohols such as methanol, ethanol, *n*-propanol or *n*-butanol used as solvents, in a reagent quality in order to avoid impurities in the particles; tetraesters of silicic acid as the tetraethyl orthosilicate (TEOS), water and typically ammonia to provide a basic ambient used as catalyst. The main reaction is the hydrolysis of the TEOS to a silanol followed by condensation reactions.

Particles obtained by the Stöber's method are very monodisperse and their diameter range between 50 *nm* and 2 μm depending on the concentration of the reagents and the nature of the alcohol used. The process has been modeled in the work by Matsoukas and Gulari (1988). In their work they stated that the silica particles growth is characterized by an incubation period after which the nucleation is not significant. However, other

alternative models for the aggregation and growth of the silica particles have been proposed in the literature [Lee *et al.* (1997)].

The synthesis of the silica particles used in this dissertation is explained in detail in Chapter 6. Briefly, two kinds of silica particles (S200 and S600) were obtained in the synthesis process. A SEM-micrograph of S600-particles is presented in Figure Mt.3. The mean particle sizes of these silica particles and their polydispersity indexes are summarized in Table 6.2. The size histogram of these samples is shown in Figure Mt.4.

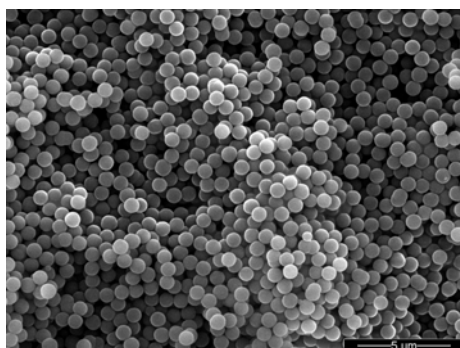


Figure Mt.3. SEM-micrograph of silica particles (S600) synthesized by the Stöber's method [Stöber *et al.* (1968)].

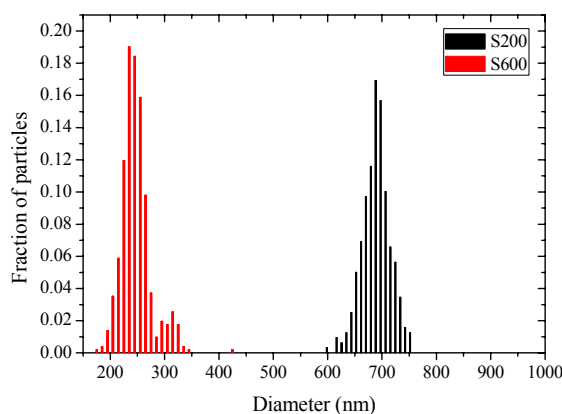


Figure Mt.4. Particle size distribution of silica particles (S200 and S600).

In the case of CMRFs, carbonyl iron powders are dispersed in silicone oils (PDMS, Sigma-Aldrich) with different viscosities. Viscosities were ranged between $20 \text{ mPa} \cdot \text{s}$ and $500 \text{ mPa} \cdot \text{s}$. Densities of the silicone oils are about 1 g/ml .

In the case of IFFs, silica particles are dispersed in a magnetite-based non-aqueous ferrofluid provided by Ferrotec Inc. The particle size distribution within the ferrofluid was calculated using the Langevin function and the obtained average particle diameter was 9 nm [Ramos *et al.* (2011), Andablo-Reyes *et al.* (2010a)]. The ferrofluid has a density of 1.12 g/ml , a viscosity of $44 \text{ mPa} \cdot \text{s}$ and a saturation magnetization of 25.5 kA/m . For a more detailed description of the characteristics of the ferrofluid used in this dissertation we refer to Ramos *et al.* (2011).

Apparatus

Two magnetorheometers (Anton Paar) were used in the experiments: MCR 501 and MCR 302. The normal force sensor has a compliance of $0.59 \mu\text{m}/\text{N}$, the normal force range is $\pm 50 \text{ N}$ and its sensitivity is around 0.01 N . The maximum torque the rheometer can achieve is 0.23 Nm and the sensitivity in torque is $0.1 \mu\text{Nm}$. The minimum angular velocity the rheometer can measure is $1.7 \cdot 10^{-8} \text{ s}^{-1}$ and the maximum 50 s^{-1} .

Two titanium parallel disks were used as the preferred configuration. Their radius is $R = 10 \text{ mm}$ and were separated by a distance, h . The plates are assumed to be perfectly parallel but a misalignment exists [Andablo-Reyes *et al.* (2010b)]. For this reason the gap between the plates was always higher than $30 \mu\text{m}$.

In a typical squeeze flow experiment the upper plate moves towards the bottom plate. Simultaneously, the normal force and gap separation are

measured. It is important to note that unavoidably, an error exists in the gap distance. Using the method reported in Connelly and Greener (1985), this gap error was estimated in $17 \mu m$.

In a typical shear experiment the upper plate rotates while the bottom plate remains stationary. In this configuration, the shear rate and the shear stress are not uniform within the sample and depend on the radial distance in the plate, r . In rotating parallel disks the shear rate is related to the angular velocity as $\dot{\gamma}(r) = \omega r/h$ and the *apparent shear stress* τ is calculated in terms of the torque T exerted on the upper plate under the assumption of a Newtonian constitutive equation for the sheared fluid, $\tau = 2T/\pi R^3$ [Macosko (1994)]. The shear rate measured in the rheometer, $\dot{\gamma}_R$ is calculated as the shear rate at the rim of the plates: $\dot{\gamma}_R = \omega R/h$. For the typical values used in this dissertation, $h \sim 300 \mu m$, the sensitivity of the rheometer in shear rate is in the order of $10^{-6} s^{-1}$ and the maximum shear rate is $10000 s^{-1}$. The sensitivity in the shear stress is $0.06 Pa$ and the maximum shear stress is $147 kPa$.

For Newtonian fluids, the torque required to turn the upper disk is exactly given by $\tau = 2T/\pi R^3$. However, in the case of Bingham-like plastic fluids, the apparent stress measured at the zero-shear limit overestimates the yield stress, τ_y , in $\tau = 4\tau_y/3$. The shear stress for a general fluid (independently of its constitutive equation) can be expressed as a function of the torque by the expression: $\tau = \frac{T}{2\pi R^3} \left[3 + \frac{d \ln T}{d \ln \dot{\gamma}_R} \right]$. Hence, for a complete description of the stress, the torque in the plate must be calculated for all the shear rates investigated and the rheology can be complicated. In this dissertation we will assume $\tau = 2T/\pi R^3$ unless otherwise stated [Macosko (1994); Bossis *et al.* (2002)].

It is important to note that other geometries can avoid this complication since the shear rate can be made constant in the sample. A typical example is the cone-plate geometry (for a sufficiently small angle). However, in magnetorheology, the cone-plate geometry induces other problems, such as the different length of connecting chains, the clogging in the apex of the cone and the difficulty to explore confinement effects and wall slip.

Uniaxial DC magnetic fields of approximately 100 kA/m are generated in this dissertation using an external electromagnetic circuit. However, the magnetic field is not totally uniform within the sample since there is a hole in the magnetic circuit to permit the plate shaft to pass. Laeuger *et al.* (2005) and later Laun *et al.* (2008) thoroughly investigated the vertical and radial magnetic field distribution within the sample. The gradient in the magnetic field was higher as the magnetic field increased. This gradient may provoke in some cases particle migration toward the rim, where the magnetic field is stronger [Andablo-Reyes *et al.* (2011), de Vicente *et al.* (2009)]. In most of the experiments, the magnetic field strength was set below 354 kA/m to ensure a reasonably uniform magnetic field and higher magnetic fields are only used to investigate the saturation regime.

Simulation method

Simulations used in this dissertation concern particle-level molecular dynamic simulations. In these simulations, the MR fluid is composed of N buoyant spherical particles dispersed in a continuous Newtonian medium of viscosity, η_c . Molecular dynamic simulations aim to solve the equations of motion of each particle. In the different chapters presented in this dissertation, the simulation method can vary accordingly to the particular approximations taken into account in each chapter. Generally,

simulations can be defined as Brownian dynamic simulations and the position of a particle i at a time t , $\vec{r}_i(t)$, is governed by the Langevin equation:

$$M_i \frac{d^2 \vec{r}_i(t)}{dt^2} = \vec{F}_i - \xi_i \left(\frac{d\vec{r}_i(t)}{dt} - \vec{u}_i^\infty \right) + \vec{f}_B(t) \quad (\text{Mt1})$$

where M_i is the mass of particle i , $\xi_i = 3\pi\eta_c\sigma_i$ is the friction coefficient of the particle i with a diameter σ_i , \vec{u}_i^∞ is the ambient fluid velocity at the center of particle i , and $\vec{f}_B(t)$ is a random force introduced to model the Brownian motion of the particles $f_B \propto \sqrt{k_B T \xi_i / \Delta t}$. Here, k_B is the Boltzmann constant, T is the absolute temperature and Δt is the time step.

Solving Algorithm

Equation Mt1 is a second-order differential equation. In order to solve the equation of motion, different algorithms have been proposed in the literature. One of the most commonly used is the Verlet algorithm [Verlet (1967)]. The Verlet algorithm states that the position of a particle i , in a time $t + \Delta t$, $\vec{r}_i(t + \Delta t)$ can be calculated using a Taylor expansion:

$$\vec{r}_i(t + \Delta t) = \vec{r}_i(t) + \Delta t \frac{d\vec{r}_i(t)}{dt} + \frac{(\Delta t)^2}{2!} \frac{d^2 \vec{r}_i(t)}{dt^2} + \frac{(\Delta t)^3}{3!} \frac{d^3 \vec{r}_i(t)}{dt^3} \dots \quad (\text{Mt2})$$

Moreover, the position of the particle i in a previous time can be also calculated by a Taylor expansion:

$$\vec{r}_i(t - \Delta t) = \vec{r}_i(t) - \Delta t \frac{d\vec{r}_i(t)}{dt} + \frac{(\Delta t)^2}{2!} \frac{d^2 \vec{r}_i(t)}{dt^2} - \frac{(\Delta t)^3}{3!} \frac{d^3 \vec{r}_i(t)}{dt^3} \dots \quad (\text{Mt3})$$

By summing Equations Mt2 and Mt3 and neglecting the terms of orders higher than the third, the position of the particle i in a time $t + \Delta t$ can be expressed as follows:

$$\vec{r}_i(t + \Delta t) = 2\vec{r}_i(t) + \vec{r}_i(t - \Delta t) + \frac{(\Delta t)^2}{2} \frac{d^2 \vec{r}_i(t)}{dt^2} \quad (\text{Mt4})$$

The term $\frac{d^2\vec{r}_i(t)}{dt^2}$ is calculated by using Equation Mt1. Obtaining the particle positions in two times, $t - \Delta t$ and t , it is possible to obtain the position in the next time and the motion of the particle can be calculated successively. However, the position of the particles at two times is often unknown and the Verlet algorithm needs to be modified to use the initial velocities of the particles. This variant is called the *Velocity-Verlet algorithm*. Thus, the position of a particle i in a time $t + \Delta t$ can be calculated using:

$$\vec{r}_i(t + \Delta t) = \vec{r}_i(t) + \vec{v}_i(t)\Delta t + \frac{(\Delta t)^2}{2!} \frac{d^2\vec{r}_i(t)}{dt^2} \quad (\text{Mt5})$$

The velocity of the particles in a time $t + \Delta t$ is calculated as follows:

$$\vec{v}_i(t + \Delta t) = \vec{v}_i(t) + \frac{(\Delta t)^2}{2} \left[\frac{d^2\vec{r}_i(t+\Delta t)}{dt^2} + \frac{d^2\vec{r}_i(t)}{dt^2} \right] \quad (\text{Mt6})$$

This method is widely used due to its simplicity and accuracy. However, other methods have improved the accuracy of the Verlet method in the solution of the second-order equations of motion of particles in molecular dynamic simulations such as the Gear methods [Gear (1971)].

Sometimes, Equation Mt1 can be simplified for MR fluids by neglecting inertial terms and Brownian motion. Thus, the equation of motion of the particles becomes a first-order differential equation and the solution can be done by using the Euler method [Klingenberg *et al.* (1989), Klingenberg *et al.* (1991)].

The time increment must be small to achieve the sufficient accuracy. However, if the time increment is too small, the total computational time will be very large. A proper choice of the time increment is necessary. The time increment must be small enough to capture the time scales in the system. Equation Mt1 provides three different time scales [Dhont (1996)]: the inertial time scale, $\tau_M \sim M_i/\xi_i$; the diffusive time, $\tau_D \sim 3\pi\eta_c\sigma_i^3/k_B T$

and the characteristic relaxation time, $\tau_R \sim 8\eta_c / \mu_0 \mu_{cr} \beta^2 H_0^2$. Here, the characteristic relaxation time was obtained assuming the typical force scales as the dipolar magnetostatic interaction. The time increment must be lower than all these three time scales to ensure the general description of all the processes in the simulations.

Simulation box and periodic boundary conditions

For computational reasons, the number of particles included in the simulations is clearly lower than the number of particles in the real system to be simulated (in the order of the Avogadro's number). A widely used method to solve this problem is the periodic boundary conditions.

In order to apply periodic boundary conditions, the system is first enclosed into a simulation box. The total volume of the simulation box must be calculated in terms of the number of particles, their diameters and the particle volume fraction: $V = \pi \sum_{i=1}^N \sigma_i^3 / 6\phi$. Periodic boundary conditions consist in the replication of the simulation box in at least one direction of the space. By repeating the replication process, the whole space can be filled with the initial simulation box and all the replicas achieving a system with much more particles. Thus, a particle leaving the box in one direction can be another entering into the box in the other side.

It is also important to note that the interactions are not restricted to the particles within the original box but extends onto other particles in the replicated boxes. Thus, the calculation of the interactions with all the particles in the original box and in the replicated boxes can be unlimitedly extended in the space domain and the calculation time would become infinite. In order to solve this problem, it is frequent to establish a cutoff distance even though it can induce some important simulation errors. Ewald (1921) developed a method to calculate the electrostatic interaction

in periodic systems. This method has been later modified and improved in order to obtain faster calculations. An extensive overview of the Ewald summations is given in Toukmaji and Board (1996). For simplicity, in this dissertation, a cutoff in the magnetostatic interactions was applied.

The shape of simulation box can be arbitrarily chosen with the only restriction to ensure that the replicas of the simulation box fill the whole space. Two obvious shapes are the cube or the prism but other shapes can be used, such as the octahedron, etc. In this dissertation, a parallelepiped is used with $L_x = L_y = L = \sqrt{\pi \sum_{i=1}^N \sigma_i^3 / 6\phi L_z}$, being L_z the height of the simulation box. Periodic boundary conditions were set in the lateral directions but not in the z -direction, where the external magnetic field was applied.

Structural parameters and physical observables

The aim of simulations performed in this dissertation is to obtain microstructural information and physical observables to compare to experimental measurements and theories.

For this, some magnitudes can be defined such as the average number of nearest neighbors, the average number of particles in clusters, the angular connectivity or the pair distribution function.

Nearest neighbors

The average number of nearest neighbors, N_n , is defined as the mean number of particles placed at a distance that is considered *near* to a central one. The distance is usually a little longer than the sum of the particle radii. In this dissertation, it is considered that a particle i is neighbor of another particle j if they are separated by a distance, d , smaller than $d \leq 1.05 (\sigma_i + \sigma_j) / 2$.

Average number of particles in clusters

Clusters are considered as sets of connected particles and the connectivity criterion is similar to nearest neighbors. Once calculated the clusters and the particles within them, it is possible to define the average number of particles in clusters, N_{pc} , as follows:

$$N_{pc} = \frac{\sum_i n_i}{N_c} = \frac{N}{N_c} \quad (\text{Mt7})$$

where n_i is the number of particles in the cluster i and N_c is the total number of clusters. As clusters with a few number of particles do not contribute much to the magnetorheological response, it could be useful to define not only the average number of particle but a weighted-average number of particles in clusters, S_2 :

$$S_2 = \frac{\sum_i n_i^2}{\sum_i n_i} = \frac{\sum_i n_i^2}{N} \quad (\text{Mt8})$$

In MR fluid simulations, the weighted-average number of particles in clusters is a good parameter of the size of a percolating cluster. Consider a system with three percolating clusters with 10 particles, and three free clusters containing 2 particles each. Hence, the total number of particles is 36. The average number of particles in clusters is $N_{pc} = 36/6 = 6$ despite of the fact that the three 2-particles clusters do not contribute significantly to the stress. However, with the weighted-average number of particles in clusters provides weighted information of the percolating clusters, $S_2 = (3 \cdot 10^2 + 3 \cdot 2^2)/36 = 312/36 = 8.7$.

Angular connectivity

The angular connectivity, $C(\theta)$, is important in non-isotropic systems. For MR fluids, it can be defined as the average number of neighboring

particles wherein the angle of the line joining their centers and the external magnetic field is θ :

$$C(\theta) = \frac{N(\theta)}{N-1} \quad (\text{Mt9})$$

Pair distribution function

The pair distribution function, $g_2(\vec{r}_1, \vec{r}_2)$, is a widely used structural parameter. In the canonical ensemble, the pair distribution function can be defined as follows [Allen and Tildesley (1987)]:

$$g_2(\vec{r}_1, \vec{r}_2) = \frac{N(N-1)}{\rho^2 Z_{NVT}} \int d\vec{r}_3 d\vec{r}_4 \dots d\vec{r}_N \exp[-U(\vec{r}_1, \vec{r}_2, \dots, \vec{r}_N)/k_B T] \quad (\text{Mt10})$$

where Z_{NVT} is the partition function in the NVT -ensemble and $U(\vec{r}_1, \vec{r}_2, \dots, \vec{r}_N)$ is the total interaction potential. In MR fluids, the pair distribution function only depends on the spherical coordinates, r and θ due to the symmetries of the system. The pair distribution function can be computed as follows [Allen and Tildesley (1987)]:

$$g(r, \theta) = \frac{V}{N^2} \langle \sum_i \sum_{j \neq i} \delta(r - r_{ij}) \delta(\theta - \theta_{ij}) \rangle \quad (\text{Mt11})$$

Physical quantities can also be defined in terms of the positions and velocities of the particles in the simulation, such as the stress tensor or the viscosity. In general, the stress tensor can be defined as follows [Irving and Kirkwood (1950)]:

$$\tau_{\alpha\beta} = -\frac{1}{V} \left(\sum_i \frac{p_i^\alpha p_i^\beta}{M_i} + \sum_{i \neq j} r_{ij}^\alpha F_{ij}^\beta \right) \quad (\text{Mt12})$$

where α and β stands for the components of the tensors, \vec{p}_i is the momentum of the particle i , M_i is the mass of the particle i , \vec{r}_{ij} is the vector position between the particles i and j , and \vec{F}_{ij} is the interparticle force between the particles i and j . In the case of inertialess simulations, the stress tensor calculation can be simplified as follows:

$$\tau_{\alpha\beta} = -\frac{1}{V} \sum_{i \neq j} r_{ij}^{\alpha} F_{ij}^{\beta} \quad (\text{Mt13})$$

On the other hand, the viscosity can be defined by the Green-Kubo relation in terms of the stress autocorrelation function [Wesp et al. (2011); Segovia-Gutierrez et al. (2013)].

References

- Allen, M. P. and D. J. Tildesley, *Computer Simulation of Liquids*, (Oxford University Press, New York, 1987).
- Andablo-Reyes, E., J. de Vicente, R. Hidalgo-Álvarez, C. Myant, T. Reddyhoff and H. A. Spikes, "Soft elasto-hydrodynamic lubrication", *Tribol. Lett.* **39**, 109-144 (2010).
- Andablo-Reyes, E., R. Hidalgo-Álvarez and J. de Vicente, "A method for the estimation of the film thickness and plate tilt angle in thin film misaligned plate-plate rheometry", *J. Non-Newtonian Fluid. Mech.* **165**, 1419-1421 (2010).
- Andablo-Reyes, E., R. Hidalgo-Álvarez and J. de Vicente, "Controlling friction using magnetic nanofluids", *Soft Matter* **7**, 880-883 (2011).
- Bombard, A. J. F., M. Knobel, M. R. Alcántara and I. Joeckes, "Evaluation of magnetorheological suspensions based carbonyl iron powders, *J. Intell. Mater. Syst. Struct.* **13**, 471-478 (2002).
- Bossis, G., O. Volkova, S. Lacis and A. Meunier, "Magnetorheology: Fluids, Structures and Rheology", in *Ferrofluids*, ed. S. Odenbach (Springer, Bremen, Germany, 2002), p. 202.
- Chiriac, H., and G. Stonian, "Influence of mixed particle size on electrorheological response", *J. Phys. Conf. Ser.* **200**, 072095 (2009).
- Connelly, R. W., and J. Greener, "High-shear viscometry with a rotational parallel-disk device", *J. Rheol.* **29**, 209-226 (1985).

-
- de Vicente, J., J. P. Segovia-Gutiérrez, E. Andablo-Reyes, F. Vereda and R. Hidalgo-Álvarez, "Dynamic rheology of sphere- and rod-based magnetorheological fluids", *J. Chem. Phys.* **131**, 194902 (2009).
- Dhont, J. K. G., *An introduction to dynamics of colloids* (Elsevier, New York, 1996).
- Ewald, P., "Die Berechnung optischer und elektrostatischer Gitterpotentiale", *Ann. Phys.* **369(3)**, 253-287 (1921).
- Gear, C. W., *Numerical initial value problems in ordinary Differential Equations* (Prentice-Hall, New Jersey, 1971).
- Irving, J. H., and J. G. Kirkwood, "The statistical theory of transport processes IV. The equations of hydrodynamics", *J. Chem. Phys.* **18**, 817-829 (1950).
- Klingenberg, D. J., F. van Swol and C. F. Zukoski, "Dynamic simulation of electrorheological suspensions", *J. Chem. Phys.* **91**, 7888-7895 (1989).
- Klingenberg, D. J., F. van Swol and C. F. Zukoski, "The small shear rate response of electrorheological suspensions. I. Simulation in the point-dipole limit", *J. Chem. Phys.* **94**, 6160-6169 (1991).
- Laeuger, J., K. Wollay, H. Stettin and S. Huck, "A new device for the full rheological characterization of magneto-rheological fluids", *Int. J. Mod. Phys. B* **19**, 1353-1359 (2005).
- Laun, H. M., G. Schmidt and C. Gabriel, "Reliable plate-plate MRF magnetorheometry based on validated radial magnetic flux density profile simulation", *Rheol. Acta* **47**, 1049-1059 (2008).
- Lee, K., A. N. Sathyagal and A. V. McCormick, "A closer look at an aggregation model of the Stöber process", *Colloids Surf. A* **144**, 115-125 (1998).
- Macosko, C. W., *Rheology: Principles, Measurements and Applications*, (Wiley-VCH, New York, 1994).

- Matsoukas, T., and E. Gulari, "Dynamics of growth of silica particles from ammonia-catalyzed hydrolysis of tetra-ethyl-orthosilicate", *J. Colloid Interf. Sci.* **124(1)**, 252-261 (1988).
- Ramos, J., D. J. Klingenberg, R. Hidalgo-Álvarez and J. de Vicente, "Steady shear magnetorheology of inverse ferrofluids", *J. Rheol.* **55(1)**, 127-152 (2011).
- Segovia-Gutiérrez, J. P., J. de Vicente, R. Hidalgo-Álvarez and A. M. Puertas, "Brownian Dynamics Simulations in Magnetorheology and Comparison with Experiments", *Soft Matter.* **9**, 6970-6977 (2013).
- Stöber, W., A. Fink and E. Bohn, "Controlled growth of monodisperse silica spheres in the micron size range", *J. Colloid Interf. Sci.* **26**, 62-69 (1968).
- Toukmaji, A. Y., and J. A. Board Jr., "Ewald summation techniques in perspective: a survey", *Comput. Phys. Commun.* **95**, 73-92 (1996).
- Verlet, L., "Computer 'Experiments' on Classical fluids. I. Thermodynamical Properties of Lennard-Jones Molecules", *Phys. Rev.* **159(1)**, 98-103 (1967).
- Wesp, C., A. El, F. Reining, Z. Xu, I. Bouras and C. Greiner, "Calculation of shear viscosity using Green-Kubo relations within a parton cascade", *Phys. Rev. C* **84**, 054911 (2011).

Results

Part I. Magnetorheology in squeeze flow mode

Chapter 1.

A micromechanical model for MR fluids under slow compression

José Antonio Ruiz-López, Roque Hidalgo-Álvarez and Juan de Vicente

This article is under review

Abstract

We propose a micromechanical model for the behavior of dilute magnetorheological fluids under unidirectional slow-compression, constant-volume squeeze flow mode. In the linear magnetization regime, the model predicts a power-law scaling of the normal stress with the particle volume fraction and magnetic field strength squared at low fields. The predictions are satisfactorily compared with experimental measurements for different particle loadings, sample volume, surface roughness and initial gap distance.

1.1. Introduction

Magnetorheological (MR) fluids are field-responsive colloids that typically exhibit a liquid-to-solid transition upon the application of a magnetic field. In current commercial applications, MR fluids are

subjected to strongly demanding deformations. Among standard kinematics, simple shear is undoubtedly the most widely studied and better known. However, the understanding of the squeeze flow behavior of MR fluids is still incomplete in spite of recent advances during the last decade (de Vicente et al. 2011a, 2011b; Ruiz-López et al. 2012; Guo et al. 2013; Xu et al. 2014).

Currently, continuum media theories are claimed to successfully explain their normal force versus gap dependence in slow compression, no-slip conditions, under constant volume operation (see Figure 1.2 in Ruiz-López et al. 2012; Guo et al. 2013; Xu et al. 2014). These theories predict the appearance of a yield compressive stress and a power law relationship between F and $1 - \varepsilon$ with exponent -2.5 (e.g. see Equation 9 in de Vicente et al. 2011b). Here F stands for the normal force and $\varepsilon = 1 - \frac{h}{h_0}$ is the compressive strain, where h is the gap distance and $h_0 = h(t = 0)$ is the initial gap. Up to now, deviations between experiments and continuum media theory are qualitatively explained in terms of a shear strengthening effect (Tang et al. 2000) and demonstrated via superposition rheology (de Vicente et al. 2011b) and optical microscopy (Ruiz-López et al. 2012).

In this manuscript we follow a microscopic approach to develop a slender-body like micromechanical model for the squeeze flow behavior of MR fluids in slow compression. The model accounts for magnetostatic forces between the particles, and predicts the appearance of a yield compressive stress (and normal force) that scales with particle volume fraction and magnetic field squared, at low fields, in the linear magnetization regime. Strictly speaking, the validity of this model is limited to infinitesimally small deformations ($\varepsilon \rightarrow 0$) and for dilute suspensions ($\phi \rightarrow 0$), where single-particle-width chains should exist and interchain interactions are

safely neglected. However, in spite of the many simplifications in this model, we will demonstrate here that it works well for a wide range of deformations ($\varepsilon \in [0 - 0.7]$) and concentrations ($\phi \in [0.001 - 0.10]$), and that it is also capable to enlighten some experimental findings reported in the literature that remain currently unexplained. In particular, the model predicts a $\log F$ versus $\log(1 - \varepsilon)$ slope of -2 in much better agreement with experimental data at very low loadings where the shear strengthening effect is expected to be negligible ($\phi \lesssim 0.05$), (Ruiz-López et al. 2012). In the second part of the manuscript, we describe carefully designed experiments at low particle concentrations to validate the model. Apart from these, we also address the influence of sample volume, surface roughness and initial gap distance in the squeeze flow behavior.

1.2. Theoretical model

We assume a collection of single-particle-width chains confined between two parallel plates separated by a distance h and approaching with a velocity v . We assume that the gap h between the plates is much larger than the diameter of the (monodisperse) particles σ : $h \gg \sigma$. Also, we assume that v is small enough so that particles, initially forming straight chains in the field direction, readjust their positions into a thicker column but they do not spread out from the aggregate.

The magnetic dipolar energy for two particles with identical magnetic moments \vec{m}_i and \vec{m}_j separated at a distance r_{ij} follows the expression:

$$U_{ij} = \frac{1}{4\pi\mu_0\mu_{cr}} \frac{\vec{m}_i \cdot \vec{m}_j - 3(\vec{m}_i \cdot \hat{r})(\vec{m}_j \cdot \hat{r})}{r_{ij}^3} \quad (1.1)$$

where $\vec{m}_i = \vec{m}_j = \vec{m} = 3\mu_0\mu_{cr}\beta_p V_p \vec{H}$. Here, μ_0 is the magnetic permeability of the vacuum, μ_{cr} is the relative permeability of the

continuous medium, β_p is the so-called contrast factor of the particles, $\beta_p = (\mu_{pr} - \mu_{cr})/(\mu_{pr} + 2\mu_{cr})$, μ_{pr} is the magnetic permeability of the particles, V_p is the particle volume and \vec{H} is the magnetic field strength. In this work the magnetic field strength is calculated using the Local Field Theory, $\vec{H} = \vec{H}_{loc}$ (Martin and Anderson 1996). According to this, the local field in the center of a particle, i , can be calculated as $\vec{H}_{loc,i} = \vec{H}_0 + \sum_{j \neq i}^{N_{pc}} \vec{H}_{m_j}$, where \vec{H}_0 is the external magnetic field and $\vec{H}_{m_j} = \frac{3(\vec{m}_j \cdot \hat{r})\hat{r} - \vec{m}_j}{4\pi\mu_0\mu_{cr}r_{ij}^3}$ is the magnetic field produced by the magnetic dipole, \vec{m}_j located in the center of the particle i . Assuming an infinite and straight (no defects) single-particle-width chain aligned in the field direction, the local field becomes $\vec{H}_{loc} = (1 - \beta_p\zeta(3)/2)^{-1}\vec{H}_0$, where ζ is the Riemann Zeta function. Obviously, as a result of the approximations performed, the local field calculation is strictly valid in the limit of infinite gaps. However, for the gap intervals explored in this work, deviations are below 5%. It is important to remark here that the use of local fields instead of external fields is crucial because the local field is about 50% to 100% higher than the external magnetic field.

The total energy of a chain U_c is obtained by the addition of the contributions from all the pairs of particles within a chain:

$$U_c = \sum_{i=1}^{N_{pc}-1} \sum_{j=i+1}^{N_{pc}} U_{ij} \quad (1.2)$$

Here N_{pc} is the number of particles per chain.

Under the hypothesis that $\sigma/h \ll 1$, it is possible to extend the summations in Equation 1.2 to the continuum and hence the magnetic energy in a chain can be written as:

$$U_c = \int \frac{1}{4\pi\mu_0\mu_{cr}} \frac{d\vec{m} \cdot d\vec{m}' - 3(d\vec{m} \cdot \hat{r})(d\vec{m}' \cdot \hat{r})}{|\vec{r} - \vec{r}'|^3} \quad (1.3)$$

with $d\vec{m} = 3\mu_0\mu_{cr}\beta_a\vec{H}dV$ and $d\vec{m}' = 3\mu_0\mu_{cr}\beta_a\vec{H}dV'$. β_a is now the contrast factor of the aggregate: $\beta_a = (\mu_a - \mu_{cr})/(\mu_a + 2\mu_{cr})$. The magnetic permeability of the aggregates μ_a is estimated in this work using a Mean Field Theory (e.g. Bötcher equation):

$$\frac{\mu_a - \mu_{cr}}{3\mu_a} = \phi_a \frac{\mu_p - \mu_{cr}}{2\mu_a + \mu_p} \quad (1.4)$$

For simplicity, we suppose now that the aggregates have a cylindrical shape and that they are thin enough to suppose that $dV = \pi r_c^2 dz$ and $dV' = \pi r_c^2 dz'$ where r_c is the radius of the cylinder. We also assume that the magnetic field points in the z -direction so $\vec{H} = H\hat{z}$. Then, the magnetic energy of a chain is obtained as follows:

$$U_c = -\frac{9}{2}\pi r_c^4 \mu_0 \mu_{cr} \beta_a^2 H^2 \int \frac{dz dz'}{|z-z'|^3} \quad (1.5)$$

The limits of integration in Equation 1.5 come from the limits of the summations in Equation 1.2. Thus, the summation from 1 to $N_{pc} - 1$ is now the integral of z from $\sigma/2$ to $h - 3\sigma/2$ and the summation from $j = i + 1$ to N_{pc} is the integral from $z + \sigma$ to $h - \sigma/2$. Bearing in mind that $\sigma \ll h$, after some algebra, Equation 1.5 can be written as:

$$U_c = -\frac{9}{4}\pi r_c^4 \mu_0 \mu_{cr} \beta_a^2 H^2 \left(\frac{h}{\sigma^2} - \frac{3}{\sigma} + \frac{1}{h} \right) \quad (1.6)$$

Next, the total energy of the system U is estimated by multiplying the energy of a chain U_c times the number of chains N_c ; $U = N_c U_c$. Here, the total number of chains N_c is obtained from the particle volume fraction in the system $N_c = 6\phi V_0 / \pi \sigma^2 h_0$ and the radius of the chain r_c can be obtained as a function of the initial radius of the chain r_{c0} . Here, we assume that the initial radius of the chain is the radius of the particle $r_{c0} = \sigma/2$ and that the volume of the aggregate remains constant during the compression $\pi r_c^2 h = \pi r_{c0}^2 h_0$. As a result, the following relation is

obtained: $r_c^4 = \sigma^4 h_0^2 / 16h^2$. Therefore, substituting r_c , the total energy U can be written:

$$U = -\frac{27}{32} \phi V_0 \mu_0 \mu_{cr} \beta_a^2 H^2 \left(\frac{h_0}{h} - \frac{3\sigma h_0^2}{h_0 h^2} + \frac{\sigma^2 h_0^3}{h_0^2 h^3} \right) \quad (1.7)$$

Considering $\sigma \ll h_0$ and the definition of the compressive strain, $\varepsilon = (h_0 - h)/h_0$, we arrive to the final expression of the magnetostatic energy:

$$U = -\frac{27}{32} \phi V_0 \mu_0 \mu_{cr} \beta_a^2 H^2 \frac{1}{1-\varepsilon} \quad (1.8)$$

With this, the normal stress in the sample is obtained as the derivative of the energy density with the instantaneous gap (de Vicente et al. 2011b):

$$\tau_{zz} = -\frac{1}{s} \frac{\partial U}{\partial h} = -\frac{1}{sh_0} \frac{\partial U}{\partial \varepsilon} = -\frac{1}{V} \frac{h}{h_0} \frac{\partial U}{\partial \varepsilon} = -\frac{1}{V} (1-\varepsilon) \frac{\partial U}{\partial \varepsilon} \quad (1.9)$$

Finally, substituting Equation 1.8 into Equation 1.9 we get:

$$\tau_{zz} = \frac{27}{32} \phi \mu_0 \mu_{cr} \beta_a^2 H^2 \frac{1}{1-\varepsilon} \quad (1.10)$$

From Equation 1.10, a yield compressive stress τ_{YC} can be calculated as the normal stress τ_{zz} in the limit of no deformation (i.e. $\varepsilon \rightarrow 0$): $\tau_{YC} \equiv \lim_{\varepsilon \rightarrow 0} \tau_{zz} = \frac{27}{32} \phi \mu_0 \mu_{cr} \beta_a^2 H^2$. As a result, the yield compressive stress shows a linear dependence on the particle concentration ϕ and a quadratic dependence on the magnetic field strength H at low fields. These predictions are similar to those obtained from other micromechanical models reported in literature for yield shear stresses (Martin and Anderson 1996; de Gans et al. 1999; de Vicente et al. 2004; Volkova et al. 2000).

The magnetic normal force F can be obtained as the normal stress τ_{zz} multiplied by the surface area of the sample. There are two possibilities for the calculation of the surface area. On the one hand we can assume that the field-induced structures slip along the surfaces and move radially

when compressing. On the other hand, we can assume that the structures remain connecting the plates and do not displace radially. In the former case the surface area can be simply calculated as $S = V_0/h$. In the latter case the aggregates do not slip over the plates, the particle volume fraction increases within the gap according to $\phi = \phi_0/1 - \varepsilon$, and the surface area is given by $S = V_0/h_0$. Nevertheless, no matter the particular assumption employed we arrive to the same final equation for the magnetic normal force acting on the plates:

$$F = \frac{27}{32} \phi \mu_0 \mu_{cr} \beta_a^2 H^2 \frac{V_0}{h_0} \frac{1}{(1-\varepsilon)^2} \quad (1.11)$$

Strictly speaking, apart from magnetostatic forces, capillary forces F_{cap} do, *a priori*, contribute as well to the normal force under compression (e.g. Ewoldt et al. 2011). F_{cap} depends on the surface tension γ , the contact angle, θ and the gap separation h according to: $F_{cap} = -2\gamma \cos(\theta) V_0/h^2$. It is an adhesive force ($F_{cap} < 0$) and therefore it tends to diminish the gap between the plates. As observed, it depends on $(1 - \varepsilon)^{-2}$, similar to the magnetostatic contribution (c.f. Equation 1.11). As a result, capillary forces contribute shifting (vertically) the normal force curves. For large particle concentrations and magnetic fields, F_{cap} is clearly much smaller than F because $F \propto \phi H^2$. However, capillary forces can be important in the case of small loadings and small fields. In order to avoid complications coming from capillary forces, the normal force transducer will be reset after loading the sample in the geometry. With this, the effect of the capillary force can be safely neglected at least in the limit of validity of the model (i.e. at low compressive strains).

Similar to τ_{YC} , a yield normal force F_Y can also be defined starting from Equation 1.11:

$$F_Y \equiv \lim_{\varepsilon \rightarrow 0} F = \frac{27}{32} \phi \mu_0 \mu_{cr} \beta_a^2 H^2 \frac{V_0}{h_0} = \tau_{YC} \frac{V_0}{h_0} \quad (1.12)$$

As observed from Equations 1.10-1.12 predictions of this model are linear with the volume fraction and quadratic with the external magnetic field strength at low fields. On the one hand, the linearity with the volume fraction comes from the assumed arrangement of particles in single-particle-width chains at the beginning of the compression. Infinite dilution is a necessary condition for this to occur. On the other hand, the quadratic dependence with the magnetic field strength is a consequence of the linear magnetization approximation employed in the calculation of the magnetic moments of the particles and it is strictly valid in the limit of low fields. Of course, a constant dependence with the field strength is expected in the saturation regime by simply replacing $\beta_a^2 H^2$ by $M_{as}^2/9$ (with M_{as} the saturation magnetization of the aggregates).

1.3. Experimental

Conventional MR fluids were prepared by carefully mixing carbonyl iron microparticles (HQ grade, BASF) in silicone oil of 20 mPa·s (Sigma-Aldrich). A parallel plate magnetorheometer MCR-501 (Anton Paar) was used to perform constant volume squeeze flow experiments in the presence of magnetic fields similarly to Ruiz-López et al. 2012. Non-magnetic titanium plates (diameter 20 mm) were employed except for the most concentrated MR fluids. Unless otherwise stated, the initial separation was $h_0 = 300 \mu\text{m}$ and the sample volume was $V_0 = 20 \mu\text{L}$. Plates were supposed to be perfectly parallel even though a small misalignment exists (Andablo-Reyes et al. 2010, 2011). Also, the distortion of the force sensor under pressures generated in this work and wall slip were neglected (de Vicente et al. 2011b). Wall slip was only noticeable for the highest concentrations and prevented using sandblasted plates. Magnetic fields were not too large (smaller than \approx

300 kA/m) to minimize magnetic field gradients within the magneto cell (Laun et al. 2008).

All compression experiments reported here were run at constant volume V_0 , and constant velocity $v = 10\mu\text{m/s}$ (elongational rate range: $\dot{\epsilon} \sim 0.03 - 0.2 \text{ s}^{-1}$). This corresponds to low plasticity numbers $S < 0.5$ and low Reynolds numbers $Re \sim 10^{-3} \ll 1$ so lubrication and creeping flow approximations can be used in the so-called “filtration” regime (McIntyre and Filisko 2010). The normal force sensor was zeroed after loading the sample in the geometry. Then, an external magnetic field was (suddenly) applied for 60 s for the field-induced structuration prior to the compression test. Results presented below are always averages over at least three separate runs. All experiments were run at 25 °C.

1.4. Results and discussion

In Figure 1.1, the model is compared to experimental data, for different external magnetic field strengths (from $H_0 = 88$ to 354 kA/m), on MR fluids formulated at a particle concentration of $\phi = 0.05$. We employ this particular loading as a reference (it is the same as in de Vicente et al. 2011b). Experimental data are represented as symbols, and solid lines correspond to theoretical predictions (Equation 1.11). In this representation, experiments exhibit a slope of -2 in good agreement with the model. However, some deviations occur for the larger gap separations that could be due to inertia at the start-up of the compression test. Overall, a reasonably good quantitative agreement is found, bearing in mind that the model does not contain any free fitting parameter.

A more convenient way to visualize the experimental data is to plot a reduced force normalizing by the yield normal force, F_Y . From a theoretical point of view, this must result in a master scaling curve as a function of $1 - \varepsilon$. Figure 1.2 represents theoretical and experimental data for a particle loading of $\phi = 0.05$. Generally speaking, a reasonably good scaling is found in agreement with the theory.

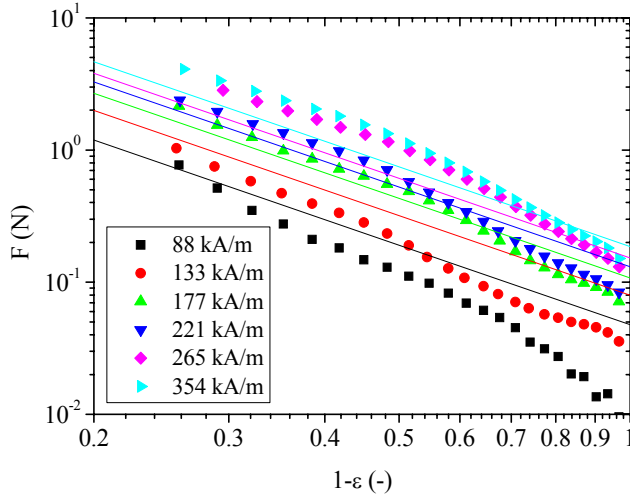


Figure 1.1 Compression tests for $\phi = 0.05$ suspensions at different external magnetic field strengths. Symbols: experimental data. Lines: theoretical predictions -Equation 1.11-. Sample volume $V_0 = 20\mu L$. Initial gap distance $h_0 = 300\mu m$.

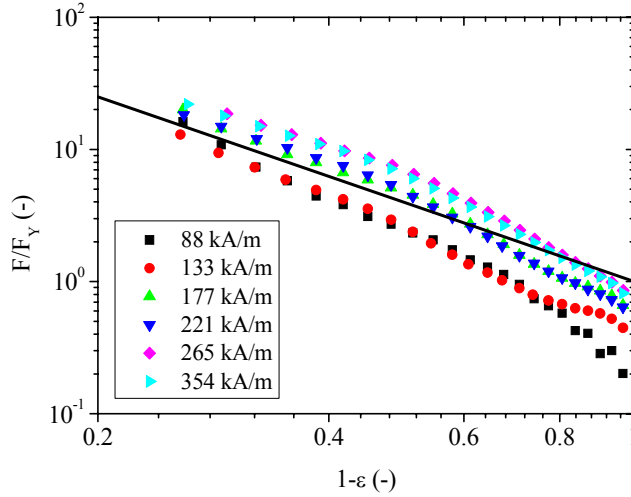


Figure 1.2 Scaling compression curves for $\phi = 0.05$ suspensions at different external magnetic field strengths. Normal forces, F , are scaled here by the yield compressive stress $F_Y = \frac{27}{32} \phi \mu_0 \mu_{cr} \beta_a^2 H^2 \frac{V_0}{h_0}$. Symbols: experimental data. Line: theoretical prediction -Equation 1.11-. Sample volume $V_0 = 20 \mu L$. Initial gap distance $h_0 = 300 \mu m$.

1.4.1. Effect of particle concentration

Next we aim to explore the influence of particle concentration. From a theoretical perspective, it is expected a better agreement the lower the particle loading. Figure 1.3a demonstrates that the model satisfactorily explains the experimental data for low particle loadings. A very good agreement with the experiments is found for concentrations below $\phi = 0.10$. This was expected to be so because interactions between aggregates (*interaggregate* interactions) are not important for dilute systems and they are neglected in the theoretical model. Figure 1.3b demonstrates that the linear scaling with particle concentration predicted by the micromechanical model actually experimentally occurs for low loadings (below $\phi = 0.10$).

For concentrations larger than $\phi = 0.10$ the model underestimates the experimental data (c.f. Figure 1.3). This is expected because of the presence of interaggregate interactions (Fernández-Toledano et al. 2014). Figure 1.3b demonstrates that the normal force is no longer proportional to the particle concentration and increases more rapidly (Ruiz-López et al. 2012). The slope is now closer to 3, in good qualitative agreement with observations by Guo et al. 2013. In their paper, see Figure 1.6, they report a larger than 2 slope for the most concentrated suspensions. However, contrary to Guo et al. 2013, where magnetic field increased under compression, in our experimental assembly, the magnetic field distribution remains essentially constant during compression and this facilitates the interpretation of the results. The deviation from a slope of 2 for the most concentrated MR fluids will be later explained in terms of slip at the walls that favors interaggregate interactions when the aggregates come into contact (see below).

In the case of the lowest concentrations investigated (below $\phi = 0.05$), the normal force sharply decreases for large $1 - \varepsilon$ values, at the early stages of the deformation. Unfortunately, the normal force resolution of our magnetorheometer is approximately 0.01 N which is very close to the typical force corresponding to this drop, and therefore we cannot get sound conclusions on this issue that, as stated above, may be related to inertia.

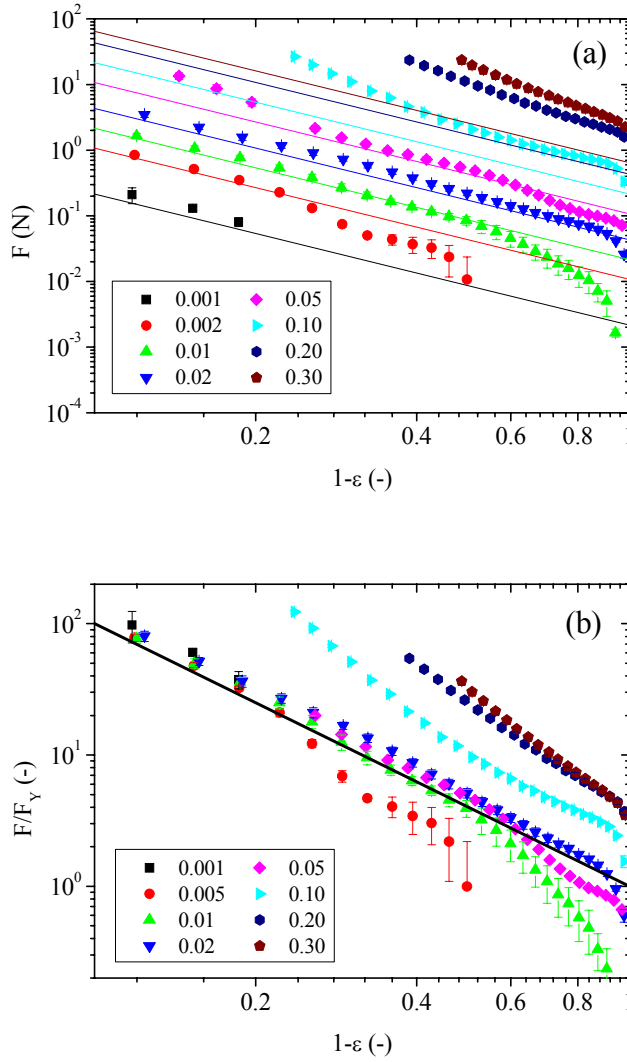


Figure 1.3 Effect of particle loading ϕ . Symbols: experimental data. Lines: theoretical predictions -Equation 1.11-. Sample volume $V_0 = 20\mu L$. Initial gap distance, $h_0 = 300\mu m$. Magnetic field strength, $H_0 = 177\text{ kA/m}$ a) Normal force, F , as a function of $1 - \varepsilon$. b) Normal force, F , divided by the yield normal force, F_Y , as a function of $1 - \varepsilon$.

1.4.2. Effect of sample volume

As commented in the discussion of Figure 1.3, the normal force resolution of the transducer impedes its accurate determination for large gap separations (large $1 - \varepsilon$ values), especially for the lowest particle loadings where the sensed normal force is very small (below 1 N). In order to better explore this region we decided to carry out further experiments involving larger sample volumes V_0 . These experiments would also be employed to test whether the theoretical prediction applies [$F \propto V_0$ according to Equation 1.11)].

Figure 1.4 contains experimental and theoretical predictions for initial volumes ranging from $V_0 = 20\mu L$ to $V_0 = 80\mu L$ in dilute MR fluids ($\phi = 0.01$). As expected, larger $1 - \varepsilon$ values (above the normal force resolution) can be reached because the resulting normal force increases. In qualitative agreement with the model, larger initial volumes give a larger normal force (c.f. Figure 1.4a). However, only for the lowest initial volume explored ($V_0 = 20\mu L$), a good quantitative agreement is found between experiments and the theoretical prediction (i.e. a linear dependence is found). For the largest initial volumes, the model again underestimates the experimental data. These results are better appreciated in Figure 1.4b. Figure 1.4b contains normalized normal force data for different sample volumes V_0 . For sufficiently small $1 - \varepsilon$ values, experimental data collapse in very good quantitative agreement with the proposed theoretical model; a linear dependence is expected. However, for large V_0 , experimental data systematically deviate from the predictions hence suggesting that inhomogeneities in the magnetic field distribution, that become more important for large V_0 and large $1 - \varepsilon$, influence the results.

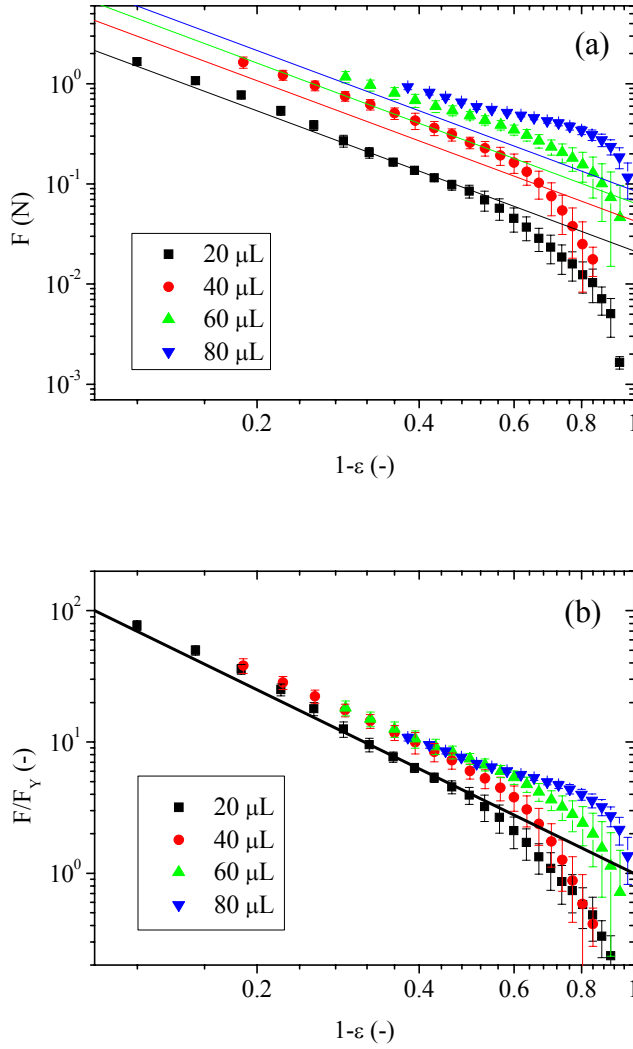


Figure 1.4 Effect of sample volume, V_0 , on the compression behavior of dilute MR fluids ($\phi = 0.01$). Symbols: experimental data. Lines: theoretical predictions -Equation 1.11-. Magnetic field strength $H_0 = 265$ kA/m. Initial gap distance $h_0 = 300$ μm . a) Normal force, F , as a function of $1 - \varepsilon$. b) Normal force, F , divided by the yield normal force, F_Y , as a function of $1 - \varepsilon$.

1.4.3. Effect of surface roughness

According to the model -Equation 1.11-, a slope of 2 should be experimentally found when plotting the normalized force as a function of $1 - \varepsilon$ independently of the existence of slip or not. However, experiments reported for the larger concentrations explored ($\phi = 0.10, 0.20$ and 0.30) give a slope of nearly 3 (c.f. Figure 1.3). To better understand these findings we decided to carry out further experiments using roughened plates. In particular, the plates employed in these new experiments were subjected to sand-blasting and had a peak-to-valley roughness of $9.2 \mu\text{m}$.

Results obtained for $\phi = 0.10, 0.20$ and 0.30 suspensions are contained in Figure 1.5 and demonstrate that the slope is very close to 2 when rougher surfaces are used, in very good qualitative agreement with the model. This suggests that the change in slope is actually mainly determined by slip of the MR fluid as a whole. Of course, the model still underestimates the experimental data because of the presence of interaggregate interactions at these particularly large particle loadings. In summary, the geometry assembly that is used by default in this work seems to prevent slip in the lowest concentrated MR fluids. However, for the largest concentrations investigated, the default roughness is not large enough to prevent slipping under this flow field. An important consequence of this is that the aggregates slipping along the surface can easily meet and form more complex interconnected structures therefore increasing the slope. By simply roughening the surfaces, slip is prevented and the slope becomes very close to 2 in agreement with the model. It is worth to note here that inhomogeneities in the field distribution do not explain the trends discussed in Figure 1.5 because the wetted area is the same for all tests.

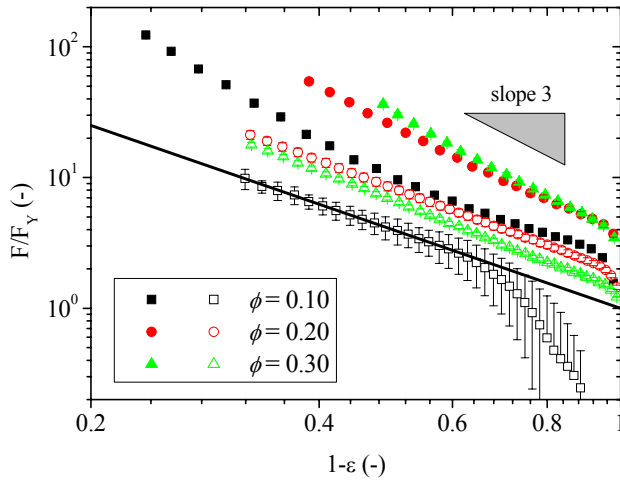


Figure 1.5 Effect of plates surface roughness on the compression behavior of concentrated MR fluids ($\phi = 0.10, 0.20$ and 0.30 vol%). Smooth plates (close symbols): $V_0 = 20 \mu\text{L}$; $h_0 = 300 \mu\text{m}$; $H_0 = 177 \text{ kA/m}$. Roughened plates (open symbols): $V_0 = 40 \mu\text{L}$; $h_0 = 600 \mu\text{m}$; $H_0 = 133 \text{ kA/m}$. Line: theoretical expression -Equation 1.11-

1.4.4. Effect of initial gap distance

According to the model described in the theoretical section, an initial gap distance, h_0 , dependence is expected. In particular, the magnetic contribution to the normal force scales with $F \propto h_0^{-1}$. Figure 1.6a demonstrates that the larger the gap distance the smaller the normal force, in good qualitative agreement with the model. This implies that the yield compressive stress decreases upon increasing the gap. The model is in a reasonably good agreement with the experiments for $h_0 > 300 \mu\text{m}$. However, for $h_0 \leq 300 \mu\text{m}$ the model underestimates the experimental normal force presumably because of the increasing importance of inhomogeneities in the magnetic field distribution in the magneto cell (note that V_0 is constant in this set of tests). Also, the hypothesis that

magnetic particles self-assemble in straight single chains prior to the test is more difficult to achieve in view of the major importance of particle-wall and interaggregate interactions at low h_0 values. In Figure 1.6b, the normal force is scaled by the yield normal force F_Y . As shown, the initial gap scaling predicted by the model ($F \propto h_0^{-1}$) is in very good agreement with the experiments for $h_0 > 300 \mu\text{m}$.

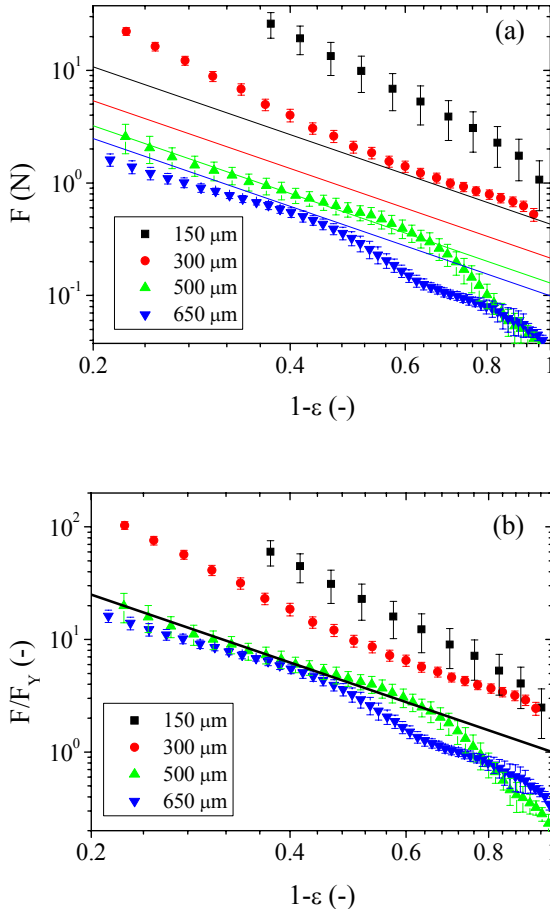


Figure 1.6 Effect of initial gap, h_0 , on the compression behavior of MR fluids. MR fluid concentration $\phi = 0.10$. Magnetic field strength $H_0 = 177 \text{ kA/m}$. Initial sample volume $V_0 = 20 \mu\text{L}$. a) Normal force, F , as a function of $1 - \varepsilon$. b) Normal force, F , divided by the yield normal force, F_Y , as a function of $1 - \varepsilon$.

1.5. Conclusions

A novel micromechanical model is proposed for the flow behavior of magnetorheological fluids in unidirectional slow compression. Even though this model is strictly valid in the dilute regime and for infinitesimally small deformations, it still explains experimental findings for a wide range of concentrations and deformations where the classical continuum media theory tends to fail (de Vicente et al. 2011b). In particular, the model provides an explanation for reported deviations from the slope of -2.5 that is theoretically predicted by continuous media theories. The predictions of the model are validated for different particle loadings, sample volume, surface roughness and gap distance.

Acknowledgements

This work was supported by MAT 2013-44429-R project (Spain) and by Junta de Andalucía P10-RNM-6630, P10-FQM-5977 and P11-FQM-7074 projects (Spain). J.A.R.-L. acknowledges financial support by the “Ministerio de Educación: Becas del Programa de Formación del Profesorado Universitario (FPU)” (AP2010-2144).

References

- Andablo-Reyes E, Hidalgo-Álvarez R, de Vicente J (2010) A method for the estimation of the film thickness and plate tilt angle in thin film misaligned plate-plate rheometry. *J Non-Newtonian Fluid Mech* 165:1419-1421.
- Andablo-Reyes E, Hidalgo-Álvarez R, de Vicente J (2011) Erratum to “A method for the estimation of the film thickness and plate tilt angle in thin film misaligned plate-plate rheometry” [*J. Non-Newtonian*

- Fluid Mech. 165 (2010) 1419–1421]. *J Non-Newtonian Fluid Mech* 166:882-882.
- de Gans BJ, Hoekstra H, Mellema J (1999) Non-linear magnetorheological behaviour of an inverse ferrofluid. *Faraday Discuss.* 112:209–224.
- de Vicente J, Klingenberg DJ, Hidalgo-Álvarez R (2011a) Magnetorheological fluids: a review. *Soft Matter* 7:3701-3710
- de Vicente J, López-López MT, Durán JDG, González-Caballero F (2004) Shear flow behavior of confined magnetorheological fluids at low magnetic field strengths. *Rheol. Acta* 44:94-103.
- de Vicente J, Ruiz-López JA, Andablo-Reyes E, Segovia-Gutiérrez JP, Hidalgo-Álvarez R (2011b) Squeeze flow magnetorheology. *J Rheol* 55:753-779
- Ewoldt RH, Piotr T, McKinley G, Hosoi AE (2011) Controllable adhesion using field-activated fluids. *Phys.Fluids* 23(7):073104.
- Fernández-Toledano JC, Rodríguez-López J, Shahrivar K, Hidalgo-Álvarez R, Elvira L, Montero de Espinosa F, de Vicente J (2014) Two-step yielding in magnetorheology. *J. Rheol.* 58(5):1507-1534.
- Guo CY, Gong XL, Xuan SH, Qin LJ, Yan QF (2013) Compression behaviors of magnetorheological fluids under nonuniform magnetic field. *Rheol. Acta* 52(2):165-176.
- Laun HM, Schmidt G, Gabriel C (2008) Reliable plate-plate MRF magnetorheometry based on validated radial magnetic flux density profile simulations. *Rheol Acta* 47:1049–1059.
- Martin JE, Anderson RA (1996) Chain model of electrorheology. *J. Chem. Phys.* 104(12):4814–4827.
- McIntyre EC, Filisko FE (2010) Filtration in electrorheological suspensions related to the Peclet number. *J Rheol* 54(3):591-603
- Ruiz-López JA, Hidalgo-Álvarez R, de Vicente J (2012) On the validity of continuous media theory for plastic materials in

magnetorheological fluids under slow compression. *Rheol. Acta* 51(7):595-602.

Tang X, Zhang X, Tao R, Rong Y (2000) Structure-enhanced yield stress of magnetorheological fluids. *J Appl Phys* 87(5):2634-2638

Volkova O, Bossis G, Guyot M, Bashtovoi V, Reks A (2000) Magnetorheology of magnetic holes compared to magnetic particles. *J. Rheol.* 44:91-104.

Xu Y, Gong X, Liu T, Xuan S (2014) Squeeze flow behaviors of magnetorheological elastomers under constant volume. *J. Rheol.* 58(3):659-679.

Chapter 2.

Squeeze Flow Magnetorheology

**Juan de Vicente, José Antonio Ruiz-López, Efrén Andablo-Reyes,
Juan Pablo Segovia-Gutiérrez and Roque Hidalgo-Álvarez**

**This article is published in: *Journal of Rheology*. Volume: 55(4).
Pages: 753-779. 2011.**

Abstract

This paper is concerned with an investigation of the rheological performance of magnetorheological fluids under squeeze flow. Preliminary results on Newtonian fluids are first compared to Stefan's equation. Then, unidirectional monotonous compression tests are carried out in the presence of uniaxial external magnetic fields at slow compression rates under constant volume operation. Results are compared to Bingham plastic, bi-viscous and single chain micromechanical squeeze-flow models. Measurements using combined deformation modes (compression + small-strain oscillatory shear) suggest a compression-induced shear strengthen effect up to strains of ~ 0.5 . Particle-level dynamic simulations are in qualitatively good agreement with experimental observations.

2.1. INTRODUCTION

Magnetorheological (MR) and electrorheological (ER) fluids are field-responsive colloids that show a rapid increase in viscosity upon the application of an external magnetic or electric field respectively [Ginder (1998); Rankin *et al.* (1998); Bossis *et al.* (2002)]. The reason for this is the formation of particle clusters aligned in the field direction. As a starting point, their flow behavior is typically modeled by the Bingham fluid like equation where, in the case of steady shear flow, the stress is given by

$$\tau = \tau_y + \eta_p \dot{\gamma} \quad (2.1)$$

Here τ_y is the yield shear stress, η_p is the plastic viscosity, and $\dot{\gamma}$ is the shear rate. In this work we will focus on MR fluids. However, many of the results presented below can be easily extended to ER fluids.

Currently, an important gap exists between commercial requirements for the strength of field-responsive fluids and their performance levels. While significant work has been done to enhance the fluid formulation [Bossis *et al.* (2002); de Vicente *et al.* (2003); Vereda *et al.* (2007); Vereda *et al.* (2009); de Vicente *et al.* (2010)], much less efforts have been made to improve the design of devices most of them being restricted to shearing operation regimes [Olabi and Grunwald (2007)]. Most devices that use MR fluids can be classified as having either fixed poles (pressure-driven flow mode), relatively moveable poles (direct-shear flow mode and squeeze-film flow mode) or a combination of these modes [Jolly and Carlson (1996)]. Diagrams of these three basic operational standard flow modes are shown in Figure 2.1. Interestingly, it has been documented that

field-responsive fluids show yield stresses in the order of direct-shear < pressure-driven < squeeze flow mode [Havelka and Piolet (1996)].

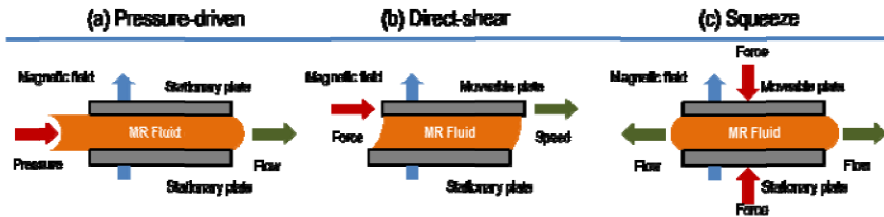


Figure 2.1. Basic operational modes for controllable MR fluid devices.

Classical direct-shear mode has been studied thoroughly in the literature under dynamic [de Gans *et al.* (1999); de Vicente *et al.* (2005); Saldivar-Guerrero *et al.* (2006); Ekwebelam and See (2007); de Vicente *et al.* (2007); de Vicente *et al.* (2009); de Vicente *et al.* (2010); Ramos *et al.* (2010a)] and steady shear regimes [Volkova *et al.* (2000); de Vicente *et al.* (2004); Park *et al.* (2006); Bell *et al.* (2008); de Vicente *et al.* (2010); Ramos *et al.* (2010b)] and several products are already present in the market [Olabi and Grunwald (2007)]. Pressure-driven flow mode investigations have also been reported because much larger and realistic shear rates can be imposed (up to $20,000 \text{ s}^{-1}$, in contrast to conventional rotational rheometry that encompasses shear rates only up to a few thousand $1/\text{s}$) [Wang and Gordaninejad (2006)]. Surprisingly, relatively limited attention has been given to the behavior of MR fluids in squeeze flow mode, even though it has been suggested that the yield stress that could be achieved would be ten times larger than that attainable with either the direct-shear or pressure-driven flow modes [Zhang *et al.* (2004)]. Furthermore a compression-assisted-aggregation process has been demonstrated to enhance the yield shear stress in field-responsive fluids by the formation of thick columns with strong and robust ends (MR

fluids [Tang *et al.* (2000)]; ER fluids [Tao *et al.* (2002)]. Despite of their importance, a complete understanding of the mechanical properties of MR fluids under valve or squeeze flow behavior is still missing in the literature [McIntyre and Filisko (2010)].

In this manuscript the squeeze flow (i.e. biaxial elongational flow) behavior of MR fluids is studied. First, the experimental procedure for investigating the normal force was checked by measuring forces with model Newtonian fluids. Then, we focused on the squeeze flow behavior of MR fluids in low Peclet numbers (slow plate motion) where “filtration” is expected to be significant. Although the interparticle interaction is the key issue in the field-responsive effect –especially at small compressive strains–, the structure of particle aggregates is known to be also important in the MR mechanism. In this sense we also investigated the structure evolution under compression through combined small-amplitude oscillatory shear (SAOS) and squeeze flows as well as using particle dynamic simulations. The manuscript is structured as follows: in Section 2.2 we review the state-of-the-art of squeeze flow behavior of field-responsive fluids. In Section 2.3 we illustrate some of the most relevant squeeze flow theories for Newtonian and plastic fluids. In Section 2.4 we describe the experiments and in Section 2.5 we show the details of the particle-level magnetorheological simulations. Results are presented Section 2.6. We end with some conclusions in Section 2.7.

2.2. BACKGROUND

A seminal paper published by Stanway *et al.* (1987) is probably the first to demonstrate the feasibility of employing field-responsive (ER) fluids under squeeze flow. Here, tensile and compressive forces were found to be considerably larger than those developed in shearing flows. This was

later confirmed through experiments by Monkman (1995) and Gong and Lim (1996). Short time later, vibration control applications followed with the construction and testing of ER squeeze-based damping devices [Stanway *et al.* (1992)] and engine mounts [Sproston *et al.* (1994a)]. On the theoretical side both macroscopic and microscopic approaches have been used. A bi-viscous model, inspired in earlier work on plastic fluids by Gartling and Phan-Thien (1984), was successfully used to explain the dynamic performance of ER fluids in squeeze [Williams *et al.* (1993); Sproston *et al.* (1994a); Sproston *et al.* (1994b)] and unidirectional monotonous compression for large gap separations [Tian *et al.* (2003a); Meng and Filisko (2005)]. Some years later, inertia was included in the theoretical derivation [Lee and Wen (2002)] and an iterative approach for the yield stress was incorporated to the model rather than using the classical power law expression [El Wahed *et al.* (2003)]. Lukkarinen and Kaski (1996, 1997) employed computer simulation methods in a comparative study of the mechanical properties of model ER structures under various dynamical loading conditions (shear, compression and tension). It was demonstrated that compressive loading transferred the largest force. Unlike simulations under shear flow, in squeeze flow simulations it is not easy to apply periodic boundary conditions so in general the number of particles needs to be increased. To avoid this problem a Message Passing Interface parallel processing technique was employed by Kim *et al.* (1999).

An investigation on the application of ER fluids to control vibration under conditions of constant voltage and constant electric field was reported by El Wahed *et al.* (1998). The effect of electric field strength, particle concentration and continuous phase viscosity were investigated by Chu *et al.* (2000). Special emphasis was paid to the appearance of normal stress fluctuations due to the deformation of field-induced chainlike structures

under the field. The effect of an AC electric field, with tunable waveform, on the performance of an ER fluid in oscillatory squeeze flow was investigated by El Wahed *et al.* (2000). The bi-viscous model was found to be equally valid for the AC case as for the DC case reported by El Wahed *et al.* (1998). See *et al.* (1999) measured field-induced force waveforms in ER fluids under oscillatory squeeze flow using a Micro-Fourier Rheometer. Their results provided experimental support for the theoretical model of ER fluids under squeeze proposed by Sproston *et al.* (1994a). El Wahed *et al.* (1999) reported an experimental investigation into the influence of particle size on the effectiveness of an ER fluid in dynamic squeeze flow. They demonstrated that small particles are generally the more effective in terms of the level of transmitted force if compared to large particles. Viera *et al.* (2001) used a Mechanical Testing Machine to investigate the mechanical properties of ER fluids under tensile, compressive and oscillatory squeeze tests. Their results showed that ER fluids are more resistant to compressive than to tensile stress. In compression tests, the compressive stress increased with the increase of the electric field strength. However, the increase of the initial gap size and the approaching velocity produced a decrease on the compressive stress. Tian *et al.* (2002a) found that both the compressive stress and the compressive modulus in ER fluids show an exponential relationship with the compressive strain while the strain is larger than 0.1. Stepwise compression experiments demonstrated that with the increase of applied voltage, ER fluids show a change of electric field-determined behavior to the plastic fluid compressive mode [Tian *et al.* (2002b)]. A comprehensive study of the volume fraction dependence in squeezed ER fluids has been traditionally impeded by the “sealing effect” appearing under constant area operation. These restrictions were avoided by using a constant volume apparatus [McIntyre and Filisko (2007)]. At high field strengths, low compression rates and low viscosity of the continuous phase most of

the particles are kept between the plates and only the dispersing phase is squeezed out [Lynch *et al.* (2006); McIntyre and Filisko (2010); Tian *et al.* (2010)]. This fact has been parametrized in the form of a Peclet number as the ratio of viscous or convective forces to diffusive terms [Collomb *et al.* (2004); McIntyre and Filisko (2010)]. Most of the squeeze flow literature reviewed above concerns ER fluids and involves constant voltage and constant area compression. In this case, the electric field strength and volume concentration increase during the process. Thus, any change in the compressive stress is associated to the change of the electric field, volume fraction and the structural strength (i.e. the so-called structure parameter [Conrad (1998); Wu and Conrad (1998)]). Even though this problem can be partially skipped in the case of tensile flow by using normalized methods [Tian and Zou (2003b)] it is an important drawback. In principle, when a MR fluid is compressed under a constant volume in the presence of a DC uniform magnetic field, the change of compressive stress may indicate mostly the change of the structure parameter in the MR fluids.

Surprisingly, the squeeze flow behavior of MR fluids has not been studied so thoroughly comparing with their ER analogues. First reports on this topic concern compression-assisted-aggregation processes to achieve high-efficiency MR fluids by the so-called squeeze-strengthening effect. This consists in enhancing the yield shear stress in field-responsive fluids by the formation of thick strong columns under compression [Tang *et al.* (2000)]. This approach was further corroborated by Zhang *et al.* (2004) and Zhang *et al.* (2009). Contrarily, See *et al.* (2006) presented experiments in a MCR (Anton Paar) rheometer where compression did not have a large effect in the shear response. A detailed comparative study of the behavior of MR fluids under steady shear flow and constant velocity squeezing flow was reported by See (2003). The measurements showed

that the mechanical response under squeezing flow scaled as $H^{0.91}$, whereas the response under shearing scaled as $H^{1.4}$. A special device was designed and fabricated to perform squeeze, torsional and squeeze combined with torsional flows on an Instron Multiaxial Testing Machine [Kulkarni *et al.* (2003)]. Contrary to what is believed [Tang *et al.* (2000)], it was experimentally observed that the introduction of a squeeze component in shearing flows (oscillatory torsional mode) does not always increase the strength of the MR fluid [Kulkarni *et al.* (2003)]. Mazlan *et al.* (2008) described the effect of compressive speed and magnetic field strength in the stress-strain curves of commercial MR fluids. On the one hand they observed a negligible effect of the compressive speed. On the other hand, the higher the magnetic field the faster stress-strain curve developed.

2.3. SQUEEZE FLOW THEORY

Under squeeze flow a material is compressed between two parallel plates. A schematic representation is shown in Figure 2.2. Here, the sample of volume V is positioned between two circular plates initially separated a gap distance h_0 . In this section we will look for the relationship between the normal force F , height of the sample layer h , and squeezing rate of the moving plate v as this dependency can be used to obtain important rheological properties of the sample, and in particular its yield stress.

To investigate the squeeze flow properties the Reynolds number Re has to be first estimated. In this operation mode, the Reynolds number can be defined as $Re = h_0 v \rho / \eta$, where ρ is the suspension density and η is the suspension viscosity [Engmann *et al.* (2005)]. The squeeze flow analysis is greatly simplified here because lubrication theory and creeping flow approximation can be invoked as $Re \sim 10^{-3} \ll 1$.

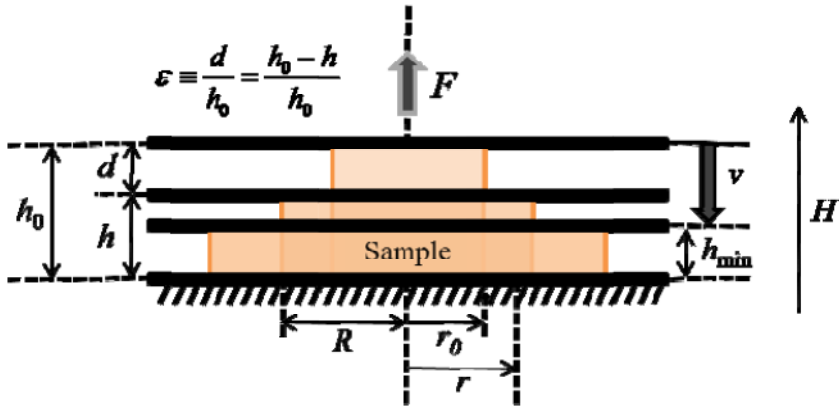


Figure 2.2. Schematic diagram of the constant volume squeeze flow experiment (not to scale). For simplicity the free surface profile is represented as a vertical line. In a typical experiment $h_0 = 300\mu\text{m}$ and $h_{\min} = 50\mu\text{m}$. The largest compressive strain was $\varepsilon \sim 0.83$.

2.3.1. Newtonian fluids

Since the pioneering work by Stefan (1874), the squeeze behavior of Newtonian fluids has received a lot of attention [e.g. Diennes and Klemm (1946); Campanella and Peleg (1987); Raphaelides and Gioldasi (2004)]. Under constant volume, V , and no-slip condition Reynolds equation predicts the following radial pressure distribution (see Figure 2.2):

$$p(r) = \frac{3\eta v}{h^3} [R^2 - r^2] \quad (2.2)$$

The normal force F acting on the plate is simply obtained by integration on the surface:

$$F = \frac{6\pi\eta v}{h^3} \int_0^R [R^2 - r^2] r dr = \frac{3\pi\eta v}{2h^3} R^4 \quad (2.3)$$

and therefore the so-called Stefan's equation results:

$$F = \frac{3\eta v V^2}{2\pi h^5} \quad (2.4)$$

Stefan's equation assumes a no-slip boundary condition at the plates surfaces. However, this fact does not always holds and generally the presence of slip at the surfaces results in a significant force reduction when squeezing the sample [Engmann *et al.* (2005)]. Actually, analytical expressions exist in the literature for no-slip (i.e. "frictional" surfaces) [Diennes and Klemm (1946)] and perfect slip (i.e. "lubricated" surfaces) [Campanella and Peleg (1987); Raphaelides and Gioldasi (2004)], the later providing a lower limit for the forces with $F \sim h^{-2}$ in the case of constant volume operation. In most cases neither no-slip nor perfect slip occurs, and partial slip arises at the moving surface where the radial velocity at the surface v_r takes on a linear form $v_r = v_s r/R$. Here, the slip parameter v_s can be adjusted between no-slip at a minimum value and perfect slip at its maximum value; $0 < v_s < \frac{vR}{2h}$. Several authors have investigated the partial slip situation in the past [Laun *et al.* (1999); McIntyre (2008)].

2.3.2. Inelastic yield stress fluids: a continuum approach

The squeeze flow behavior of inelastic yield stress fluids under no-slip conditions was initially studied by Scott (1929). The problem was later addressed by Covey and Stanmore (1981) who revisited it and reported theoretical and experimental investigations using a parallel-plate plastometer. Fluids obeying a Bingham constitutive equation were analyzed in their paper under both constant volume and constant radius operation regimes.

When dealing with yield stress fluids a plasticity number can be introduced [Covey and Stanmore (1981)]:

$$S = \frac{\eta_p v R}{h^2 \tau_y} \quad (2.5)$$

The plasticity number separates two regimes. At low S number the resistance to deformation arises from the yield shear stress component. However, at large S number the major resistance to flow arises from viscous effects. Analytic expressions exist for the limits $S < 0.05$ and $S > 10$ whereas intermediate values of S require numerical methods. In MR experiments presented in this work, S was found to be always smaller than 0.05 whatever the gap distance and magnetic field strength applied hence suggesting that particle aggregates will dominate the flow behavior.

Starting from the Cauchy-momentum equation for an incompressible fluid, Covey and Stanmore (1981) calculated the pressure on the fluid. Then, integrating the pressure over the total plate area gives a relation between the normal force F and the approaching velocity v :

$$F = \frac{2\pi\tau_y R^3}{3h} + \frac{4\pi}{7h^2} \sqrt{2\tau_y \eta_p v R^7} \quad (2.6)$$

It must be noted here that Equation 2.6 was originally obtained for constant radius experiments, however, change to the constant volume condition can be simply made substituting $V = \pi R^2 h$ [Covey and Stanmore (1981)].

Subsequent publications in this field demonstrated that theoretical work was in some conflict with regard to the flow pattern produced in the geometry [Lipscomb and Denn (1984)]. Moreover the Bingham model was found to be unnecessarily complicated for numerical simulations. Gartling and Phan-Thien (1984) carried out a theoretical analysis that paralleled the method proposed by Covey and Stanmore (1981) this time using a bi-viscosity model instead of the Bingham description. This bi-viscosity model was later used by Williams *et al.* (1993) in the development of a time-dependent sinusoidal squeeze flow theory for ER

fluids that was successfully applied to a prototype automotive engine mount.

According to the theory by Williams *et al.* (1993), initially developed for ER fluids and adapted here for MR fluids, the normal force acting on the plates can be expressed by the following equation:

$$F = \frac{2\pi\tau_y R^3}{h\chi^3} \left[\frac{\gamma^3}{108} + \int_{\gamma/3}^{\chi} S^2 G dS \right] \quad (2.7)$$

where γ , χ , S and G are parameters defined by:

$$\gamma = \frac{\eta}{\eta_r}; S = \frac{\eta v r}{h^2 \tau_y}; \chi = S(r = R); G = -\frac{h}{2\tau_y} \frac{dp}{dr} \quad (2.8)$$

Here, η_r is the preyield viscosity and η is the viscosity above the yield point in the bi-viscous model.

Interestingly, when the plasticity number S is small, pressure gradient G and thus the compressive force are driven by the yield shear stress and the viscous contribution is negligible. Under this condition, Equation 2.7 is simplified to [Meng and Filisko (2005)]:

$$F = \frac{2\pi\tau_y R^3}{3h} \quad (2.9)$$

which also corresponds to the low S limit of Equation 2.6 that was obtained from a Bingham approach. This finding allows us to conclude that both macroscopic descriptions, involving Bingham or bi-viscous models, result in a normal force that varies with the gap distance as $h^{-5/2}$ under constant volume operation.

Whereas the theory presented above treats field-responsive fluids as homogeneous materials and model them as simplified Bingham (c.f. Equation 2.6) or bi-viscous fluids (c.f. Equation 2.7), in reality, field-

responsive fluids are two-phase fluids consisting of particle aggregates immersed in a continuous liquid phase. In the next section we provide a squeeze flow theory under a simplified microscopic description.

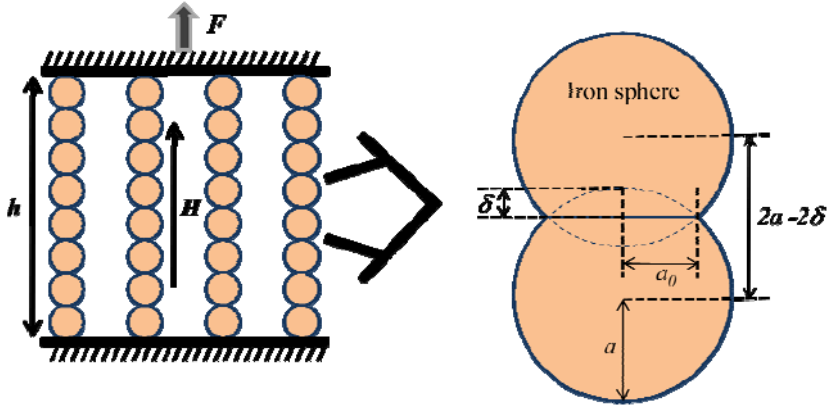


Figure 2.3. Schematic representation illustrating the standard micromechanical model consisting in a cubic network of single chains.

2.3.3. Dilute magnetorheological fluids: a microscopic description

Yang first studied the compressive and tensile behavior of dilute ER fluids by the electrostatic polarization model and Hertzian contact theory [Yang (1997)]. In this section we will adapt Yang's theory to the case of MR fluids.

A first microscopic insight in the normal force versus gap dependence of dilute MR fluids can be obtained under the assumption that particles aggregate to form single chains of particles aligned with the field (see Figure 2.3). With this, the gap thickness h can be expressed as:

$$h = 2N_{pc}(a - \delta) \quad (2.10)$$

and the normal force F acting on the plate is:

$$F = N_c f \quad (2.11)$$

Here, N_{pc} is the number of particles in a chain, a is the radius of the particle, δ is the indentation depth, N_c is the number of chains and f is the force between the particles.

Assuming that the particles behave as purely elastic materials, Hertz contact theory states that the radius of the contact area between the particles a_0 is given by

$$a_0^3 = \frac{3a}{4} \frac{1-\nu^2}{E} (f + f_m) \quad (2.12)$$

where ν is the Poisson ratio, E is the Young's modulus, f_m is the magnetostatic interaction force between the spheres and the indentation depth is $\delta = a_0^2/a$.

As a first approximation, we can assume dipolar magnetic interactions for aligned dipoles. Hence,

$$f_m = f_0 \frac{a^6}{(a-\delta)^4} H^2 \quad (2.13)$$

where $f_0 = (3/2)\pi\mu_0\mu_{cr}\beta^2$ and $\beta = (\mu_{pr} - \mu_{cr})/(\mu_{pr} + 2\mu_{cr})$. Here, μ_0 is the permeability of vacuum, μ_{pr} is the relative permeability of the particles, μ_{cr} is the relative permeability of the continuous phase, β is the magnetic contrast factor, and H is the magnetic field strength.

After some algebra, combining Eqs. (10-13) we arrive to:

$$F = \frac{3}{2} \frac{\phi V f_0 H^2}{\pi h} \left[\frac{4E}{3f_0 H^2 (1-\nu^2)} \left(\frac{\delta}{a}\right)^{3/2} \left(1 - \frac{\delta}{a}\right) - \left(1 - \frac{\delta}{a}\right)^{-3} \right] \quad (2.14)$$

Interestingly, the force – gap dependence scales with a power of -1 . This is a significantly weaker gap distance dependence if compared to predictions obtained from macroscopic models (c.f. Equation 2.9). As

observed, the sustainable load increases nonlinearly with decreasing separation of the surfaces and is a linear function of the elastic modulus of the particles.

2.4. EXPERIMENTAL: SQUEEZE FLOW MAGNETORHEOMETRY

2.4.1. Apparatus

A MCR 501 (Anton Paar) magnetorheometer was employed to investigate the squeeze flow MR behavior. Non-magnetic (titanium-based) parallel plates of diameter 20mm were used. A scheme of the experimental squeeze flow test is sketched in Figure 2.2. In the compression tests the original commanded gap was set as $h_0 = 300\mu\text{m}$, then the upper plate moved slowly down towards the stationary bottom plate at a constant velocity v while the normal force acting on the upper plate was monitored. The measuring range of the force sensor is $\pm 50\text{N}$ and its elastic factor is $0.59\mu\text{m}/\text{N}$. The distortion of the force sensor under the pressures handled in this work was neglected. As a measure of the deformation, the compressive strain was defined here as $\varepsilon = (h_0 - h)/h_0 = d/h_0$. Typically, in our experiments the maximum compressive strain achieved was $\varepsilon \sim 0.8$ while the strain rate was around $\dot{\varepsilon} \sim 0.03 - 0.2\text{s}^{-1}$.

An external magnetic circuit was used to generate uniaxial DC magnetic fields of the order of $\sim 100\text{kA}/\text{m}$ in the gap between the plates [Wollny *et al.* (2002)]. Due to geometrical constrictions, a central hole exists to pass the rheometer shaft through. As a consequence, the generated magnetic field is not absolutely uniform in the radial direction. This may result in some particle migration, especially at the largest field strengths

investigated [Andablo-Reyes *et al.* (2010a)]. A wide range of magnetic field strengths were examined up to 354 kA/m –well within the linear magnetization regime of the particles and suspensions–. Even though larger magnetic fields can be applied in the magnetorheological cell, particle migration enhances as a consequence of magnetic field gradients making it difficult to interpret the experimental results [de Vicente *et al.* (2009)]. It should also be remarked that preliminary tests were carried out on non-magnetic samples to confirm that the application of the magnetic field did not result in a measurable normal force. It should also be stressed that the magnetic field density in the MR fluid changes upon changing the gap since the magnetic resistance associated to the gap is modified. However, this fact has not been addressed in the present analysis. The plates were assumed to be perfectly parallel even though a small misalignment is feasible [Andablo-Reyes *et al.* (2010b)]. Nonetheless, our experiments did not reach strains larger than $\varepsilon = 0.8$ which helped to prevent a serious error caused by the nonparallelism of the plates. The gap error was accounted for by calibration using a semiempirical approach that involves running measurements on Newtonian fluids at different gap distances. In particular, following the method by Connelly and Greener (1985) a gap error of $17\mu\text{m}$ was estimated in our plate-plate geometry.

2.4.2 Materials preparation and experimental protocol

Newtonian fluids used in this study were silicone oils having different viscosities (100 mPa s and 350 mPa s). These were obtained from Sigma-Aldrich and used without further purification. MR fluids were prepared by carefully mixing carbonyl iron powder (HQ, BASF; diameter $\sim 800\text{nm}$) in silicone oil (20 mPa s, Sigma-Aldrich) to get suspensions having a volume fraction of 5 vol% (metallic iron density 7.8 g/cm^3). This concentration is small enough for the models to be applied [c.f. Section 2.3.3] and large enough to get a measurable normal force signal. The

preparation of suspensions consisted of the following steps: (i) magnetic powder and silicone oil were mixed in a polyethylene container; (ii) the mixture was stirred first by hand, and then in an ultrasonic bath; (iii) step (ii) was repeated several times to ensure the required final homogeneity.

Basically, two possibilities exist when studying the squeeze behavior of a material: constant area or constant volume approaches. Here, the tests were carried out under constant volume conditions. This means that, a priori, the area of the plate in contact with the sample changes accordingly to the change in gap thickness. With this, the concentration of the particles that stay in between the plates is known throughout the experiment in contrast to what happens for ER fluids under conventional constant area experiments because of the so-called “sealing effect”. Another advantage of using constant volume tests is the fact that inertial effects are minimized contrarily to constant area experiments where corrections are usually needed [McIntyre (2008); McIntyre and Filisko (2010)].

Generally speaking, squeeze flow tests are typically run under constant normal force applied F or constant approaching velocity v (i.e. constant rate loading/compression). The experiments presented in this manuscript concern constant approaching speed investigations ($1 - 10 \mu\text{m/s}$) in a displacement control mode resulting in non-steady tests with variable strain rate. In this case, the inertial terms contained in the force equation vanish [Bird (1987)]. Furthermore, the small approaching speeds used guarantee that results presented here corresponded to low S numbers [Covey and Stanmore (1981)] and to the so-called “filtration” regime of operation [McIntyre and Filisko (2010)].

In a typical experiment a small amount of the MR fluid (initial radius $r_0 = 3.8 \pm 0.3 \text{ mm}$, volume $V \sim 14 \mu\text{L}$) was deposited on top of the lower plate using a microliter syringe (MV17990 Boeco Germany). Once

the sample had relaxed the normal force transducer was reset to zero. Next, a uniaxial DC magnetic field was suddenly applied across the plates with the sample subjected to no deformation. This period was long enough to allow the aggregates to form. After 60 seconds, the compression test was started at a constant approaching speed v still in the presence of the magnetic field. Results presented below are always averages over at least three separate runs with fresh new samples. All experiments were run at 25 °C. It is worth to remark that the normal force did not experience any measurable variation when the magnetic field was applied in the quiescent state due to the small particle concentration in the MR fluid. Finally, the way how to increase the magnetic field, either suddenly or gradually, was also checked and was found not to be important in the compression test results.

2.5. PARTICLE-LEVEL SIMULATIONS

3-D MR simulations were carried out following a simplified method developed by Klingenberg and coworkers [Klingenberg *et al.* (1989); Klingenberg *et al.* (1991); Heine *et al.* (2006)]. The MR fluid was modeled as a suspension of N buoyant, inertialess particles in a Newtonian fluid of viscosity η_c and relative magnetic permeability μ_{cr} . The particles were considered to be monodisperse with diameter $2a$ and relative magnetic permeability μ_{pr} . When a magnetic field is applied the particles are magnetized due to their difference of permeability with respect to the continuum medium. Assuming pairwise additivity and taking the point dipole approximation, the magnetic force exerted on the particle i by the rest of the particles is:

$$\vec{F}_i^m = \sum_{j=1, j \neq i}^N F_0 \left(\frac{2a}{r_{ij}} \right)^4 [(3\cos^2\theta_{ij} - 1)\hat{r} + \sin(2\theta_{ij})\hat{\theta}] \quad (2.15a)$$

$$F_0 = \frac{3}{4}\pi\mu_0\mu_{cr}\beta^2 a^2 H^2 \quad (2.15b)$$

where F_0 is the so-called magnetic field dependent constant, \hat{r} and $\hat{\theta}$ are the unit vectors parallel and perpendicular to the line joining the pair of particles respectively, r_{ij} is the distance between the centers of particle i and j , and θ_{ij} is the angle between the vector joining the centers of particle i and j and the external magnetic field H (Figure 2.4). In contrast to previous simulations on ER fluids, where the voltage is kept constant and the electric field strength increases upon decreasing the gap, here H is assumed to be uniform and constant while compressing the fluid. Multibody and multipolar interactions are neglected.

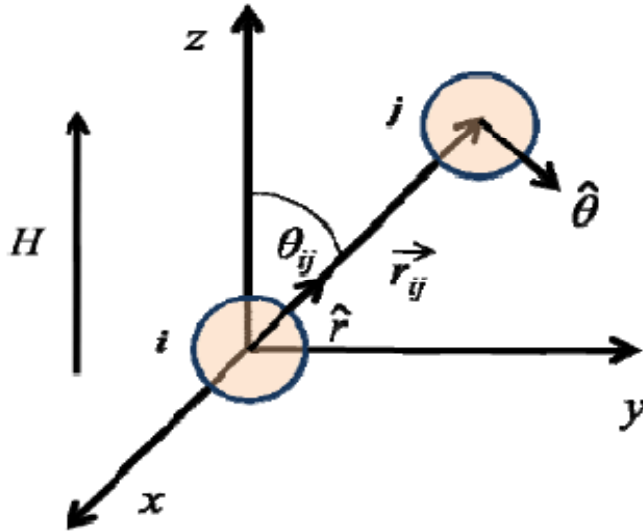


Figure 2.4. Schematic representation of the coordinate reference system used in particle-level simulations.

To prevent the particles from overlapping we introduced a short-range repulsive exponential interaction force:

$$\vec{F}_i^r = -\sum_{j=1, j \neq i}^N F_0 \exp \left[-100 \left(\frac{r_{ij}}{2a} - 1 \right) \right] \hat{r} \quad (2.16)$$

The particles were also subjected to a drag viscous force. In the free draining approximation the hydrodynamic force on particle i is given by:

$$\vec{F}_i^h = -6\pi\eta_c a \left(\frac{d\vec{r}_i}{dt} - \vec{u}_i^\infty \right) \quad (2.17)$$

where \vec{u}_i^∞ stands for the laminar viscous fluid velocity at the center of particle i . For squeeze flow under no-slip boundary conditions in the limit of creeping flow ($Re \rightarrow 0$) the velocity field is given by [Kim *et al.* (1999)]:

$$\vec{u}_i^\infty = \left(\frac{3\rho_i z_i v}{h^2} \right) \left(1 - \frac{z_i}{h} \right) \hat{\rho} - 3v \left(\frac{z_i}{h} \right)^2 \left(1 - \frac{2z_i}{3h} \right) \hat{z} \quad (2.18)$$

where ρ_i and z_i are the coordinates of particle i and $\hat{\rho}$ and \hat{z} are the radial unit vectors in cylindrical coordinates.

The particles were confined between two walls, represented by two rigid and parallel planes positioned at $z = 0$ and $z = h$. Again, to prevent particles from penetrating into the plates we employed a short-ranged repulsive potential:

$$\vec{F}_i^w = F_0 \exp \left[-100 \left(\frac{\xi_i^{l,u}}{2a} - \frac{1}{2} \right) \right] \hat{n}, \quad (2.19)$$

where \hat{n} is the normal vector to the walls and $\xi_i^l = z_i$ and $\xi_i^u = h - z_i$ are the distances between the particle and the lower and upper wall, respectively. Particles at a distance of $1.1a$ from the plates are fixed to them.

The position of the lower plate $z = 0$ was fixed and the system was compressed by moving the upper plate at a constant approaching speed v .

Thus, the position of the upper wall $h(t)$ at the instant $t_{i+1} = t_i + \Delta t$ was calculated as follows:

$$h(t_{i+1}) = h(t_i) - v\Delta t \quad (2.20)$$

From the force expressions reported above arise natural length, force and time scales: $l_s = 2a$, $F_s = F_0$, and $t_s = \frac{12\pi\eta_c a^2}{F_0}$, respectively. Hence, for inertialess particles, neglecting Brownian forces, the equation of motion for particle i can be written as:

$$\frac{d\vec{r}_i^*}{dt^*} = \vec{F}_i^{m*} + \vec{F}_i^{r*} + \vec{F}_i^{w*} + \vec{u}_i^{\infty*} \quad (2.21)$$

where dimensionless variables are denoted with an asterisk.

The equations of motion were integrated numerically using an explicit Euler method with a dimensionless time step $\Delta t^* = 5 \times 10^{-4}$. Using a smaller time step had a negligible effect. On the one hand, interparticle exponential repulsive interactions were evaluated for sphere separations less than a cut-off radius $4a$. On the other hand, wall-particle repulsive interactions were evaluated only for a perpendicular distance from wall to particle center smaller than $3a$. A further increase of the previously mentioned distances had no significant influence on the results. Periodic boundary conditions were not applied.

In the filtration regime of operation (slow compression), the normal force F^* acting on the upper plate was calculated from the normalized total magnetic energy U^* ,

$$U^* = \sum_{i=1}^N \sum_{j=1, j \neq i}^N \frac{1}{3} \left(\frac{1}{r_{ij}^*} \right)^3 (1 - 3\cos^2\theta_{ij}) \quad (2.22)$$

according to:

$$F^* = -\frac{dU^*}{dh^*}, \quad (2.23)$$

It is worth to remark here that other approaches exist in the literature for the stress transfer determination between the system and bounding plates [Lukkarinen and Kaski (1996)].

When compressing any field-responsive colloid it is important to distinguish between the normal force contributions coming from the number of percolating field-induced clusters, N_c , and their internal structure. Basically, it is not only the number of percolating structures that contributes to the normal force but also their thickness and strength. For this purpose we define a new parameter Π_i , for every percolating aggregate i in the system, as follows:

$$\Pi_i = \frac{N_{pi}h_0}{h} \quad (2.24)$$

where N_{pi} is the number of particles contained in the percolating cluster i , h_0 is the initial separation between the plates and h is the plates separation at time t . For every gap an averaged value can be calculated using the following expression:

$$\Pi = \frac{\sum_{i=1}^{N_c} \Pi_i}{N_c} = \frac{\sum_{i=1}^{N_c} \frac{N_{pi}h_0}{h}}{N_c} \quad (2.25)$$

2.6. RESULTS AND DISCUSSION

2.6.1. Squeeze flow of Newtonian fluids

Figure 2.5 shows the normal compressive force F versus gap distance h for Newtonian silicone oils (100mPas and 350mPas) by moving the upper plate at a constant speed in the range $v = 10 - 50\mu\text{m/s}$ while the lower plate remained stationary. Experiments correspond to constant volume tests to make it possible a straightforward comparative study with MR fluids. As expected from the lubrication theory, in all cases

investigated, the relationship between the force and the gap follows a power law behavior. At very large gap separations (early stages of the compression experiment) data are not reliable because of the transient regime where some inertia may artifact the data.

The approaching speed does not seem to have any clear effect in changing the slope; an average slope is obtained that is around -3.2 well in the range $[-5, -2]$ corresponding to the behavior of Newtonian fluids under constant volume approach and in agreement with literature predictions (see Section 2.3.1). It seems that the only effect of changing the approaching speed is shifting the curves in the vertical direction. As anticipated, the larger the viscosity, the larger the normal forces obtained.

Constant volume squeeze flow (no-slip and perfect slip) theories for Newtonian fluids suggest that experiments for different viscosity fluids and approaching speeds can be collapsed in a master curve if plotting the ratio $F/\eta v$ versus h [Stefan (1874), Diennes and Klemm (1946); Campanella and Peleg (1987); Raphaelides and Gioldasi (2004)]. As observed in Figure 2.6, a good collapse is obtained especially at narrow gaps where the lubrication approximation holds. No-slip Stefan equation does qualitatively explain the trend observed. However, the smaller than -5 slope observed may be ascribed to the presence of some partial slip. As is generally found, Stefan's equation with no-slip gives an exponent that is too high and perfect slip gives an exponent that is too low.

The relationship between force and gap distance is essential in all squeeze flow deformations. Nevertheless, it is generally more convenient to use related magnitudes such as the compressive strain, defined here as the ratio of the moving distance of the upper plate to the initial distance between the plates $\varepsilon = d/h_0$, to make a straightforward comparative study with the rheological behavior under different standard flow

conditions such as direct-shear and pressure-driven flows. We will use this description in the next section which is devoted to MR fluids.

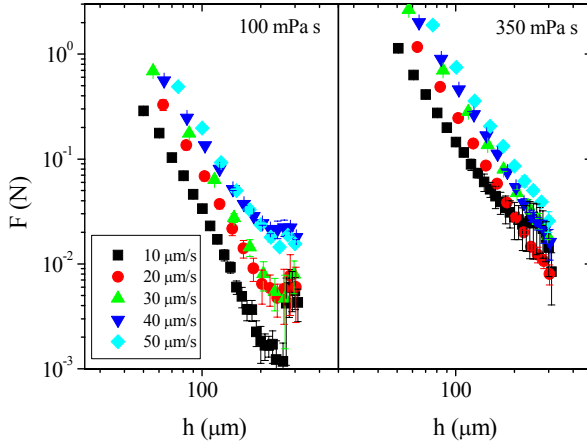


FIGURE 2.5. Normal force F versus gap distance h at various approaching speeds for two Newtonian silicone oils.

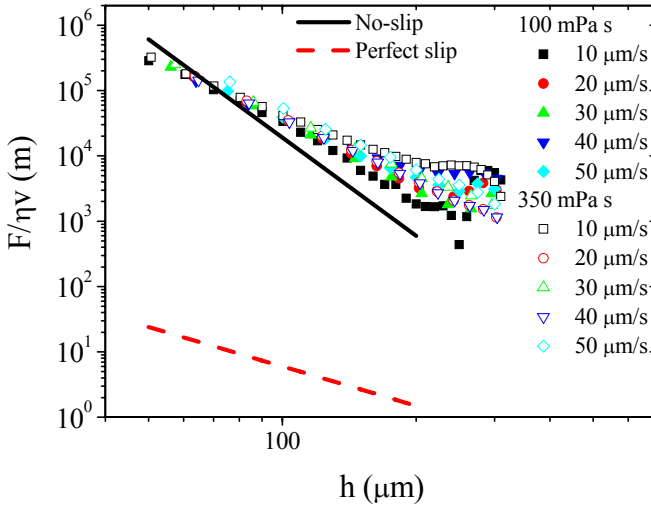


FIGURE 2.6. Compressive force F from Figure 2.5 divided by the viscosity η and approaching speed v as a function of gap distance h . Lines correspond to Stefan's model predictions under no-slip and perfect slip conditions. The experimental error is contained within the symbol size.

2.6.2. Squeeze flow of magnetorheological fluids

A. Unidirectional monotonous compression tests

Experiments were carried out for a wide range of magnetic field strengths up to 354 kA/m . Magnetic fields investigated were high enough to discard the normal force contribution coming from the pure oil which is expected to be of only $\sim 10^{-3} \text{ N}$ (c.f. Figure 2.6). Negligible differences were observed for the two approaching speeds investigated ($1 \mu\text{m/s}$ and $10 \mu\text{m/s}$) in agreement with experimental data reported by Mazlan *et al.* (2008). This is possibly due to the small plasticity number (Equation 2.5) thus allowing the particles to find a minimum energy configuration in a well organized field-induced structure [Lukkarinen and Kaski (1996)]. It is worth to point out that no-slip at the surfaces was checked by using plates previously coated with a thin layer of carbonyl iron powder. Experiments that were carried out using these plates were coincident with those obtained using conventional non-coated titanium plates.

For the sake of brevity, in Figure 2.7 we only illustrate results for an approaching speed of $10 \mu\text{m/s}$. Here we show the influence of the DC magnetic field strength on the normal force – compressive strain curves for a 5 vol% MR fluid. As observed, the force increases as we increase the magnetic field applied. This is anticipated to be a consequence of the MR effect. It is well known that under slow compressive strains ($\varepsilon \lesssim 0.05$) MR fluids withstand the load without “breaking” (data not shown in Figure 2.7 because of the limited strain resolution). Upon increasing the strain the squeeze flow behavior is expected to largely depend on the repeated formation / breakdown process of microscopic and macroscopic structures [Lukkarinen and Kaski (1998)]. Hence, structure breakdown occurs for $\varepsilon \sim 0.05$ and the subsequent steadily increasing force suggests that the metastable field-induced structure partially recovers from

compression. It has been documented in the literature that for very rapidly compressed systems, the force decreases just after breakdown of the structure suggesting that in this case the particles do not have time to recover. A rough estimation of the so-called plastic modulus increase under compression can be obtained by the ratio of the compressive stress and the associated true strain $\varepsilon_t = \ln(h/h_0)$ [Monkman (1995)]. Taking $H = 354$ kA/m and $v = 10$ $\mu\text{m/s}$ we estimated a change of approximately one order of magnitude from 2 kPa to 62 kPa. Curves presented in Figure 2.7 are very similar to stress – strain curves for ER fluids under constant area tests by Vieira *et al.* (2001). Moreover, our experimental results are in qualitative agreement with slow rate dynamic simulations by Lukkarinen and Kaski (1996) in the range $\varepsilon = 0 - 0.25$ (see Figure 2.2 in their letter).

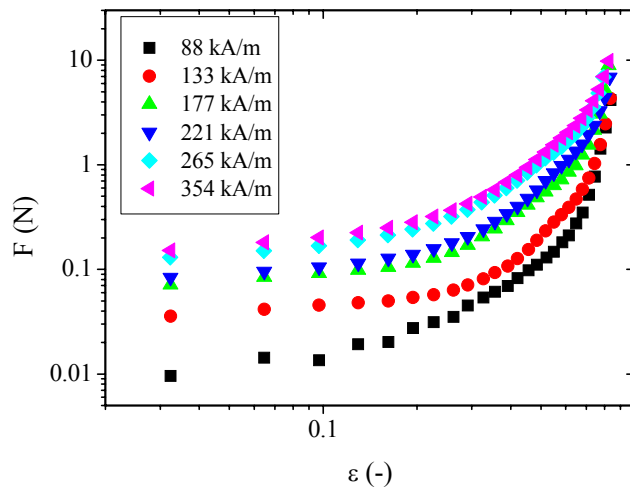


Figure 2.7. Typical normal force, F , versus compressive strain, ε , curves of MR fluids at different magnetic field strengths, H (5 vol% MR fluid, $v = 10\mu\text{m/s}$).

B. Low-strain normal force plateau

According to Bingham and bi-viscous macroscopic models (c.f. Equation 2.9), the normal force is expected to vary as $F = A/(1 - \varepsilon)^{5/2}$. Here, A represents the low-strain normal force and is associated to the yield compressive stress. Experimental data shown in Figure 2.7 were fitted to this equation and fitting parameters A_{Exp} are reported in Table 2.1. To make it possible a straightforward comparative study with macroscopic theoretical predictions, steady shear flow experiments were also carried out for a gap distance of $h_0 = 300 \mu\text{m}$ with 5 vol% MR fluids (results not shown here for brevity). Static yield shear stresses τ_{ys} were determined from extrapolation in shear stress *versus* shear-rate ramp-up curves following the standard procedure [de Vicente *et al.* (2010)]. With this, a theoretical prediction for the constant A is obtained under a macroscopic description along with $A_{Macro} = (2\pi\tau_{ys}r_0^3)/(3h_0)$ (c.f. Equation 2.9). Results are also included in the third column of Table 2.1. Macroscopic theories slightly overestimate experimental results. However, the agreement is quite good bearing in mind that there are not free parameters. The discrepancy with experimental data may be explained because of the strong cubic dependence with the sample radius and the pipette error when depositing the drop on the rheometer plate.

H (kA/m)	A_{Exp} (N)	A_{Macro} (N)	δ/a ($\times 10^{-4}$) (-)
88	0.0156 ± 0.0018	0.025	1.208
133	0.0406 ± 0.0012	0.059	1.611
177	0.084 ± 0.003	0.103	1.945
221	0.099 ± 0.005	0.153	2.175
265	0.163 ± 0.010	0.227	2.424
354	0.192 ± 0.012	0.311	2.700

Table 2.1. Fitting parameter A_{Exp} for normal force – compressive strain curves reported in Figure 2.7 according to $F = A/(1 - \varepsilon)^{5/2}$. A_{Macro} corresponds to macroscopic model predictions, Equation 2.9, using the static yield shear stress as an input. In these calculations we assumed $r_0 = 3.8$ mm as visually determined. δ/a corresponds to the indentation depth calculated by fitting Equation 2.14 to the experimental A_{Exp} values. In these calculations we have taken $\nu = 0.29$ and $E = 211 \times 10^9$ Pa which correspond to typical values for pure iron.

H (kA/m)	μ_{sr} (-)	β (-)
88	1.125	0.802
133	1.117	0.751
177	1.110	0.706
221	1.103	0.665
265	1.098	0.630
354	1.088	0.568

Table 2.2. Suspension relative magnetic permeability μ_{sr} and magnetic contrast factor β calculated using Maxwell-Garnett and Fröhlich-Kennelly equations [Jiles (1991)].

The microscopic model described in Section 2.3.3 qualitatively captures the low-strain normal force plateau as well. A quantitative theoretical estimation can also be obtained as follows. Since the particle volume fraction investigated here was significantly low, as a first approximation

the internal magnetic field could be assumed to be simply the applied external magnetic field. As a consequence, the relative suspension permeability μ_{sr} and the contrast factor β can be calculated straightforward from Maxwell-Garnett and Fröhlich-Kennelly equations [Jiles (1991)] for the magnetization – magnetic field strength dependence for the particles where the relative initial permeability of the solid phase is 40 and their saturation magnetization 1550kA/m [de Vicente *et al.* (2010)]. Results for μ_{sr} and β for a range of magnetic fields investigated are shown in Table 2.2. With these, the microscopic model prediction can be fitted to the experimental A_{Exp} parameter resulting in a field dependent indentation depth δ/a . The indentation depth is tabulated in the fourth column in Table 2.1 and increases when increasing the magnetic field. Some work is currently done in this direction to check whether these indentation values can be experimentally ascertained.

One of the most relevant rheological properties of a MR fluid is the yield stress that must be overcome to initiate gross material deformation or flow. The yield stress is associated to the minimum stress value required for the onset of flow and is known to be strongly dependent on the mode of operation. Under compression, the so-called yield compressive stress can be determined from the low-strain normal force plateau. The low-strain normal force plateau A is expected to mimic the strength of the initial field-induced structure. In fact, it increases with the magnetic field strength following a power law function with exponent 1.89 ± 0.25 , in good agreement with an exponent of 2 predicted by dipolar magnetostatic models [Bossis *et al.* (2002)]. The yield compressive stress can be estimated by the ratio between the low-strain normal force plateau and the wetted plate surface area. A comparative study on the yielding properties under shear and compression is shown in Figure 2.8. Here we show both the dynamic and static yield shear stresses as well as the yield

compressive stress for MR fluids having 5 vol % concentration. It is observed that the yield compressive stress is significantly larger than the yield shear stresses in good agreement with other experiments reported in the literature (see Section 2.2).

To sum up, Bingham, bi-viscous and micromechanical models do satisfactorily explain the existence of a yielding low-strain normal force plateau under constant volume compression. In the case of macroscopic models, a reasonably good agreement exists when comparing theoretical and experimental results. The next question to answer is whether these models suffice to explain the flow behavior at larger compressive strains.

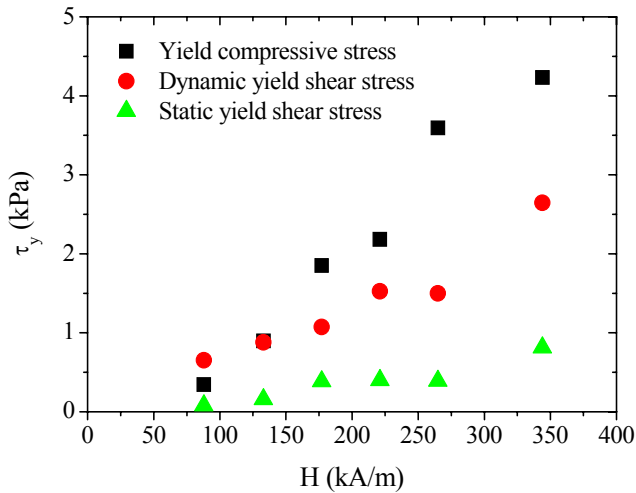


Figure 2.8. Comparison between yield compressive stresses and yield shear stresses for 5 vol% MR fluids. For the calculation of the compressive stress we have assumed an initial radius of $r_0 = 3.8 \text{ mm}$. For completeness we also show results for dynamic yield shear stresses obtained by extrapolation in lin-lin representations of shear stress versus shear rate at large deformations [Bossis *et al.* (2002)].

C. Compressive flow behavior

Interestingly, experimental results presented in Figure 2.7 can be reasonably collapsed when dividing by the low-strain normal force as shown in Figure 2.9. Included in Figure 2.9 we show theoretical predictions from macroscopic (Equation 2.9) and microscopic (Equation 2.14) models. As observed, the microscopic theoretical curve (dashed line) stays below the experimental data. As expected, this model does not conveniently capture the force-strain dependence at intermediate and large strain values as it simply assumes that only single chains of particles exist under flow behavior. On the contrary, a much better agreement is observed for the macroscopic prediction (solid line). In this case, the slightly faster than theoretically expected increase of the normal force can be qualitatively explained under the framework of Equation 2.9 in terms of a yield shear stress that exponentially increases with the compressive strain (dotted line). We will come back to this point in Section 2.4.2 D.

Similarly to Tian *et al.* (2002a), the intermediate strain region ($0.2 < \varepsilon < 0.5$) is also satisfactorily captured by an exponential function $F = \alpha_1 e^{\alpha_2 \varepsilon}$ (fitting parameters contained in Table 2.3). On the one hand, α_1 values were found to increase with the magnetic field strength. On the other hand, α_2 values were approximately constant and very close to experiments reported by Tian *et al.* (2002a) for ER fluids under constant area and variable electric field strength (constant voltage). The physical meaning of this exponential relationship is not clear yet by simply observing normal force changes during compression.

As reported above, when using low viscosity continuous medium with low squeezing speed the viscous contribution to the normal force is expected to be minimal. As the plates compress the structures, the columns become shorter and thicker as some particles break away and

reform the structure [McIntyre (2008)]. These re-formed structures are actually stronger than the original and hence it is expected a squeeze-driven strengthening effect [Tang *et al.* (2000)] eventually resulting in a yield shear stress that increases with the compressive strain. In order to get a better understanding of the structural evolution under compression we now perform combined flow tests.

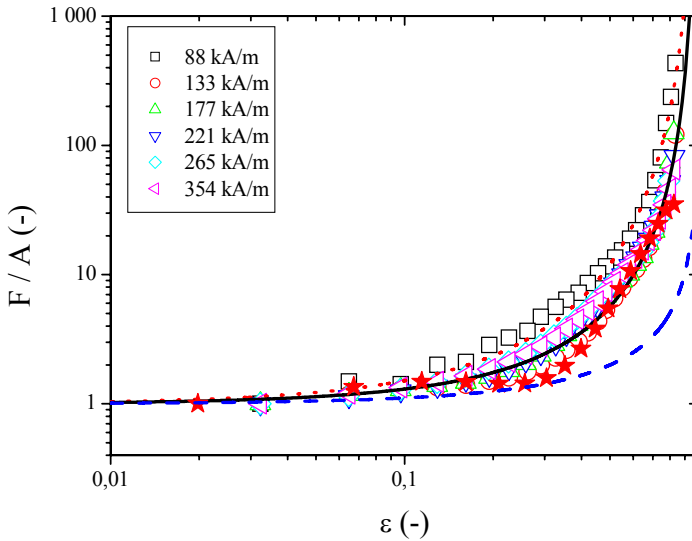


Figure 2.9. Dimensionless normal force, F , as a function of compressive strain, ε , for different magnetic fields. Blue dashed line corresponds to Equation 2.14; $F/A = 1/(1 - \varepsilon)$. Black solid line corresponds to Equation 2.9; $F/A = 1/(1 - \varepsilon)^{5/2}$. Red dotted line corresponds to the expression $F/A = e^{1.5\varepsilon}/(1 - \varepsilon)^{5/2}$. Red stars represent particle-level simulation results.

D. Squeeze combined with torsional small-amplitude oscillatory flow

To further investigate the structural changes during squeeze, we carried out compression tests by superposition of a small-amplitude oscillatory

shearing (SAOS) flow where the upper plate was made to undergo rotary oscillations about a mean position ($5 \times 10^{-6} \text{rad}$) at a given frequency ($f = 10 \text{Hz}$) in the viscoelastic linear region. This kind of test would allow us to monitor viscoelasticity changes at the same time the sample is being compressed. It is worth to remark here that few works exist in the literature concerning combined flows in spite of their

H (kA/m)	α_1 (N)	α_2 (-)
88	0.0107 ± 0.0004	4.81 ± 0.09
133	0.0174 ± 0.0020	4.90 ± 0.26
177	0.0425 ± 0.0019	4.98 ± 0.10
221	0.0463 ± 0.0028	5.21 ± 0.13
265	0.0904 ± 0.0021	4.93 ± 0.05
354	0.1030 ± 0.0034	4.91 ± 0.07

Table 2.3. Fitting parameters α_1 and α_2 for normal force – compressive strain curves reported in Figure 2.7 in accordance with $F = \alpha_1 e^{\alpha_2 \varepsilon}$. The approaching speed is $v = 10 \mu\text{m/s}$. The strain fitting range is $\varepsilon \sim 0.1 - 0.5$.

importance to get structural information. Relevant papers on this subject are those by Kulkarni *et al.* (2003) and See (2006).

Preliminary tests were carried out to ensure that SAOS was not affecting the resulting normal force measured under compression. We obtained a very good reproducibility using different samples. The typical viscoelastic response is shown in Figure 2.10a for an approaching speed of $v = 10 \mu\text{m/s}$. We observe that G' initially increases with increasing the strain in agreement with experiments carried out by See *et al.* (2006). Then, the viscoelastic moduli reach a peak at a gap thickness corresponding to $\varepsilon \sim 0.5$. These results suggest that when the MR fluid is squeezed, not

only the compressive stress (as demonstrated above) but also the shear resistance increases with the gap reduction in an initial stage. However, for strains larger than $\varepsilon \sim 0.5$, the loss factor $\tan\delta = \frac{G''}{G'}$ becomes 1 and then viscous shear flow occurs for larger strains. In Figure 2.10b we show that the shear viscoelastic moduli scale with $\mu_0\mu_{sr}\beta^2H^2$ suggesting that dipolar magnetostatic interactions drive the microstructural evolution under compression. As anticipated in section above, the squeeze-strengthening effect is found to roughly increase following an exponential law as demonstrated by the dashed line in Figure 2.10b. This further supports the idea of a filtration-dominated regime and also the fact that the internal magnetic field is not significantly changing upon compression.

In summary, experiments presented above provide a complicated picture of the squeeze flow behavior of MR fluids under constant volume in the presence of DC magnetic fields. At very low strains structures are able to resist without breaking (results not shown here because of a technical limitation of our magnetorheometer). Upon increasing the compressive strain structures do eventually break. The behavior at larger strains is dictated by the balance between reformation and fragmentation processes. In the case of slow compression rates particles do have time to find a minimum energy configuration and structures reform under compression. This is manifested in an increase of the normal force and an enhancement of the shear storage and loss moduli. Interestingly, for very large strains normal forces do continue increasing. However, viscoelastic moduli stop growing entering in a region that is shear viscosity dominated.

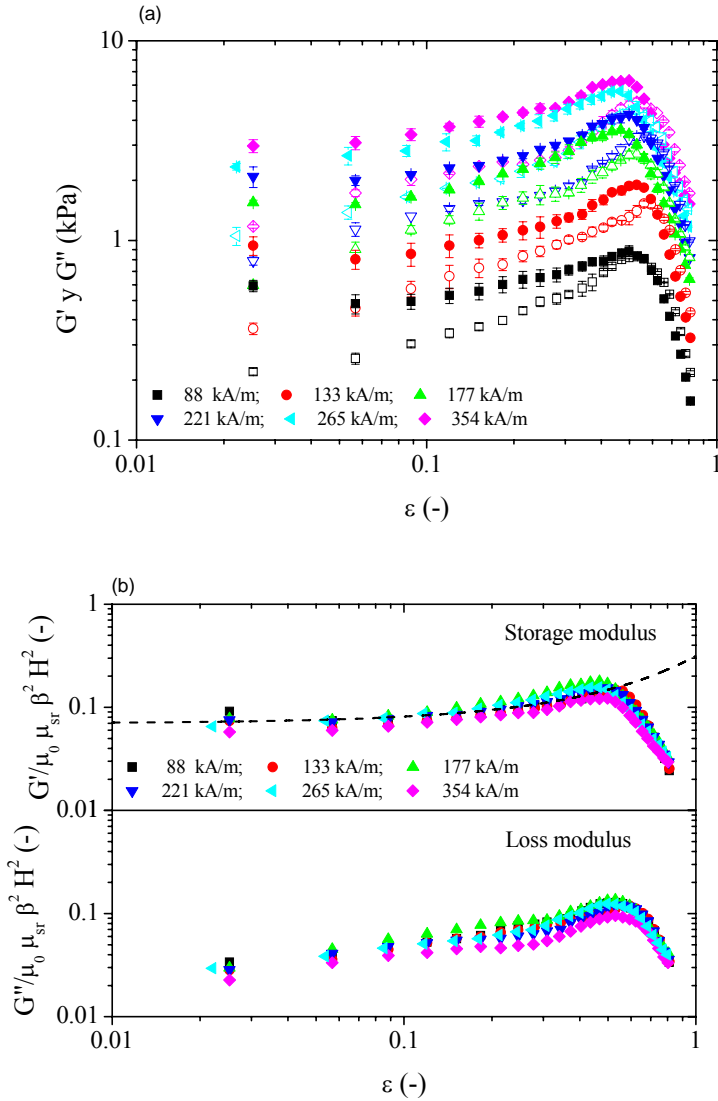


Figure 2.10. Strain dependence of the shear viscoelastic moduli for different magnetic field strengths. a) Storage and loss moduli as a function of compressive strain. Closed symbol, G' ; open symbol, G'' . b) Normalized storage and loss moduli as a function of strain. Dashed line corresponds to $G'/(\mu_0\mu_{sr}\beta^2H^2) = 0.07e^{1.5\varepsilon}$.

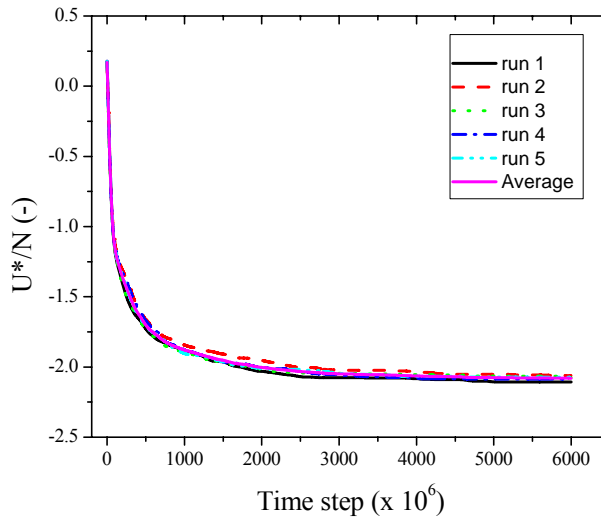


Figure 2.11. Evolution of the magnetic energy normalized with the number of particles in the absence of flow for five different replicates. $h_0 = 40a$.

Both macroscopic and microscopic models employed above suffer from important drawbacks at medium and large strains mostly due to the fact that the field-induced microstructure evolves under compression. A more direct approach involves the use of particle-level computer simulation techniques.

2.6.3. Simulations

Initially, 600 particles are placed in a cylindrical volume (radius $48a$, height $40a$) at random positions. This corresponds to a volume fraction of ~ 1 vol%. Then, at $t^* = 0$ the magnetic field is applied instantaneously. Soon after the application of the magnetic field short chains are formed that rapidly result in longer chains created by tip-to-tip aggregation. Five runs were performed with different initial configurations to obtain averages. In Figure 2.11 we show the development of the magnetic energy

U^* –normalized with the number of particles N – with time for five randomly generated structures. Very similar results are obtained independently of the initial configuration. Also, average energy values are shown for replicate simulations. As expected, the magnetic energy decreases towards a minimum energy value which is around $U^*/N = -2$.

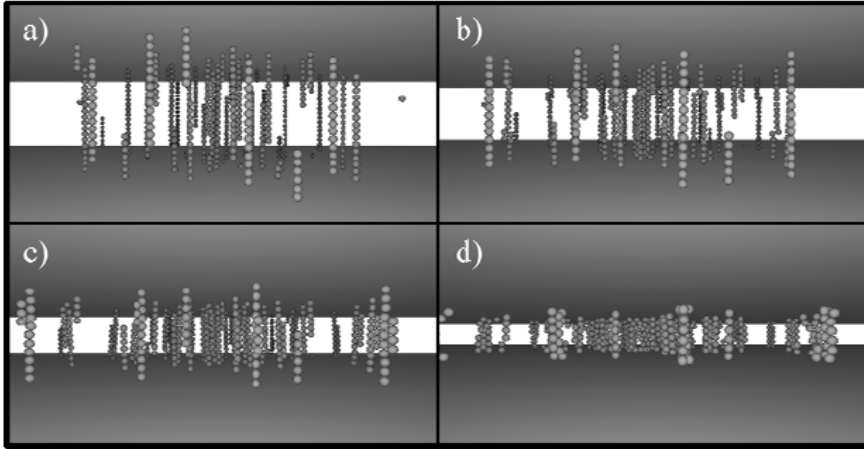


Figure 2.12. Side view snapshots of 3D simulations squeezed at (a) $h = 40a$ (a), (b) $h = 32a$, (c) $h = 22a$ and (d) $h = 12a$. $\sim 1 \text{ vol}\%$. $v^* = 10^{-2}$.

Grown structures, previously annealed in the presence of a magnetic field, were later squeezed at a very slow constant speed of $v^* = 10^{-2}$, resulting in a nonstationary flow where magnetic forces dominate over the hydrodynamic forces. To do so the gap was taken from an initial height of $40a$ to a final height of $10a$ according to Equation 2.20. In Figure 2.12 we show snapshots of the systems under slow compression at a constant approaching speed. As expected, the particles are able to find a minimum energy configuration in a more or less static condition.

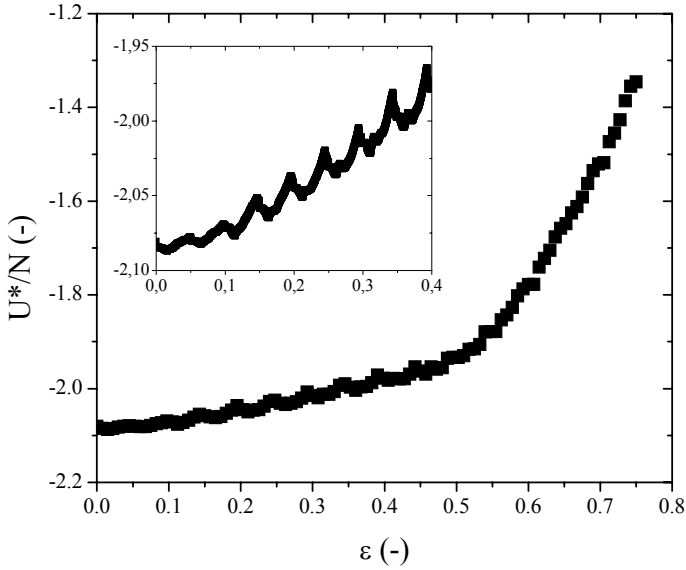


Figure 2.13. Average magnetic energy normalized with the number of particles as function of the compressive strain. The periodic fluctuation of the normal force shown in the inset is associated to macroscopic rearrangements.

The straight chain-like structure is mostly conserved and the excess stress is relieved through minor dislocations. Similar results were found in simulations by Lukkarinen and Kaski (1998).

In Figure 2.13 the average magnetic energy is shown as function of the compressive strain. At small strains, the energy increases slowly with the strain. However, violent fluctuations occur partially caused by macroscopic rearrangements of the chain-like structures in agreement with Chu *et al.* (2000) (see inset in Figure 2.13). At a certain strain value, the curve deviates from this behavior, with the energy increasing much more rapidly. By derivation of the magnetic energy, Equation 2.23, we calculated the normal force exerted by the field-induced structures. These results are shown in Figure 2.9 for their comparison with experimental

and analytical models predictions. Interestingly, particle level simulations qualitatively capture the normal force increase under compression. The extent of the quantitative agreement is somewhat surprising given the approximations in the simulation model.

To get a better understanding of the normal force evolution with the compressive strain, the kinetics of structure formation was first probed by following the number of percolating clusters, N_c , as a function of strain since the appearance of percolating clusters should be related to appearance of normal forces. Cluster statistics were evaluated using the connectivity matrix method where sphere pairs with separations $r < 2.2a$ are considered directly connected. The number of percolating clusters, averaged over five simulation runs, are plotted as a function of compressive strain in Figure 2.14. As observed, the number of percolating clusters is a linear function of the strain and consequently it does not solely explain the significant increase in normal force for strains larger than $\varepsilon \sim 0.5$.

The number of percolating clusters is not the only contribution to the normal force since the compression-driven structural evolution of these percolating clusters does also contribute to the normal force. A simple estimation of the aspect ratio, thickness and strength of the aggregates may be obtained through the Π parameter. The existing correlation between this parameter and the resulting normal force is manifested by the linear relationship shown in Figure 2.15. This suggests that the normal force increase under compression is governed by the average strength and thickness of the percolating aggregates. This was somehow expected because we calculated the normal force acting on the surfaces by taking the derivative of the magnetic energy.

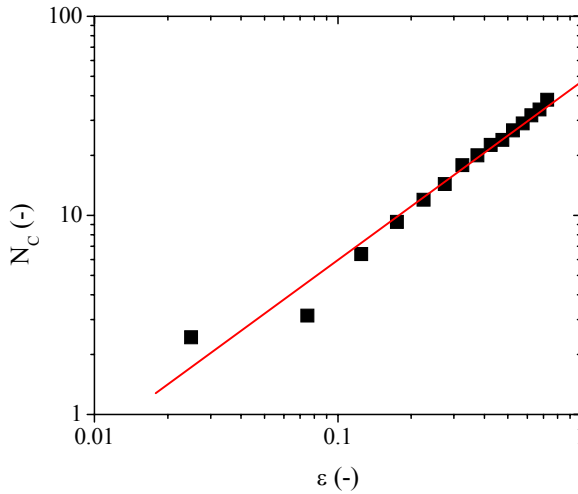


Figure 2.14. Evolution of the number of percolating clusters, N_c , as a function of the compressive strain. The number of percolating clusters is strongly dependent on the connectivity criterion employed and roughly increases linearly with the strain. The red solid line is a linear fit with slope 0.89 ± 0.04 and correlation coefficient $r = 0.99$.

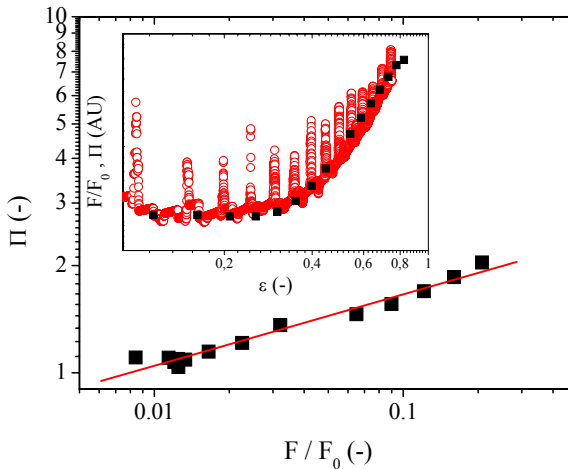


Figure 2.15. Π parameter as a function of the normalized normal force. The red solid line is a linear fit with slope 0.20 ± 0.01 and correlation coefficient $r = 0.99$. Inset corresponds to the correlation between F/F_0 (black squares) and Π (red open circles) versus the compressive strain dependence.

2.7. CONCLUSIONS

It is well known that compression resistance of field-responsive fluids increases when the gap separation is reduced and compressive strain increases. Much of the work reported to date on the squeeze flow behavior of field-responsive fluids has focused on ER fluids under constant area and constant voltage operation. As a consequence, as the gap closes both the electric field intensity and particle concentration increase causing an extra-hardening in the ER fluid. A significantly more simplified scenario results when compressing MR fluids under constant volume conditions. In this case, any compression-assisted hardening must be significantly dependent on the structural reorganization.

In this work the structural reorganization of MR fluids was proved using very small compressive speeds in the so-called filtration regime under the creeping flow approximation. Hence, the compressive stress can be looked as all contributed by the field-induced yield shear stress of the fluid and the contribution of the viscous force to the compressive stress can be neglected. Even though it is well known that continuum Bingham and bi-viscous equations for ER fluids in oscillatory squeeze flow underestimate experimental results for the compressive stress under constant area operation, to date, this model had not been checked yet in the case of MR fluids. In this work we verified that Bingham and bi-viscous equations are able to reasonably predict compressive stresses in the case of MR fluids under constant volume operation. Furthermore, a standard micromechanical model consisting in a cubic network of single chains is able to predict the low-strain plateau as well by considering Hertzian contacts between the particles. However, the micromechanical model underestimates the normal force increase at large strains mainly due to the fact that only single chains are permitted in this model. This

point was later demonstrated through the use of particle-level simulations. A close inspection of the experimental data reveals that macroscopic models slightly underestimate the compressive resistance when the gap separation decreases. This larger than expected increase of the normal force under compression can be explained in terms of a shear strengthening effect as proved here using combined squeeze and small-amplitude shear tests.

Experiments reported here concern low-concentration, no-slip and very-slow-rate loading conditions where the strain rate although small is not constant during compression (maximum strain rate $\dot{\epsilon} \sim 0.2 \text{ s}^{-1}$). Simulation studies demonstrate that normal forces are strongly strain rate dependent. Actually, fast loading rates introduce an additional time scale which together with the structure evolution time scale, makes the system very complicated. Commercial application of this technology requires the utilization of highly concentrated suspensions ($\sim 30 \text{ vol}\%$), large loading rates and partial slip conditions. So, in our opinion, future work should be devoted to better understand the effect of volume fraction, elongational rate and slip at the surfaces in the squeeze flow behavior of MR fluids.

ACKNOWLEDGMENTS

This work was supported by MAT 2010-15101 project (Spain), by the European Regional Development Fund (ERDF) and by Junta de Andalucía P07-FQM-02496, P07-FQM-03099 and P07-FQM-02517 projects (Spain). J. A. Ruiz-López acknowledges support by the “Universidad de Granada. Becas de iniciación a la investigación” and “Ministerio de Educación. Becas de colaboración.”

References

- Andablo-Reyes, E, R. Hidalgo-Álvarez, and J. de Vicente “Controlling friction using magnetic nanofluids,” *Soft Matter*, submitted for publication (2010a).
- Andablo-Reyes, E, R. Hidalgo-Álvarez, and J. de Vicente “A method for the estimation of the film thickness and plate tilt angle in thin film misaligned plate-plate rheometry,” *J. Non-Newtonian Fluid Mech.* **165**, 1419-1421 (2010b).
- Bell, R. C., J. O. Karli, A. N. Vavreck, D. T. Zimmerman, G. T. Ngatu, and N. M. Wereley, “Magnetorheology of submicron diameter microwires dispersed in silicon oil,” *Smart Mater. Struct.* **17**, 015028-1-6 (2008)
- Bird, R. B. “Dynamics of polymeric liquids,” New York, 1987, 22.
- Bossis, G., O. Volkova, S. Lacis, and A. Meunier, “Magnetorheology: fluids, structures and rheology,” in: S. Odenbach (Ed) *Ferrofluids. Magnetically controllable fluids and their applications (Lecture notes in Physics, 594, Springer-Verlag 2002)* pp 202-230.
- Campanella, O. H., and M. Peleg, “Lubricated squeezing flow of a Newtonian liquid between elastic and rigid plates,” *Rheol. Acta* **26(4)**, 396-400 (1987).
- Chu, S. -H., S. J. Lee, and K. H. Ahn, “An experimental study on the squeezing flow of electrorheological suspensions,” *J. Rheol.* **44(1)**, 105-120 (2000).
- Collomb, J., F. Chaari, and M. Chaouche, “Squeeze flow of concentrated suspensions of spheres in Newtonian and shear-thinning fluids,” *J. Rheol.* **48(2)**, 405-416 (2004).
- Connelly, R. W., J. Greener, “High-shear viscometry with a rotational parallel-disk device,” *J. Rheol.* **29**, 209-226 (1985).

- Conrad, H. "Properties and design of electrorheological suspensions," *MRS Bull* **23**, 35-42 (1998).
- Covey, G. H., and B. R. Stanmore, "Use of the parallel-plate plastometer for the characterization of viscous fluids with a yield stress," *J. Non-Newtonian Fluid Mech.* **8**, 249-260 (1981).
- de Gans, B. J., C. Blom, A. P. Philipse, and J. Mellema, "Linear viscoelasticity of an inverse ferrofluid," *J. Phys. Rev. E* **60**, 4518-4527 (1999).
- de Vicente, J., and J. Ramírez, "Effect of friction between particles in the dynamic response of model magnetic structures," *J. Colloid Interf. Sci.* **316**, 867-876 (2007).
- de Vicente, J., F. Vereda, J. P. Segovia-Gutiérrez, M. P. Morales, and R. Hidalgo-Álvarez, "Effect of particle shape in magnetorheology," *J. Rheol.* in press (2010).
- de Vicente, J., J. P. Segovia-Gutiérrez, E. Andablo-Reyes, F. Vereda, and R. Hidalgo-Álvarez, "Dynamic rheology of sphere- and rod-based magnetorheological fluids," *J. Chem. Phys.* **131**, 194902-1-10 (2009).
- de Vicente, J., M. T. López-López, F. González-Caballero, J. D. G. Durán, "A rheological study of the stabilization of magnetizable colloidal suspensions by addition of silica nanoparticles," *J. Rheol.* **47(5)**, 1093-1109 (2003).
- de Vicente, J., M. T. López-López, J. D. G. Durán, and G. Bossis, "A slender-body micromechanical model for viscoelasticity of magnetic colloids: Comparison with preliminary experimental data," *J. Colloid Interf. Sci.* **282**, 193-201 (2005).
- de Vicente, J., M. T. López-López, J. D. G. Durán, and F. González-Caballero, "Shear flow behavior of confined magnetorheological fluids at low magnetic field strengths," *Rheol. Acta* **44**, 94-103 (2004).

-
- Diennes, G. J., and H. F. Klemm, "Theory and application of the parallel plate plastometer," *J. Appl. Phys.* **17**, 458-471 (1946).
- Ekwebelam, C. C., and H. See, "Using oscillatory shear to probe the effects of bidispersity in inverse ferrofluids," *Korea-Aust. Rheol. J.* **19**, 35-42 (2007).
- El Wahed, A. K., J. L. Sproston, and E. W. Williams, "The effect of a time-dependent electric field on the dynamic performance of an electrorheological fluid in squeeze," *J. Phys. D: Appl. Phys.* **33**, 2995-3003 (2000).
- El Wahed, A. K., J. L. Sproston, and R. Stanway, "The performance of an electrorheological fluid in dynamic squeeze flow: the influence of solid phase size," *J. Colloid Interf. Sci.* **211**, 264-280 (1999).
- El Wahed, A. K., J. L. Sproston, and R. Stanway, "The performance of an electrorheological fluid in dynamic squeeze flow under constant voltage and constant field," *J. Phys. D: Appl. Phys.* **31**, 2964-2974 (1998).
- El Wahed, A. K., J. L. Sproston, R. Stanway, and E. W. Williams, "An improved model of ER fluids in squeeze-flow through model updating of the estimated yield stress," *Journal of Sound and Vibration* **268**, 581-599 (2003).
- Engmann, J., C. Servais, and A. S. Burbidge, "Squeeze flow theory and applications to rheometry: A review," *J. Non-Newtonian Fluid Mech.* **132**, 1-27 (2005).
- Gartling, D. K., and N. Phan-Thien, "A numerical simulation of a plastic fluid in a parallel-plate plastometer," *J. Non-Newtonian Fluid Mech.* **14**, 347-360 (1984).
- Ginder, J. M., "Behavior of magnetorheological fluids," *MRS Bulletin*, August, 26-29 (1998).

- Gong, H., and M. K. Lim, "Experimental investigation on tension and compression properties of an electro-rheological material," *J. Intel. Mat. Syst. Str.* **7**, 89-96 (1996).
- Havelka, K. O., and J. W. Piolet, "Electrorheological technology : The future is now," *CHEMTECH* **36**, 36-45 (1996).
- Heine, M. C., J. de Vicente, and D. J. Klingenberg, "Thermal transport in sheared electro- and magnetorheological fluids," *Physics of Fluids* **18**, 023301 (2006).
- Jiles, D. *Introduction to magnetism and magnetic materials* (Chapman and Hall, London, 1991).
- Jolly, M. R., and J. D. Carlson, *Actuator 96*, 5th Int. Conf. on New Actuators, eds. H. Borgmann and K. Lenz, Axon Technologies Consult GmbH (1996).
- Kim, D. H., S. -H. Chu, K. H. Ahn, and S. J. Lee, "Dynamic simulation of squeezing flow of ER fluids using parallel processing," *Korea-Aust. Rheol. J.* **11(3)**, 233-240 (1999).
- Klingenberg, D. J., F. van Swol, and C. F. Zukoski, "The small shear rate response of electrorheological suspensions. I. Simulation in the point-dipole limit," *J. Chem. Phys.* **94**, 6160-6169 (1991).
- Klingenberg, D. J., F. van Swol, and C. F., Zukoski, "Dynamic simulation of electrorheological suspensions," *J. Chem. Phys.* **91**, 7888-7895 (1989).
- Kulkarni, P., C. Ciocanel, S. L. Vieira, and N. Naganathan, "Study of the behavior of MR fluids in squeeze, torsional and valve modes," *J. Intel. Mat. Syst. Str.* **14**, 99-104 (2003).
- Laun, H. M., M. Rady, and O. Hassager, "Analytical solutions for squeeze flow with partial wall slip," *J. Non-Newtonian Fluid Mech.* **81**, 1-15 (1999).

-
- Lee, C. Y., and C. Y. Wen, "The oscillatory squeeze flow of electrorheological fluid considering the inertia effect," *Smart Mater. Struct.* **11**, 553-560 (2002).
- Lipscomb, G. G., and M. M. Denn, "Flow of Bingham fluids in complex geometries," *J. Non-Newtonian Fluid Mech.* **14**, 337-346 (1984).
- Lukkarinen, A., and K. Kaski, "Computational studies of compressed and sheared electrorheological fluid," *J. Phys. D: Appl. Phys.* **29**, 2729-2732 (1996).
- Lukkarinen, A., and K. Kaski, "Simulation studies of electrorheological fluids under shear, compression, and elongation loading," *J. Appl. Phys.* **83(3)**, 1717-1725 (1998).
- Lynch, R., Y. Meng, and F. E. Filisko, "Compression of dispersions to high stress under electric fields: effects of concentration and dispersing oil," *J. Colloid Interf. Sci.* **297**, 322-328 (2006).
- Mazlan, S. A., K. H. Ekreem, and A. G. Olabi, "An investigation of the behaviour of magnetorheological fluids in compression mode," *Journal of Materials Processing Technology* **201**, 780-785 (2008).
- McIntyre, E. C., "Compression of smart materials: squeeze flow on electrorheological and magnetorheological fluids," The University of Michigan PhD Thesis (2008).
- McIntyre, E. C., and F. E. Filisko, "Filtration in electrorheological suspensions related to the Peclet number," *J. Rheol.* **54(3)**, 591-603 (2010).
- McIntyre, E. C., and F. E. Filisko, "Squeeze flow of electrorheological fluids under constant volume," *J. Intel. Mat. Syst. Str.* **18**, 1217-1220 (2007).
- Meng, Y., and F. E. Filisko, "Unidirectional compression of electrorheological fluids in electric fields," *J. Appl. Phys.* **98**, 074901 (2005).

- Monkman, G. J., "Design and application of magneto-rheological fluid," *J. Phys. D: Appl. Phys.* **28**, 588-593 (1995).
- Olabi, A. G., and A. Grunwald, "Design and application of magneto-rheological fluid," *Materials and Design* **28**, 2658-2664 (2007).
- Park, B. J., I. B. Jang, H. J. Choi, A. Pich, S. Bhattacharya, and H. -J. Adler, "Magnetorheological characteristics of nanoparticle-added carbonyl iron system," *J. Magn. Magn. Mater* **303**, 290-293 (2006).
- Ramos, J., D. J. Klingenberg, R. Hidalgo-Álvarez and J. de Vicente, "Steady shear magnetorheology of inverse ferrofluids", *J. Rheol.* **55(1)**, 127-152 (2011).
- Ramos, J., J. de Vicente, and R. Hidalgo-Álvarez, "Small-amplitude oscillatory shear magnetorheology of inverse ferrofluids," *Langmuir* **26(12)**, 9334-9341 (2010a).
- Rankin, P. J., J. M. Ginder, and D. J. Klingenberg, "Electro- and magnetorheology," *Curr. Opin. Colloid In.*, **3**, 373-381 (1998).
- Raphaelides, S. N., and A. Gioldasi, "Elongational flow studies of set yogurt," *J. Food Engineering* **70(4)**, 538-545 (2004).
- Saldivar-Guerrero, R., R. Richter, I. Rehberg, N. Aksel, L. Heymann, and O. S. Rodríguez-Fernández, "Viscoelasticity of mono- and polydisperse inverse ferrofluids," *J. Chem. Phys.* **125**, 084907-1-7 (2006).
- Scott, J. R. *Trans. Inst. Rubber Ind.* **4**, 347 (1929).
- See, H., "Field dependence of the response of a magnetorheological suspension under steady shear flow and squeezing flow," *Rheol. Acta* **42**, 86-92 (2003).
- See, H., J. S. Field, and B. Pfister, "The response of electrorheological fluid under oscillatory squeeze flow," *J. Non-Newtonian Fluid Mech.* **84**, 149-158 (1999).

-
- See, H., S. Mackenzie, and B. T. Chua, "Effect of compression on the response of a magneto-rheological suspension," *Korea-Australia Rheology Journal* **18(3)**, 121-126 (2006).
- Sproston, J. L., S. G. Rigby, E. W. Williams, and R. Stanway, "A numerical simulation of electrorheological fluids in oscillatory compressive squeeze-flow," *J. Phys. D: Appl. Phys.* **27**, 338-343 (1994b).
- Sproston, J. L., R. Stanway, E. W. Williams, and S. G. Rigby, "The electrorheological automotive engine mount," *J. Electrostatics* **32**, 253-259 (1994a).
- Stanway, R., J. L. Sproston, and N. G. Stevens, "Non-linear modelling of an electro-rheological vibration damper," *J. Electrostatics* **20**, 167-184 (1987).
- Stanway, R., J. L. Sproston, M. J. Prendergast, J. R. Case, and C. E. Wilne, "ER fluids in the squeeze-flow mode: an application to vibration isolation," *J. Electrostatics* **28**, 89-94 (1992).
- Stefan, J., "Versuche uber der scheinbare adhasion," *Sitz. Kais. Akad. Wiss Math. Nat. Wien* **69(2)**, 713-735 (1874).
- Tang, X., X. Zhang, R. Tao, and Y. Rong, "Structure-enhanced yield stress of magnetorheological fluids," *J. Appl. Phys.* **87(5)**, 2634-2638 (2000).
- Tao, R., Y. C. Lan, and X. Xu, "Structure-enhanced yield shear stress in electrorheological fluids," *Int. J. Mod. Phys. B* **16**, 2622-2628 (2002).
- Tian, Y., Y. Meng, H. Mao, and S. Wen, "Electrorheological fluid under elongation, compression, and shearing," *Phys. Rev. E* **65**, 031507 (2002a).
- Tian, Y., Y. Meng, H. Mao, and S. Wen, "Mechanical property of electrorheological fluid under step compression," *J. Appl. Phys.* **92**, 6875-6879 (2002b).

- Tian, Y., S. Wen, and Y. Meng, "Compressions of electrorheological fluids under different initial gap distances," *Phys. Rev. E* **67**, 051501 (2003a).
- Tian, Y., M. Zhang, X. Zhu, Y. Meng, and S. Wen, "Ultra-high yield stress in a general electrorheological fluid under compression," *Smart Mater. Struct.* **19**, 035009 (2010).
- Tian, Y., and Q. Zou, "Normalized method for comparing tensile behaviors of electrorheological fluids," *App. Phys. Lett.* **82(26)**, 4836-4838 (2003b).
- Vereda, F., J. de Vicente, and R. Hidalgo-Álvarez, "Influence of a magnetic field on the formation of magnetite particles via two precipitation methods," *Langmuir* **23**, 3581-3589 (2007).
- Vereda, F., J. de Vicente, and R. Hidalgo-Álvarez, "Physical properties of elongated magnetic particles: magnetization and friction coefficient anisotropies," *ChemPhysChem* **10**, 1165-1179 (2009).
- Vieira, S. L., M. Nakano, R. Oke, and T. Nagata, "Tension and compression of electrorheological fluid," *Int. J. Mod. Phys. B* **15**, 714-722 (2001).
- Volkova, O., G. Bossis, M. Guyot, V. Bashtovoi, and A. Reks, "Magnetorheology of magnetic holes compared to magnetic particles," *J. Rheol.* **44**, 91-104 (2000).
- Wang, X., and F. Gordaninejad, "Study of magnetorheological fluids at high shear rates," *Rheol. Acta* **45**, 899-908 (2006).
- Williams, E. W., S. G. Rigby, J. L. Sproston, and R. Stanway, "Electrorheological fluids applied to an automotive engine mount," *J. Non-Newtonian Fluid Mech.* **49**, 221-238 (1993).
- Wollny, K., J. Lauger, and S. Huck, "Magneto sweep - a method for characterizing the viscoelastic properties of magneto-rheological fluids," *Appl. Rheol.* **12**, 25-31 (2002).

- Wu, C. W., and H. Conrad, "Shear strength of electrorheological particle clusters," *Mater Sci. Eng. A*, **248**, 161-164 (1998).
- Yang, F., "Tension and compression of electrorheological fluid," *J. Colloid Interf. Sci.* **192**, 162-165 (1997).
- Zhang, M. L., Y. Tian, J. L. Jiang, X. L. Zhu, Y. G. Meng, and S. Z. Wen, "Compression enhanced shear yield stress of electrorheological fluid," *Chin. Phys. Lett.* **26(4)**, 048301 (2009).
- Zhang, X. Z., X. L. Gong, P. Q. Zhang, and Q. M. Wang, "Study on the mechanism of the squeeze-strengthen effect in magnetorheological fluids," *J. Appl. Phys.* **96(4)**, 2359-2364 (2004).

Chapter 3.

On the validity of continuous media theory for plastic materials in MR fluids under slow compression

José Antonio Ruiz-López, Roque Hidalgo-Álvarez and Juan de Vicente.

This article is published in *Rheological Acta*. Volume: 51(7). Pages: 595-602. 2012.

Abstract

In this manuscript, we address the long-standing question of whether a single theory for model plastic fluids is suitable to deal with the unidirectional compression problem in magnetorheological (MR) fluids. We present an extensive experimental investigation of the performance of MR fluids in slow-compression, no-slip, constant-volume squeeze mode under different magnetic field strengths (0 – 354 kA/m), dispersing medium viscosities (20 – 500 mPa·s) and particle concentrations (5 – 30 vol%). Normal force versus compressive strain curves reasonably collapse when normalizing by the low-strain normal force. Deviations from the squeeze flow theory for field-responsive yield stress fluids are associated

to microstructural rearrangements under compression in good agreement with the so-called squeeze strengthening effect. Yield compressive stresses are found to scale as $\sim \eta^{0.33} \phi^{2.0} H^{2.0}$.

3.1. Introduction

Magnetorheological (MR) fluids are magnetically responsive colloidal suspensions with tunable mechanical properties (de Vicente et al. 2011a; Park et al. 2010). In the case of conventional MR fluids, dispersed micron-sized particles become magnetized in the presence of external magnetic fields, eventually aggregating in the direction of the field and forming elongated chain-like structures. MR fluids are typically characterized by a field-dependent yield stress (i.e. the minimum stress value required for the suspension to flow).

Because of their unique mechanical properties, MR fluids are already used in a wide range of commercial applications including automobile suspension systems, shock absorbers, etc (Carlson 2007; Olabi and Grunwald 2007). In general, available devices using these fluids can be classified according to their flow mode as direct-shear flow mode, pressure-driven flow mode and squeeze-film flow mode. Among the three modes, it is well known that the squeeze flow mode provides the largest yield stress under the same field (Havelka and Pialet 1996). The rheological properties of MR fluids under shearing flows (i.e. direct-shear and pressure-driven flows) have been extensively investigated in the literature. However, the understanding of the behavior of MR fluids under non-shearing elongational flows, and particularly in squeeze flow mode is still far to be complete mainly because of the lack of both a thorough understanding of the basic MR mechanisms and reliable experimental data (de Vicente et al. 2011b).

First reports on squeeze flow magnetorheology were devoted to investigate the enhancement of MR performance by the so-called compression-assisted aggregation process (Tang et al. 2000; Zhang et al. 2004; Zhang et al. 2009). This consists of enhancing the yield shear stress by the formation of thick strong columns under compression. Later, See (2003) reported a series of low-strain tests on MR fluids where the behaviors under constant velocity squeezing flow and shear flow were compared. A field dependence of $H^{0.91}$ was found for compression in contrast to the $H^{1.4}$ dependence observed under shearing. Constant area squeeze flow MR experiments were carried out by Mazlan et al. (2007, 2008). More recently, Gstöttenbauer et al. (2008) designed a test rig to explore the flow behavior of MR fluids under sinusoidal loading modes.

Traditionally, the squeeze flow behavior of field-responsive fluids has focused on the electric counterparts of MR fluids; i.e. electrorheological (ER) fluids (El Wahed et al. 1998; Meng and Filisko 2005; Stanway et al. 1987; Tian et al. 2002a; Tian et al. 2003b). Currently, the use of MR fluids under non-shearing flows has received attention mostly because of two reasons: i) border effects, that are unavoidably present when working with electrorheological (ER) fluids, are not an issue for MR fluids; ii) the magnetic field strength can be kept essentially constant (when neglecting/controlling the change in magnetic resistance when decreasing the gap) if compared to ER analogues working under constant voltage operation. However, a thorough investigation of the stress-strain characteristics of MR fluids in compression mode is still not complete. To the best of our knowledge, only the effect of magnetic field strength has been investigated under slow-compression, no-slip, constant-volume squeeze mode (de Vicente et al. 2011b; See 2003).

On the one hand, the effect of medium viscosity in the squeeze flow performance has been scarcely investigated. Chu et al. (2000) observed that the normal stresses in ER fluids containing lower medium viscosity not only possessed larger value but also increased more rapidly with the strain. These findings were explained in terms of a smaller drag force acting on field-induced structures. Interestingly, the medium viscosity does also influence the sedimentation rate of the dispersed particles. Experimental work and particle-level simulations demonstrate that body forces can significantly influence the structure and rheology of ER and MR suspensions even when the magnitude of the body force is small compared to the field-induced force (eg. in the filtration-dominated squeeze regime) (Klingenberg et al. 2007). On the other hand the understanding of the effect of particle concentration has been traditionally impeded by the fact that most experiments reported in the literature concern ER fluids working under constant area operation. For these systems, once the field is applied, the volumetric concentration increases under compression due to the "sealing/condensation effect" originated by the field intensification near the electrodes edges (Chu et al. 2000; Lynch et al. 2006; McIntyre and Filisko 2007; Tian et al. 2002a).

In the current work we follow a previous paper where we investigated the effect of magnetic field strength in the appearance of normal forces under no-slip compression in the filtration dominated regime (de Vicente et al. 2011b). In that paper we demonstrated a good scaling when normalizing by the low-strain normal force and a reasonably good agreement with macroscopic plastic models at large enough magnetic fields and particle level dynamic simulations --see Figure 9 in de Vicente et al. (2011b)--. In the present manuscript we report new experimental data to better understand the effect of dispersing liquid viscosity and particle content in the squeeze flow behavior. We also address a macroscopic model that

may capture dependencies with magnetic field strength, dispersing medium viscosity and particle concentration. The development of a general constitutive framework for MR fluids would find use in the design of better MR engineering devices.

3.2. Theory

The squeeze flow behavior of inelastic yield stress fluids under no-slip conditions has been extensively investigated in the literature since the pioneering work by Scott (1929). Usually, a plasticity number S is defined that separates the preyield and postyield regimes (Covey and Stanmore 1981):

$$S = \frac{\eta_p v R}{h^2 \tau_y} \quad (3.1)$$

Here η_p is the Bingham plastic viscosity, v is the approaching speed, R is the radius of the sample, h is the gap thickness and τ_y is the yield shear stress.

Starting from the Bingham constitutive equation, Covey and Stanmore (1981) obtained an analytical relation between the normal force F and the gap thickness h for small S numbers ($S < 0.5$):

$$F = \frac{2\pi\tau_y R^3}{3h} + \frac{4\pi}{7h^2} \sqrt{2\tau_y \eta_p v R^7} \quad (3.2)$$

Later Williams et al. (1993) analytically solved the squeeze flow problem for a bi-viscous fluid instead of a Bingham plastic. The final result reads as follows:

$$F = \frac{2\pi\tau_y R^3}{h\chi^3} \left[\frac{\gamma^3}{108} + \int_{\gamma/3}^{\chi} S^2 G dS \right] \quad (3.3)$$

where γ , χ , and G are parameters defined by:

$$\gamma = \frac{\eta}{\eta_r}; \chi = S(r = R); G = -\frac{h}{2\tau_y} \frac{dp}{dr} \quad (3.4)$$

Here η_r is the preyield viscosity and η the viscosity above the yield point in the bi-viscous model.

Interestingly, for $S \ll 1$, in the so-called filtration dominated regime (McIntyre and Filisko 2010), both Equation 3.2 and Equation 3.3 converge to the following analytical expression:

$$F = \frac{2\pi\tau_y R^3}{3h} \quad (3.5)$$

After some algebra, the normal force in the case of constant volume tests can be written as follows:

$$F = \frac{2\tau_y V^{3/2}}{3\sqrt{\pi}h_0^{5/2}(1-\varepsilon)^{5/2}} \quad (3.6)$$

where V represents the total volume of the sample ($V = \pi R^2 h$) and the elongational strain ε is defined here as the ratio of the moving distance of the upper plate to the initial distance between the plates $\varepsilon = (h_0 - h)/h_0$.

It is worth to remark here that in the derivation of Equation 3.6 we have assumed a small gap to radius ratio and a constant plastic yield stress that is independent of the deformation rate. Also, surface tension effects are neglected. Importantly, Equation 3.6 reveals that the resistance to deformation for low plasticity numbers comes from the yield shear stress component while viscous stresses are negligible. Equation 3.6 has been validated in the literature for the compression of ER fluids under constant area operation (Tian et al. 2002b). However, deviations from this description have been also reported (Tian et al. 2003b).

3.3. Experimental

Conventional MR fluids were prepared by carefully mixing carbonyl iron microparticles (HQ grade, BASF) in silicone oil (Sigma-Aldrich). A parallel plate magnetorheometer MCR-501 (Anton Paar) was used to perform constant volume squeeze flow experiments in the presence of magnetic fields. The schematic of the compression test system is shown in Figure 3.1. Non magnetic titanium plates (diameter 2 cm) were employed. The initial separation was $h_0 = 300 \mu\text{m}$. Plates were supposed to be perfectly parallel even though a small misalignment exist (Andablo-Reyes et al. 2010, 2011). The distortion of the force sensor under pressures generated in this work was neglected. Previous work suggested that no-slip assumptions do apply for all experiments reported in this manuscript (de Vicente et al. 2011b). Also, magnetic fields are expected to be reasonably uniform in the MRD-180 magnetocell employed as the typical magnetic field strength values remained smaller than 300 kA/m (Laun et al. 2008).

Compression experiments were run at constant volume V , and constant velocity $v = 10 \mu\text{m}/\text{s}$ (elongational rate range: $\dot{\epsilon} \sim 0.03 - 0.2 \text{ s}^{-1}$). This corresponds to low plasticity numbers $S < 0.5$ and low Reynolds numbers $Re \sim 10^{-3} \ll 1$ so lubrication and creeping flow approximations can be used. Additionally, preliminary tests were performed under different approaching speeds and constant compressive rates to ensure that the tests were safely done in the so-called “filtration” regime (McIntyre and Filisko 2010). Prior to the test, the sample was equilibrated at rest in the presence of a suddenly applied external magnetic field during 60 s. Results presented below are always averages over at least three separate runs. All experiments were run at 25 °C.

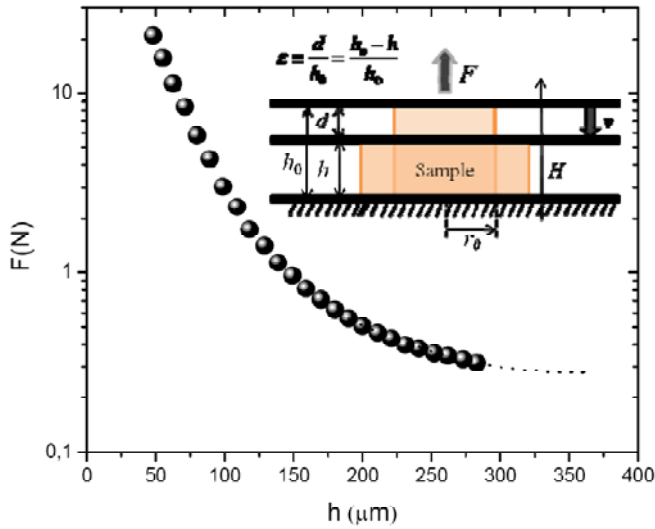


Figure 3.1 Schematic view of the constant volume squeeze flow experiment and typical behavior of normal force growth for a 5 vol% MR fluid. Magnetic field strength 177 kA/m. Dispersing medium viscosity 200 mPa·s. Approaching speed $v = 10 \mu\text{m/s}$.

Static and dynamic yield shear stress measurements were carried out in controlled shear stress mode. In a first step a preshear ($\dot{\gamma} = 200 \text{ s}^{-1}$) is applied in the absence of a magnetic field for 30 seconds. Then, the magnetic field is turned on without any shear applied yet. After 30 seconds of equilibration the shear stress was logarithmically increased from 0.1 Pa at a rate of 10 points per decade. On the one hand, the static yield stress is determined from the low-shear extrapolation in double logarithmic representations of shear stress versus shear rate. On the other hand, the dynamic yield stress is obtained from curve fitting using the Bingham model at large shear rates in a lin-lin representation.

3.4. Results and discussion

A series of unidirectional slow compression tests has been carried out with different magnetic field strengths, dispersing medium viscosities and

particle volume fractions. As a way of example, a typical result is shown in Figure 3.1. In general, when a MR fluid is compressed under the presence of a magnetic field, its compressive resistance increases with the gap reduction. At large gaps (i.e. low strains), the normal force tends towards a limiting plateau value that is associated to the yield compressive stress of the field-induced structure.

In a previous work we reported on the collapse of slow compression curves obtained for different magnetic field strengths when normalizing by the low strain normal force plateau (de Vicente et al. 2011b). In Figure 3.2 we reproduce these data along with new experiments for a wide range of dispersing liquid viscosities and particle volume fractions. As observed, a reasonably good collapse is also found. As a reference, included in Figure 3.2 we also show the theoretical prediction according to Equation 3.6 for yield stress fluids. At first glance, the theoretical prediction satisfactorily explains experimental data.

Next, we will take a closer look to the experimental data in a more convenient way by plotting the normal force F versus $1 - \varepsilon$ in a log-log representation (see Figure 3.3). Results show a reasonably good linear relationship as theoretically predicted (cf Equation 3.6). Deviations from linearity appear at large $1 - \varepsilon$ values may be due to inertia and initial transient effects. A least squares fitting routine was used to fit normal force data according to $F = A/(1 - \varepsilon)^B$ in a log-log representation. Intercept A and slope B fitting parameters are included in Table 3.1.

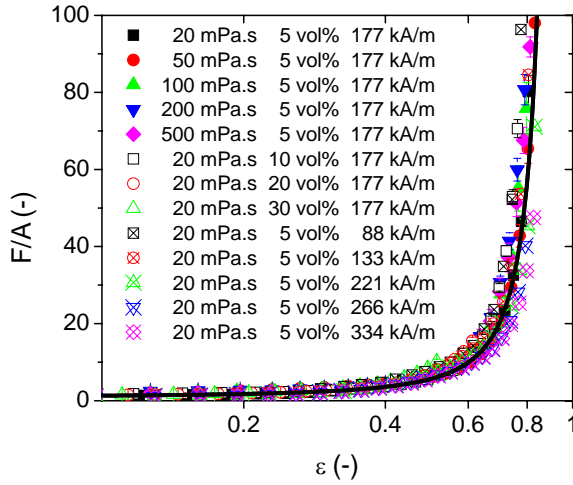
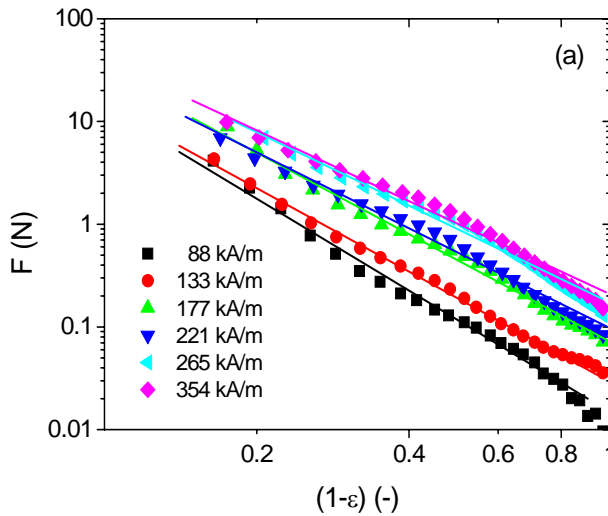


Figure 3.2 Dimensionless normal force F as a function of compressive strain ε for different magnetic field strength, dispersing medium viscosity and particle volume fraction. The force F is normalized by the low-strain normal force value A . Solid line corresponds to the prediction by the continuous media theory for plastic materials Equation 3.6. Approaching speed $v = 10 \mu\text{m/s}$.



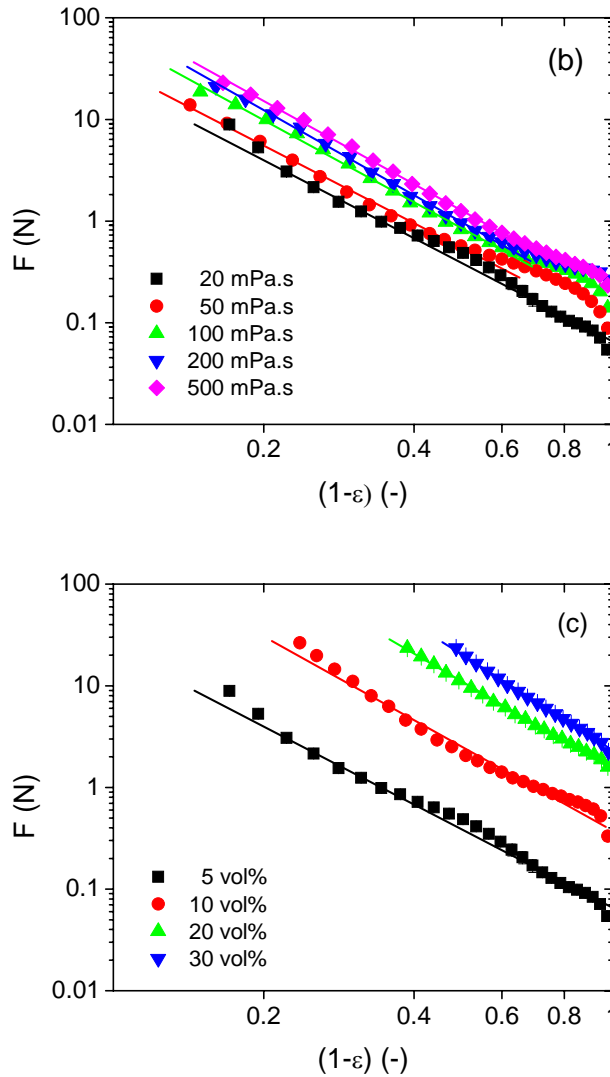


Figure 3.3 Log-log representation of normal force F vs. $1 - \varepsilon$ curves. Solid lines are best fits to $F = A/(1 - \varepsilon)^B$ with fitting parameters included in Table 3.1. (a) $\eta = 20 \text{ mPa} \cdot \text{s}$, $\phi = 5 \text{ vol}\%$; (b) $H = 177 \text{ kA/m}$, $\phi = 5 \text{ vol}\%$; and (c) $H = 177 \text{ kA/m}$, $\eta = 20 \text{ mPa} \cdot \text{s}$. Approaching speed $v = 10 \text{ } \mu\text{m/s}$.

H (kA/m)	η (mPas)	ϕ (vol%)	ε (-)	A (N)	B (-)	R^2 (-)	Static (Pa)	Dynamic (Pa)
88	20	5	0.1-0.8	0.015 ± 0.001	2.98 ± 0.07	0.991	80	650
133	20	5	0.1-0.8	0.030 ± 0.001	2.70 ± 0.03	0.997	160	880
177	20	5	0.1-0.8	0.066 ± 0.001	2.55 ± 0.01	0.989	380	1070
221	20	5	0.1-0.8	0.097 ± 0.002	2.45 ± 0.06	0.989	400	1530
266	20	5	0.1-0.8	0.172 ± 0.004	2.37 ± 0.06	0.986	390	1500
354	20	5	0.1-0.8	0.207 ± 0.005	2.28 ± 0.06	0.984	810	2650
177	20	5	0.1-0.8	0.066 ± 0.001	2.55 ± 0.01	0.989	380	1070
177	50	5	0.4-0.8	0.093 ± 0.006	2.54 ± 0.05	0.995	708	2500
177	100	5	0.4-0.8	0.132 ± 0.006	2.68 ± 0.04	0.997	1580	4000
177	200	5	0.4-0.8	0.140 ± 0.006	2.78 ± 0.03	0.998	708	3200
177	500	5	0.4-0.8	0.191 ± 0.006	2.72 ± 0.03	0.999	2240	5250
177	20	5	0.1-0.8	0.066 ± 0.001	2.55 ± 0.01	0.989	380	1070
177	20	10	0.1-0.8	0.375 ± 0.003	2.74 ± 0.01	0.983	990	2800
177	20	20	0.1-0.6	1.51 ± 0.04	2.86 ± 0.04	0.999	4750	5620
177	20	30	0.1-0.5	2.32 ± 0.05	3.11 ± 0.05	0.998	5690	7380

Table 3.1. Fitting parameters (A and B) and correlation coefficients (R^2) for normal force vs. $1 - \varepsilon$ curves reported in Figure 3.3 according to $F = A/(1 - \varepsilon)^B$. The compressive strain range used in the fitting routine is also showed. Also exposed are the values of the static yield shear stress (static) and the dynamic yield shear stress (dynamic) obtained from the ramp-up shear flow rheograms.

On the one hand, intercept values A do increase with increasing the magnetic field strength, medium viscosity and particle concentration. This finding suggests that the yield compressive stress is a function of these quantities. On the other hand, the slopes of the experimental curves B approach the theoretical value of 2.5 (in agreement with results presented in Figure 3.2). However, non-negligible deviations in B parameters with respect to the theoretical value exist (ranging from 2.4 to 3.1). These deviations may suggest that the compression resistance increases

generally faster than the prediction of the squeeze flow theory, for example with a τ_y that increases when decreasing the gap. To check this hypothesis we took pictures of the MR fluids under compression using a rheomicroscopy device. In Figure 3.4 we show a typical example where field induced structures are seen to actually evolve under compression leading to thicker columnar aggregates. These thicker structures are presumably more resistant to deformation and eventually would give a larger τ_y in view of the squeeze strengthen effect (Tang et al. 2000).

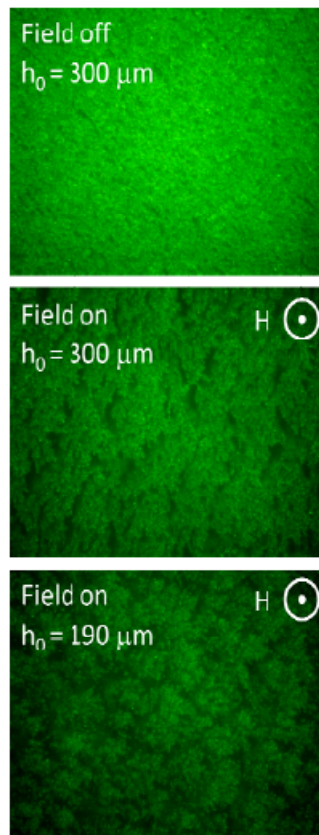


Figure 3.4 Structure evolution of a 5 vol% suspension in a 20 mPa·s silicone oil under compression, in the presence of an external magnetic field that is perpendicular to the paper. (a) initial gap $h_0 = 300 \mu\text{m}$ in the absence of an external magnetic field; (b) initial gap $h_0 = 300 \mu\text{m}$ in presence of an external magnetic field; (c) intermediate gap $h_0 = 190 \mu\text{m}$ in presence of an external magnetic field.

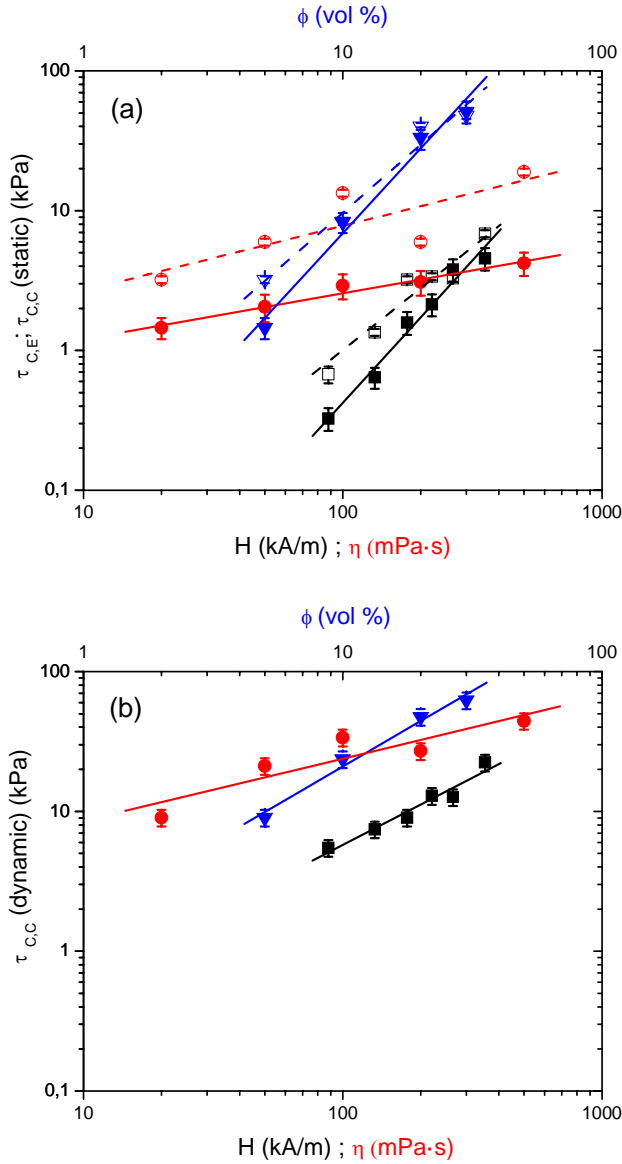


Figure 3.5. Low-strain compressive stresses as a function of magnetic field strength H (squares), dispersing medium viscosity η (circles) and particle volume fraction ϕ (triangles). (a) Comparison between experiments $\tau_{C,E}$ and calculations $\tau_{C,C}$ using Equation 3.7 for the static yield shear stress; solid symbols, experimental; open symbols, calculations. (b) Calculations of the low-strain compressive stresses using dynamic yield shear stress measurements in Equation 3.7.

A further insight into the compressive behavior of MR fluids can be obtained by directly measuring the static yield shear stress τ_y of the samples using conventional steady simple shear rheometry (de Vicente et al. 2011a). With this, compressive stresses can be calculated from Equation 3.6 as follows:

$$\tau_{C,C} = \frac{2\tau_y V^{3/2}}{3\pi^{3/2} h_0^{5/2} r_0^2} = \frac{2\tau_y r_0}{3h_0} \quad (3.7)$$

where r_0 is the initial sample radius ($r_0 = 3.8 \pm 0.3 \text{ mm}$). For a comparative analysis, in Figure 3.5 we show experimentally measured compressive yield stresses $\tau_{C,E} = A/\pi r_0^2$ (solid symbols) as well as calculations $\tau_{C,C}$ using Equation 3.7 (open symbols). As demonstrated, calculated compressive yield stresses compare reasonably well with experimental measurements especially taking into account that there are not free parameters in these calculations. The yield compressive stress does increase with increasing the magnetic field strength, medium viscosity and particle content. A power law dependence is found in the three cases. Even though similar values are obtained for the experimental and calculated yield compressive stresses, the slopes seem to differ from each other (see Table 3.2).

	H	η	ϕ
$\tau_{C,E}$ (kPa)	2.0 ± 0.1	0.33 ± 0.08	2.0 ± 0.2
$\tau_{C,C}$ (static) (kPa)	1.47 ± 0.07	0.46 ± 0.02	1.62 ± 0.04
$\tau_{C,C}$ (dynamic) (kPa)	1.0 ± 0.1	0.44 ± 0.06	1.0 ± 0.1

Table 3.2. Power law exponent α for the yield compressive stress τ_C according to $\tau_C \propto X^\alpha$ being $X = H, \eta$ or ϕ . Data used are taken from Figure 3.5.

The experimentally measured yield compressive stress $\tau_{C,E}$ varies with the magnetic field strength as $H^{2.0 \pm 0.1}$. This H dependency of normal stresses in the squeezing flow turns out to be larger than the well-known $H^{1.5}$ dependence of shear stresses in simple shearing flow (de Vicente et al. 2011a; Ginder et al. 1996; See 2003). In agreement with the literature, our MR fluid exhibited a yield shear stress that scaled as $H^{1.47}$ (see Table 3.2). Similarly to our results, Tian et al. (2003b) reported that the yield compressive stress in ER fluids was proportional to the square of the external electric field for large gap separations. They argued that the exponent should be 2 if there is no saturation effect in ER fluids according to the polarization model (Wen et al. 2008). On the contrary, Chu et al. (2000) measured an exponent larger than 4 in ER fluids for the E dependence, and See (2003) found that in the case of highly concentrated MR fluids the normal force varies with $H^{0.91}$ under the higher fields investigated.

The dispersing medium viscosity dependence is significantly low as expected in a slow compression filtration-dominated regime ($\approx \eta^{0.33 \pm 0.08}$). The slight increase in the stress with increasing viscosity may be due to an enhancement in the kinetic stability and hence slightly stronger field induced structures (Klingenberg et al. 2007). This hypothesis is confirmed from yield shear stress measurements; actually, the yield shear stress did also slightly increase with increasing the medium viscosity ($\approx \eta^{0.46 \pm 0.02}$, see Table 3.2).

As expected, the effect of particle concentration is found to be significantly more important than the effect of oil viscosity. Again, a power law dependence is found between the yield compressive stress and the volume fraction ($\approx \phi^{2.0 \pm 0.2}$). This result is larger than the slope obtained from yield shear stress measurements, that predict a power law

of approximately 1.5 (see Table 3.2), and in qualitative good agreement with Tian et al. (2003a). It is worth to remark here that contrary to ER fluids where ϕ increases with decreasing the electrode separation, in our experiments, ϕ remains constant as the magnetic field is presumably uniform (Laun et al. 2008).

For completeness, in Figure 3.5b we show calculated compressive stresses by substituting the dynamic yield shear stress --instead of the static yield shear stress-- in Equation 3.9. By comparing Figure 3.5a and Figure 3.5b, we observe that a much better accordance between experiments and calculations is obtained when using the static yield stress data. This was expected as the field-induced structures were not supposed to slip on the plates.

3.5. Conclusions

Most of the squeeze flow results reported in the literature on field-responsive fluids deal with ER fluids where both the electric field strength and particle concentration change during compression. Many efforts have been done in the past to better understand their squeeze flow behavior under the framework of continuum media theories. In some cases, experimental data are satisfactorily explained using a continuum squeeze-flow theory whereas it has been recently reported that this theory fails for small initial gaps and high voltages (Meng and Filisko 2005; Tian et al. 2003b).

In this paper we performed a systematic experimental study of conventional MR fluids under conditions of slow compression, no-slip, and constant volume. We proposed a unified description of the behavior of MR fluids in terms of a continuous media theory for plastic materials. This allowed us to collapse compression curves obtained for a wide range

of magnetic field strengths, medium viscosity and particle concentration. Deviations from the theory were explained in terms of the squeeze strengthening effect. On the one hand, a quadratic dependence with the magnetic field strength (2.0 ± 0.1) and particle concentration (2.0 ± 0.2) is found. On the other hand, a $\eta^{0.33 \pm 0.08}$ dependence of the compressive stress is found. Experiments reported here suggest another procedure to determine static yield shear stresses when slowly compressing the MR fluids.

Acknowledgements

This work was supported by MICINN MAT 2010-15101 project (Spain), by the European Regional Development Fund (ERDF) and by Junta de Andalucía P10-FQM-5977 and P10-RNM-6630 projects (Spain). J.A.R.-L. acknowledges financial support by the “Ministerio de Educación: Becas del Programa de Formación del Profesorado Universitario (FPU)” (AP2010-2144).

References

- Andablo-Reyes E, Hidalgo-Álvarez R, de Vicente J (2010) A method for the estimation of the film thickness and plate tilt angle in thin film misaligned plate-plate rheometry. *J Non-Newtonian Fluid Mech* 165:1419-1421.
- Andablo-Reyes E, Hidalgo-Álvarez R, de Vicente J (2011) Erratum to “A method for the estimation of the film thickness and plate tilt angle in thin film misaligned plate-plate rheometry” [*J. Non-Newtonian Fluid Mech.* 165 (2010) 1419–1421]. *J Non-Newtonian Fluid Mech* 166:882-882.

-
- Carlson JD (2007) MR fluid technology – Commercial status in 2006. In Proceedings of the 10th International Conference on Electrorheological Fluids and Magnetorheological Suspensions, edited by F. Gordaninejad, O. A. Graeve, A. Fuchs and D. York, World Scientific, Singapore, pp. 389-395.
- Chu SH, Lee SJ, Ahn KH (2000) An experimental study on the squeezing flow of electrorheological suspensions. *J Rheol* 44(1):105-120.
- Covey GH, Stanmore BR (1981) Use of the parallel-plate plastometer for the characterization of viscous fluids with a yield stress. *J Non-Newtonian Fluid Mech* 8:249-260.
- de Vicente J, Klingenberg DJ, Hidalgo-Álvarez R (2011a) Magnetorheological fluids: a review. *Soft Matter* 7:3701-3710.
- de Vicente J, Ruiz-López JA, Andablo-Reyes E, Segovia-Gutiérrez JP, Hidalgo-Álvarez R (2011b) Squeeze flow magnetorheology. *J Rheol* 55:753-779.
- El Wahed AK, Sproston JL, Stanway R (1998) The performance of an electrorheological fluid in dynamic squeeze flow under constant voltage and constant field. *J Phys D: Appl Phys* 31:2964-2974.
- Ginder JM, Davis L, Elie L (1996) Rheology of magnetorheological fluids: Models and measurements. *Int J Mod Phys B* 10:3293-3303.
- Gstöttenbauer N, Kainz A, Manhartgruber B, Scheidl R (2008) Experimental and numerical studies of squeeze mode behaviour of magnetic fluid. *Proc IMechE C* 222:2395-2407.
- Havelka KO, Pialet JW (1996) Electrorheological technology: The future is now. *CHEMTECH* 36:36-45.
- Klingenberg DJ, Ulicny JC, Smith AL (2007) Effects of body forces on the structure and rheology of ER and MR fluids. *Int J Mod Phys B* 21:4841-4848.

- Laun HM, Schmidt G, Gabriel C (2008) Reliable plate-plate MRF magnetorheometry based on validated radial magnetic flux density profile simulations. *Rheol Acta* 47:1049–1059.
- Lynch R, Meng Y, Filisko FE (2006) Compression of dispersions to high stress under electric fields: effects of concentration and dispersing oil. *J Colloid Interf Sci* 297:322-328.
- Mazlan SA, Ekreem NB, Olabi AG (2007) The performance of magnetorheological fluid in squeeze mode. *Smart Mater Struct* 16, 1678-1682.
- Mazlan SA, Ekreem NB, Olabi AG (2008) An investigation of the behaviour of magnetorheological fluids in compression mode. *Journal of Materials Processing Technology* 201:780-785.
- McIntyre EC, Filisko FE (2007) Squeeze flow of electrorheological fluids under constant volume. *J Intel Mat Syst Str* 18:1217-1220.
- McIntyre EC, Filisko FE (2010) Filtration in electrorheological suspensions related to the Peclet number. *J Rheol* 54(3):591-603.
- Meng Y, Filisko FE (2005) Unidirectional compression of electrorheological fluids in electric fields. *J Appl Phys* 98:074901.
- Olabi AG, Grunwald A (2007) Design and application of magnetorheological fluid. *Materials and Design. Materials and Design* 28:2658-2664.
- Park BJ, Fang FF, Choi HJ (2010) Magnetorheology: materials and application. *Soft Matter* 6:5246-5253.
- Scott JR (1929) *Trans Inst Rubber Ind* 4:347-347.
- See H (2003) Field dependence of the response of a magnetorheological suspension under steady shear flow and squeezing flow. *Rheol Acta* 42:86-92.
- Stanway R, Sproston JL, Stevens NG (1987) Non-linear modelling of an electro-rheological vibration damper. *J Electrostatics* 20:167-184.

-
- Tang X, Zhang X, Tao R, Rong Y (2000) Structure-enhanced yield stress of magnetorheological fluids. *J Appl Phys* 87(5):2634-2638.
- Tian Y, Meng Y, Mao H, Wen S (2002a) Electrorheological fluid under elongation, compression, and shearing. *Phys Rev E* 65:031507.
- Tian Y, Meng Y, Mao H, Wen S (2002b) Mechanical property of electrorheological fluid under step compression. *J Appl Phys* 92:6875-6879.
- Tian Y, Meng Y, Wen S (2003a) Particulate volume effect in suspensions with strong electrorheological response. *Materials Letters* 57:2807-2811.
- Tian Y, Wen S, Meng Y (2003b) Compressions of electrorheological fluids under different initial gap distances. *Phys Rev E* 67:051501.
- Wen W, Huang X, Sheng P (2008) Electrorheological fluids: structures and mechanisms. *Soft Matter* 4:200-210.
- Williams EW, Rigby SG, Sproston JL, Stanway R (1993) Electrorheological fluids applied to an automotive engine mount. *J Non-Newtonian Fluid Mech* 49:221-238.
- Zhang ML, Tian Y, Jiang JL, Zhu XL, Meng YG, Wen SZ (2009) Compression enhanced shear yield stress of electrorheological fluid. *Chin Phys Lett* 26(4):048301.
- Zhang XZ, Gong XL, Zhang PQ, Wang QM (2004) Study on the mechanism of the squeeze-strengthen effect in magnetorheological fluids. *J Appl Phys* 96(4):2359-2364.

Chapter 4.

Continuous media theory for MR fluids in non-shearing flows

José Antonio Ruiz-López, Roque Hidalgo-Álvarez and Juan de Vicente.

This article is published in Journal of Physics: Conference Series. Volume: 412. Pages: 012057. 2013

Abstract

The enhanced mechanical response of magnetorheological fluids under slow compression has been investigated by means of experiments, theory and particle-level simulations. A wide range of magnetic field strengths (0–354 kA/m), dispersing medium viscosities (20–500 mPa·s) and particle concentrations (5–30 vol%) were investigated. Plastic media theory in compressive flow was in good agreement with experimental data. Slight deviations from the theory were associated to the so-called strengthening effect as the yield shear stress could increase during compression. Particle-level simulations were in good agreement with both experiments and simulations.

4.1. Introduction

In general, available devices using magnetorheological (MR) fluids can be classified according to their flow mode as direct-shear flow mode, pressure-driven flow mode and squeeze-film flow mode. Among the three modes, it is well known that the squeeze flow mode provides the largest yield stress under the same field [1]. The rheological properties of MR fluids under shearing flows have been extensively investigated in the literature. However, the understanding of the behavior of MR fluids under non-shearing elongational flows, and particularly in squeeze flow mode is still far to be complete mainly because of the lack of both a thorough understanding of the basic MR mechanisms and reliable experimental data [2, 3].

First reports on squeeze flow magnetorheology were devoted to investigate the enhancement of MR performance by the so-called compression-assisted aggregation process [4-6]. Later, in a study, a series of low-strain tests on MR fluids where the behaviors under constant velocity squeezing flow and shear flow were compared [7]. A field dependence of $H^{0.91}$ was found for compression in contrast to the $H^{1.4}$ dependence observed under shearing.

In this work, we follow previous papers where we experimentally demonstrated the appearance of normal forces under no-slip compression in the filtration dominated regime [3, 8]. In the present study the long-standing question of whether a single theory for model plastic fluids is suitable to deal with the unidirectional compression problem in MR fluids was addressed. In this work, an extensive experimental and particle-level simulation investigation of the performance of MR fluids in slowcompression, no-slip, constant-volume squeeze mode under different

magnetic field strengths (0–354 kA/m), dispersing medium viscosities (20–500 mPa s) and particle concentrations (5–30 vol%) were investigated.

4.2. Theory

Plastic media theory in squeeze flow mode was first developed by Covey and Stanmore [9]. The solution of the motion equation for a Bingham fluid depends of the plasticity number, defined as:

$$S = \frac{\eta_p v R}{h^2 \tau_y} \quad (4.1)$$

where η_p is the Bingham plastic viscosity, v is the approaching speed, R is the radius of the sample, h is the gap thickness and τ_y is the yield shear stress. For low plasticity numbers, in the so-called filtration dominated regime, both Bingham and biviscous theories are applied that reduce to the following analytical expression in the case of constant volume tests [8]:

$$F = \frac{2\tau_y V^{3/2}}{3\sqrt{\pi} h_0^{5/2} (1-\varepsilon)^{5/2}} \quad (4.2)$$

where V represents the total volume of the sample ($V = \pi R^2 h$) and the elongational strain ε is defined here as the ratio of the moving distance of the upper plate to the initial distance between the plates $\varepsilon = (h_0 - h)/h_0$.

4.3. Simulations

A three-dimensional particle-level simulation method to understand the effect of particle concentration was also employed. Magnetic forces were approximated by the point-dipole limit and high-order magnetic multipoles were neglected. A free draining approximation was used for

including hydrodynamic interactions. Short-range repulsive interactions between particles, and particles and walls were taken as an exponential interaction [3, 8].

Finally, the normal force, F^* , acting on the plate is calculated by simply differentiating the total magnetic energy, U^* , according to:

$$F^* = -\frac{dU^*}{dh^*}, \quad (4.3)$$

4.4. Results and discussion

Uniaxial monotonic compression tests were carried out in the presence of a uniaxial magnetic field at low compression rates under constant volume conditions. In all cases, the resulting normal force shows an initial ‘plateau’ in the low-strain region related to the compressive yield stress. This initial plateau is in agreement with Equation 4.2 [3].

The compressive yield stress was obtained from experimental data by dividing the initial normal force plateau value by the MR fluid area. For a comparative analysis, in Figure 4.1, experimentally measured compressive yield stresses $\tau_{C,E} = A/\pi r_0^2$ (open symbols) as well as calculations

$$\tau_{C,C} = \frac{2\tau_y V^{3/2}}{3\pi^{3/2} h_0^{5/2} r_0^2} = \frac{2\tau_y r_0}{3h_0} \text{ (open symbols) were shown. As demonstrated,}$$

calculated compressive yield stresses compare reasonably well with experimental measurements especially taking into account that there are not free parameters in these calculations. The yield compressive stress does increase with increasing the magnetic field strength, medium viscosity and particle content. A power law dependence is found in the three cases.

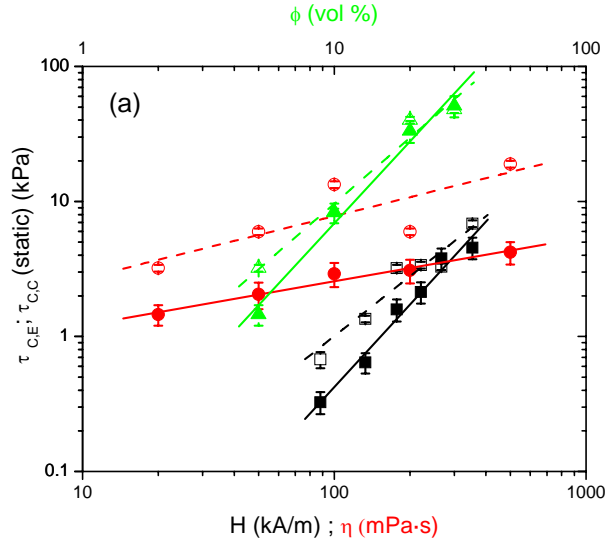


Figure 4.1 Low-strain compressive stresses as a function of magnetic field strength H (squares), dispersing medium viscosity η (circles) and particle volume fraction ϕ (triangles).

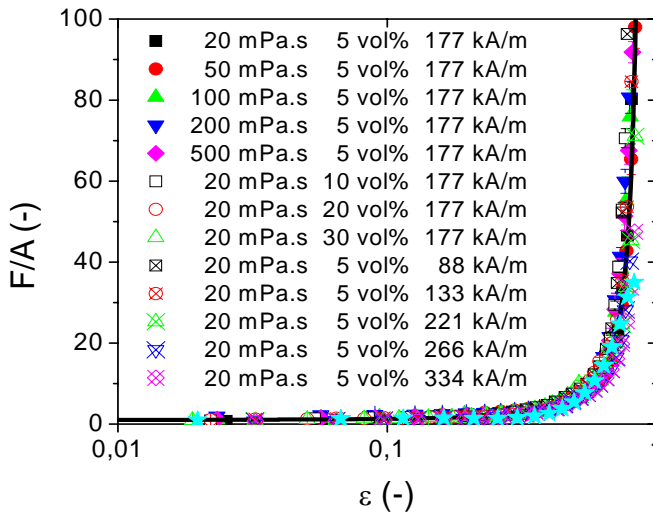


Figure 4.2 Dimensionless normal force as a function of compressive strain ϵ for different magnetic field strength, dispersing medium viscosity and particle volume fraction. Solid line corresponds to the prediction by the continuous media theory for plastic materials Eq. 1. Stars correspond to particle level dynamic simulations.

In order to compare theory, experiments and particle-level simulations, a normalization of the normal force with the low-strain plateau value was carried out. According to equation 2, this normalized normal force must only depend on the elongational strain. As shown in Figure 4.2, experimental data reasonably collapse in a master curve and are in good agreement with both theoretical plastic models and simulations [3, 8].

4.5. Conclusions

A unified description of the behavior of MR fluids in terms of a continuous media theory for plastic materials were proposed. This allowed us to obtain collapsed compression curves for a wide range of magnetic field strengths, medium viscosity and particle concentration. Deviations from the theory were explained in terms of the squeeze strengthening effect. On the one hand, a quadratic dependence with the magnetic field strength (2.0 ± 0.1) and particle concentration (2.0 ± 0.2) was found. On the other hand, a negligible dependence with the continuous phase viscosity was found. Experiments reported here validated another procedure to determine static yield shear stresses when slowly compressing the MR fluids. Particle-level dynamic simulations at large $1 - \varepsilon$ suggest a quadratic volume fraction dependence (1.94 ± 0.22) in good agreement with experimental data.

Acknowledgements

This work was supported by MICINN MAT 2010-15101 project (Spain), and by Junta de Andalucía P10-FQM-5977, P10-RNM-6630 and P11-FQM-7074 projects (Spain). J.A.R.-L. acknowledges financial support by the “Ministerio de Educación: Becas del Programa de Formación del Profesorado Universitario (FPU)” (AP2010-2144).

References

- [1] Havelka K O and Pialet J W 1996 *CHEMTECH* **26** 26.
- [2] de Vicente J, Klingenberg D J and Hidalgo-Álvarez R 2011 *Soft Matter* **7** 3701.
- [3] de Vicente J, Ruiz-López J A, Andablo-Reyes E, Segovia-Gutiérrez J P and Hidalgo-Álvarez R 2011 *J. Rheol.* **55** 753
- [4] Tang X, Zhang X, Tao R and Rong Y 2000 *J. Appl. Phys.* **87** 2634
- [5] Zhang X Z, Gong X L, Zhang P Q, Wang Q M 2004 *J. Appl. Phys.* **96** 2359
- [6] Zhang M L, Tian Y, Jiang J L, Zhu X L, Meng Y G, Wen S Z 2009 *Chin. Phys. Lett.* **26** 048301
- [7] See H 2003 *Rheol. Acta* **42** 86
- [8] Ruiz-López J A, Hidalgo-Álvarez R and de Vicente J 2012 *Rheol. Acta* **51** 595
- [9] Covey G H and Stanmore B R 1981 *J. Non Newtonian Fluid Mech.* **8** 249
- [10] Tang X, Zhang R, Tao R and Rong Y 2000 *J. Appl. Phys.* **87**(5) 2634

Chapter 5.

Simulations of model magnetorheological fluids in squeeze flow mode

José Antonio Ruiz-López, Zuowei Wang, Roque Hidalgo-Álvarez and Juan de Vicente.

This article is under review.

Abstract

A methodology is proposed to simulate the squeeze flow behavior of model magnetorheological (MR) fluids. The model includes Brownian motion and local field corrections. Results are presented for preassembled structures comprising single-particle-width chains, random and lattice structures, and particle suspensions. Calculations are compared to experimental data and a recently developed microscopic model. Single-particle-width simulations predict larger normal stresses than experiments and the micromechanical model. However, simulations on particle suspensions are in much better agreement.

5.1. INTRODUCTION

Magnetorheological (MR) fluids are typically suspensions of magnetizable particles in a liquid carrier fluid. In the presence of a magnetic field, the particles aggregate forming anisotropic structures as a result of interparticle magnetostatic interactions. These structures are behind a rich rheological behavior that spans from a liquid-like system at low fields to a solid-like paste, exhibiting an apparent yield stress, in the presence of sufficiently large fields [Bossis *et al.* (2002); de Vicente *et al.* (2011a); Wereley (2013)].

Currently, there exists an important portfolio of devices incorporating this technology, most of them related to stress transfer control. In these devices, MR fluids are subjected to very complex flows. However, most of the studies reported in the literature concern viscometric flows, and in particular, steady shear flow tests. Very few works have been done involving other kinds of flows (e.g. elongational flows) in spite of the fact that recent investigations on squeeze (i.e. compression) flows demonstrate a significantly larger yield stress than in conventional shearing flows [Havelka and Pialet (1996); de Vicente *et al.* (2011b); Galindo-Rosales *et al.* (2015)]. Undoubtedly, the rheological behavior of MR fluids under compression is not completely understood yet.

During the last decade, several experimental studies have been reported under constant volume operation, creeping flow approximation and for low plasticity numbers (slow speeds) [de Vicente *et al.* (2011b); Ruiz-López *et al.* (2012); Guo *et al.* (2013); Xu *et al.* (2014)]. In these works, experimental data are reasonably well confronted to predictions from continuous media theories in Bingham plastics. These theories lead to a yield compressive stress τ_{YC} that is related to the usual shear yield stress

as follows: $\tau_{YC} = \frac{2}{3} \sqrt{\frac{V}{\pi h_0^3}} \tau_y$, where V is the constant volume, h_0 is the initial gap and τ_y is the shear yield stress. Therefore, the yield compressive stress dependence on the magnetic field strength and the particle volume fraction is solely provided by the dependence of the shear yield stress on these two magnitudes. It is also important to note that if the initial gap is small compared to the initial radius of the sample, $h_0 \ll r_0$, the yield compressive stress can be much higher than the shear yield stress.

Interestingly, previous works demonstrate that the shear yield stress increases during the compression stage due to the so-called strengthening effect [Tang *et al.* (2000)]. This is claimed to be so because chain-like structures become thicker under compression [Becnel *et al.* (2015)]. The strengthening effect was theoretically explained using local field theory by Zhang *et al.* (2004). Recently, the strengthening effect was also explained in terms of the Péclet number [Bigué *et al.* (2015)]

In a recent study, Ruiz-López *et al.* (2015) developed a micromechanical model to explain the rheological properties of MR fluids under slow compression. They found that the yield compressive stress depends linearly on the particle volume fraction and on the magnetic field strength squared: $\tau_{YC} \sim \phi H^2$. The validity of this model is limited to dilute MR fluids at sufficiently small deformations and therefore some deviations with experimental results were obtained at the particle volume fractions used in commercial applications. To get a better insight, in the current manuscript we aim to use particle-level simulations to explore the yielding behavior of MR fluids under compression flows.

Simulations of field-responsive fluids under compression are very scarce in the literature. Simulations for electrorheological (ER) fluids were

carried out by Lukkarinen and Kaski (1996 and 1998) and Kim *et al.* (1999). In these works the compressive stress sharply increases as a function of the compressive strain and the yield compressive stress is higher than the shear yield stress (in accordance with available experimental data). However, these simulations were carried out at a constant voltage and therefore, the electric field strength increases under compression complicating the analysis. To the best of our knowledge there is only one paper dealing with the simulation of MR fluids under compression [de Vicente *et al.* (2011b)]. In this particular study, the external magnetic field strength remains constant during compression facilitating the interpretation of the results. The authors reported particle-level molecular dynamic simulations and satisfactorily confronted these data with experimental results. However, the number of particles in those simulations was scarce due to the non-periodical boundary conditions and results were only obtained at a particle volume fraction of 5 vol %.

In this manuscript we propose a novel particle-level simulation methodology to explore the squeeze flow behavior of MR fluids using periodic boundary conditions and local field corrections. We pay special attention to the influence of particle microstructures in the compressive yield stress as a function of the particle volume fraction. Results are compared to experimental data, continuous media theories and micromechanical models available in the literature [de Vicente *et al.* (2011b); Ruiz-López *et al.* (2015)].

5.2. SIMULATION MODEL

Brownian molecular dynamic simulations were carried out to study the rheological behavior of model MR fluids under slow compression. The

MR fluid was modeled as a suspension of N monodisperse buoyant and inertialess particles with a diameter, σ , in a Newtonian fluid confined in a rectangular box of volume V . The volume of the simulation box is a function of the number of particles N and the particle volume fraction ϕ as follows: $V = \pi\sigma^3 N/6\phi$. We chose a coordinates system centered in the simulation box as shown in the Figure 5.1.

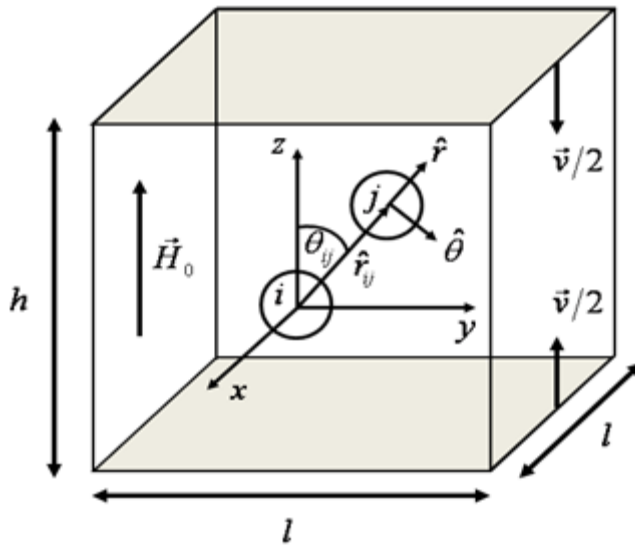


Figure 5.1 Schematics of the simulation box and coordinates systems.

During the compression test, the horizontal plates approach together with a relative constant velocity, v ; the upper plate moves down towards the lower plate with a velocity $-v/2 \hat{z}$ while the lower plate moves up towards the upper plate with a velocity $+v/2 \hat{z}$. Here \hat{z} is the unit vector in the z -direction. Periodic boundary conditions were applied in the vertical walls (x - and y -directions). Stick boundary conditions were applied for particles within a distance to the walls of 0.55σ . These stick boundary conditions could prevent the chain-like structures to move in the

radial direction and therefore the local concentration could increase during compression. In order to make the simulations more realistic, Brownian motion was also included in the simulations to allow the structures to move in the radial direction following the flow. Simulations were run keeping V constant. This means that during the compression, the lateral box length l increases, while the gap between the plates h diminishes according to $l = \sqrt{V/h}$.

For simplicity, magnetostatic interaction was modeled using the point-dipole approximation. Hence, the magnetostatic force between two particles, i and j , separated by a distance, r_{ij} , is given by:

$$\vec{F}_{ij}^{mag} = \frac{3\mu_0\mu_{cr}}{4\pi} \frac{[3(\vec{m}_i \cdot \hat{r})(\vec{m}_j \cdot \hat{r}) - \vec{m}_i \cdot \vec{m}_j]\hat{r} - [(\vec{m}_i \cdot \hat{\theta})(\vec{m}_j \cdot \hat{r}) + (\vec{m}_i \cdot \hat{r})(\vec{m}_j \cdot \hat{\theta})]}{r_{ij}^4} \quad (5.1)$$

where μ_0 is the magnetic permeability of the vacuum, μ_{cr} is the relative magnetic permeability of the continuous medium, \vec{m}_i and \vec{m}_j are the magnetic moments of the particles i and j , respectively, and \hat{r} and $\hat{\theta}$ are the radial and polar angle unit vectors, respectively. In this work, the magnetic moments of the particles are assumed to be of equal strength ($m_i = m_j = m$).

Under the so-called mean-magnetization approximation, the magnetic moments can be expressed as a function of the magnetic field strength [Ruiz-López *et al.* (2015)]: $\vec{m}_i = \pi\sigma^3\beta\vec{H}/2$. Here, β is the so-called contrast factor that depends on the difference between the magnetic permeabilities of the particles and the continuous medium, $\beta = (\mu_{pr} - \mu_{cr})/(\mu_{pr} + 2\mu_{cr})$, μ_{pr} is the relative magnetic permeability of the particles, and \vec{H} is the magnetic field strength. The magnetic field strength was calculated using the Local Field Theory, $\vec{H} = \vec{H}_{loc}$. At the position of the particle i , the local field can be expressed as follows:

$$\vec{H}_{loc,i} = \vec{H}_0 + \sum_{j \neq i}^N \vec{H}_{m_j} \quad (5.2)$$

$$\vec{H}_{m_j} = \frac{3(\vec{m}_j \cdot \hat{r})\hat{r} - \vec{m}_j}{r_{ij}^3} \quad (5.3)$$

where \vec{H}_0 is the external magnetic field, applied in the z -direction, and \vec{H}_{m_j} is the magnetic field produced by the magnetic dipole, \vec{m}_j at the center of the particle i . As the local magnetic field depends on the magnetic moments of the particles and the magnetic moments depend on the local magnetic field, both magnitudes must be solved in a self-consistent manner. Although the magnetic interactions are long-ranged, in order to reduce the total simulation time, a cutoff $r_{c,mag} = l/2$ in the magnetic interaction was included. The external magnetic field used in all the simulations was $H_0 = 177 \text{ kA/m}$ and the contrast factor for this magnetic field strength was estimated from the magnetization curves of typical MR fluids, $\beta = 0.706$ [de Vicente *et al.* (2011b)].

The fluid-particle interaction was simulated by the Stokes law. According to this, the drag force, \vec{F}_i^{hyd} , exerted by the fluid on the particle i , is given by the expression: $\vec{F}_i^{hyd} = -3\pi\eta_c\sigma \left(\frac{d\vec{r}_i}{dt} - \vec{u}_i^\infty \right)$, where η_c is the continuous medium viscosity and \vec{u}_i^∞ is the laminar viscous fluid velocity at the center of the particle i (in the absence of particles). In the squeeze flow mode, under no slip conditions and creeping flow approximation, the velocity of the fluid is given by [Engmann *et al.* (2005)]:

$$\vec{u}_i^\infty = \frac{3v}{4} \frac{\rho_i}{h} \left(1 - \frac{4z_i^2}{h^2} \right) \hat{\rho} + \frac{v}{2} \frac{z_i}{h} \left(3 - \frac{4z_i^2}{h^2} \right) \hat{z} \quad (5.4)$$

where, ρ_i and z_i stand for the cylindrical coordinates of the particle i , and $\hat{\rho}$ and \hat{z} are its corresponding unit vectors. Due to the periodic boundary conditions applied in the simulation box and the radial increase of the

fluid velocity, a particle moving outside the box would have a radial velocity leading the particle into the box and an artificial equilibrium could occur at the edges of the simulation box. However, it is worth to note that the lateral box edges are also moving and it can be shown that the velocity of the lateral side of the box is equal to the average velocity of the fluid at this lateral side. Thus, a particle cannot move outside the box because of the drag force.

An exponential short-range repulsive force was used in order to avoid an overlap between particles and particles and walls, \vec{F}_{ij}^{rep} and \vec{F}_i^{wall} respectively:

$$\vec{F}_{ij}^{rep} = -F_0 \exp[-k(r_{ij} - \sigma)] \hat{r} \quad (5.5)$$

$$\vec{F}_i^{wall} = F_0 \exp[-k(d_i - 0.5\sigma)] \hat{n} \quad (5.6)$$

Here, F_0 is defined as the magnetostatic force between two magnetic dipoles in a head-to-tail configuration aligned in the direction of the external magnetic field (neglecting local field corrections): $F_0 = \frac{3}{16} \pi \mu_0 \mu_{cr} \beta^2 H_0^2 \sigma^2$, k is the stiffness constant of the repulsive force and it was chosen to be $k = 100/\sigma$, d_i is the particle distance to any horizontal wall ($d_i = h/2 - z_i$ for the upper wall and $d_i = h/2 + z_i$ for the lower wall) and \hat{n} is the unit vector normal to the particular wall. Two cutoff radii in the repulsive forces for particles and particles and walls were also applied for particles within a distance of $r_{c,rep} = 2\sigma$ and $r_{c,wall} = \sigma$, respectively.

Overall, the motion of a particle i , is governed by the Langevin equation:

$$3\pi\eta_c\sigma \frac{d\vec{r}_i}{dt} = 3\pi\eta_c\sigma \vec{u}_i^\infty + \vec{F}_i + \vec{f}_B(t) \quad (5.7)$$

where \vec{F}_i is the total force exerted on the particle i , and $\vec{f}_B(t)$ is a random force introduced to mimic the Brownian motion of the particles. The random force was calculated as $f_B \propto \sqrt{3\pi\eta_c\sigma k_B T/\Delta t}$, where k_B is the Boltzmann constant, T is the temperature and Δt is the time variation. In this work we focus on isothermal conditions; the temperature was fixed at $T = 298 \text{ K}$. We used the following scales for the length, force and time: $l_s = \sigma$, $F_s = F_0$ and $t_s = 3\pi\eta_c\sigma^2/F_0$ in order to work in dimensionless units. Equation 5.7 was solved in this work using the Euler algorithm and the time variation was calculated at every step taking into account that the maximum displacement of a particle in any direction is $\Delta x, \Delta y, \Delta z = 0.05\sigma$. The maximum of the time step was imposed to be 10^{-3} in dimensionless units and the approaching velocity of the plates was set at $v^* = 10^{-2}$.

The normal stress in the suspension was estimated as follows:

$$\tau_{zz} = -\frac{1}{V} \sum_{i < j}^N z_{ij} F_{z,ij} \quad (5.8)$$

where z_{ij} is the difference between the z -coordinates of the particles i and j , and $F_{z,ij}$ is the z -component of the total pair-wise force between the particles i and j . However, a more easily accessible experimental observable is the normal force instead of the normal stress. The normal force was calculated in this work using two different approaches. On the one hand, the normal force acting on the upper plate is computed by multiplying the normal stress times the surface area of the plate (l^2). Another possibility is to calculate the normal force by differentiating the magnetic energy with the gap thickness similarly to de Vicente *et al.* (2011b). It is important to remark here that fluctuations in the energy due to the limited number of particles make it difficult to carry out the differentiation [Ahnert and Abel (2007)]. In this work we first fitted the

simulation data to a fourth-order polynomial and then differentiated the polynomial expression.

Three different kinds of simulations were carried out. In the first set of simulations, we compressed single-particle-width chains (having different number of particles) placed at the center of the simulation box. In the second set of simulations, the effect of the increasing local concentration in the normal force, due to the stick boundary conditions, was tested using random and lattice structures. Finally, in the third set of simulations, we compressed collectivities of magnetizable particles randomly distributed in the box. The methodology consisted in two differentiated steps. First, particles within the box were subjected to a suddenly applied magnetic field for structuration. Once the system reached a stationary state, in a second step, a squeeze flow field was superimposed still in the presence of the magnetic field. In both steps, magnetic energy, normal stresses and the average of nearest neighbors were monitored as a function of time. In the second step the normal force acting on the compressing plates (see Figure 5.1) was also calculated from the normal stress distribution acting on it.

5.3. SINGLE-PARTICLE-WIDTH CHAINS

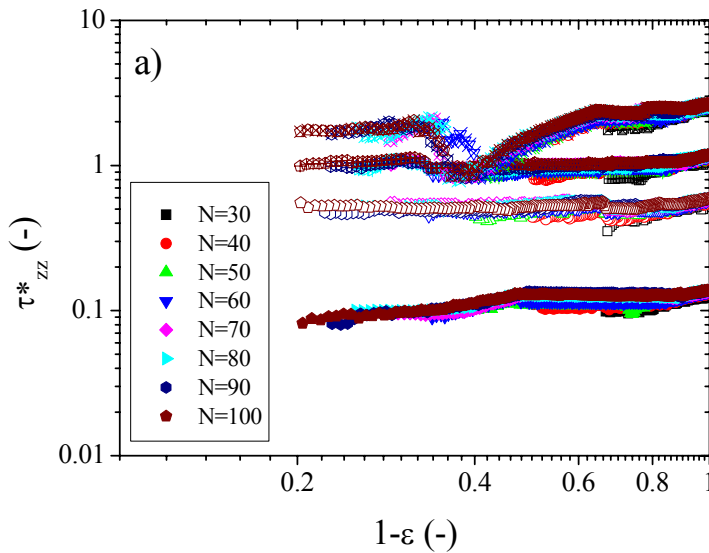
The first simulations to be studied concerned isolated single-particle-width chains. These constitute the simplest structures possible and a first approximation to the squeeze flow behavior of real suspensions. Preassembled chains were initially aligned in the z -direction in head-to-tail configuration spanning the whole separation between plates. Hence, the number of particles in the simulation was proportional to the initial gap between plates according to $N = h_0/\sigma$. Tests were carried out for different number of particles and initial gaps ($N \in [30,100]$) and different

particle loadings ($\phi \in [0.01, 0.20]$). In all simulations the final separation gap was fixed at $h_f = 20\sigma$.

Figure 5.2a depicts the dimensionless normal stress τ_{zz}^* as a function of $1 - \varepsilon$, where $\varepsilon = (h_0 - h)/h_0$ is the compressive strain, at different particle loadings for chains of different lengths. The normal stress seems to be independent on the number of particles in the chain (N) and therefore the initial gap (h_0). The stress remains essentially constant upon compression for the lowest particle concentrations although some jumps are observed at high strains. These jumps can be related to the single-to-double chain transitions especially in the most dilute case where the interaction with other chains is minimal. However, for the highest concentration, $\phi = 0.20$, the stress decreases upon compression for $1 - \varepsilon \approx 0.4$. This different trend can be explained by the fact that single-particle-width chains do not actually exist for this concentration, bearing in mind the particles we consider in the periodical boundary conditions can affect to the stress in the chain. These results suggest that there is a critical concentration at approximately $\phi = 0.10$ above which the hypothesis of single-particle-width chains is not valid. This finding is in good agreement with previous reports in the recent literature involving both experiments and shearing flows [Ruiz-López *et al.* (2015); Segovia-Gutiérrez *et al.* (2012); Fernández-Toledano *et al.* (2014)].

From the inspection of Figure 5.2a, the dimensionless normal stress seems to be linearly dependent on the particle concentration. This result is in good agreement with a recently proposed micromechanical model for squeeze flow Ruiz-López *et al.* (2015). According to this model, the yield compressive stress, obtained in the zero-strain limit, can be written as follows: $\tau_{YC} = \frac{27}{32} \phi \mu_0 \mu_{cr} \beta_a^2 H^2$. Here, β_a is the contrast factor of the aggregates, $H = (1 - \beta\zeta(3)/2)^{-1} H_0$ is the local field of an infinite chain

and ζ is the Riemann Zeta function. Figure 5.2b shows the dimensionless normal stress divided by the dimensionless yield compressive stress from the referred micromechanical model: $\tau_{YC}^* = \frac{9}{2\pi} \phi \frac{\beta_a^2 H^2}{\beta^2 H_0^2}$. Here, β is the contrast factor of the particles. As shown in Figure 5.2b, the dimensionless normal stress reasonably scales with the theoretical compressive yield stress. The variations among all data, for different concentrations and chain sizes, in the zero-strain limit are below 25% suggesting that results reasonably collapse in a master curve. Obviously, deviations become apparent for the largest concentrations as a result interaggregate interactions. These interactions are not included in the micromechanical model.



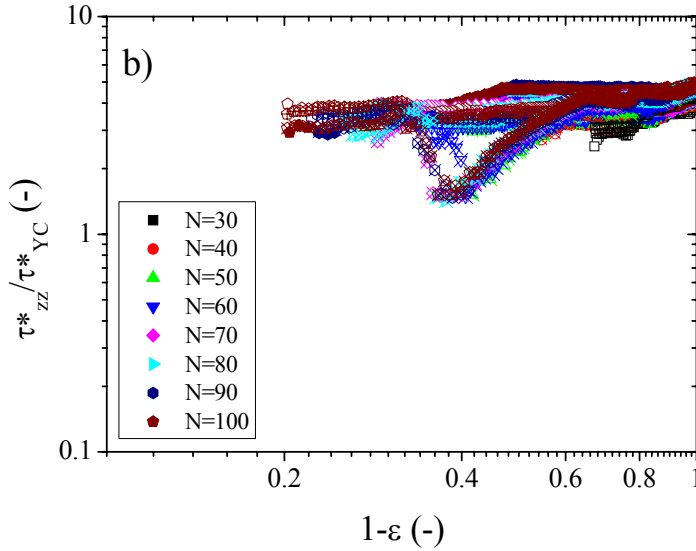


Figure 5.2.- a) Dimensionless normal stress τ_{zz}^* in single-particle-width chains simulations for chains of different lengths ($N \in [30,100]$) and particle loadings ($\phi \in [0.01,0.20]$). b) Dimensionless normal stress divided by the dimensionless yield compressive stress from the micromechanical model by Ruiz-López *et al.* (2015): $\tau_{YC}^* = \frac{9}{2\pi} \phi \frac{\beta_a^2 H^2}{\beta^2 H_0^2}$. Closed symbols: $\phi = 0.01$. Open symbols: $\phi = 0.05$. Vertically and horizontally crossed symbols: $\phi = 0.10$. Diagonally crossed symbols: $\phi = 0.20$.

Next, the normal force F acting on the confining plates was calculated from τ_{zz} by simply multiplying by the surface S (Figure 5.3):

$$F = \tau S = \tau \frac{V}{h} = -\frac{V}{h} \frac{1}{V} \sum_{i \neq j}^N z_{ij} F_{z,ij} = -\frac{1}{h} \sum_{i \neq j}^N z_{ij} F_{z,ij} \quad (5.9)$$

Hence, the normal force is simply the normal stress divided by the gap, and scales as $1 - \epsilon$. Thus, because the normal stress remains essentially constant, the normal force obtained becomes proportional to $1/(1 - \epsilon)$. Similarly to the case of the normal stress, the normal force reasonably collapses onto a master curve for the range of ϕ and N values investigated. This result was expected bearing in mind that the force scale is $F_0 = \frac{9}{8} \mu_0 \mu_{cr} \beta^2 H_0^2 \phi \frac{V}{h_0}$. It is important to remark that the force scale is

proportional to the yield force obtained in the micromechanical model proposed by Ruiz-López *et al.* (2015).

Although the simulations for the normal stress and the normal force scale with both the yield compressive stress and the yield normal forces predicted by theoretical approaches, the simulation dependence on the compressive strain is different to the model. Simulations predict a scaling with $(1 - \varepsilon)^{-1}$ and the theoretical model predicts a scaling with $(1 - \varepsilon)^{-2}$. This can be explained because in the simulations explored till now, the stress remains essentially unaltered during compression as the contact with the surface is only due to one single particle. However, both the experiments and the micromechanical model consider multiple contacts. In these simulations, particles on the sides slip along the gap-spanning chain and hence their contribution to the stress is not important.

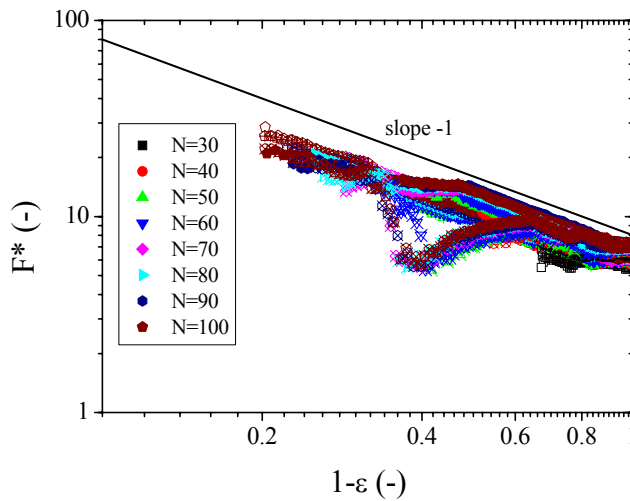


Figure 5.3 Dimensionless normal force F^* as a function of $1 - \varepsilon$ in single-particle-width chains simulations for chains of different lengths ($N \in [30, 100]$) and particle loadings ($\phi \in [0.01, 0.20]$). Closed symbols: $\phi = 0.01$. Open symbols: $\phi = 0.05$. Vertically and horizontally crossed symbols: $\phi = 0.10$. Diagonally crossed symbols: $\phi = 0.20$.

5.4. RANDOM AND LATTICE STRUCTURES

Another important aspect in the simulation performance of MR fluids under squeeze flow could be whether the structures move in the radial direction with the flow or contrarily they are stuck in their initial positions and the local concentration of particles increases under compression. In fact, the normal force can increase upon compression because of two reasons: i.- by an increase in the local concentration of particles, and ii.- by changes in the aspect ratio of the field induced structures under squeeze.

In order to evaluate the effect of local concentration we calculated the normal stress for different preassembled structures at different gaps. In this case, the number of particles was fixed to $N = 3600$ and we considered either the external field strength or the local field theory. In the simulations, the normal surface area of the structures was the same for all the gaps, hence showing the effect of the increase in the local concentration.

Results obtained are included in Figure 5.4. The first observation is that the particular arrangement of the particles either in a lattice or in random distribution is not relevant; the same results are obtained for lattice and random structures. The second observation is that the normal stress strongly depends on the field approximation used. In the case where the external magnetic field is considered, the normal stress monotonically increases under compression. However, when considering the local field, a stress maximum is found for a dimensionless gap distance in between 10 and 20. In practice, such a small separation distance cannot be achieved because of experimental limitations (misalignment between the plates and surface roughness). However, the slope of the normal stress as a function

of gap distance for large gaps is the same for both approximations. This was expected due to the increment of the number of chains. But there were not effects due to the increment of the local concentration. Hence, the effect of the interaction between aggregates (at least at low concentrations) is not important and it is enough to consider only a single chain and then multiplying results by the number of chains.

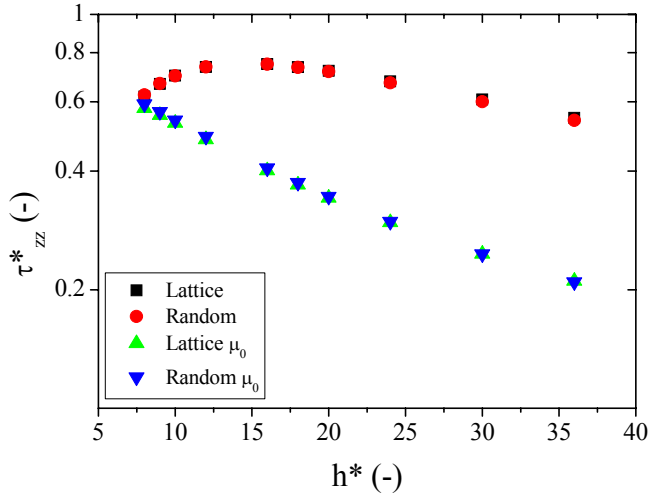


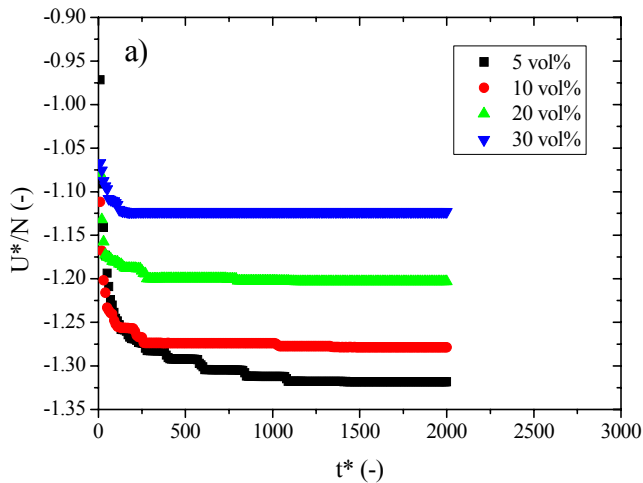
Figure 5.4 Dimensionless normal stress τ_{zz}^* as a function of h^* demonstrating the importance of particle concentration and local field correction in the squeeze flow. Squares and circles: external magnetic field. Triangles: local field correction.

5.5. MAGNETORHEOLOGICAL FLUIDS

5.5.1. Field-induced structuration at rest

As a way of example, magnetic energy, U^*/N , normal stress, τ_{zz}^* , and average nearest neighbors, N_{near}/N , are shown as a function of time during field-driven structuration for MR fluids at a range of particle loadings $\phi \in [0.05, 0.30]$ in Figure 5.5.

For dimensionless times larger than approximately $t^* = 500$ the magnetic energy becomes constant (Figure 5.5a). This suggests that the structure achieves a stationary state for $t^* > 500$. Concomitantly, the stress and average number of nearest neighbors also reach a constant value (Figure 5.5b and Figure 5.5c, respectively). The magnetic energy per particle at the stationary state prior to compression increases upon increasing the particle concentration. This can be explained as the particles cannot find their equilibrium position in the more compact structures generated at higher particle volume fractions. As a consequence, the stress of the system is also higher when increasing the particle volume fraction and obviously the number of nearest neighbors increases when the particle concentration increases. It is important to remark that the average number of nearest neighbours is larger than 2, so the ideal model of single-particle-width chains is not suitable to explain these results even for a $\phi = 0.05$ MR fluid.



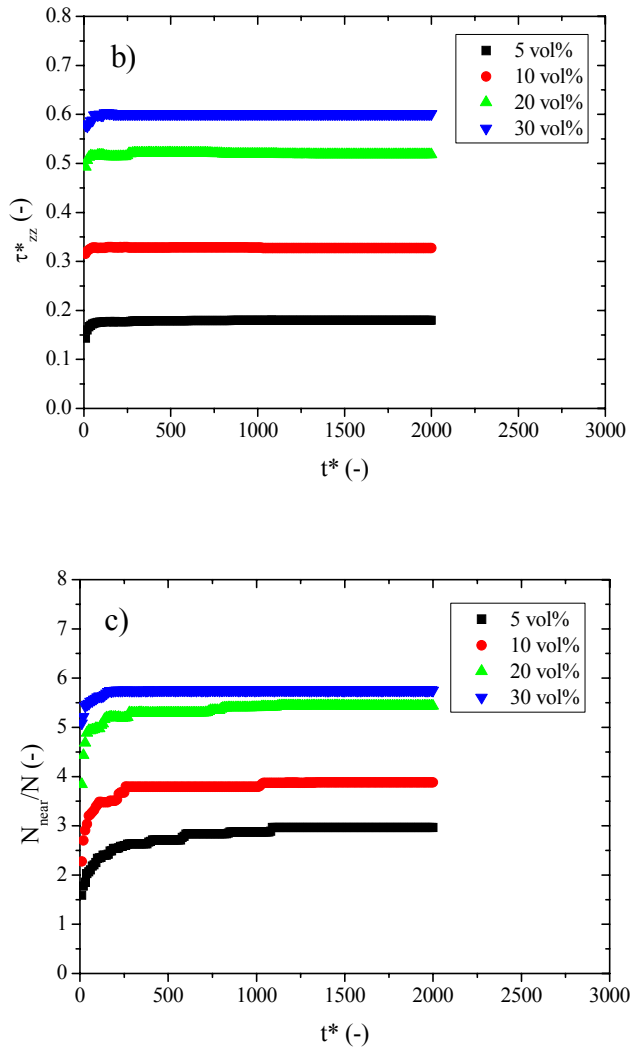


Figure 5.5.- Field-induced structuration of quiescent MR fluids: a) magnetic energy, b) normal stress, c) average nearest neighbors.

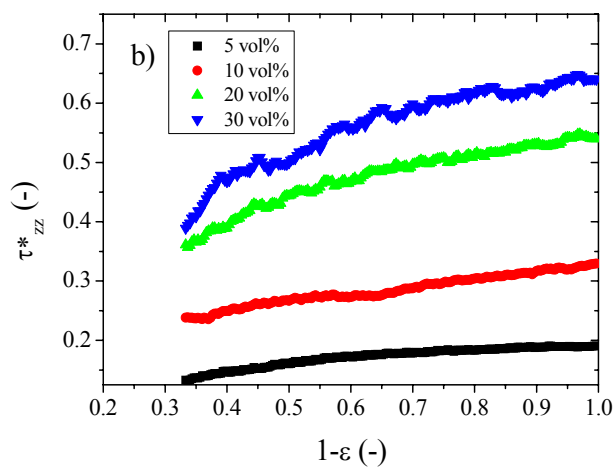
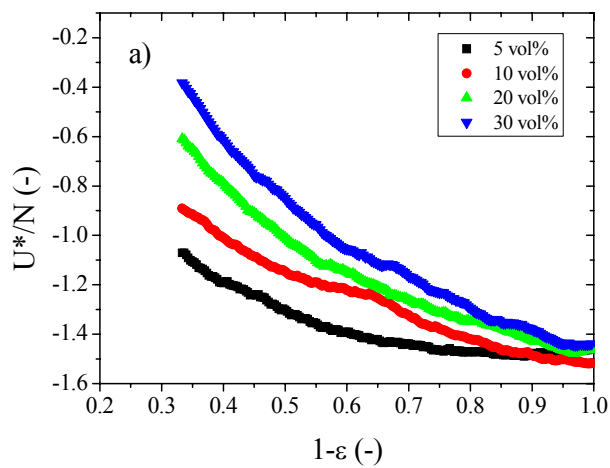
5.5.2 Squeeze flow

In Figure 5.6, magnetic energy, normal stress and average nearest neighbours are shown as a function of $1 - \varepsilon$ during the compression of the MR fluid. Figure 5.6a shows that the magnetic energy increases as the

strain increases. The magnetic energy increases more sharply in the case of higher particle volume fractions than in the case of low concentrations. This result was expected due to the fact that the derivative of the magnetic energy gives the normal force and the later is well known to increase when increasing the particle concentration [Ruiz-López *et al.* (2012); Guo *et al.* (2013); Xu *et al.* (2014)].

In Figure 5.6b, the normal stress is represented as a function of $1 - \varepsilon$. As expected, similarly to the normal stress results for single-particle-width chains, the normal stress increases when increasing the concentration (see Figure 5.2a). Although the normal stress decreases upon compression, the normal surface increases more rapidly, and this will lead to a increasing normal force.

In Figure 5.6c we show the average number of nearest neighbors. For $\phi = 0.05$ the number of nearest neighbors increases upon compression as expected because compression can assist the formation of thicker aggregates. However, for higher concentrations, the number of nearest neighbors initially increases for higher gaps but then decreases. It can be explained due to the fact that thicker aggregates can be formed in the initial stages of compression but for at certain strain, the structure breaks due to the viscous drag and the number of nearest neighbors decreases.



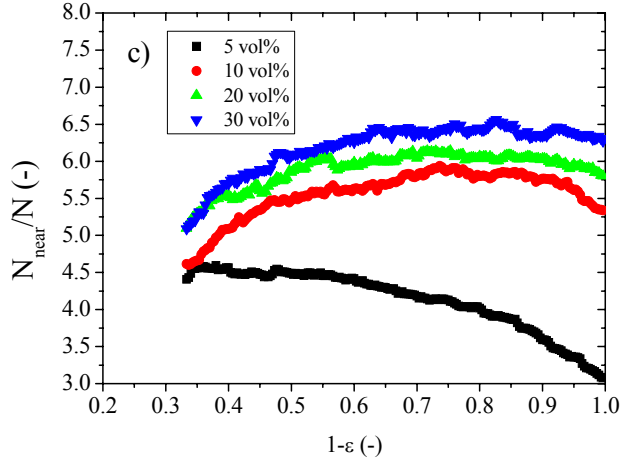


Figure 5.6.- Squeeze flow simulation of MR fluids: a) magnetic energy, b) normal stress, c) average nearest neighbours.

Figure 5.7 represents the compression evolution of the simulated normal force divided by the dimensionless yield normal force predicted by the micromechanical model [Ruiz-López *et al.* (2015)]: $F_Y^* = \frac{9}{2\pi} \phi \frac{\beta_a^2 H^2 v^*}{\beta^2 H_0^2 h_0^*}$. The normal force is calculated using two different procedures: i) by taking the derivative of the energy with the gap [see Equation 23 in de Vicente *et al.* (2011b)] and ii) by using Equation 5.9. The two paths used here to obtain the normal force give very different results especially at the onset of the compression. The normal force obtained by multiplying the normal stress by the surface area is higher than the normal force obtained by taking the derivative of the magnetic energy. However, the normal force obtained by taking the derivative of the magnetic energy increases more rapidly under compression than the normal force obtained by multiplying the normal stress by the surface area. These differences can be explained by the numerical differences of these processes. In order to compare with the micromechanical model the theoretical prediction is also included in Figure 5.7 (see the black line). A slope of -2 is found for the

micromechanical model, simulations from energy differentiation and experimental data.

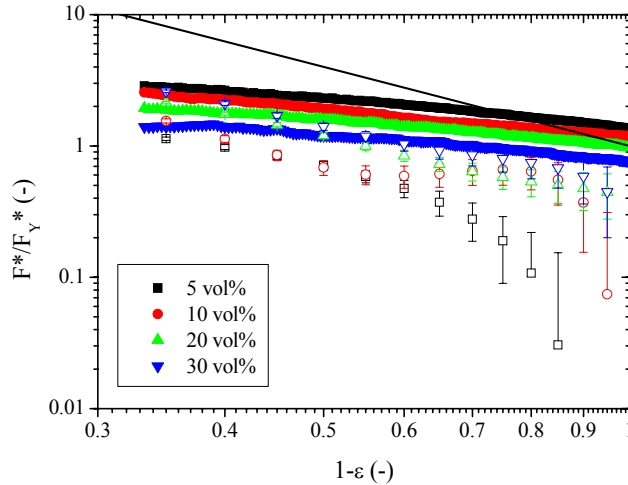


Figure 5.7 Dimensionless normal force F^*/F_Y^* as a function of $1 - \varepsilon$ for MR fluids calculated by the multiplication of the stress by the surface area using Equation 5.9 (closed symbols) and calculated by the derivative of the energy with the gap using Equation 23 in de Vicente et al. (2011) (open symbols). The normal force F^* is divided by the dimensionless yield normal force F_Y^* from the micromechanical model for squeeze: $F_Y^* = \frac{9}{2\pi} \phi \frac{\beta_a^2 H^2 V^*}{\beta^2 H_0^2 h_0^*}$. Black line corresponds to the micromechanical model for squeeze [Ruiz-López et al. (2015)]: $F^*/F_Y^* = 1/(1 - \varepsilon)^2$.

The zero-strain limiting values in Figure 5.7 correspond to the so-called yield compressive stress. Figure 5.8 depicts these yield compressive stresses as a function of the concentration in single-particle-width chain simulations, suspensions simulations and experiments. The micromechanical model prediction is also included for completeness. The yield compressive stress corresponding to single-particle-width chain simulations overestimates suspensions simulations and the theoretical prediction. This implies that the assumption of single-particle-width chains is not plausible whatever the concentration. For the lowest concentrations investigated ($\phi = 0.05$) a good agreement is found

between experiments and suspensions simulations. However, for higher concentrations ($\phi > 0.05$), the yield compressive stress for experiments increases more rapidly than the theoretical and simulated compressive yield stress. Overall, the volume fraction dependence of the yield compressive stress is linear according to the simulations and theoretical prediction. However, experimental data exhibit a larger than linear dependence above $\phi = 0.05$ in good agreement with other experimental works reported in the literature.

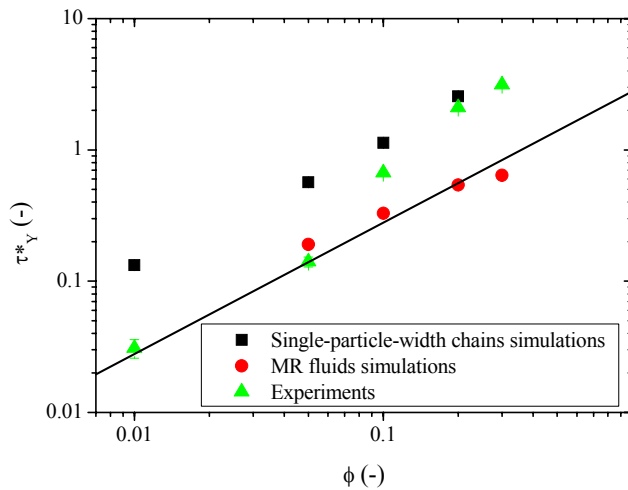


Figure 5.8 Yield compressive stress τ_Y^* as a function of the particle concentration. Squares: simulations in single-particle-width chains. Circles: simulations in MR fluids. Triangles: Experimental data from Ruiz-López et al. (2015).

5.6. CONCLUSIONS

Brownian molecular dynamic simulations were carried out under squeeze flow using periodic boundary conditions for different initial structures: single-particle-width chains, random and lattice structures and initially randomly-distributed particles at different concentrations. Results from

single-particle-width chains showed that the normal force and the compressive stress scales with the particle volume fraction and the magnetic field strength squared, in agreement with the micromechanical model developed by Ruiz-López *et al.* (2015). Random and lattice structures demonstrated that the use of the Local Field Theory in the simulations is important for plate-plate separations below 15σ . Simulations for initially randomly-distributed particles showed that the results are strongly dependent on the method used to calculate the normal force. Two possibilities are explored in this work: either the normal force is calculated from the compressive stress or the normal force is calculated from the derivative of the magnetic energy.

The analytical dependence of the normal force (and the compressive stress) on the compressive strain differed from the micromechanical model and experimental data. This fact was rationalized because the structures interact with the walls at individual points in single particles.

The yield compressive stress was obtained as a function of the particle loading from single-particle-width simulations, initially randomly-distributed particle simulations, experiments and a micromechanical model. As expected, single-particle-width simulations lead to a linear particle-loading dependence of the yield compressive stress in good agreement with the micromechanical model. On the contrary, in experiments, deviations from linearity appear for higher concentrations. Although this discrepancy between micromechanical models and experimental results has been usually explained by the existence of interactions between chain-like structures [e.g. Zhang *et al.* (2004), Ruiz-López *et al.* (2015)], initially randomly-distributed simulations showed that the yield compressive stress increases linearly or even less-than-linearly as a function of the concentration.

Acknowledgements

This work was supported by MAT 2013-44429-R project (Spain) and by Junta de Andalucía P10-RNM-6630, P10-FQM-5977 and P11-FQM-7074 projects (Spain). J.A.R.-L. acknowledges the financial support by the “Ministerio de Educación: Becas del Programa de Formación del Profesorado Universitario (FPU)” (AP2010-2144).

References

- Ahnert, K. and M. Abel, “Numerical differentiation of experimental data: local versus global methods,” *Comput. Phys. Commun.* **117(10)**, 764-774 (2007).
- Becnel, A. C., S. G. Sherman, W. Hu and N. M. Wereley, “Squeeze strengthening of magnetorheological fluids using mixed mode operation”, *J. Appl. Phys.* **117**, 17C708 (2015).
- Bigué, J.P.L, F. Charron and J.-S. Plante, “Understanding the super-strong behaviour of magnetorheological fluid in simultaneous squeeze-shear with the Péclet number”, *J. Intell. Mater. Sys. Struct.* **26(14)**, 1844-1855 (2015).
- Bossis, G., O. Volkova, S. Lacis and A. Meunier, “Magnetorheology: fluids, structures and rheology,” in: S. Odenbach (Ed) *Ferrofluids. Magnetically controllable fluids and their applications (Lecture notes in Physics, 594, Springer-Verlag 2002)* pp 202-230.
- de Vicente J., J. A. Ruiz-López, E. Andablo-Reyes, J. P. Segovia-Gutiérrez and R. Hidalgo-Álvarez, "Squeeze flow magnetorheology," *J. Rheol.* **55**, 753-779 (2011b).
- de Vicente, J., D. J. Klingenberg and R. Hidalgo-Álvarez, "Magnetorheological fluids: a review", *Soft Matter* **7**, 3701-3710 (2011a).

- Engmann, J., C. Servais, and A. S. Burbidge, "Squeeze flow theory and applications to rheometry: A review," *J. Non-Newtonian Fluid Mech.* **132**, 1-27 (2005).
- Fernández-Toledano, J. C., J. Rodríguez-López, K. Shahrivar, R. Hidalgo-Álvarez, L. Elvira, F. M. de Espinosa and J. de Vicente, "Two-step yielding in magnetorheology," *J. Rheol.* **58(5)**, 1507-1534 (2014).
- Galindo-Rosales, F. J., J. P. Segovia-Gutiérrez, F. T. Pinho, M. A. Alves and J. de Vicente, "Extensional Rheometry of Magnetic Dispersions," *J. Rheol.* **59(1)**, 193-209 (2015).
- Guo, C.Y., X. L. Gong, S. H. Xuan, L. J. Qin and Q. F. Yan, "Compression behaviors of magnetorheological fluids under nonuniform magnetic field," *Rheol. Acta* **52(2)**, 165-176 (2013).
- Havelka, K. O., and J. W. Piolet, "Electrorheological technology : The future is now," *CHEMTECH* **36**, 36-45 (1996).
- Heine, M. C., J. de Vicente, and D. J. Klingenberg, "Thermal transport in sheared electro- and magnetorheological fluids," *Physics of Fluids* **18**, 023301 (2006).
- Kim, D. H., S. -H. Chu, K. H. Ahn, and S. J. Lee, "Dynamic simulation of squeezing flow of ER fluids using parallel processing," *Korea-Aust. Rheol. J.* **11(3)**, 233-240 (1999).
- Klingenberg, D. J., F. van Swol, and C. F. Zukoski, "The small shear rate response of electrorheological suspensions. I. Simulation in the point-dipole limit," *J. Chem. Phys.* **94**, 6160-6169 (1991).
- Klingenberg, D. J., F. van Swol, and C. F., Zukoski, "Dynamic simulation of electrorheological suspensions," *J. Chem. Phys.* **91**, 7888-7895 (1989).
- Lukkarinen, A., and K. Kaski, "Computational studies of compressed and sheared electrorheological fluid," *J. Phys. D: Appl. Phys* **29**, 2729-2732 (1996).

-
- Lukkarinen, A., and K. Kaski, "Simulation studies of electrorheological fluids under shear, compression, and elongation loading," *J. Appl. Phys.* **83(3)**, 1717-1725 (1998).
- Ruiz-López, J. A., R. Hidalgo-Álvarez and J. de Vicente, A micromechanical model for magnetorheological fluids under slow compression, submitted (2015).
- Ruiz-López, J.A., R. Hidalgo-Álvarez and J. de Vicente, "On the validity of continuous media theory for plastic materials in magnetorheological fluids under slow compression," *Rheol. Acta* **51(7)**, 595-602 (2012).
- Segovia-Gutiérrez, J. P., C. Berli and J. de Vicente, "Nonlinear viscoelasticity and two-step yielding in magnetorheology: A colloidal gel approach to understand the effect of particle concentration," *J. Rheol.* **56(6)**, 1429-1448 (2012).
- Tang, X., X. Zhang, R. Tao, and Y. Rong, "Structure-enhanced yield stress of magnetorheological fluids," *J. Appl. Phys.* **87(5)**, 2634-2638 (2000).
- Wereley N. 2013 *Magnetorheology : Advances and Applications*: Royal Society of Chemistry.
- Xu, Yangguang, X. Gong, T. Liu and S. Xuan, "Squeeze flow behaviors of magnetorheological elastomers under constant volume", *J. Rheol.* **58(3)**, 659-679 (2014).
- Zhang, X. Z., X. L. Gong, P. Q. Zhang, and Q. M. Wang, "Study on the mechanism of the squeeze-strengthen effect in magnetorheological fluids," *J. Appl. Phys.* **96(4)**, 2359-2364 (2004).

Part II. Model

magnetorheology: inverse
ferrofluids

Chapter 6.

Model magnetorheology: a direct comparative study between theories, particle-level simulations and experiments, in steady and dynamic oscillatory shear

José Antonio Ruiz-López, Juan Carlos Fernández-Toledano, Daniel Klingenberg, Roque Hidalgo-Álvarez and Juan de Vicente.

This article is under review

Abstract

We investigate model magnetorheological fluids (inverse ferrofluids) under both steady and dynamic oscillatory shear. Analytical theories, particle-level simulations and magnetorheometry are used in an attempt to obtain universal master curves. Steady shear flow data can be collapsed when plotted as a function of a dimensionless Mason number. The critical Mason number associated to the transition from magnetostatic to hydrodynamic control of the suspension structure is demonstrated to linearly increase with particle concentration in good agreement with theories and our simulations. Experimental linear viscoelastic moduli are in good agreement with micromechanical and macroscopic models in the

dilute regime. However, upon increasing particle concentration, theoretical predictions underestimate experimental data while particle-level simulations are in good agreement. The accordance with particle-level simulations suggests that the mean (average) magnetization approximation gives a good prediction and multibody and hydrodynamic forces are not expected to play a crucial role in the shear flow behavior of model magnetorheological fluids.

6.1. INTRODUCTION

Magnetorheological (MR) fluids are magnetic-field responsive colloids that exhibit a dramatic change in their rheological properties upon the application of an external magnetic field. In practice they exhibit a “liquid-to-solid” transition for sufficiently large Λ ratios (i.e. ratio between the magnetostatic energy to the thermal energy). This field-induced transition is currently exploited in many commercial applications [Rabinow (1948); Parthasarathy and Klingenberg (1996); Ginder (1998); Klingenberg (2001); Vekas (2008); Olabi and Grunwald (2008); Park *et al.* (2011); de Vicente *et al.* (2011a)].

Traditionally, MR fluids are grouped in conventional MR fluids that consist in carbonyl iron microparticles dispersed in a non-magnetic carrier fluid, and inverse ferrofluids that consist in non-magnetic microparticles dispersed in a ferrofluid. In both cases, (spherical) particles (either being magnetic or not) aggregate under magnetic fields forming field-directed structures that strongly affect the fluid flow and hence the rheological properties of the colloid at the macroscale [de Gans *et al.* (1999a); de Gans *et al.* (1999b); Volkova *et al.* (2000); Bossis *et al.* (2002); Saldivar-Guerrero *et al.* (2006); Ramos *et al.* (2010), Ramos *et al.* (2011); de Vicente (2013)].

Conventional MR fluids are clearly preferred in commercial applications because of the exceedingly large MR effect if compared to inverse ferrofluids; the response of inverse ferrofluids is severely limited by the saturation magnetization of the ferrofluid. However, inverse ferrofluids are preferred as model magnetic suspensions when exploring the driving physical mechanisms associated to the yielding and flow regimes. This is so because: i) in inverse ferrofluids the magnetic permeability difference between particles and carrier fluid is generally small and therefore, the interaction between particles can be approximated in terms of dipoles located at the centers of the particles [Fujita and Mamiya (1986)]; ii) in the case of inverse ferrofluids magnetic moments are co-linear with the external field at any field strength; iii) remanence and multipolar interactions complicate the use of conventional MR fluids in model studies [Skjeltorp (1983)]. For these reasons, in this work we will employ inverse ferrofluids as model magnetorheological fluids.

The size of the non-magnetic particles constituting inverse ferrofluids has been demonstrated in the past to play a significant role in their shear flow behavior [de Gans *et al.* (2000); Ramos *et al.* (2011)]. Below a certain size (approx. 100 nm diameter), chainlike structures induced by the field are not long enough to connect the bounding surfaces and a purely shear thinning behavior prevails. For these particularly small sizes Brownian and depletion forces come into play as the ferrofluid is not a continuum anymore. On the contrary, for larger particle sizes the rheological behavior seems to be essentially independent on the particle size [de Gans *et al.* (2000)]. In this work we are interested in inverse ferrofluids constituted by large enough silica particles where gap spanning structures necessarily exist.

Generally speaking two of the main variables that determine the MR response are magnetic field strength and particle concentration. While the former has been extensively investigated in the past and seems to be currently well understood [Ginder (1998); Klingenberg (2001); Klingenberg *et al.* (2007); de Vicente *et al.* (2011a)], the understanding of the later in the MR performance is still not complete. The reason for this is probably the lack of reliable and sufficient data for a wide range of particle concentrations. In the particular case of conventional MR fluids, Volkova *et al.* (2000) found that both static and dynamic yield stresses increase monotonically with the particle concentration. For the larger concentrations employed, a faster than linear increase was reported. On the other hand, experiments by Segovia-Gutiérrez *et al.* (2012) demonstrate that material functions such as the apparent yield stress and the storage moduli rapidly increase with particle loadings below 10 vol% and then continue increasing but at a lower rate for concentrations larger than 10 vol%. Recently, a *two-step yielding* has been proposed to explain this different trend in behavior that occurs as a result of the interplay of short-range attractive interactions [Fernández-Toledano *et al.* (2014)]. In the case of inverse ferrofluids the effect of particle loading has been scarcely investigated and in many cases the monodispersity of the non-magnetic particles is not assured. Volkova *et al.* (2000) did not arrive at a clear conclusion about the volume fraction dependence of the static yield stress. However, they found that the dynamic yield stress exhibited a maximum (or saturates) for concentrations of approximately 30 vol%. This maximum was explained in terms of macroscopic models and is in disagreement with micromechanical ones that predict a linear increase because according to them the yield stress is proportional to the number of percolating chains. Unfortunately, only four concentrations were explored and therefore it becomes difficult to get sound conclusions. One of the

goals of this manuscript is to get a deeper understanding of the effect of particle concentration in highly monodisperse inverse ferrofluids.

Available micromechanical models and theories in magnetorheology are restricted to the case of dilute systems (generally lower than ≈ 1 vol%) where interaggregate interactions can be neglected. As a result, their applicability is severely limited because most of the applications involve highly concentrated suspensions (generally larger than ≈ 10 vol%). A possibility to address this issue is through a particle-level simulation approach. Particle-level simulations have been extensively used in the past to get a better understanding of the physical mechanisms underlying the MR effect [e.g. steady shear flows in Chen *et al.* (1995) and Lager *et al.* (2014, 2015); rotating fields in Melle *et al.* (2003); poiseuille flow in Pappas and Klingenberg (2006); heat transfer mechanisms in Heine *et al.* (2006); effect of non-magnetic interparticle forces in Klingenberg *et al.* (2010); bidisperse suspensions in Kittipoomwong and Klingenberg (2005); squeeze flows in de Vicente *et al.* (2011b); polydisperse MR fluids in Fernández-Toledano *et al.* (2015)]. These simulations are most frequently done under Stokes drag approximation and neglecting multibody and multipolar interactions [Melrose and Heyes (1993); Lager *et al.* (2015)]. In spite of the many simplifications within particle-level simulations, predictions agree qualitatively with experimental data reported in the literature. However, in the vast majority of cases, experimental systems used for the comparison were not appropriate because of remanence and multipolar interactions (conventional MR fluids are generally used), and the effect of particle loading was not studied (comparisons are typically done at only one concentration that is chosen for convenience). In general, simulation models underestimate the viscosities of conventional MR (and ER) fluids and this is not surprising as the point dipole model underestimates the magnetic interactions.

Imposing more realistic electro and magnetostatics on the point dipole configurations improves the comparison. Besides this, comparisons with experiments and theories are very scarce and limited.

Current simulation models are based on a mean (average) magnetization approximation according to which the magnetic force on a spherical particle can be treated as the force on a magnetic dipole of strength equal to the volume times the magnetization of the sphere. This approximation is exact in two limiting scenarios: i) when the particles are saturated, ii) when the particles are isolated in the presence of a uniform magnetic field [Klingenberg *et al.* (2007)]. However, in many circumstances, these conditions are not achieved. In this work we also aim to elucidate the validity of this approximation by direct comparison of particle-level dynamic simulations to experiments on inverse ferrofluids. With respect to inverse magnetorheological fluids, Ramos *et al.* (2010, 2011) carried out a systematic experimental investigation on monodisperse inverse ferrofluids. They demonstrated a very good agreement with analytical predictions for the lower concentrations investigated in steady [Ramos *et al.* (2011)] and linear dynamic oscillatory shear [Ramos *et al.* (2010)]. Unfortunately, only three particle loadings were studied and the comparison of either experimental data or theoretical predictions with numerical simulations was not done. Another goal of this manuscript is to ascertain the applicability range of particle-level simulations to explore whether these simulations are capable of explaining the mechanical behavior of model MR fluids (in steady and unsteady shear flow) at high concentrations.

In this contribution we employ analytical theories, Brownian molecular dynamic simulations and torsional rheometry to extensively explore the rheological properties in steady and dynamic oscillatory shear of model

MR fluids (highly monodisperse inverse ferrofluids) at different magnetic field strengths and especially in a very wide range of particle loadings. The minimum particle loading investigated will be given by the sensitivity of the MR device (~ 1 vol%). On the other hand, the maximum particle concentration will be limited by the poor redispersibility of the suspension at high loadings (20 vol%). For the suspensions investigated in this work, the so-called Lambda ratio (i.e. the ratio between magnetostatic to thermal energy) ranges from 10 to 1000.

The manuscript is structured as follows. First we will review the theoretical models and simulation techniques employed in this work. Then we will describe the preparation of the model MR fluids and experimental rheological techniques. Finally, the experimental, theoretical and simulation results will be compared and discussed.

6.2. ANALYTICAL THEORIES

In this section, we review some of the existing theories and models published in the MR literature. We classify these models in two groups. Those named as "macroscopic" come from magnetic energy minimization principles and assume a bi-continuous structure consisting of spheroidal, cylindrical or layered particle aggregates [Rosensweig (1995); Bossis *et al.* (1997)]. A second group is formed by "microscopic" models including single-width particle chains sheared under an external field [Martin and Anderson (1996); de Vicente *et al.* (2004); de Gans *et al.* (1999a); Volkova *et al.* (2000)].

In all analytical models considered in this manuscript, the ferrofluid is assumed to be a continuous phase on the length scale of the diameter of the dispersed non-magnetic particles. The shear stress is dominated by the magnetostatic interactions between the non-magnetic particles, and shear-

induced deformation is assumed to be affine. Furthermore, field-induced structures are assumed not to interact between them. The latter assumption restricts the applicability of these models to low particle concentrations (dilute limit).

Most analytical theories predict a Bingham-like plastic behaviour under steady shear flow. In dimensionless form, this equation can be written:

$$\frac{\eta}{\eta_{\infty}} = 1 + \frac{\text{Mn}^*(\phi)}{\text{Mn}} \quad (6.1)$$

where, Mn is the so-called Mason number which is a dimensionless shear rate that can be defined as the ratio of hydrodynamic and magnetostatic forces acting on the particles. In the linear magnetization regime, the Mason number reads as follows [de Vicente *et al.* (2011a)]:

$$\text{Mn} = \frac{8\eta_c \dot{\gamma}}{\mu_0 \mu_{cr} \beta^2 H_0^2} \quad (6.2)$$

Here, η_c is the continuous phase (ferrofluid) viscosity, η_{∞} is the field-independent high-shear viscosity, $\dot{\gamma}$ is the magnitude of the shear rate tensor, μ_0 is the permeability of vacuum, μ_{cr} is the relative permeability of the continuous phase, $\beta = (\mu_{pr} - \mu_{cr}) / (\mu_{pr} + 2\mu_{cr})$ is the contrast factor, μ_{pr} is the relative permeability of the particles, H_0 is the external magnetic field strength, and $\text{Mn}^*(\phi)$ is a critical Mason number (see below). In the case of inverse ferrofluids β can take values between -0.5 (low fields) and 0 (large fields). Other definitions for Mn exist that are especially useful for conventional MR fluids away from linearity [Klingenberg *et al.* (2007)]. However, in the case of inverse ferrofluids Equation 6.2 works extraordinarily well because the mean magnetization

of the particle remains $\langle M_p \rangle = 3\beta H_0$ for a very wide range of magnetic field strengths [Ramos *et al.* (2010); Ramos *et al.* (2011); Ruiz-López *et al.* (2015)].

The critical Mason number $Mn^*(\phi)$ determines the transition from magnetisation to hydrodynamic control of suspension structure. It exactly corresponds to the intersection of the linear fall of the $\log(\eta/\eta_\infty)$ versus $\log Mn$ with the horizontal line representing the high shear viscosity plateau. Interestingly, it solely contains the volume fraction dependence of MR fluids under flow. Concretely, according to existing (microscopic) micromechanical models, the volume fraction dependence is captured by η_∞ and ϕ according to the following expression [de Vicente *et al.* (2011a)]:

$$Mn^*(\phi) = C \frac{\phi \eta_c}{\eta_\infty} \quad (6.3)$$

where different values for C are derived in the literature depending on specific assumptions and/or simplifications in the mechanical stability conditions in the problem; Martin and Anderson (1996) ($C = 8.82$), de Vicente *et al.* (2004) ($C = 8.485$), de Gans *et al.* (1999a) ($C = 5.25$), and Volkova *et al.* (2000) ($C = 1.91$). In all case, the C coefficients given in parentheses have been calculated assuming the bare point-dipole approximation although in some of the original models multipolar corrections are provided. These micromechanical models have shown to qualitatively explain experimental data for a wide range of MR fluids [Volkova *et al.* (2000); Saldivar-Guerrero *et al.* (2006); Ramos *et al.* (2011)]. A linear dependence with the volume fraction is strictly expected

for $Mn^*(\phi)$ in the case of dilute suspensions because in this case

$$\lim_{\phi \rightarrow 0} \eta_{\infty} = \eta_c.$$

Recently, Berli and de Vicente (2012) developed a structural viscosity model for magnetorheology to account for typical deviations from the Bingham model predictions. According to this model, the steady shear flow behavior is rationalized in terms of a constitutive equation that, in its general form, reads:

$$\frac{\eta}{\eta_{\infty}} = \left[\frac{1 + (Mn/Mn^*)^{1/2}}{(\eta_{\infty}/\eta_0)^{1/2} + (Mn/Mn^*)^{1/2}} \right]^2 \quad (6.4)$$

This equation was successful in explaining a low shear viscosity plateau that is frequently observed in inverse ferrofluids, and a smoother transition from the magnetostatic to the hydrodynamic dominated regime with respect to the classical Bingham model. However, when interparticle magnetic interactions are very strong the low shear viscosity plateau value (if exists) is exceedingly large and hence it becomes very difficult to be observed within the experimental time scales typically explored. As a consequence, an apparent yield stress and a plastic-like behavior come up. Actually, expanding Equation 6.4 for $\eta_0 \gg \eta_{\infty}$, the following expression is obtained:

$$\eta/\eta_{\infty} = 1 + (Mn/Mn^*)^{-1} + 2(Mn/Mn^*)^{-1/2} \quad (6.5)$$

It can be demonstrated that Equation 6.5 is a dimensionless form of the Casson plastic equation. This new model provides a more gradual transition from the pre-yield to the flow region as is otherwise experimentally observed in many experiments [Wang and Gordaninejad (1999); Gabriel and Laun (2009); Berli and de Vicente (2012)]. Finally, it is worth to stress here, that under this framework, the critical Mason

number, $Mn^*(\phi)$, contained in Equations 6.1 and 6.5 physically corresponds to an apparent (Bingham or dynamic) yield stress τ_y that in the linear regime scales with $\propto \mu_0 \mu_{cr} \beta^2 H_0^2$ [de Vicente *et al.* (2011)]. Hence, a larger yield stress under field always results in a larger $Mn^*(\phi)$. According to our definition of Mn , both Equation 6.1 and Equation 6.5 correspond to:

$$Mn^*(\phi) = \frac{8\tau_y}{\mu_0 \mu_{cr} \beta^2 H_0^2} \frac{\eta_c}{\eta_\infty} \quad (6.6)$$

There are currently a large number of analytical models in magnetorheology compatible with the existence of an apparent yield stress -for a recent review on yield stress theories we refer to Ramos *et al.* (2011)-. An overview of some of these models is included in Table 6.1. The yield stress is the result of interparticle forces. Therefore, for the field range investigated here, a convenient way to describe the yielding properties of MR fluids is by using the normalized yield stress defined as $\tau_{y,n} = \tau_y / (\mu_0 \mu_{cr} H_0^2)$. On the one hand, macroscopic models only take into account the shape anisotropy of the strained aggregates under small deformation. Three different macroscopic model structures are tested in this work: spheroidal, cylindrical and layered particles aggregates. Following Bossis *et al.* (1997) we will make the following simplifications and assumptions. i.- we will assume a random close packing of spheres within the aggregates ($\phi_a = 0.64$). ii.- we will also assume an aspect ratio for the aggregates of 10, and iii.- a mean field theory (Maxwell-Garnett theory in this case) will be used in the calculation of the permeability of the aggregates and the inverse ferrofluid. On the other hand, micromechanical models involve a microscopic description of the aggregates where interparticle forces are considered. All micromechanical

models predict a yield stress, which linearly depends on volume fraction and, in contrast to macroscopic models, quadratically on the contrast factor.

The understanding of MR fluids in the dynamic regime is also of outstanding interest, especially in commercial applications. The material functions most commonly employed in the description of the viscoelastic properties of MR fluids are the (normalized) linear viscoelastic moduli defined as $G'_n = G' / (\mu_0 \mu_{cr} H_0^2)$ and $G''_n = G'' / (\mu_0 \mu_{cr} H_0^2)$. There are also a large number of analytical models in the literature for the prediction of, particularly, the storage modulus (see Table 6.1). These analytical theories have been thoroughly tested against rheological measurements on inverse ferrofluids [Saldivar-Guerrero *et al.* (2006); Ramos *et al.* (2010)]. The effect of magnetic field strength in the linear viscoelastic regime is well known in the literature on inverse ferrofluids. In fact, experimental data are reported to collapse reasonably well when scaled with $\mu_0 \mu_{cr} \beta^2 H_0^2$ [Saldivar-Guerrero *et al.* (2006); Ramos *et al.* (2010) and references therein]. Conversely, the effect of particle concentration is definitely not well understood. Typically, material functions scale with ϕ at low particle concentrations

Table 6.1 Overview of the different micromechanical and macroscopic models for magnetorheology. $\tau_{y,n} = \tau_y / (\mu_0 \mu_{cr} H_0^2)$. $G'_{0n} = G'_0 / \mu_0 \mu_{cr} H_0^2$. ϕ is the non-magnetic particle volume fraction. $\phi_a = 0.64$ is the packing fraction of the particles within the aggregates. n_1 and n_2 are the demagnetization factors in the directions parallel and perpendicular to the magnetic field, respectively. $\phi_s \equiv \phi / \phi_a$, $\tilde{\mu}_a = (\mu_a / \mu) - 1$ is the relative permeability difference between the aggregate (μ_a) and the inverse ferrofluid (μ). ζ represents the Riemann function and k_3 is defined as $k_3 = \left(1 - \frac{k}{4} - \frac{k^2}{8}\right)^{-1}$, $k = \zeta(3)\beta = 1.202\beta$

	Authors	$\tau_{y,n} = \tau_y / (\mu_0 \mu_{cr} H_0^2)$	$G'_{0n} = G'_0 / \mu_0 \mu_{cr} H_0^2$
Micromechanical	Klingenberg and Zukoski (1990)	$\tau_{y,n,KZ} = 1.026\phi\beta^2$	$G'_{0n,KZ} = \frac{9}{2}\phi\beta^2$
	Martin and Anderson (1996)	-	$G'_{0n,MA} = \frac{9}{4}\zeta(3)\phi\beta^2 k_3$
	de Gans <i>et al.</i> (1999a)	$\tau_{y,n,dG1} = 1.11\phi\beta^2$	$G'_{0n,dG} = \frac{3}{4}\zeta(4)\phi\beta^2 \left\{ 2 \left[1 - \frac{\beta\zeta(3)}{2} \right]^{-2} + \left[1 + \frac{\beta\zeta(3)}{2} \right]^{-2} \right\}$
	de Vicente <i>et al.</i> (2005)	-	$G'_{0n,dV1} = \frac{9}{8}\frac{\phi}{\phi_a}\beta^2$; $G'_{0n,dV2} = \frac{1}{2}\frac{\phi}{\phi_a}\frac{(\mu_a - 1)^2}{\mu_a + 1}$
	Macroscopic	Spheroidal aggregates Bossis <i>et al.</i> (1997)	$\tau_{y,n,S} = -0.32\phi_s \frac{1+2\phi\beta}{1-\phi\beta} \tilde{\mu}_a \left(\frac{1}{1+\tilde{\mu}_a n_2} - \frac{1}{1+\tilde{\mu}_a n_1} \right)$
Cylindrical aggregates Rosensweig (1995), Bossis <i>et al.</i> (1997)		$\tau_{y,n,C} = 0.32\phi_s (\mu_a / \mu_c - 1)^2 \frac{1-\phi_s}{2 + (\mu_a / \mu_c - 1)(1-\phi_s)}$	$G'_{0n,C} = \phi_s (\mu_a / \mu_c - 1)^2 \frac{1-\phi_s}{2 + (\mu_a / \mu_c - 1)(1-\phi_s)}$
Layered aggregates Rosensweig (1995), Bossis <i>et al.</i> (1997)		$\tau_{y,n,L} = 0.32\phi_s (\mu_a / \mu_c - 1)^2 \frac{1-\phi_s}{1 + (\mu_a / \mu_c - 1)(1-\phi_s)}$	$G'_{0n,L} = \phi_s (\mu_a / \mu_c - 1)^2 \frac{1-\phi_s}{1 + (\mu_a / \mu_c - 1)(1-\phi_s)}$

However, when the particle concentration increases, a larger dependence with ϕ is typically found that is not predicted by neither microscopic nor macroscopic approaches. More important, to the best of our knowledge, experimental data and theoretical predictions for steady and dynamic oscillatory shear have not been directly compared to particle-level simulation data yet.

6.3. Particle-level simulations

In this work we consider Brownian molecular dynamic simulations already described in a previous work by Fernández-Toledano *et al.* (2015) but restrict ourselves to monodisperse MR fluids. Briefly, the MR fluid was composed by $N = 1000$ neutrally buoyant hard spheres of diameter σ immersed in a Newtonian continuous phase with a viscosity η_c and confined between two parallel walls. The particles are displaced by solving the Langevin equation:

$$M \frac{d^2 \vec{r}_i(t)}{dt^2} = -\zeta \left(\frac{d\vec{r}_i(t)}{dt} - \vec{u}_i^\infty \right) + \vec{F}_i + \vec{f}_B(t) \quad (6.7)$$

where M is the mass of the particles, $\vec{r}_i(t)$ is the position of particle i at the time t , $\zeta = 3\pi\eta_c\sigma$ is the friction coefficient, \vec{u}_i^∞ is the ambient fluid velocity at the center of particle i , and $\vec{f}_B(t)$ is a random force introduced to model the Brownian motion of the particles $f_B \propto \sqrt{\kappa_B T \zeta / \Delta t}$. Here, κ_B is the Boltzmann constant, T is the absolute temperature and Δt is the time step.

In general, the motion of the sphere i is governed by the sum of the magnetostatic polarization forces under the field, the interaction of the

particle with other particles and the walls, and the hydrodynamic resistance. Point-dipole approximation is used here to calculate magnetic forces using the mean magnetization approximation. Therefore, multipolar interactions are neglected. The dimensionless magnetic field strength was fixed to $H_0^* = 150$. Stokes' law is used to approximate the hydrodynamic force acting on each sphere with a dimensionless friction coefficient of $\zeta^* = 722.1$ [Fernández-Toledano *et al.* (2015)]. Hence, hydrodynamic interactions are also neglected. Models that incorporate hydrodynamic interactions are generally restricted to small numbers of particles in monolayers and in this work we are interested in 3D simulations involving a large number of particles. A recent publication by Lager and co-workers demonstrates that only if the hydrodynamic stress constitutes the main contribution to the total stress, a coupled model might be necessary since the hydrodynamic contribution might be overestimated in the pure discrete element method (DEM) model [Lager *et al.* (2015)]. A quasi-hard sphere exponential model is used to mimic the short range repulsive forces between particles-walls and particles-particles. Contrary to stiff power law repulsions, this particular interaction force predicts the formation of thick aggregates in agreement with experimental observations reported in the literature [Melrose and Heyes (1993); Segovia-Gutiérrez *et al.* (2013)]. The dimensionless temperature was fixed at $T^* = k_B T / F_B \sigma = 0.1$. Here, F_B is the force scale, taken as the magnetostatic force considered for a magnetic field of 200 A/m [see Fernández-Toledano *et al.* (2015) for details].

We consider two shearing flows: stress growth tests (start-up tests) and unsteady oscillatory shear tests. In both cases, we switch-off the Langevin thermostat in the direction in which non-conservative external forces are applied. In this way, the momentum is conserved in the shear direction

and we recovers momentum conservation in the shear direction, while conserving the temperature by applying the thermostat the others directions. The detailed computation of the stress tensor under these flows can be also found in Fernández-Toledano *et al.* (2015).

In the start-up tests, the steady shear stress is calculated by averaging the large-strain value of the stress tensor in 500 configurations over the strain of $\gamma = 2$ to $\gamma = 10$. The long time (large strain) stress value is taken here as the steady stress corresponding to the fixed shear rate. In unsteady oscillatory shear tests, the measurements are taken after 10 cycles to safely overcome initial transients. The frequency used in the simulations of oscillatory flow was 0.021 Hz in real units. According to the normalization used in this work, this particular frequency corresponds to a reduced frequency of $\omega^* = 0.2$. However, using the Klingenberg (1993) scaling, the result is $\omega_K^* = 0.014$ that is two orders of magnitude lower than the transition frequency. Experimental dimensionless frequency using the Klingenberg scaling depends on the magnetic field and is ranged within $\omega_K^* \in [0.06, 0.37]$. Although experimental dimensionless frequency is in general higher than the frequency used in simulations, the frequency dependence is expected to be insignificant since all the frequencies studies in this manuscript are below the transition frequency reported in Klingenberg (1993). Due to the inclusion of the inertial term and the Brownian motion in the equation of movement, the calculation of the particles positions is quite expensive. Therefore, we select this value for the frequency because it is affordable for computer simulations and also from the experimental point of view. The time step in all simulations was set as $\Delta t^* = 10^{-4}$ in order to capture the inertia time scale as explained in Fernández-Toledano *et al.* (2015).

The simulation technique employed here has successfully predicted a wide range of experimental observations on MR and ER fluids. However, none of the experimental systems employed in those previous works can be considered to be model systems in the sense that multipolar, remanence and other colloidal interactions exist as well and therefore a full quantitative agreement was never found.

6.4. EXPERIMENTAL

6.4.1. Materials

Tetraethyl orthosilicate (TEOS) (Acros Organics, 98%), ethanol absolute (Scharlau, reagent grade), ammonia (Scharlau, solution 32%), and ultrapure distilled water (Milli-Q Academic, Millipore) were used for the synthesis of silica nanoparticles. The ferrofluids were purchased from Ferrotec Co. They have a density of 1120 kg/m^3 , an initial magnetic susceptibility of 1.81, a saturation magnetization of 25.5 kA/m and a shear viscosity of $44 \text{ mPa}\cdot\text{s}$. The magnetic properties of the ferrofluids used in this work are summarized in Figure 3 in Ramos *et al.* (2010) and in Table III in Ramos *et al.* (2011) and the magnetization curve is included in the Supplemental material (see Figure S6.1). These data were used in the calculation of the β parameter.

6.4.2. Synthesis of silica particles

Two kinds of spherical monodisperse silica nanoparticles with number diameters of $\sigma_n = 248$ (S200) and 689 nm (S600) were prepared by condensation polymerization of tetraethyl orthosilicate (TEOS) using the Stöber method [Stöber and Fink (1968)] as follows. Absolute ethanol, ammonia, and water were mixed in a 500 mL reaction vessel. Then TEOS was added quickly and the reaction mixture was stirred at 350 rpm at

room temperature during 1 day. The molar concentration of the mixed solution determined the desired size of silica nanoparticles. In this case, the molar concentrations were water/ammonia = 2.49/1.06 and 7.01/3.00 for S200 and S600 respectively. The volume of absolute ethanol was adjusted in each reaction up to 500 mL, and the concentration of TEOS was fixed to 0.2 M. Silica nanoparticles were collected by centrifugation (15,000 rpm, 15 min) and washed by repeating redispersion in absolute ethanol three times. The final product was dried in vacuum oven at 80 °C for 24 h. The most relevant particle size results are shown in Table 6.2.

Silica Particle	σ_n (nm)	σ_w (nm)	σ_v (nm)	PDI
S200	248	251	255	1.044
S600	689	690	691	1.004

Table 6.2 Number, weight-, and volume-average diameters ($\sigma_n, \sigma_w, \sigma_v$) and polydispersity indices (PDIs) of synthesized silica nanoparticles.

6.4.3. Preparation of inverse ferrofluids

Inverse ferrofluids were prepared as follows: 1) First, silica powders and ferrofluids were mixed. 2) Next, the suspension was ultrasonicated for 5 min. 3) Finally, the sample was manually stirred for another 10 min. Steps 2) and 3) were repeated to get a homogeneous dispersion. Suspensions therefore prepared were found to be stable, and phase separation was not observed over the course of several days. The volume fractions of silica nanoparticles ranged from 1 vol% to 25 vol% assuming a silica density of 2.64 g/mL. Lower concentrations did not provide significant torque to obtain reproducible data in the rheometer. On the other hand, larger concentrations did not result in kinetically stable dispersions and the redispersibility was hard. Also, the mean distance between particles was too small for the continuum approach to hold.

6.4.4. Magnetorheometry

Rheology tests were carried out using parallel disks (diameter 20 mm, gap thickness 300 μm) in a MCR 501 stress-controlled Anton Paar rheometer with the MRD180 magnetorheology fixture. In this assembly, the magnetic field is applied perpendicular to the plates in the velocity gradient direction. External magnetic field strengths investigated ranged from 17 to 354 kA/m. All the tests reported in this contribution were carried out under isothermal conditions (25 $^{\circ}\text{C}$).

Steady shear flow tests were performed using the following protocol: (i) precondition at a constant shear rate of 100 s^{-1} for 30 s, (ii) suspension is left to equilibrate for 1 min, (iii) shear stress is logarithmically increased at a rate of 10 points/decade from 0.1 to 1000 Pa. The tests were stopped if the shear rate exceeded 1000 s^{-1} . The acquisition time was 5 s per data point. Once the resulting strain was measured, the apparent viscosity was calculated by dividing the applied shear stress, calculated at the rim of the plates, by the shear rate. We used stress instead of strain control tests to obtain the flow curves because the effect of duration time used in ramp-up rate of stress is not as severe as in the case of strain controlled experiments, in agreement with Ekwebelam and See (2008). Precautions were taken for the measurements to be as close as possible to the steady state [for further details see Ramos *et al.* (2011)]. Viscosity curves of the inverse ferrofluids in the absence of magnetic fields are shown in the Supplemental material (Figure S6.2).

Dynamic oscillatory strain amplitude sweep tests were performed at a frequency of 1 Hz. The experimental procedure is summarized as follows: (i) precondition at a constant shear rate of 100 s^{-1} for 30 s, (ii) suspension is left to equilibrate for 1 min, (iii) strain amplitude is logarithmically increased at a constant excitation frequency (1 Hz). Then the resulting

stress and phase lag between strain and stress signals are measured, and from them both storage modulus, G' , and loss modulus, G'' , are calculated. The storage and loss moduli were apparently not dependent on the frequency used in the accessible range with the device (from 0.01 Hz to 100 Hz).

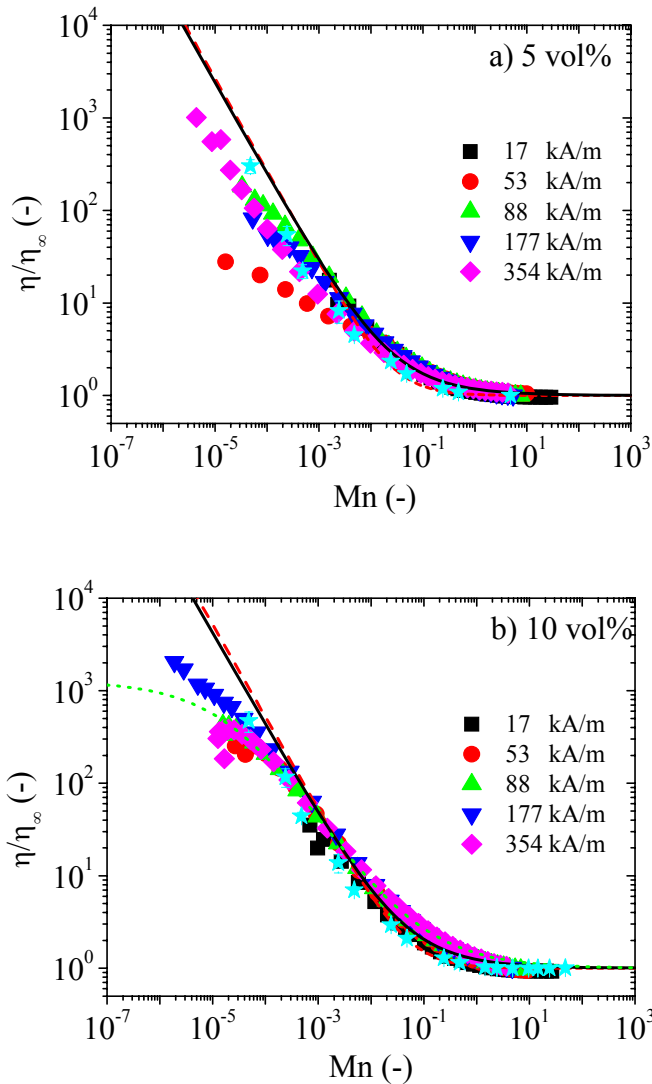
When desired, a magnetic field was applied during steps (ii) and (iii). To check reproducibility, in all cases, experiments were repeated at least three times with fresh new samples. Error bars will not be shown in the figures below if the uncertainty falls within the symbol size.

6.5. RESULTS AND DISCUSSION

6.5.1. Viscosity curves: magnetic field strength dependence

As a way of example, Figure 6.1 contains some results for steady shear tests in dimensionless form for S600 suspensions (results for S200 are very similar as demonstrated in the Supplementary material, Figure S6.3). Inspection of Figure 6.1 reveals that all experimental data under shear, for various silica contents and magnetic field strengths, reduce to a master curve when the relative viscosity (η/η_∞) is plotted as a function of the Mason number (Mn). This was expected because the silica particles within the inverse ferrofluids essentially interact through dipolar magnetostatic interactions. Furthermore, this scaling demonstrates that inverse ferrofluids formulated in this work do actually serve as model MR fluids and the mean magnetization approximation applies [Klingenberg *et al.* (2007); Ruiz-López *et al.* (2015)]. As observed, the collapse is worse for the less concentrated suspension (5 vol%) because the torque signal is lower here and therefore the error is larger. In any case, as expected, contrary to Figure 6 in Klingenberg *et al.* (2007), the lowest viscosities in

Figure 6.1 are not associated to larger fields. Generally speaking viscosity curves move downwards for larger fields when scaling is not appropriate. A marked shear thinning trend is found in a wide range of Mn values in good agreement with theoretical predictions. For large enough concentrations, the viscosity at low Mn flattens out as discussed in previous works [Ramos *et al.* (2011); Berli and de Vicente (2012)].



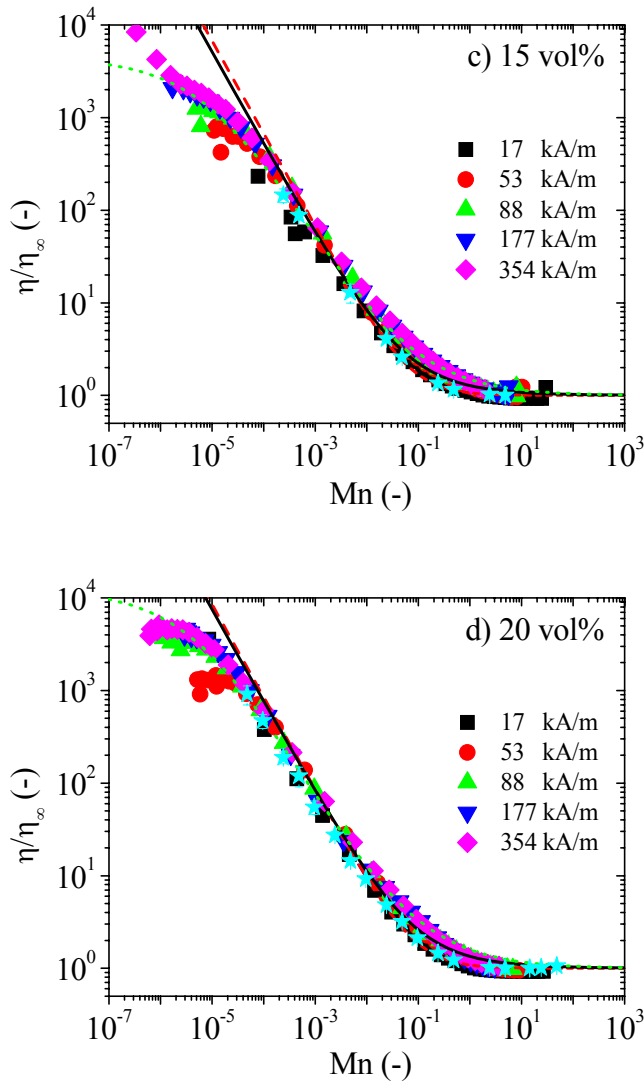


Figure 6.1 Dimensionless viscosity (η/η_∞) as a function of the Mason number (Mn). Experimental data on inverse ferrofluids prepared with S600 silica particles are represented as solid symbols. Lines correspond to theoretical predictions: Black solid line corresponds to Berli and de Vicente predictions (Equation 6.5). Red dashed line corresponds to Bingham predictions (Equation 6.1). Green dotted lines correspond to the full structural model of Berli and de Vicente (Equation 6.4). Cyan stars correspond to particle-level simulations.

Apart from experimental data, in Figure 6.1 we also include best fittings to theoretical predictions. Black solid lines correspond to the classical Bingham model (Equation 6.1) and red dashed lines correspond to the Berli and de Vicente model (Equation 6.5). For completeness we also include green dotted lines that correspond to regression fitting results for the full structural model of Berli and de Vicente (Equation 6.4). As observed, experimental data are reasonably well described with all of the theoretical models used. The full structural model is definitely needed to capture the low shear viscosity plateau, for the most concentrated inverse ferrofluids, and the Casson model is needed to better fit the transition region. As expected, the Bingham model overestimates the experimental data at low shear and underestimates them in the transition region. These findings are in good agreement with Berli and de Vicente (2012).

In Figure 6.1 we also include simulation data (cyan star symbols). Again, the simulation approach that was followed in this work does not predict a low shear viscosity plateau. For this to occur, the no-slip condition should be modified. In spite of the many simplifications in the model, simulated viscosity data seem to be in very good agreement with experiments. A good agreement is also observed for the S200 inverse ferrofluid (see Supplementary information, Figure S6.3). No free fitting parameters are needed to construct simulation data contained in Figure 6.1. Generally speaking, a good agreement is found between experiments, simulations and analytical theories under steady shear flow for all particle loadings explored.

As stated in the Introduction, the performance of an MR fluid essentially depends on two variables: the magnetic field strength and the particle loading. From the inspection of Eqs. 1, 4 and 5, it is clear that the field dependence is fully captured by Mn (within the field range explored) and

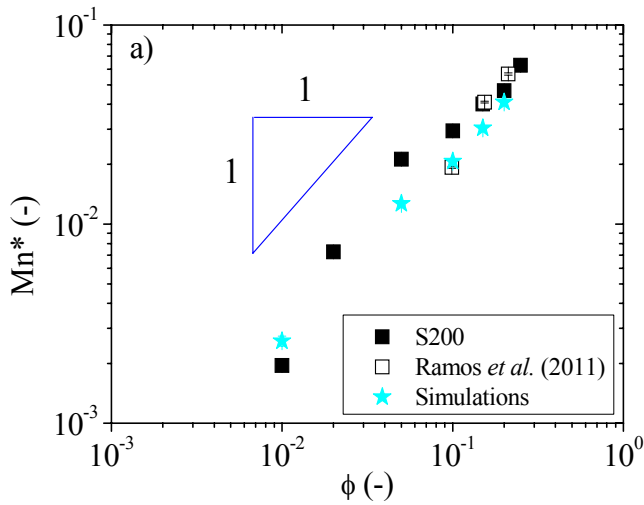
the loading dependence is solely contained in Mn^* . The field dependence is demonstrated in Figure 6.1 and has been extensively reported in the literature [e.g. Marshall *et al.* (1989)]. Next we aim to study the concentration dependence within Mn^* which in its turn is clearly less understood.

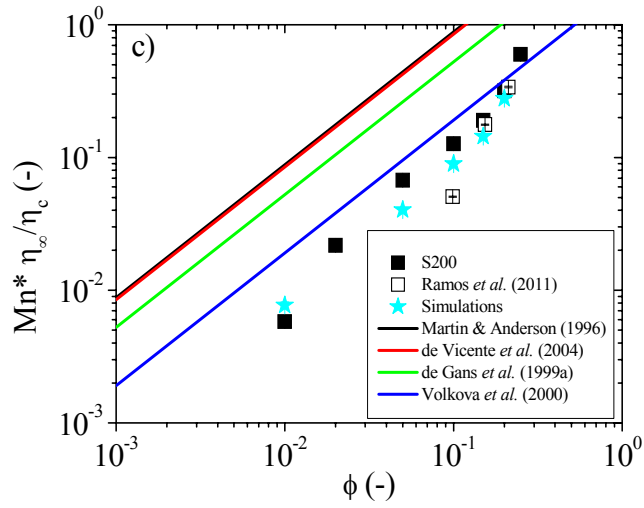
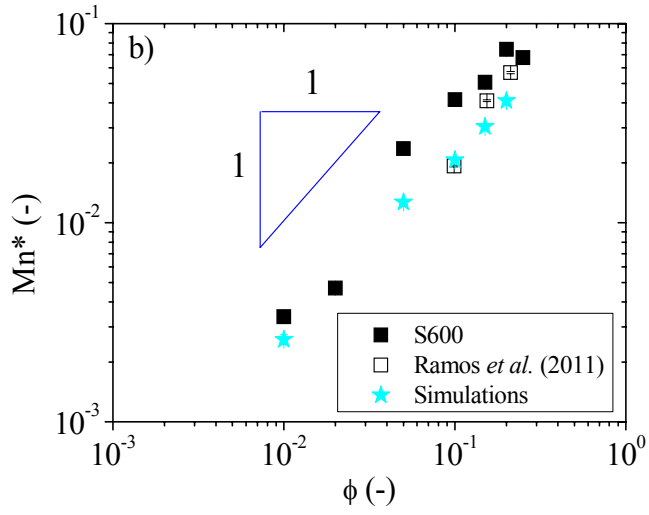
Importantly, any difference in the shear flow behavior of any MR fluid is given by the Mn^* parameter only. This means that the difference in the flow behavior resides only in the way the *transition* from magnetostatic to hydrodynamic control of the suspension structure occurs. Actually, all MR fluids should scale in the same curve by simply rescaling the X-axis as a new dimensionless number Mn/Mn^* [see Berli and de Vicente (2012)]. However, it is important to remark here, that Mn^* is, a priori, dependent on the specific formulation of the MR fluid and in particular contains the particle concentration dependence. Next we aim to interrogate the volume fraction dependence of Mn^* using analytical theories, simulations and experiments.

6.5.2. Critical Mason number: concentration dependence

The critical Mason number Mn^* was obtained by fitting the experimental and simulation data with the form of dimensionless viscosity (η/η_∞) as a function of the Mason number (Mn). Of course, the particular value of Mn^* depends on the fitting equation employed. However, differences are minimal and within experimental error when using Equation 6.4 and Equation 6.5. It is worth to stress again that the Mn^* value is analogous to a dynamic yield stress following the terminology by Volkova *et al.* (2000) and Ramos *et al.* (2011) in contrast to the so-called static yield stress which is typically smaller in these systems [see Figure 9 in Ramos *et al.* (2011)].

In Figure 6.2 we show the Mn^* obtained from fitting the Berli and de Vicente plastic equation (Equation 6.5). Equation 6.5 is used for the fitting because it has been reported that a better accordance with the experimental data exists in the transition regime when using this equation if compared to the classic Bingham model. These data are shown as a function of concentration ϕ in log-log representation. The standard deviation, which is calculated with averages for measurements at five different magnetic field strengths, falls within the symbol size and are indications of the confidence of the fit. In Figure 6.2a we show the results for S200 particles, while in Figure 6.2b we show the results for S600 particles. Together with experimental data, we also include experimental data reported by Ramos *et al.* (2011) (755 nm in diameter) and particle-level simulation data.





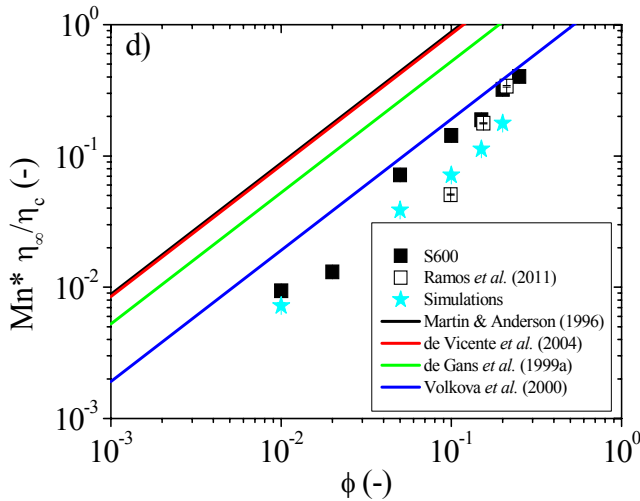


Figure 6.2 Volume fraction dependence of Mn^* as obtained from fittings to Berli and de Vicente plastic equation (Equation 6.5). a) and b) Mn^* versus ϕ for S200 and S600 respectively. c) and d) $Mn^* \frac{\eta_\infty}{\eta_c}$ versus ϕ for S200 and S600 respectively. The error bars in the figures are obtained from the average to all field strengths.

As expected from inspection of Figure 6.1, a reasonably good collapse is observed. Experiments are in good agreement with previous literature data and simulation results. As anticipated above, we can appreciate a quasi-linear slope ($Mn^* \propto \phi$). However, for the largest concentration (25 vol%), in the case of S600 particles, the experimental slope slightly decreases (c.f. Figure 6.2b). This can be explained because the linear dependence is expected at low loadings where $\eta_\infty = \eta_c$. For larger concentrations, η_∞ can become noticeably larger than η_c and therefore the dependence of Mn^* with particle loading becomes smaller (cf. Equation 6.3). A similar volume fraction dependence of Mn^* has been reported on ER fluids by Marshall *et al.* (1989) and on inverse ferrofluids by Ramos *et al.* (2011). However, in both cases the number of volume

fractions investigated was too low to get sound conclusions and a comparison to simulation data was missing.

Figures 6.2c and 6.2d compare all experimental and simulation data to micromechanical model predictions [Martin and Anderson (1996), de Vicente *et al.* (2004), de Gans *et al.* (1999a), and Volkova *et al.* (2000)]. For this aim, in these Figures 6.2c and 6.2d we show $Mn^* \eta_\infty / \eta_c$ versus ϕ . This kind of representation corrects the volume fraction dependence of η_∞ and allows a direct comparison to micromechanical models. As observed, experiments and simulations data do exhibit a linear slope (power law behavior) in good agreement with micromechanical models. All micromechanical models predict a yield stress that scales linearly with the volume fraction of the particles. This is due to the fact that interchain interactions are neglected in the models. Recalling the fact that the magnetic moment scales linearly with the particle volume, the yield stress, and consequently Mn^* , is found to be independent of particle size. In general, micromechanical models in steady shear flow overestimate the experimental and simulation data. The fact that micromechanical models usually overestimate the experimental data on inverse ferrofluids is not novel as was reported by Ramos *et al.* (2011) and de Gans (1999a). The model that more closely fits the experimental and simulation data is the one by Volkova *et al.* (2000). This finding is in agreement with experiments reported by Ramos *et al.* (2011) (see Figure 6.3b in their paper) and suggests that the particular hydrodynamic stress considered in the model is crucial for a better comparison.

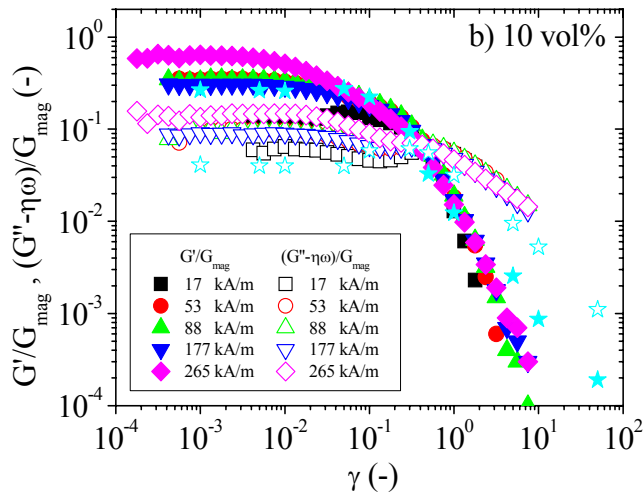
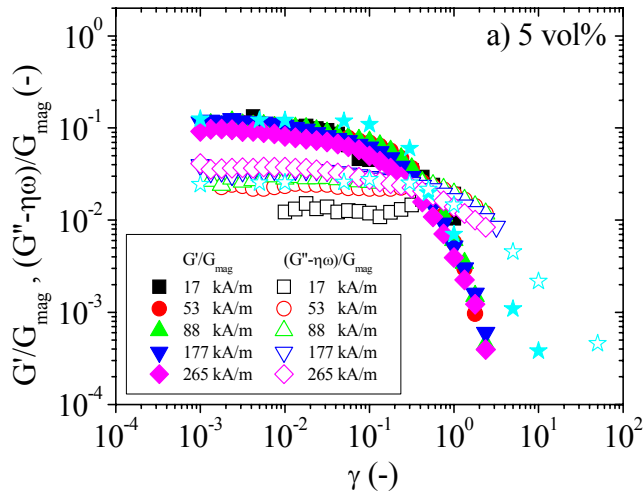
The data were also fit with the Bingham model and the results are shown in the Supplementary material (Figure S6.4). Results are qualitatively similar and therefore not included in this manuscript. It is also worth to remark here that the comparison to macroscopic models is not possible

under the frame of Figure 6.2 because the β dependence of the yield stress according to these models is not quadratic [see Table 6.1].

As shown above, the simulation results in steady shear are in reasonably good agreement with experimental and theoretical calculations. To better appreciate the goodness of this comparison, we next employ oscillatory shear flow to again compare simulation data with experiments and theoretical models. Strain amplitude sweep tests are used to explore the non-linear region as well, contrary to de Gans *et al.* (1999b) and Ramos *et al.* (2010) where only linear viscoelastic data are reported.

6.5.3. Dynamic oscillatory shear

Figure 6.3 depicts the normalized storage and loss moduli as a function of strain amplitude for a constant frequency for a range of different silica (S600) concentrations from 5 vol% to 20 vol%. For a direct comparison with simulation data, experimental viscoelastic moduli are normalized by $G_{mag} = \mu_0 \mu_{cr} \beta^2 H_0^2$ and the contribution of the dispersing medium to the loss modulus was subtracted since it is not considered in simulations ($G''_p = G'' - \eta\omega$). When increasing the volume fraction, both storage and loss moduli increase. This is expected because more gap spanning and compacted aggregates appear.



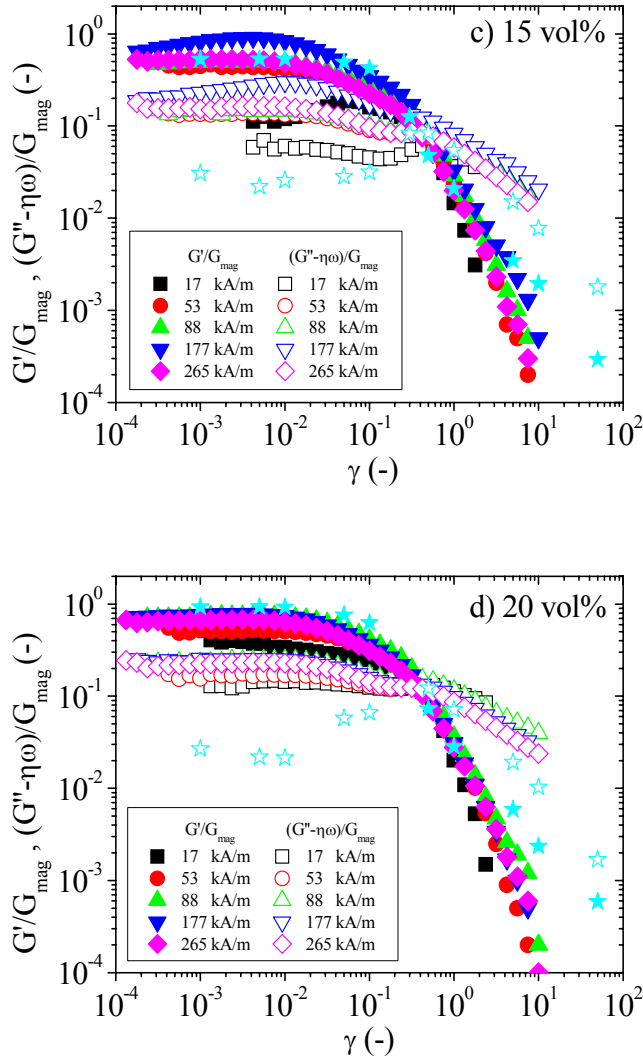


Figure 6.3 Strain amplitude sweep oscillatory shear data normalized by $G_{mag} = \mu_0 \mu_{cr} \beta^2 H_0^2$. The "non-magnetic" contribution was subtracted to the total loss modulus: $G'' - \eta\omega$. Here, η was estimated using Quemada expression $\eta = \eta_c (1 - \phi/\phi_a)^{-2}$ with $\phi_a = 0.64$. Symbols correspond to experimental measurements at different magnetic field strengths. Cyan stars correspond to particle-level simulations. Excitation frequency: 1 Hz in experiments and 100 Hz in simulations. Below 5 vol% the storage modulus remains lower than the loss modulus.

The presence of these aggregates would store more energy hence increasing the storage modulus and also generate a stronger viscous dissipation. In general, the loss modulus embeds contributions from: i) magnetic field-driven structuration, ii) interparticle solid friction and iii) hydrodynamic forces [Ramos *et al.* (2010)].

The inspection of Figure 6.3 reveals that, as expected, the normalized experimental data for various silica contents and magnetic field strengths reduce to a master curve when the normalized viscoelastic moduli are plotted as a function of the strain amplitude. Also, a good agreement is found for the storage and loss moduli between experimental data and simulation results, especially in the low strain amplitude regime and for the less concentrated suspensions. For larger concentrations (≥ 10 vol%), the simulated loss moduli become remarkably smaller than the experimental values. It could be explained because hydrodynamic interactions are not satisfactorily included in the simulations. The simulated storage modulus decreases at a lower rate at high strains compared to the experimental values. Currently we do not have an explanation for this observation.

A. *Linear viscoelastic regime*

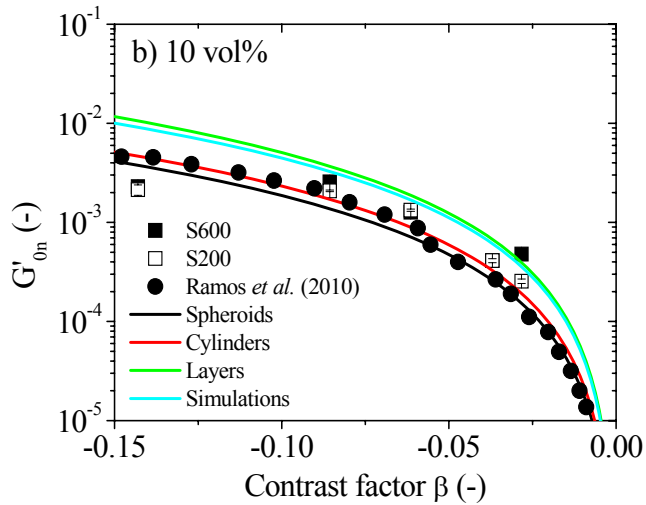
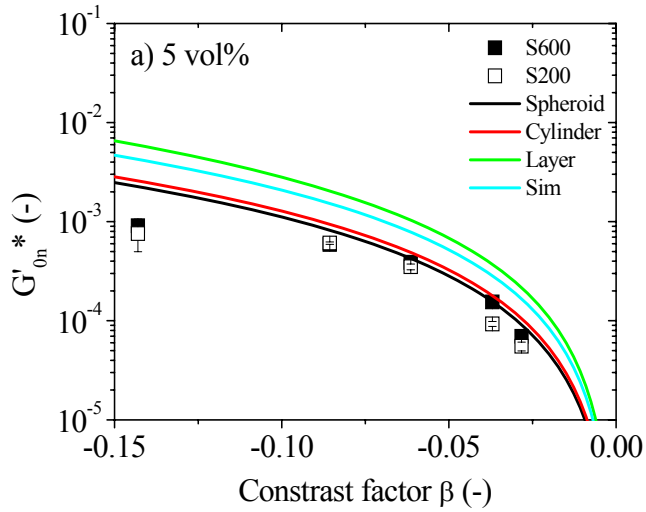
To get a better understanding of the behavior in the linear viscoelastic region, in Figure 6.4 we show the normalized low strain storage modulus $G'_{0n} = G'_0 / \mu_0 \mu_{cr} H_0^2$ as a function of the contrast factor β for different concentrations. The contrast factor β is tuned by changing the magnetic field strength and therefore the ferrofluid permeability. Together with the experimental data we also show experimental data from the literature, macroscopic model theories and simulation data. In general, a good agreement is found between experiments, theories and simulations bearing

in mind the error in the measurements. Similarly to Ramos *et al.* (2010), the macroscopic spheroidal model captures well the observed trend, especially for the less concentrated suspensions. However, upon increasing the particle concentration, the macroscopic theoretical models tend to underestimate the experimental results. It is believed that this discrepancy comes from the presence of mutual interactions between particle aggregates. At this stage it is worth to note that macroscopic models were also capable to explain the Bingham yield stresses in inverse ferrofluids investigated by Ramos *et al.* (2011).

The comparison with microscopic chain-like models is performed in Figure 6.5 (normalizing experimental values by G_{mag}). These models are only valid at infinitesimal deformation. As a result, in this figure we plot the normalized low strain amplitude viscoelastic moduli G'_0/G_{mag} and G''_0/G_{mag} as a function of particle loading. Experimental data are shown for inverse ferrofluids having two different diameters. For completeness, in Figure 6.5 we also include experimental data on other inverse ferrofluids involving other carrier fluids and particle sizes by Ramos *et al.* (2010). The collapse of all experimental data demonstrates that the low strain viscoelastic moduli are independent of particle size in agreement with Saldivar-Guerrero *et al.* (2006) and de Gans *et al.* (2000).

Lines in Figure 6.5a correspond to micromechanical model predictions. As observed, a good agreement is found with experimental and simulation results for the less concentrated inverse ferrofluids. In agreement with Ramos *et al.* (2010) (see Figure 7 in that paper) the better agreement is found with de Vicente model. Similar to our observation for macroscopic models, as the concentration increases, the micromechanical models underestimate experimental results as a result of aggregate-aggregate

interactions and/or the formation of thick columnar structures instead of isolated slender bodies.



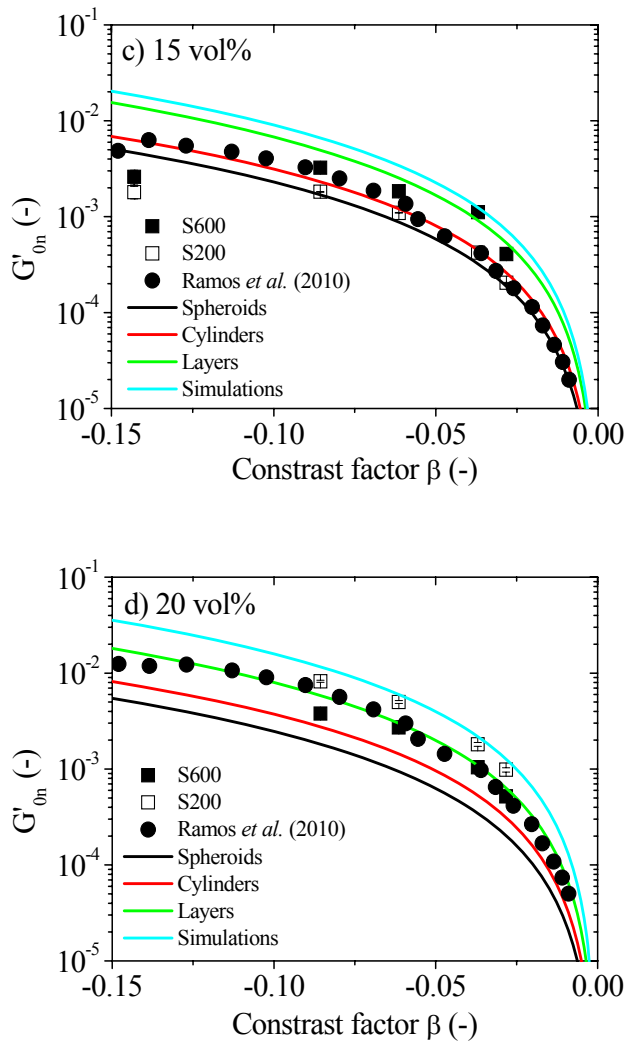


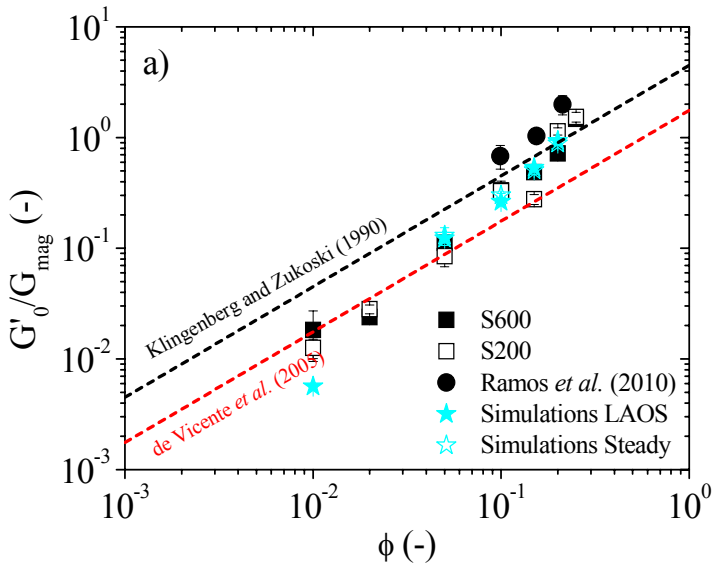
Figure 6.4 Comparison between experiments, macroscopic theoretical models (see Table 6.1) and simulations for inverse ferrofluids at four different particle volume fractions 5, 10, 15 and 20 vol %. Solid squares: S600; Open squares: S200; Black circles: experimental data from Ramos *et al.* (2010). Black solid line: spheroidal model. Red dashed line: cylindrical model. Green dotted line: layered aggregates model. Cyan dashed-dotted line: simulations. Y-axis represents the normalized low strain storage modulus $G'_{on} = G'_0 / \mu_0 \mu_{cr} H_0^2$. Note that a different density for silica is assumed in Ramos *et al.* (2010); data reported here for 10, 15 and 20 vol% correspond to 9.9, 15.4, and 21.2 vol% in Ramos *et al.* (2010) paper, respectively.

Two regions are clearly identified from oscillatory shear flow tests reported in Figure 6.5a. At low particle concentrations (below 10 vol%), a power law dependence on volume fraction is found for the storage modulus similar to the case of other weakly-flocculated colloidal dispersions. This linear dependence is explained in terms of both macroscopic and microscopic models (see Table 6.1). When the particle concentration is larger than 10 vol% the power law exponent clearly increases at a higher rate. This finding has been previously noted in the literature and has been tentatively associated with the interaction of thicker structures [e.g. Ramos *et al.* (2010)]. In the literature it has been reported a linear dependence between the storage modulus and the volume fraction up to loadings of 26 vol% [de Gans *et al.* (1999b)]. From the inspection of Figure 6.5a their finding is not very different from ours. The two regions, clearly observed in oscillatory shear flows, were not found in steady shear flow tests (see Figure 6.2) suggesting a qualitative difference in the structures under both kinematics.

Interestingly, experimental data for the storage modulus contained in Figure 6.5a compare very well with steady shear and large amplitude oscillatory shear particle-level simulations. The storage modulus was calculated from the slope of the stress as a function of the strain using steady shear data. Simulations capture reasonably well the change in slope that is observed around 10 vol% and demonstrate a change in the inner structure of the clusters from single linear chains to more interconnected aggregates at equilibrium for concentrations above 10 vol% [see Figure 6.5c]. This is in good agreement with the observations in Figure 6.4.

The effect of particle concentration in the normalized low-strain loss modulus is shown in Figure 6.5b. The important point here is that simulations clearly underestimate the experimental loss moduli for large

enough concentrations. This is a consequence of hydrodynamic interactions between aggregates being neglected in the simulations. The influence of magnetic multipoles is expected to be negligible because of the weak magnetostatic interactions in the inverse ferrofluid. As expected, the critical concentration where the deviation from experiments occurs is clearly correlated to the deviation from the linear slope in the G' versus ϕ curve. Unfortunately, analytical theories for G'' are not available in the MR literature.



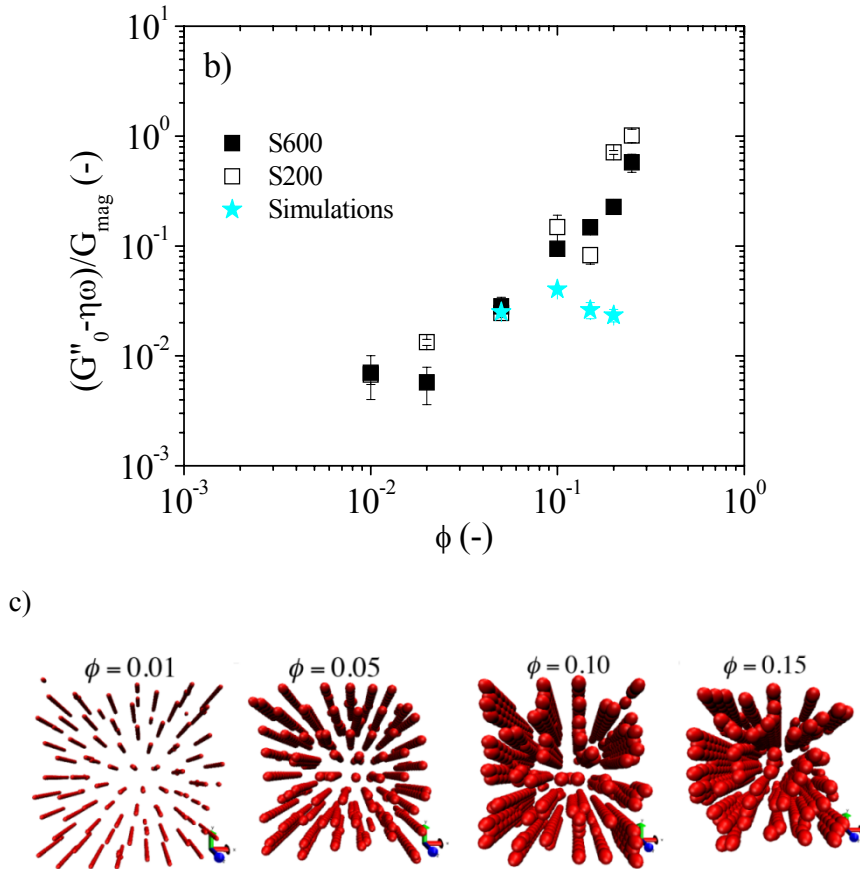


Figure 6.5 Volume fraction dependence of the linear viscoelastic moduli normalized by $G_{mag} = \mu_0 \mu_{cr} \beta^2 H_0^2$. a.- Low strain storage modulus G' . b.- Low strain loss modulus $G'' - \eta\omega$. "Simulations LAOS" data correspond to low strain values in dynamic oscillatory shear particle-level simulations. "Simulations Steady" data correspond to the storage modulus obtained from the slope of stress versus strain in steady shear particle-level simulation curves. Black circles from Ramos *et al.* (2011) correspond to 756 nm diameter silica particles dispersed in a ferrofluid of viscosity 44 mPa.s. Lines correspond to analytical theories. c.- Quasiequilibrium configurations for four packing fractions 1, 5, 10 and 15 vol% evidencing the distinct lateral aggregation between single-width gap spanning chains above 10 vol%.

Paragraphs above demonstrate that particle-level simulations can explain the linear viscoelastic regime at low particle concentration. In the case of

the storage modulus, particle-level simulations also reproduce well the behavior at large particle loadings. However, in the case of the loss modulus, clear deviations between experiments and simulations appear at larger concentrations (> 10 vol%) due to interaggregate interactions between gap spanning structures that are not included in the simulations because the medium contribution to the loss modulus is not considered.

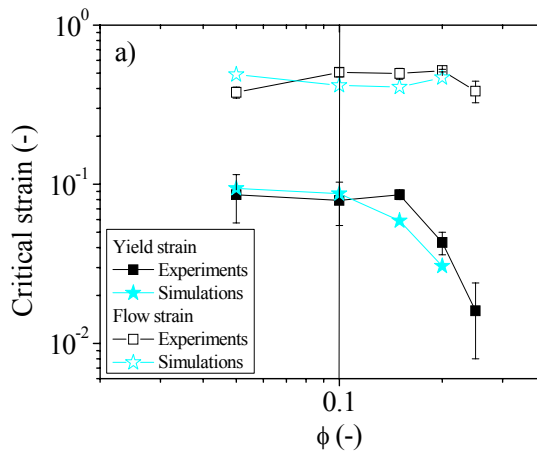
Upon further increasing the strain amplitude in Figure 6.3, the inverse ferrofluids start to deviate from the linear regime (at the *yield* point) and eventually flow when G'' overcomes G' (at the *flow* point). In the next section we investigate the onset of flow regime.

B. Onset of flow under oscillatory shear

In Figure 6.6a we illustrate the critical yield and flow strain values as a function of particle concentration as obtained from experiments and simulations. The yield point is defined as the strain where G' reduces 90 % with respect to its value in the viscoelastic linear region. On the other hand, the flow point is defined as the strain where $G' = G''$. Figure 6.6a clearly shows that the experimentally observed onset of flow of the field-induced structures is also reasonably well captured using particle-level simulations.

The yield strain, which corresponds to the onset of nonlinearity, occurs at very low strain values (see Figure 6.6a). This fact is well documented in the literature, especially in the case of conventional MR fluids, and, in general, is expected to be due to small particle-level cluster arrangements under shear [Parthasarathy and Klingenberg (1999)]. The reasonably good agreement between experiments and simulations suggests that, as expected, wall slip does not occur in the experiments. In the case of using conventional MR fluids prepared by dispersion of micrometric iron

particles in a non-magnetic carrier, the simulated yield strain is typically much larger than the experimental one [Parthasarathy and Klingenberg (1995)]. Consistently, the yield strain values reported here are very similar to those reported in Table II by de Gans *et al.* (1999a). Also, as expected, these yield strain values very closely correspond to the yield strains obtained from the stress-strain tangent method on steady shear flow data reported in section 6.5.1 [results not show here for the sake of brevity. For more details see Ramos *et al.* (2011)].



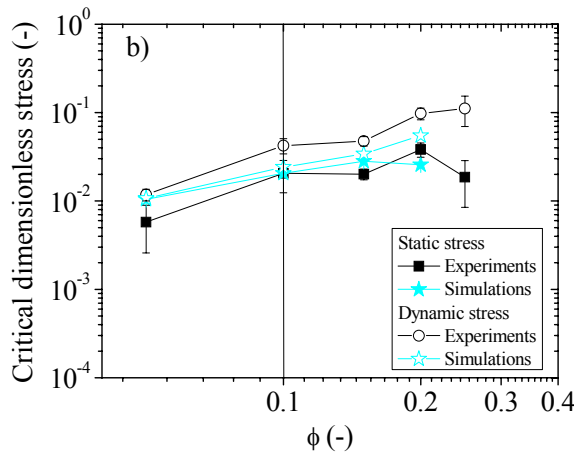


Figure 6.6 a) Critical strain and b) critical dimensionless stress, τ/G_{mag} , as obtained from the strain amplitude sweep data from experimental (S200 particles) and simulation curves. Error bars correspond to measurement at different field strengths. For each field there were three independent measurements. Closed symbols correspond to the "yield" points. Open symbols correspond to the onset of "flow".

Again, two regions are clearly differentiated in the yield strain data from experiments and simulations. At low particle concentrations, the yield strain remains constant at a very low value. Next, the yield strain decreases when increasing the particle content for particle concentrations larger than 10 vol% suggesting the formation of thicker aggregates. Chain-like bead-rod model predictions in MR fluids provide the right order of magnitude for the yield strain observed at low concentrations (approximately 10 %) [de Gans *et al.* (1999a)] and suggests that the aggregates break at the tips in contrast to the middle of the aggregate.

The flow strain value is largely independent of particle concentration. In this case, again a good agreement is found between simulation data and experiments. These results are expected because the flow strain is basically determined by the rupture of the last doublet present in suspension whose strength is essentially determined by magnetostatic

dipolar forces. This is essentially the strain corresponding to the dynamic (Bingham) yield stress reported in section 6.5.1 in the form of a critical Mason number Mn^* . In fact, the average value for the flow strain is around 40 %, which is in good agreement with conventional micromechanical models for MR fluids available in the literature such as Klingenberg and Zukoski (1990) and de Gans *et al.* (1999b) that predict a flow strain of exactly 38.9 %.

The volume fraction dependence of the critical stress is represented in Figure 6.6b. These critical stresses are expected to be the multiplication of the critical strain (yield or flow) by the corresponding storage modulus ($\tau = G' \gamma$). In view of Figures 6.5a and 6.6a, the volume fraction dependence of the critical stress is dominated by the storage modulus at low particle loadings. However, for larger concentrations (above 10 vol%) both the storage modulus and the critical strain contribute to the stress; as a result, the stress levels off. The particle concentration dependence of the critical stress strongly differs from that observed in conventional MR fluids prepared by simple dispersion of carbonyl iron in silicone oils [Segovia-Gutiérrez *et al.* (2012)]. In the current case, a single yielding is found as clearly demonstrated by strain amplitude sweep curves.

Results presented in this section suggest two well-differentiated regions. At low particle concentrations, isolated chain-like structures may exist connecting the plates that support the shear stresses acting on the suspension. For higher concentrations, chain-like structures start to interact resulting in a volume-filling colloidal gel structure. The fact that the storage modulus further increases and the (limiting) yield strain decreases for this particular concentration range is in accordance with the existence of a strong-link gel. However, a priori one may think that an aggregate of chains will have a higher critical strain, as the breaking of

one of the chains will not have as a consequence the collapse of the entire structure.

6.6. CONCLUSIONS

The rheological behavior of inverse ferrofluids under steady shear and time-dependent (dynamic oscillation) flow regimes has been revisited under the frame of particle-level simulations, the structural viscosity model recently proposed by Berli and de Vicente (2012) and other micromechanical and macroscopic models reported in the MR literature. Special attention has been given to the effect of particle loading in an attempt to understand the Mn^* versus concentration dependence and the behavior under large-amplitude oscillatory shear.

Under steady shear, simulations, theories and experiments are in good agreement and demonstrate a linear dependence between Mn^* and particle loading ϕ . Differences appear under oscillatory shear flow. Here, as expected, a good agreement is generally found between particle-level simulations, analytical theories and experiments in the dilute regime. However, upon increasing the particle loading, analytical theories clearly underestimate experimental observations while particle-level simulations still give a correct prediction. The only disagreement between simulations and experiments is found in the loss modulus. However, this discrepancy was expected and is attributed to the fact that hydrodynamics is not properly considered in the simulations.

Overall, taking into account that the simulation model contains considerable simplifications the agreement with other analytical theories and experiments is remarkably good.

ACKNOWLEDGEMENTS

This work was supported by MAT 2013-44429-R project (Spain) and by Junta de Andalucía P10-RNM-6630, P10-FQM-5977 and P11-FQM-7074 projects (Spain). J.A.R.-L. acknowledges the financial support by the “Ministerio de Educación: Becas del Programa de Formación del Profesorado Universitario (FPU)” (AP2010-2144). J.C.F.-T. acknowledges the Interuniversity Attraction Poles Programme (IAP 7/38 MicroMAST) of the Belgian Science Policy Office for the financial support.

Supplemental material

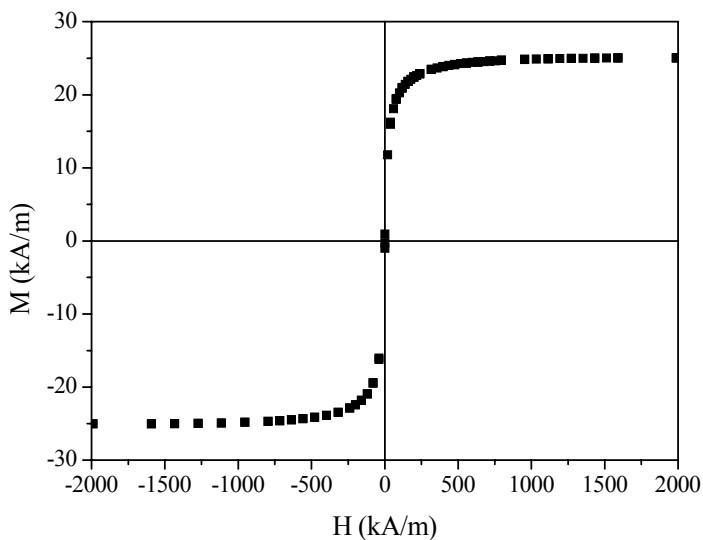


Figure S6.1 Magnetization curve of the ferrofluid at room temperature.

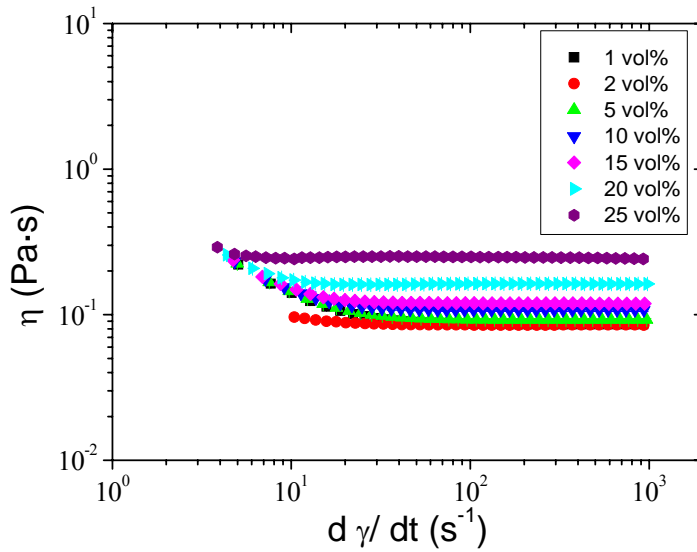
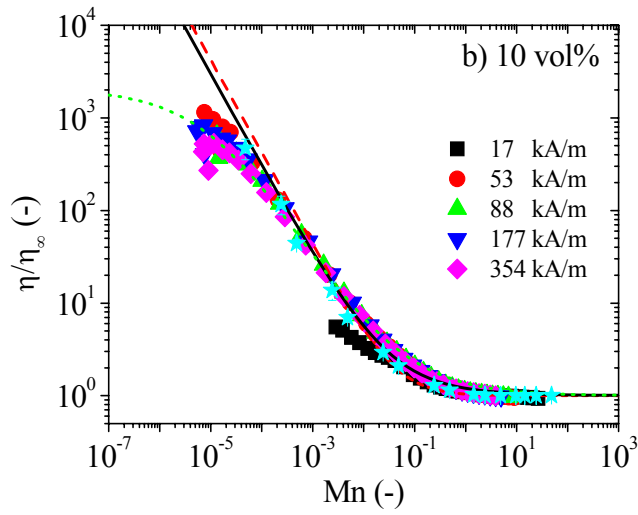
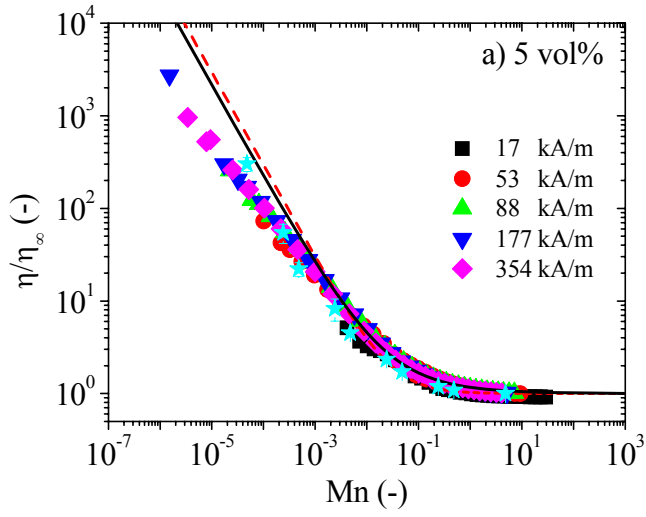


Figure S6.2 Viscosity curves of the inverse ferrofluids (S600) in the absence of magnetic fields for different silica concentrations. The curves were obtained using a stress sweep starting at 1 Pa.



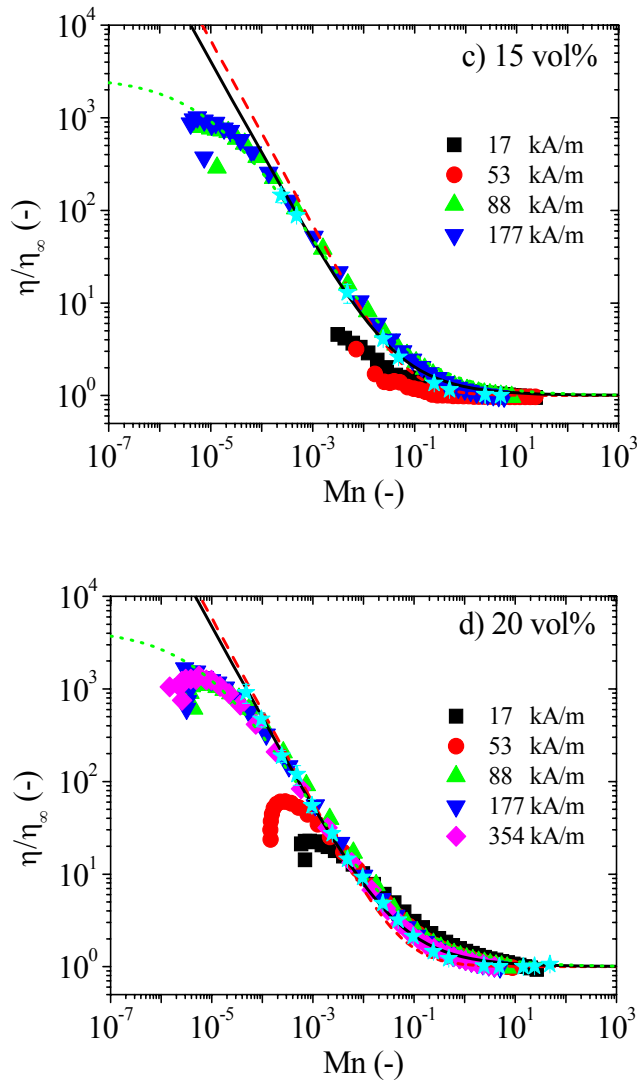
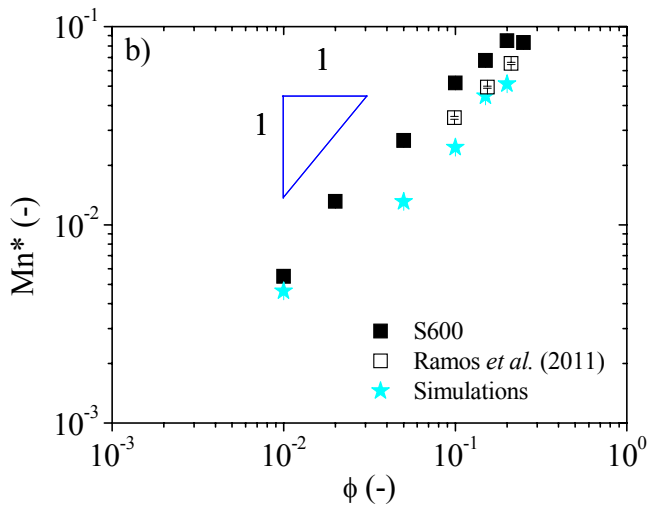
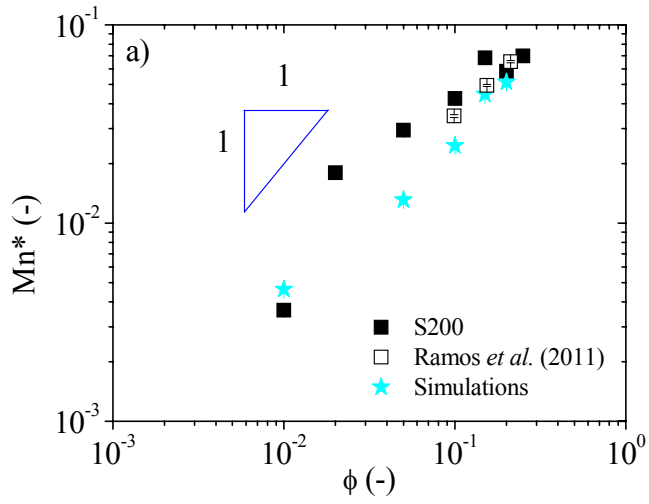


Figure S6.3 Dimensionless viscosity (η/η_∞) as a function of the Mason number (Mn). Experimental data on inverse ferrofluids prepared with S200 silica particles are represented as solid symbols. Lines correspond to theoretical predictions: Black solid line corresponds to Berli and de Vicente predictions (Equation 5). Red dashed line corresponds to Bingham predictions (Equation 1). Green dotted lines correspond to the full structural model of Berli and de Vicente (Equation 4). Cyan stars correspond to particle-level simulations.



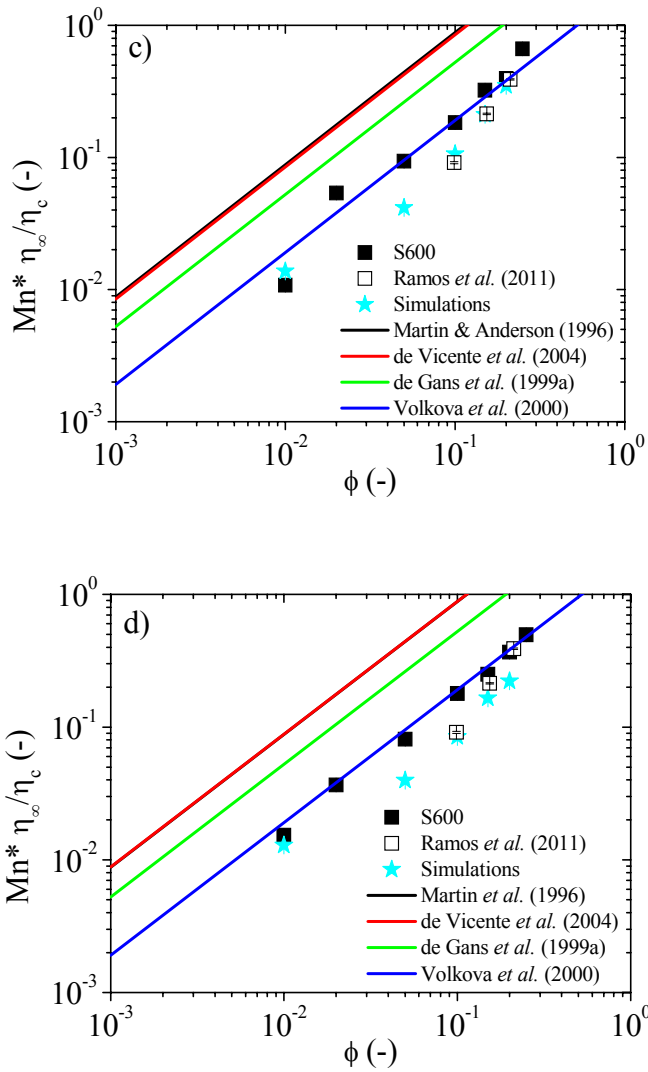


Figure S6.4 Volume fraction dependence of Mn^* as obtained from fittings to the Bingham plastic equation (Equation 5). a) and b) Mn^* versus ϕ for S200 and S600 respectively. c) and d) $Mn^* \frac{\eta_\infty}{\eta_c}$ versus ϕ for S200 and S600 respectively. The error bars in the figures are obtained from the average to all field strengths.

REFERENCES

- Berli, C. L. A. and J. de Vicente, "A structural viscosity model for magnetorheology," *Appl. Phys. Lett.* **101**(2), 021903-1-4 (2012).
- Bossis, G., E. Lemaire, O. Volkova, and H. Clercx, "Yield stress in magnetorheological and electrorheological fluids: a comparison between microscopic and macroscopic structural models," *J. Rheol.* **41**, 687-704 (1997).
- Bossis, G., O. Volkova, S. Lacis and A. Meunier, "Magnetorheology: fluids, structures and rheology," in: S. Odenbach (Ed) *Ferrofluids. Magnetically controllable fluids and their applications* (Lecture notes in Physics, 594, Springer-Verlag 2002) pp 202-230.
- Chen, T. Y., B. J. Briscoe and P. F. Luckham, "Microstructural studies of electrorheological fluids under shear," *J. Chem. Soc. Faraday Trans.* **91**(12), 1787-1794 (1995).
- de Gans B. J., H. Hoekstra and J. Mellema, "Non-linear magnetorheological behaviour of an inverse ferrofluid," *Faraday Discuss.* **112**, 209–224 (1999a).
- de Gans, B. J., C. Blom, A. P. Philipse and J. Mellema, "Linear viscoelasticity of an inverse ferrofluid," *J. Phys. Rev. E* **60**, 4518-4527 (1999b).
- de Gans, B. J., N. J. Duin, D. van den Ende and J. Mellema, "The influence of particle size on the magnetorheological properties of an inverse ferrofluid," *J. Chem. Phys.* **113**, 2032-2042 (2000).
- de Vicente, J., "Magnetorheology: A Review," *e-rheo-iba* **1**, 1-18 (2013).
- de Vicente, J., D. J. Klingenberg, and R. Hidalgo-Alvarez, "Magnetorheological Fluids: A Review," *Soft Matter* **7**, 3701-3710 (2011a).

-
- de Vicente, J., J. A. Ruiz-López, E. Andablo-Reyes, J. P. Segovia-Gutiérrez and R. Hidalgo-Alvarez, “Squeeze flow magnetorheology,” *J. Rheol.* **55**(4), 753-779 (2011b).
- de Vicente, J., M. T. López-López, J. D. G. Durán and G. Bossis, “A Slender-body Micromechanical Model for Viscoelasticity of Magnetic Colloids. Comparison with Preliminary Experimental Data,” *J. Colloid Interf. Sci.* **282**, 193-201 (2005).
- de Vicente, J., M. T. López-López, J. D.G. Durán and F. González-Caballero, “Shear flow behavior of confined magnetorheological fluids at low magnetic field strengths,” *Rheol. Acta* **44**, 94-103 (2004).
- Ekwebelam, C. C. and H. See, “Determining the flow curves for an inverse ferrofluid,” *Korean-Aust. Rheol. J.* **20**(1), 35-42 (2008).
- Fernández-Toledano, J. C., J. A. Ruiz-López, R. Hidalgo-Álvarez and J. de Vicente, “Simulations of Polydisperse Magnetorheological Fluids: a Structural and Kinetic Investigation,” *J. Rheol.* **59**(2), 475-498 (2015).
- Fernández-Toledano, J. C., J. Rodríguez-López, K. Shahrivar, R. Hidalgo-Álvarez, L. Elvira, F. M. de Espinosa and J. de Vicente, “Two-step yielding in magnetorheology,” *J. Rheol.* **58**(5), 1507-1534 (2014).
- Fujita, F. and T. Mamiya, “Interaction forces between nonmagnetic particles in the magnetized,” *J. Magn. Magn. Mater.* **65**, 469 (1986).
- Gabriel, C. and H. M. Laun “Combined slit and plate-plate magnetorheometry of a magnetorheological fluids (MRF) and parametrization using the Casson model,” *Rheol. Acta* **48**, 755-768 (2009).
- Ginder, J. M., “Behavior of magnetorheological fluids,” *MRS Bulletin*, August, 26-29 (1998).

- Heine, M. C., J. de Vicente and D. J. Klingenberg, "Thermal transport in sheared electro- and magnetorheological fluids," *Phys. Fluids* **18** (2), 023301-1-11 (2006).
- Kittipoomwong, D. and D. J. Klingenberg, "Dynamic yield stress enhancement in bidisperse magnetorheological fluids," *J. Rheol.* **49**(6), 1521-1538 (2005).
- Klingenberg, D. J. and C. F. Zukoski, "Studies on the steady-shear behavior of electrorheological suspensions," *Langmuir* **6**, 15-24 (1990).
- Klingenberg, D. J., "Magnetorheology: applications and challenges," *AIChE J.* **47**, 246-249 (2001).
- Klingenberg, D. J., "Simulation of the dynamic oscillatory response of electrorheological suspensions: demonstration of a relaxation mechanism," *J. Rheol.* **37**(2), 199-214 (1993).
- Klingenberg, D. J., C.H. Olk, M.A. Golden and J.C. Ulicny, "Effects of nonmagnetic interparticle forces on magnetorheological fluids," *J. Phys.: Condens. Matter* **22** (32), 324101 (2010).
- Klingenberg, D.J., J.C. Ulicny and M.A. Golden, "Mason numbers for magnetorheology," *J. Rheol.*, **51**, 883-893 (2007).
- Lagger, H. G., C. Bierwisch, J. G. Korvink and M. Moseler, "Discrete element study of viscous flow in magnetorheological fluids," *Rheol. Acta* **53**, 417-443 (2014).
- Lagger, H. G., T. Breinlinger, J. G. Korvink, M. Moseler, A. Di Renzo, F. Di Maio and C. Bierwisch, "Influence of hydrodynamic drag model on shear stress in the simulation of magnetorheological fluids," *J. Non-Newtonian Fluid Mech.* **218**, 16-26 (2015).
- Marshall, L., C., F. Zukoski, and J. Goodwin, "Effects of electric fields on the rheology of non-aqueous concentrated suspensions," *J. Chem. Soc., Faraday Trans.* **85**, 2785-2795 (1989).

-
- Martin J. E., and R. A. Anderson, "Chain model of electrorheology," *J. Chem. Phys.* **104** (12), 4814–4827 (1996).
- Melle, S., O.G. Calderón, M.A. Rubio and G.G. Fuller, "Microstructure evolution in magnetorheological suspensions governed by mason number," *Phys. Rev. E* **68** (4), 041503 (2003).
- Melrose, J. R., and D. M. Heyes, "Simulations of electrorheological and particle mixture suspensions: agglomerate and layer structures," *J. Chem. Phys.* **98**(7), 5873-5886 (1993).
- Olabi, A. G. and A. Grunwald, "Design and application of magnetorheological fluid," *Materials and Design* **28**, 2658-2664 (2007).
- Pappas, Y. and D. Klingenberg, "Simulations of magnetorheological suspensions in poiseuille flow," *Rheol. Acta* **45** (5), 621–629 (2006).
- Park, B. J., F. F. Fang, and H. J. Choi, "Magnetorheology: materials and application," *Soft Matter* **6**, 5246-5253 (2010).
- Parthasarathy, M and D. J. Klingenberg, "Electrorheology: mechanisms and models," *Mater. Sci. Eng.* **R17**, 57-103 (1996).
- Parthasarathy, M. and D. J. Klingenberg "A microstructural investigation of the nonlinear response of electrorheological suspensions. 2. Oscillatory shear-flow," *Rheol. Acta* **5**, 430-439 (1995)
- Parthasarathy, M. and D. J. Klingenberg, "Large amplitude oscillatory shear of ER suspensions," *J. Non-Newtonian Fluid Mech.* **81**, 83-104 (1999).
- Rabinow, J., "The magnetic fluid clutch," *Trans. Am. Inst. Electr. Eng.* **67**, 1308–1315 (1948)
- Ramos, J., D. J. Klingenberg, R. Hidalgo-Alvarez and J. de Vicente, "Steady shear magnetorheology of inverse ferrofluids," *J. Rheol.* **55**, 127-152 (2011).

- Ramos, J., J. de Vicente and R. Hidalgo-Álvarez, “Small-amplitude oscillatory shear magnetorheology of inverse ferrofluids,” *Langmuir* **26**(12), 9334-9341 (2010).
- Rosensweig, R. E., “On magnetorheology and electrorheology as states of unsymmetric stress,” *J. Rheol.* **39**, 179-192 (1995).
- Ruiz-López, J. A. et al., “Testing the mean magnetization approximation in magnetorheology,” submitted.
- Saldivar-Guerrero, R., R. Richter, I. Rehberg, N. Aksel, L. Heymann and O. S. Rodríguez-Fernández, “Viscoelasticity of mono- and polydisperse inverse ferrofluids,” *J. Chem. Phys.* **125**, 084907-1-7 (2006).
- Segovia-Gutiérrez, J. P., C. Berli and J. de Vicente, “Nonlinear viscoelasticity and two-step yielding in magnetorheology: A colloidal gel approach to understand the effect of particle concentration,” *J. Rheol.* **56**(6), 1429-1448 (2012).
- Segovia-Gutiérrez, J. P., J. de Vicente, R. Hidalgo-Alvarez and A. M. Puertas, “Brownian Dynamics Simulations in Magnetorheology and Comparison with Experiment,” *Soft Matter* **9**, 6970-6977 (2013).
- Skjeltorp, A. T., “One- and two-dimensional crystallization of magnetic holes,” *Phys. Rev. Lett.* **51**, 2306-2309 (1983).
- Stöber, W. and A. Fink, “Controlled growth of monodisperse silica spheres in the micron size range,” *J. Colloid Interf. Sci.* **26**, 62-69 (1968).
- Vekas, L., “Ferrofluids and magnetorheological fluids,” *Advances in science and technology* **54**, 127-136 (2008).
- Volkova, O., G. Bossis, M. Guyot, V. Bashtovoi and A. Reks, “Magnetorheology of magnetic holes compared to magnetic particles,” *J. Rheol.* **44**, 91-104 (2000).

Wang, X. J. and F. Gordaninejad, "Flow analysis of field-controllable, electro- and magneto-rheological fluids using Herschel-Bulkley model," *J. Intel. Mat. Syst. Str.* **10(8)**, 601-608 (1999).

Chapter 7.

Testing the mean magnetization approximation, dimensionless and scaling numbers in magnetorheology

José Antonio Ruiz-López, Juan Carlos Fernández-Toledano, Roque Hidalgo-Álvarez y Juan de Vicente.

This article is under review

Abstract

The mean magnetization (MM) approximation is undoubtedly the most widely used approximation in magnetorheology both from a theoretical and simulation perspective. According to this, spherical magnetizable particles under field can be replaced by effective dipole moments m placed at their center with strength $m = V_p \langle M_p \rangle$. Here V_p and $\langle M_p \rangle$ are the volume and mean (average) magnetization of the particles, respectively. In spite of being extensively used, there is not a mathematical justification to do so in most cases. In this manuscript, we test this approximation using experiments, theories and simulations, for a wide range of magnetic field strengths and particle loadings, in both conventional magnetorheological fluids (CMRFs) and inverse ferrofluids

(IFFs). Results demonstrate that the MM approximation is applicable in IFFs for a very wide range of field strengths (up to external fields of 265 kA/m) and particle loadings (up to 20 vol%). For CMRFs, the MM approximation is only applicable in two particular circumstances; in magnetic saturation or in infinite dilution.

7.1. Introduction

Generally speaking, magnetorheological (MR) fluids are non-Brownian magnetic field-responsive suspensions. There are essentially two kinds of MR fluids: i) conventional MR fluids (CMRFs) prepared by dispersion of magnetizable particles in a non-magnetic liquid carrier,¹ and ii) inverse ferrofluids (IFFs) prepared by dispersion of non-magnetic particles within a ferrofluid.²⁻³ In the absence of magnetic fields, MR fluids behave as regular dispersions. However, in the presence of magnetic fields particles interact through magnetic forces eventually forming elongated structures in the field direction.⁴⁻⁷

Despite their different magnetization mechanisms, the mechanical (rheological) behavior of CMRFs and IFFs can be understood using the same principles -under the *Particle Magnetization Model*.⁷ CMRFs are clearly preferred in commercial applications, while IFFs are considered model systems and generally used for fundamental studies.^{5,6,8} The main reason for this is that magnetostatic interactions in IFFs are weak and the dispersed particles can be easily prepared with a very high monodispersity level.⁴

At large field strengths colloidal interactions do not play a role and, as a result, only two dimensionless numbers are needed to describe the rheology of MR fluids: the Mason number, Mn , and particle

concentration, ϕ . Currently, the scaling with Mason number seems well understood. However, the understanding of the effect of particle loading is still incomplete.⁷⁻¹⁰ Interestingly, the effect of particle concentration in the dimensionless shear viscosity (normalized by the high-shear viscosity) is solely contained in the critical Mason number Mn^* (i.e. an apparent yield stress) that is associated to the transition from magnetostatic to hydrodynamic control.^{8,11}

A major approximation that is commonly used in the description of MR fluids is the so-called mean (average) magnetization (MM) approximation. According to this, dispersed particles can be substituted by a magnetic dipole placed at their center. This approximation is not justified in most experimental cases and only becomes exact in two limiting scenarios: i) at low field strengths in dilute systems, and ii) in magnetic saturation. For a given particle concentration, the MM approximation has been successful in the description of the field dependence in CMRFs.^{12,13} Also, the MM approximation has been successfully employed as well in the case of IFFs to ascertain the effect of particle loading on the MR performance. A linear dependence with volume fraction $Mn^* \propto \phi$ has been reported in very good agreement with analytical theories and experiments in the dilute regime.⁸

To the best of our knowledge, the MM approximation has not been exhaustively tested yet in the case of CMRFs and IFFs for different concentrations. The benefit of using this approximation with appropriate dimensionless numbers is that the effect of shear rate, field strength and particle concentration can be ascertained with only a few experimental measurements. Thus, in this work we aim to test the MM approximation using theoretical developments, particle level simulations and experimental data on CMRFs and IFFs for a wide range of field strengths

(from the linear to nearly the saturation regime) and particle concentrations (from dilute to concentrated suspensions).

7.2. Mean magnetization (MM) approximation

Within the MM approximation, the interaction force between two spherical particles can be calculated in the equivalent problem of two dipoles located at the center of the spheres. In particular, a given particle (radius a , volume V_p) with average magnetization $\langle M_p \rangle$ is assimilated as a magnetic moment of strength:

$$m = V_p \langle M_p \rangle = \frac{4\pi}{3} a^3 \langle M_p \rangle \quad (7.1)$$

In this work we will use $\langle M_p \rangle = M_{susp} / \phi$, where M_{susp} is the suspension magnetization and ϕ is the particle concentration.

The magnetostatic interaction force between two dipoles of strength m separated a distance r can be written as:

$$\begin{aligned} \vec{F} &= \frac{3\mu_0\mu_{cr}m^2}{4\pi r^4} [(3\cos^2\theta - 1)\hat{r} + \sin(2\theta)\hat{\theta}] = \\ &= F_{mag} \left(\frac{2a}{r} \right)^4 [(3\cos^2\theta - 1)\hat{r} + \sin(2\theta)\hat{\theta}] \end{aligned} \quad (7.2)$$

where θ is the angle formed between the center-to-center line and the magnetic field direction, μ_0 is the permeability of vacuum, μ_{cr} is the relative permeability of the continuous phase, and F_{mag} is a measure of

the strength of the magnetostatic force. By substitution of Equation 7.1 in Equation 7.2 we get an expression for F_{mag} as a function of $\langle M_p \rangle$:

$$F_{mag} = \frac{1}{12} \pi \mu_0 \mu_{cr} a^2 \langle M_p \rangle^2 \quad (7.3)$$

As stated above, for MR fluids, the Lambda ratio (i.e. ratio between magnetostatic and thermal forces; $\lambda = \pi \mu_0 \mu_{cr} a^3 \langle M_p \rangle^2 / 18 \kappa_B T$) is generally very large, and as a result their flow behavior is governed by only two dimensionless numbers: particle volume fraction ϕ and Mason number Mn .⁷ The Mason number is defined as the ratio between the viscous shear forces, $F_{drag} = 6\pi\eta_c \dot{\gamma} a^2$, and the magnetostatic forces, F_{mag} . Here η_c stands for the viscosity of the continuous phase and $\dot{\gamma}$ is the magnitude of the shear rate tensor. It is important to remark that different considerations for F_{mag} lead to different definitions of the Mason numbers. Using Equation 7.3, the Mason number can be written as follows:

$$Mn \equiv \frac{F_{drag}}{F_{mag}} = Mn_{<M>} = \frac{72\eta_c \dot{\gamma}}{\mu_0 \mu_{cr} \langle M_p \rangle^2} \quad (7.4)$$

Improvements to Equations 7.3 and 7.4 for non-dilute suspensions involve the substitution of η_c (and μ_{cr}) by the viscosity (and permeability) of the suspensions as a whole. Interestingly, the use of Equation 7.4 permits the construction of scaling rheological curves also facilitating the modeling and simulation of these systems. Actually, Equation 7.4 has been successfully used in the past to collapse steady shear viscosity data for CMRFs^{12,14,15} and IFFs⁴.

However, in spite of being widely used, strictly speaking, the MM approximation is not applicable in most of the experimental data reported on MR fluids to date. The reason for this is that the MM approximation is only valid for homogeneous magnetic fields (i.e. generally speaking, exceedingly low concentrations) and/or magnetically saturated suspension (i.e. exceedingly large field strengths). On the one hand, the former condition is never realized in practice because MR fluids are never dilute by definition. On the other hand, the later condition is only guaranteed for sufficiently large magnetic field strengths and this is difficult to achieve because of field-induced particle migration and/or undesirable heating of the samples. In summary, most of the available data reported in the literature concern concentrated, non-saturated MR fluids and therefore, strictly speaking, the MM approximation is not applicable.

7.3. Validity of the MM approximation: Mason numbers and magnetic stress

7.3.1. Low fields and dilute suspensions

In the case of very low magnetic field strengths in dilute suspensions (i.e. within the linear magnetization regime), the magnetostatic interparticle force F_{mag} is proportional to the external magnetic field strength squared (

$$F_{mag} \propto H_0^2) \quad \text{because} \quad \langle M_p \rangle = 3\beta H_0. \quad \text{Here}$$

$\beta = (\mu_{pr} - \mu_{cr}) / (\mu_{pr} + 2\mu_{cr})$ is the contrast factor (or coupling parameter) and μ_{pr} is the relative permeability of the particles.

Under these conditions, it can be demonstrated that Equations 7.3 and 7.4 reduce to:⁷

$$F_{mag,L} = \frac{3}{4} \pi \mu_0 \mu_{cr} \beta^2 a^2 H_0^2 \quad (7.5a)$$

$$\text{Mn}_L = \frac{8\eta_c \dot{\gamma}}{\mu_0 \mu_{cr} \beta^2 H_0^2} \quad (7.5b)$$

According to Equation 7.5a, the magnetic force between the particles comes from the permeability mismatch between the two phases, β . Interestingly, β is a function of the magnetic field strength. In the case of CMRFs β can take values between 0 (large fields) and 1 (low fields). In contrast, in the case of IFFs the contrast factor reduces to $\beta = (1 - \mu_{cr}) / (1 + 2\mu_{cr})$ and, as a consequence, β can take values between -0.5 (low fields) and 0 (large fields). Equation 7.5b has been successfully used in the past to collapse steady shear viscosity data for low and intermediate (non-linear) magnetic field strengths in CMRFs,¹¹ IFFs,⁶ and ER systems.¹⁶

When the magnetic field strength is further increased the suspensions approach to the saturation regime and Equations 7.5a and 7.5b do not apply anymore. In particular, in this regime the magnetostatic interparticle force is no longer proportional to $\beta^2 H_0^2$ because the magnetization vector varies with position inside each interacting particle; in particular the magnetization in the polar regions begins to saturate (see Klingenberg¹² and references therein). FEM simulations carried out by Ginder and Davies¹⁷ demonstrate that in this case the power law exponent of the magnetic field strength becomes smaller than 2.

7.3.2. Saturating fields

For very large magnetic field strengths the suspensions completely magnetize; $M_{susp} = M_{susp,sat}$. In the case of magnetically saturated

suspensions the particles acquire a uniform magnetization within their volume, $M_{p,sat}$, and the MM approximation is truly applicable. Here $\langle M_p \rangle = M_{p,sat} = M_{susp,sat} / \phi$. In this case, Equations 7.3 and 7.4 become independent of the magnetic field strength and reduce to:¹²

$$F_{mag,sat} = \frac{1}{12} \pi \mu_0 \mu_{cr} a^2 M_{p,sat}^2 \quad (7.6a)$$

$$\text{Mn}_{sat} = \frac{72 \eta_c \dot{\gamma}}{\mu_0 \mu_{cr} M_{p,sat}^2} \quad (7.6b)$$

7.3.3. Magnetic stress scale

Starting from the expressions for the magnetostatic force in every field strength regime (linear and saturation), a magnetic stress τ_{mag} can be simply estimated by the ratio of the corresponding magnetostatic force (Equations 7.3, 7.5a and 7.6a) divided by the particle area A_p . A simple estimation of A_p can be carried out if we assume a single-width particle chain like structuration. In this particular case, it can be demonstrated that $A_p \propto 2\pi a^2 / 3\phi$ (see Annex), and therefore the magnetic stress reads as follows:

$$\tau_{mag} \equiv \tau_{mag,<M>} = \frac{1}{8} \phi \mu_0 \mu_{cr} \langle M_p \rangle^2 \quad (7.7a)$$

$$\tau_{mag,L} = \frac{9}{8} \phi \mu_0 \mu_{cr} \beta^2 H_0^2 \quad \text{Low fields (Linear)} \quad (7.7b)$$

$$\tau_{mag,sat} = \frac{1}{8} \phi \mu_0 \mu_{cr} M_{p,sat}^2 \quad \text{Large fields (Saturation)} \quad (7.7c)$$

$\mu_{cr} \approx 1$ in the case of saturating fields for IFFs (e.g. see Figure 7.3b in reference 5).

At this point it is very important to emphasize that the particle area A_p expression assumes a single-width particle chain arrangement that is not necessarily the case in highly concentrated and strongly magnetized MR fluids where more complex structures appear. As a result, Equation 7.7 is only strictly applicable in the case of dilute MR fluids. Magnetostatic stresses given by Equation 7.7 physically correspond to a typical stress scale in terms of particle loading and magnetic field strengths. In the absence of other interparticle interactions, the magnetic stress, τ_{mag} will be proportional to the so-called yield stress, τ_y (i.e. the minimum stress required for the onset of flow).

7.4. Analytical theories

To model the rheological behavior of MR fluids, plastic analytical theories are generally employed. The Bingham model is undoubtedly the most widely used for steady shear flow. In dimensionless form it can be written as follows:

$$\frac{\eta}{\eta_{\infty}} = 1 + \frac{\text{Mn}^*}{\text{Mn}} \quad (7.8)$$

where η_{∞} is the (field-independent) high-shear viscosity and Mn^* is the critical Mason number. Mn^* essentially represents the apparent yield stress in the MR fluid. For a given concentration, if $\text{Mn} < \text{Mn}^*$ magnetostatic interactions predominate and the viscosity diverges. However, if $\text{Mn} > \text{Mn}^*$ hydrodynamic interactions predominate and the viscosity approaches to the high-shear viscosity. In general, assuming that other colloidal interactions are small, the only dependence of the critical Mason number would be on the particle loading; $\text{Mn}^* = \text{Mn}^*(\phi)$.

Microscopic models have been proposed in the literature to explain the critical Mason number dependence on the volume fraction: $Mn^*(\phi) = C\eta_c\phi/\eta_\infty$ where C is a constant whose particular value depends on the particular assumptions or simplifications of the model.^{4,18-20} According to these models a linear dependence with the volume fraction is expected for $Mn^*(\phi)$ in the case of dilute suspensions because, in this case, $\lim_{\phi \rightarrow 0} \eta_\infty = \eta_c$. For larger concentrations a non-linear dependence would be expected and indeed a maximum with particle concentration could also appear (see below).

In spite of the success of the Bingham model, deviations from the Bingham model have also been described in the literature with regards to CMRFs and IFFs (e.g. see Ramos *et al.*⁶ and references therein). In order to explain these discrepancies, a structural viscosity model was recently proposed by Berli and de Vicente:¹¹

$$\frac{\eta}{\eta_\infty} = \left[\frac{1 + (Mn/Mn^*)^{1/2}}{(\eta_\infty/\eta_0)^{1/2} + (Mn/Mn^*)^{1/2}} \right]^2 \quad (7.9)$$

This model predicts a smoother transition between the magnetostatic and hydrodynamic regimes in the case of CMRFs and a low-shear viscosity plateau for IFFs. In the particular case of CMRFs, the low-shear plateau is not experimentally accessible because i) $\eta_0 \gg \eta_\infty$ and ii) limited torque resolution of the rheometers. In this case, Equation 7.9 can be reduced to a dimensionless Casson-like equation:¹¹

$$\eta/\eta_\infty = 1 + (Mn/Mn^*)^{-1} + 2(Mn/Mn^*)^{-1/2} \quad (7.10)$$

Interestingly, both Bingham and Casson models predict a divergent viscosity for low shear rates that corresponds to an apparent yield stress

τ_y . This yield stress τ_y is related to the critical Mason number Mn^* as follows:

$$Mn^* \equiv Mn^*_{<M>} = \frac{72\tau_y}{\mu_0\mu_{cr}\langle M_p \rangle^2} \frac{\eta_c}{\eta_\infty} \quad (7.11a)$$

$$Mn^*_L = \frac{8\tau_y}{\mu_0\mu_{cr}\beta^2 H_0^2} \frac{\eta_c}{\eta_\infty} \quad \text{Low fields (Linear)} \quad (7.11b)$$

$$Mn^*_{sat} = \frac{72\tau_y}{\mu_0\mu_{cr}M_{p,sat}^2} \frac{\eta_c}{\eta_\infty} \quad \text{Large fields (Saturation)} \quad (7.11c)$$

Starting from the Casson model, the dimensionless shear stress τ/τ_{mag} can be expressed, as a function of the critical Mason number Mn^* as follows:

$$\frac{\tau}{\tau_{mag}} = \frac{\eta_\infty}{9\phi\eta_c} \left(Mn^* + Mn + 2Mn^{*1/2} Mn^{1/2} \right) \quad (7.12)$$

In Equation 7.12, the first term is independent of the Mason number and, hence, independent of the shear rate (i.e. it is the apparent yield stress). Thus, the yield stress can be expressed scaled by the magnetic stress, $\tau_y/\tau_{mag} = \eta_\infty Mn^*/9\phi\eta_c$. Micromechanical models^{4,18-20} and experiments for IFFs⁸ suggest that $\eta_\infty Mn^*/\eta_c \propto \phi$, and therefore the ratio τ_y/τ_{mag} is independent on both the particle loading and the magnetic field strength. As a consequence, the magnetic stress τ_{mag} is a suitable scale for the dipolar magnetostatic interactions and the particle volume fraction. Obviously, similar to Equation 7.10, a master curve can be obtained for the stress simply dividing by the yield stress:

$$\frac{\tau}{\tau_y} = 1 + \frac{Mn}{Mn^*} + 2 \left(\frac{Mn}{Mn^*} \right)^{1/2} \quad (7.13)$$

Equation 7.13 provides different curves for the different values of the critical Mason number. However, all these curves can be collapsed into only one curve if the Mason number is normalized by the critical Mason number. Thus, the knowledge of the magnetization of the suspension and the particle loading suffice to describe the rheology of the MR fluids under the assumptions considered.

7.5. Particle level simulations

Brownian molecular dynamic simulations were carried out in order to test the MM approximation. The simulation method was originally described in Fernández-Toledano *et al.*²¹ and is now restricted to monodisperse particles (i.e. the particle diameter was fixed to σ). MR fluids were modeled by $N = 1000$ neutrally buoyant Hard Spheres in a Newtonian continuous medium. The system was confined between two parallel walls perpendicular to the field direction, z , and periodic boundary conditions were applied in the x and y direction. The system was subjected to a constant dimensionless temperature $T^* = 0.1$.

The Langevin equation involved contributions coming from interparticle magnetostatic interactions, hydrodynamic drag and short range repulsions. We assumed pair-wise and point-dipole approximation to calculate magnetic forces. The dimensionless external magnetic field was fixed to $H_0^* = 150$. Hydrodynamic interactions were neglected and particles were subjected to an external flow by using Stokes' law. This approximation was used bearing in mind that the hydrodynamic stress is not the main contribution of the total stress as demonstrated in Lager *et al.*²² The friction coefficient was set as $\zeta^* = 722.1$. In order to avoid overlapping between particles and between a particle and the walls, short-range

exponential repulsive forces were used. Exponential law forces were used instead of power law forces since the former promotes the formation of thick aggregates that are actually observed experimentally.^{23,24}

The Langevin thermostat was switched-off in the direction of non-conservative forces. Therefore, the momentum is conserved in the shear direction while the temperature was conserved by applying the thermostat in the other directions.²¹ Shear stress was calculated using the following equation at each time step:

$$\tau_{\alpha\beta} = -\frac{1}{V} \left(\sum_{i=1}^N \frac{p_i^\alpha p_i^\beta}{M_i} + \sum_{i \neq j} r_{ij}^\alpha F_{ij}^\beta \right) \quad (7.14)$$

where $\tau_{\alpha\beta}$ is the α - β -component of the stress tensor, V is the volume of the simulation box, p_i^α and p_i^β are respectively the α and β -components of the linear momentum of the particle i , M_i is the mass of the particle i , r_{ij}^α is the α -component of the distance between a particle i and j and F_{ij}^β is the β -component of the total pair-wise interaction between the particle i and j .

Stress growth simulations were carried out under external magnetic fields. They consisted in three stages: First, the particles were randomly distributed in the simulation box. Secondly, the MR fluid was structured at rest (quiescent conditions) under the presence of magnetostatic interactions. Finally, a start-up test was initiated. The dimensionless shear rate was ranged between $\dot{\gamma}^* = 0.001$ and $\dot{\gamma}^* = 1000$ and the shear stress for each shear rate was calculated by averaging the large-strain values of the stress tensor over 500 configurations in the interval $\gamma \in [2,10]$ where the shear stress achieves an steady value. The time step was fixed as

$\Delta t^* = 10^{-4}$. From start-up tests, full rheograms were first obtained and latter, the Equation 7.10 was fitted to the data to ascertain Mn^* .

7.6. Experimental

Two kinds of MR fluids were tested in this work. On the one hand, conventional MR fluids (CMRFs) prepared by dispersion of carbonyl iron microparticles (grade HQ from BASF SE Germany) in silicone oils ($\eta_c = 20\text{mPa}\cdot\text{s}$ from Sigma-Aldrich). On the other hand we formulated inverse ferrofluids (IFFs) by dispersion of silica particles (obtained from Stöber method) in a commercial APG ferrofluid ($\eta_c = 44\text{mPa}\cdot\text{s}$ from Ferrotech). Further details on the preparation and characterization of the IFFs can be found in Ruiz-López *et al.*⁸

Magnetic properties of carbonyl iron particles and ferrofluids were obtained by measuring their hysteresis cycles at room temperature in a Quantum Design (San Diego, CA) MPMS-XL 5.0 T magnetometer. The external magnetic field strength was varied from 4000 kA/m to -4000 kA/m . The magnetization curves of the suspensions were also measured in order to calculate the mean magnetization of the particles to use the MM approximation. More details on the characterization of the ferrofluids used in this work can be found in Ramos *et al.*⁶

As stated above, the MM approximation is strictly valid only in the case of low fields at infinite dilution and at saturating fields. As a result, to test this approximation we decided to explore intermediate fields and concentrated suspensions. Magnetic fields investigated ranged $H_0 \in [17, 665]\text{ kA/m}$. Concentrations investigated were $\phi \in [0.01, 0.50]$ in the case of CMRFs and $\phi \in [0.10, 0.20]$ in the case of IFFs.

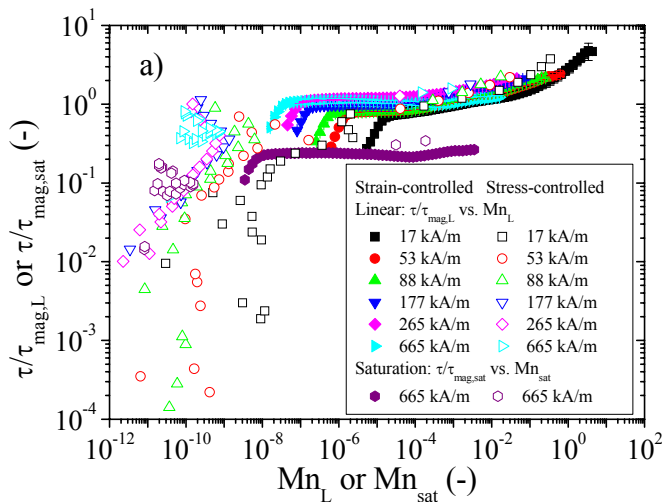
Steady shear flow curves were obtained in a commercial magnetorheometer (MCR 501 with the MRD70/1T magnetocell, Anton Paar) in plate-plate configuration (20 mm diameter, 300 microns gap). All tests were carried out in isothermal conditions (25 °C). The protocol consisted as follows: (i) precondition at a constant shear rate of 100 s^{-1} for 30 s, (ii) the magnetic field is suddenly applied and the suspension is left to equilibrate for 1 min, (iii) the rheogram starts. Two kinds of tests were performed to obtain the rheograms either controlling the shear stress or the shear rate: (a) in the first test, the shear stress was logarithmically increased at a rate of 10 points/decade from 10^{-1} Pa to 10^5 Pa in the case of CMRFs and from 10^{-1} to 10^3 Pa in the case of IFFs. In the particular case of CMRFs, the stress range depended on the particle volume fraction. In all cases, the acquisition time was 5 s per data point and the test was stopped if the shear rate overpassed 10^3 s^{-1} ; (b) in the second test, for CMRFs the shear rate was logarithmically increased at a rate of 10 points/decade from 10^{-2} to 10^4 s^{-1} . The acquisition time was 10 s per data point. Once the resulting shear rate in (a) or shear stress in (b) was measured, the apparent viscosity was calculated by dividing the applied shear stress by the shear rate, calculated at the rim of the plates. Precautions were taken for the measurements to be as close as possible to the steady state (for further details see Ramos *et al.*⁶).

Rheograms for CMRFs did not exhibit a high-shear viscosity plateau under field. Several attempts were performed to reach it by using highly viscous Newtonian carriers (up to 790 Pa.s). However the high-shear viscosity plateau was still not observable. In this work, we estimated the high-shear viscosity using the Quemada expression: $\eta_{\infty} = \eta_c (1 - \phi/\phi_a)^{-2}$, where ϕ_a is the maximum packing fraction. Here, we assumed a Random Close Packing fraction for spheres, $\phi_a = 0.64$. As we will see

latter, this resulted in a reasonably good estimation of the high-shear viscosity in view of the scaling curves (c.f. Figure 7.3).

7.7. Results and discussion

Figure 7.1 represents typical steady shear rheograms for 20 vol% CMRFs at different external magnetic fields. Experimental data are shown for stress-controlled and strain-controlled tests demonstrating a reasonably good collapse in steady regime, as otherwise expected. Although not shown in this manuscript, rheograms were also obtained for other particle concentrations giving qualitatively similar results. The rheograms exhibit three clearly differentiated regions: i) an initial region with a noticeable noise because of the limited torque resolution of the magnetorheometer, ii) a plateau in the stress as expected in yield-stress materials, and iii) an increase in stress at large Mn corresponding to the flow region.



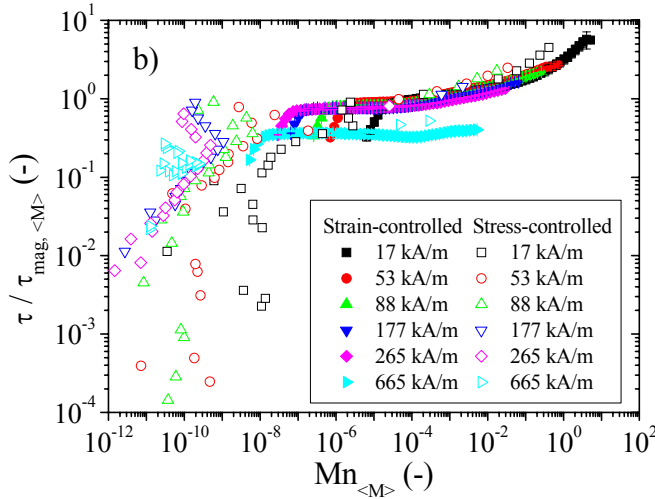


Figure 7.1 Dimensionless shear stress ($\tau/\tau_{mag,L}$, $\tau/\tau_{mag,sat}$, $\tau/\tau_{mag,<M>}$) curves as a function of the Mason number (Mn_L , Mn_{sat} , $Mn_{<M>}$) for CMRFs at 20 vol% concentration: a) scaled by the linear magnetostatic stress, $\tau_{mag,L}$ and saturated magnetostatic stress, $\tau_{mag,sat}$ as a function of Mn_L and Mn_{sat} ; b) scaled by the mean magnetization magnetostatic stress, $\tau_{mag,<M>}$ as a function of $Mn_{<M>}$. These rheograms were constructed using both strain-controlled (closed symbols) and stress-controlled (open symbols) modes. Labels correspond to the external magnetic field strength.

In Figure 7.1a we show scaling curves within the linear and *saturation* regimes according to Equations 7.7b and 7.5b, and 7.7c and 7.6b, respectively. The curves tend to collapse for the lowest field strengths (below 665 kA/m). Deviations in the collapse are due to the fact that this particular MR fluid is actually not dilute and hence a perfect scaling is not expected. The perfect scaling does not occur because single-width particle chains do not necessarily exist at this concentration (e.g. see Figure 9 in Fernández-Toledano *et al.*¹⁰). As expected, a better scaling was observed for particle concentrations below 20 vol% (results not shown here for brevity). Interestingly, the curve corresponding to 665 kA/m (that is very

close to saturation as we will demonstrate later) is clearly below measurements in the linear regime. This suggests that other interparticle interactions (remanence, short range attractions, colloidal interactions, etc ...) exist between the particles, that become noticeable at low fields, by increasing the stress level. These interactions have been already reported in the literature, for instance, under the frame of a two-step yielding.¹⁰ Interestingly, when the magnetic field strength increases up to saturation, magnetostatic forces govern and therefore the stress curves stay below those corresponding to the linear regime.

In Figure 7.1b we show the rheograms in dimensionless form now using Equations 7.7a and 7.4. The calculation of $\tau_{mag, <M>}$ and $Mn_{<M>}$ requires the computation of the magnetization of the particle $\langle M_p \rangle$ using the internal magnetic field strength H instead of the external one H_0 . For the calculation of the internal magnetic field strength we used the

expression: $H = \frac{3\mu_{cr}}{\mu_{pr} + 2\mu_{cr}} H_0$, that corresponds to the internal field in

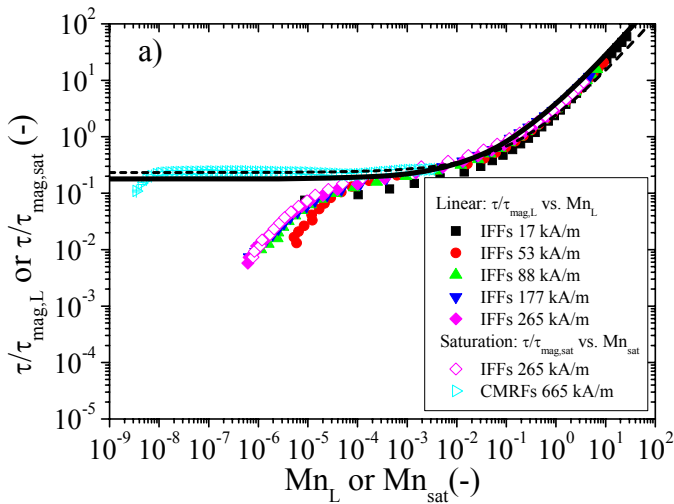
an isolated and magnetically linear spherical particle (see section 5.11 in reference 25). Here, μ_{pr} and μ_{cr} were calculated from the experimental magnetization curves using the MM approximation. The process required a self-consistent approach: (i) the internal magnetic field was calculated using the magnetic permeabilities for the external magnetic field, (ii) the magnetization was calculated by interpolation in the magnetization curve, (iii) the magnetic permeabilities for the internal field were calculated, (iv) the steps (ii) and (iii) were repeated until convergence. The magnetization and the internal magnetic field were thus obtained. The inspection of Figure 7.1b reveals that, as expected, the collapse in the linear regime is now much better than in Figure 7.1a (note that there are not free fitting

parameters), and *saturation* values (at 665 kA/m) still remain clearly below the data corresponding to the linear regime, as previously discussed, because of the presence of other interparticle interactions.

Rheograms for IFFs are represented in Figure 7.2. The scaling in the linear and saturation regimes is shown in Figure 7.2a. Obviously, the scaling with the magnetic field strength for IFFs is even better than in the case of CMRFs for the same particle concentration. A very good collapse is found for all magnetic field strengths investigated because in this case $\langle M_p \rangle \approx 3\beta H_0$ in a very wide range of magnetic fields in agreement with Ruiz-López *et al.*⁸ (we will come back later to this point in the discussion of Figure 7.4). The good collapse with measurements on CMRFs at 665 kA/m (i.e. very close to saturation) also reinforces the statement that other interparticle interactions exist in CMRFs that appear at low fields (c.f. Figure 7.2a). Contrary to the case of CMRFs, IFFs tend to exhibit a low-shear viscosity plateau instead of an apparent yield stress. For more details on the appearance of this low-shear viscosity plateau we refer to Berli and de Vicente¹¹. Together with experimental data we also show the predictions of Equation 7.12 in Figure 7.2a. As expected a very good agreement is found. In Figure 7.2b we show the stress versus Mason number curves scaled by $\tau_{mag <M>}$ and $Mn_{<M>}$ under the MM approximation. The good scaling demonstrates that the MM approximation is valid in these systems and solely magnetostatic and hydrodynamic interactions play a role, contrary to CMRFs where other interparticle interactions exist.

Next, rheograms contained in Figures 7.1 and 7.2 are plotted in the form of dimensionless viscosity curves for a direct comparison to theoretical models, using the mean magnetization of the particles. Results are shown for 20 vol% MR fluids in Figure 7.3. They demonstrate again that the MM

approximation works reasonably well for a wide range of external magnetic field strengths from 17 kA/m to 265 kA/m in both MR fluids investigated, independently of the obvious physical differences in the magnetization mechanism of the suspensions. The shift towards the right in the viscosity curves for the lowest fields, when compared to saturation, is again a consequence of the existence of other interparticle interactions. In agreement with Figure 7.2, data for IFFs collapse reasonably well with CMRFs at fields close to saturation. From the inspection of Figure 7.3 we can appreciate again the difficulty in identifying the high-shear viscosity plateau in CMRFs and justifies the use of Quemada expression to estimate it (see Experimental section). The good scaling obtained demonstrates that taking the viscosity from this particular analytical expression is a reasonable approximation.



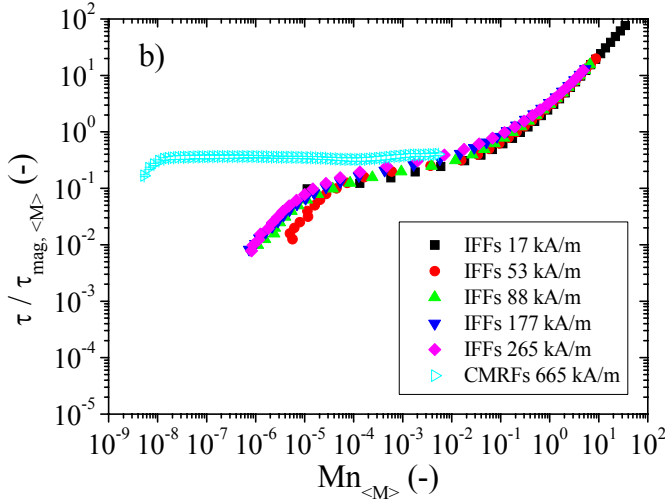


Figure 7.2 Dimensionless shear stress ($\tau/\tau_{mag,L}$, $\tau/\tau_{mag,sat}$, $\tau/\tau_{mag,<M>}$) curves as a function of the Mason number (Mn_L , Mn_{sat} , $Mn_{<M>}$) for IFFs at 20 vol% concentration: a) scaled by the linear magnetostatic stress, $\tau_{mag,L}$ and saturated magnetostatic stress, $\tau_{mag,sat}$ as a function of Mn_L and Mn_{sat} ; b) scaled by the mean magnetization magnetostatic stress, $\tau_{mag,<M>}$ as a function of $Mn_{<M>}$. These rheograms were constructed using stress-controlled mode. Labels correspond to the external magnetic field strength. Solid and dashed lines correspond to Equation 7.12 for IFFs and CMRFs in saturation regime, respectively.

Curves similar to those shown in Figure 7.3 were also measured for a wide range of concentrations in both CMRFs and IFFs. The collapse was similarly good to the 20 vol% example reported in this work. Once the viscosity curves were measured for a given concentration at a range of magnetic field strengths, a Casson plastic model (Equation 7.10) was fitted to obtain the critical Mason number Mn^* associated to the transition from magnetostatic to hydrodynamic control of the suspension structure.

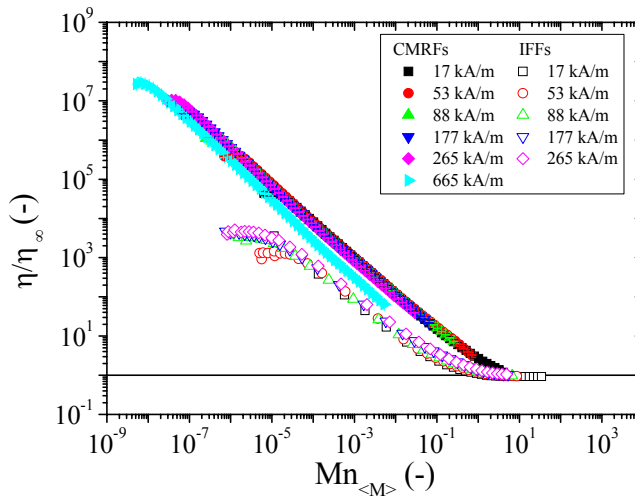


Figure 7.3 Dimensionless viscosity η curves (scaled by the high-shear viscosity η_∞ of the MR fluid) as a function of Mason number $Mn_{\langle M \rangle}$ for MR fluids at 20 vol% reported in Figures 1 and 2. For CMRFs the high-shear viscosity is taken from the Quemada expression (see text).

At this point, it is important to highlight that for a very wide range of particle loadings, the mean magnetization of a particle in suspension is not dependent on the particle loading: $\langle M_p \rangle \neq \langle M_p \rangle(\phi)$. This is clearly appreciated in Figure 7.4 for both CMRFs and IFFs. This finding means that the magnetic stress τ_{mag} is proportional to the particle volume fraction because in its derivation we assumed a linear dependence of the particle area with concentration: $A_p \propto \phi$ (see Equation 7.7 and Annex). The later assumption is valid in a wide range of experimental data for IFFs. However, in the case of CMRFs this assumption is only valid at very low concentrations (see below). Bearing in mind that in dilute systems $\tau_y \propto \tau_{mag}$ and $\eta_\infty \approx \eta_c$, in view of Equation 7.11 the MM approximation predicts a linear dependence of the critical Mason number Mn^* with the particle concentration.

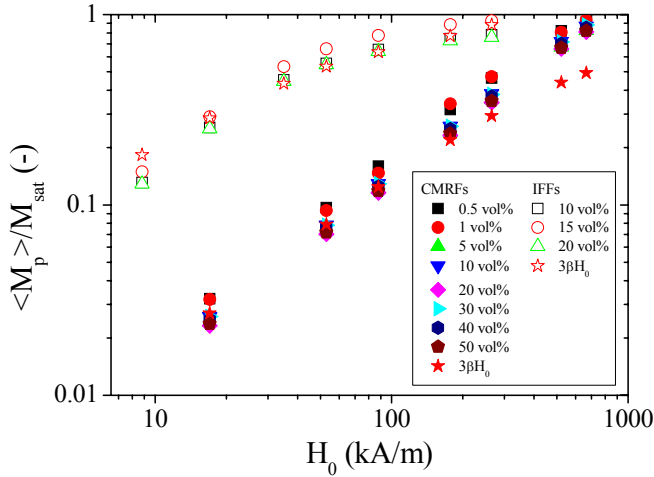


Figure 7.4 Mean magnetization of the particle $\langle M_p \rangle$ scaled with the saturation magnetization as a function of the external magnetic field strength H_0 for different particle loadings ϕ in CMRFs (closed symbols) and IFFs (open symbols). For details on the self-consistent approach used to calculate $\langle M_p \rangle$ we refer to the text. $M_{sat} = 1707$ kA/m for CMRFs and $M_{sat} = 25.5$ kA/m for IFFs.

To test this prediction we now discuss the volume fraction dependence of the critical Mason number Mn^* . The scaling for the linear (Mn^*_L) and saturation (Mn^*_{sat}) approximations gave very similar results to $Mn^*_{<M>}$. As expected, a slightly better collapse was observed for $Mn^*_{<M>}$. Hence, in this discussion we will focus on the scaling of $Mn^*_{<M>}$. Results obtained for the critical Mason number $Mn^*_{<M>}$ as a function of particle concentration ϕ are contained in Figure 7.5. We observe that the stress-controlled and strain-controlled tests provide very similar numbers giving also an estimate of the consistency of the fitting to the Berli and de Vicente model (Equation 7.10). IFFs closely follow a straight line of slope one in very good agreement with the MM

approximation for a very wide range of particle loadings (up to 20 vol%); the larger the particle concentration, the larger the number of single-width particle chains per unit surface. As a result this will promote a linearly increasing τ_y and Mn^* with concentration. Together with our data on IFFs we also include data from Ramos *et al.*⁶ These data are in reasonably good agreement with our data on IFFs. Our simulation data are also contained in Figure 7.5 and demonstrate again a linear dependence with volume fraction. This was expected because the MM approximation is employed in the simulations and because only magnetostatic interactions are considered between Hard Spheres. Interestingly the simulation results are very close to experiments on IFFs in spite of the many simplifications in the simulation model. This was expected in view of Ruiz-López *et al.*⁸

In Figure 7.5 we also include experimental data on CMRFs both in the linear ($H_0 \in [17kA/m, 265kA/m]$) and saturation ($H_0 = 665kA/m$) regimes. In the low concentration regime (below 5 vol%), results collapse very well with simulations and experiments on IFFs. This was expected because the MM approximation becomes exact in this limit. However, results for CMRFs in the linear regime are clearly higher than in saturation for particle loadings above 5 vol%. The reason for this is that other contributions to the yield stress τ_y play a role in the linear regime in agreement with the discussion of Figure 7.1. This gives a stronger than linear dependence of τ_y with ϕ . Mn^* data for saturated CMRFs are obviously closer to those obtained in IFFs because dipolar magnetostatic interactions prevail. However, data for CMRFs do not exactly overlap onto IFFs suggesting that complete saturation is not fully reached in CMRFs (c.f. Figure 7.4).

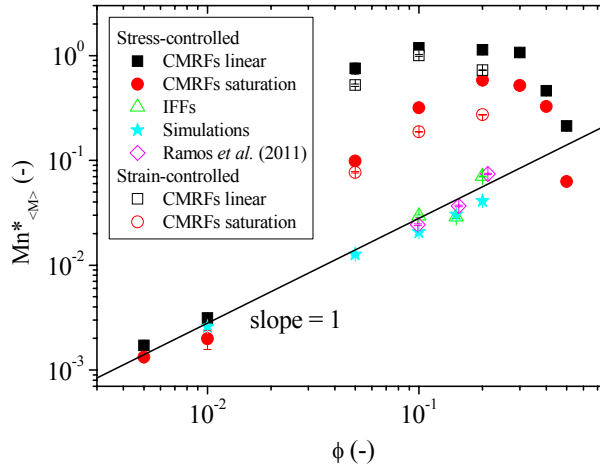


Figure 7.5 Volume fraction dependence of the critical Mason number $Mn^*_{<M>}$ for CMRFs and IFFs as obtained by fitting the dimensionless viscosity curves to the Casson model (Equation 7.10). In these fittings the high-shear viscosity for the CMRFs is taken from the Quemada equation and for the IFFs is taken from the high-shear viscosity in the absence of fields during the preshear.

For even larger concentrations a maximum with particle concentration is observed because of two contributions to Mn^* : on the one hand, for larger concentrations, the high-shear viscosity contribution to Mn^* becomes more important and therefore, according to Equation 7.11a the volume fraction dependence reduces as follows: $\eta_c/\eta_\infty = (1 - \phi/\phi_a)^2$. On the other hand, when the volume fraction increases, the permeability of the carrier fluid μ_{cr} in Equation 7.11a must be replaced by the permeability of the suspension μ_{sr} . This is so because μ_{sr} will become closer and closer to the permeability of the particles when increasing the concentration. Hence, the τ_y and Mn^* will decrease with the particle loading because the magnetostatic interactions will decrease as well.

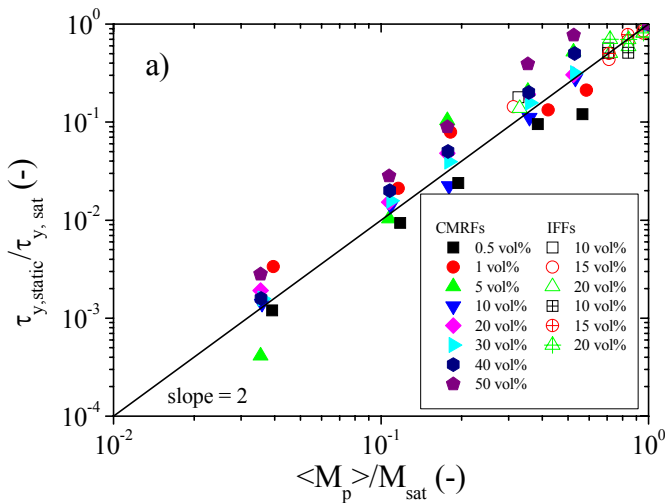
At this point it is worth to remark that we explored different possibilities in the calculation of the Mason number for the saturated CMRFs (Equation 7.6b). In particular, we explored three cases: i) the suspension magnetization was directly measured in a magnetorheometer, ii) the suspension magnetization was calculated using $M_{susp} = \phi \langle M_p \rangle$ from magnetization measurements in carbonyl iron powders, and iii) the suspension magnetization was calculated again using $M_{susp} = \phi \langle M_p \rangle$ from Frohlich-Kennelly equation fittings to magnetization curves in carbonyl iron powders. Results for the three cases demonstrate that the particular way of calculating the suspension magnetization in saturation was negligible in the results presented in this work.

Overall, Figure 7.5 suggests that even though the MM approximation is not strictly applicable to these systems, it is still a very good approximation for IFFs and it is also valid for CMRFs in both the dilute case and saturation regimes.

Finally, in Figure 7.6 we show the dimensionless yield stresses as a function of the dimensionless mean magnetization of the particles $\langle M_p \rangle / M_{sat}$. This figure allows us to evaluate the theoretical quadratic dependence predicted by Equation 7.7 in dilute MR fluids. In Figure 7.6a we include the static yield stresses as obtained from the low-shear stress plateau in log-log representation (see Figures 7.1 and 7.2). In the case of the IFFs, an *apparent static yield stress* is estimated using two approaches (tangent method⁶ and the stress level at $\dot{\gamma} = 0.1s^{-1}$). In both kinds of MR fluids a quadratic dependence with the particle magnetization is observed suggesting that the MM approximation is valid. In fact, under the assumption that $\tau_y \approx \tau_{mag}$, from Equation 7.7 we get

$\tau_y / \tau_{y, \text{sat}} = \langle M_p \rangle^2 / M_{\text{sat}}^2$. This equation is plotted as a solid line in Figure 7.6a and as observed is in very good agreement with the data.

In Figure 7.6b we show results for the dynamic yield stress obtained by fitting the shear stress as a function of the shear rate in lin-lin representation, for shear rates above 100s^{-1} . In the case of CMRFs, it was necessary to work under strain-controlled mode to increase the number of points for better statistics in the fittings (see Experimental section). In this case, the data clearly deviate and do not superimpose although the slope seems to be still 2. In our opinion, a key point to understand the deviation of the data on the dynamic yield stress is the fact that extrapolations are done on a narrow range of shear rates (or stresses) and the high-shear viscosity is hardly ever achieved in CMRFs. These results are coherent with the shift towards the right in the viscosity curves for the lowest fields observed in Figure 7.3 as a consequence of the existence of other interparticle interactions. As expected, for the largest fields investigated and the lower concentrations the agreement is much better with data on IFFs and theoretical predictions.



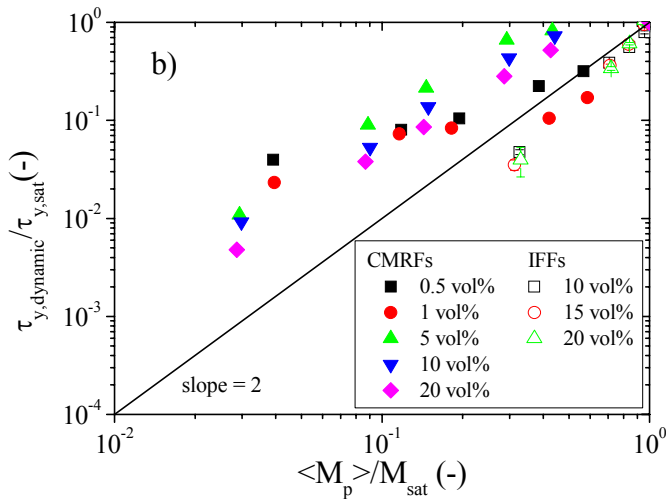


Figure 7.6 Particle magnetization dependence of the static $\tau_{y,static}$ (a) and dynamic $\tau_{y,dynamic}$ (b) yield stresses, normalized by the yield stress in saturation $\tau_{y,sat}$. Particle magnetization $\langle M_p \rangle$ was normalized by the saturation magnetization M_{sat} . Solid line corresponds to the theoretical prediction $\tau_y/\tau_{y,sat} = \langle M_p \rangle^2 / M_{sat}^2$. Open symbols in Figure 7.6a: $\dot{\gamma} = 0.1 s^{-1}$. Crossed open symbols in Figure 6a: tangent method.

7.8. Conclusions

The mean magnetization (MM) approximation has been tested against conventional MR fluids (CMRFs) and inverse ferrofluids (IFFs). Results demonstrate that although the approximation is not strictly valid in the field strength and concentration range of general interest, and in spite of the physical differences in the magnetization mechanism of the suspensions, the approximation is still applicable in some particular cases. In IFFs the MM approximation applies very well for all magnetic field strengths and concentrations studied. However, in the case of CMRFs the

MM approximation is only applicable in the dilute regime and/or magnetic saturation.

Acknowledgements

This work was supported by MAT 2013-44429-R project (Spain) and by Junta de Andalucía P10-RNM-6630, P10-FQM-5977 and P11-FQM-7074 projects (Spain). J.A.R.-L. acknowledges the financial support by the “Ministerio de Educación: Becas del Programa de Formación del Profesorado Universitario (FPU)” (AP2010-2144). J.C.F.-T. acknowledges the Interuniversity Attraction Poles Programme (IAP 7/38 MicroMAST) of the Belgian Science Policy Office for the financial support.

Annex: Estimation of the area per particle

The estimation of the area per particle was achieved assuming the following statements: First, the MR fluid is assumed to be formed by single-width particle chains, and confined in a plate-plate configuration with upper and lower area, A , and a gap between the plates, h . The volume fraction can be expressed as the volume of all the particles divided by the total volume of the suspension:

$$\phi = \frac{N_p V_p}{V} = \frac{4\pi N_p a^3}{3Ah} \quad (7.A1)$$

Here N_p is the number of particles in the sample, V_p is the particle volume, a is the particle radius and $V = Ah$ is the total volume of the MR fluid. Assuming gap-spanning single-width particle chains, the number of chains, N_C , can be written as $N_C = 2aN_p/h$. In terms of

stress, the total force is going to be exerted on the surfaces by the upper or the lower particles. So, the area per particle, A_p can be obtained as the total area divided by the number of chains and all the particles have a surrounding area distributed in shells around the fluid in cylindrical symmetry:

$$A_p = \frac{A}{N_c} = \frac{Ah}{2aN_p} = \frac{2\pi a^2}{\phi} \quad (7.A2)$$

References

- 1 J. Rabinow, *AIEE Trans.*, 1948, **67**, 1308–1315.
- 2 A. T. Skjeltorp, *Phys. Rev. Lett.*, 1983, **51**, 2306-2309.
- 3 R. E. Rosensweig, *Ferrohydrodynamics*, Dover, New York, 1997.
- 4 B. J. de Gans, H. Hoekstra and J. Mellema, *Faraday Discuss.*, 1999, **112**, 209–224.
- 5 J. Ramos, J. de Vicente and R. Hidalgo-Álvarez, *Langmuir*, 2010, **26**(12), 9334-9341.
- 6 J. Ramos, D. J. Klingenberg, R. Hidalgo-Álvarez and J. de Vicente, *J. Rheol.*, 2011, **55**, 127-152.
- 7 J. de Vicente, D. J. Klingenberg and R. Hidalgo-Álvarez, *Soft Matter*, 2011, **7**, 3701-3710.
- 8 J. A. Ruiz-López, J. C. Fernández-Toledano, D. J. Klingenberg, R. Hidalgo-Álvarez and J. de Vicente, *J. Rheol.*, 2015, (submitted).

-
- 9 J. P. Segovia-Gutiérrez, C. Berli and J. de Vicente, *J. Rheol.*, 2012, **56**(6), 1429-1448.
 - 10 J. C. Fernández-Toledano, J. Rodríguez-López, K. Shahrivar, R. Hidalgo-Álvarez, L. Elvira, F. Montero de Espinosa and J. de Vicente, *J. Rheol.*, 2014, **58**(5), 1507-1534.
 - 11 C. L. A. Berli and J. de Vicente, *Appl. Phys. Lett.*, 2012, **101**(2), 021903-1-4.
 - 12 D. J. Klingenberg, J. C. Ulicny and M.A. Golden, *J. Rheol.*, 2007, **51**, 883-893.
 - 13 M. Ocalan, *Magnetorheological fluids for extreme environments: stronger, lighter, hotter*, Ph. D. Thesis, Massachusetts Institute of Technology, 2011.
 - 14 F. Vereda, J. de Vicente, J. P. Segovia-Gutiérrez and R. Hidalgo-Álvarez, *J. Appl. Phys.*, 2011, **110**, 063520.
 - 15 F. Vereda, J. P. Segovia-Gutiérrez, J. de Vicente and R. Hidalgo-Álvarez, *J. Phys. D: Appl. Phys.*, 2015, **48**, 015309.
 - 16 L. C. Marshall, F. Zukoski and J. Goodwin, *J. Chem. Soc., Faraday Trans.*, 1989, **85**, 2785-2795.
 - 17 J. M. Ginder and L. C. Davis, *Appl. Phys. Lett.*, 1994, **65**, 3410-3412.
 - 18 J. E. Martin and R. A. Anderson, *J. Chem. Phys.*, 1996, **104**(12), 4814-4827.

- 19 J. de Vicente, M. T. López-López, J. D. G. Durán and F. González-Caballero, *Rheol. Acta*, 2004, **44**, 94-103.
- 20 O. Volkova, G. Bossis, M. Guyot, V. Bashtovoi and A. Reks, *J. Rheol.*, 2000, **44**, 91-104.
- 21 J. C. Fernández-Toledano, J. A. Ruiz-López, R. Hidalgo-Álvarez and J. de Vicente, *J. Rheol.*, 2015, **59**(2), 475-498.
- 22 H. G. Lager, T. Breinlinger, J. G. Korvink, M. Moseler, A. Di Renzo, F. Di Maio and C. Bierwisch, *J. Non-Newtonian Fluid Mech.*, 2015, **218**, 16-26.
- 23 J. R. Melrose and D. M. Heyes, *J. Chem. Phys.*, 1993, **98**(7), 5873-5886.
- 24 J. P. Segovia-Gutiérrez, J. de Vicente, R. Hidalgo-Alvarez and A. M. Puertas, *Soft Matter*, 2013, **9**, 6970-6977.
- 25 J. D. Jackson, *Classical Electrodynamics (3rd Edition)*, Wiley & Sons, New York, 1999.

Part III. Effect of the
polydispersity in particle size
in magnetorheology

Chapter 8.

Simulations of Polydisperse Magnetorheological Fluids: a Structural and Kinetic Investigation

Juan Carlos Fernández-Toledano, José Antonio Ruiz-López, Roque Hidalgo-Álvarez and Juan de Vicente.

**This article is published in *Journal of Rheology*. Volume: 59(2).
Pages: 475-498. 2015.**

Abstract

A simulation method is proposed to explore the effect of particle size polydispersity in magnetorheology including Brownian motion. The method aims to extend the classical particle-level simulation methodology developed by Klingenberg and co-workers in the 90's for the case of polydisperse MR fluids. The simulation study concerns the aggregation kinetics at rest as well as the rheological behavior under start-up of steady shear and dynamic oscillatory shear tests at increasing strain amplitudes. Results demonstrate that the effect of polydispersity is only relevant at the transition regime between magnetostatic to hydrodynamic control of the suspension structure. The yielding behavior is correlated to the structural

characteristics (radial distribution functions, pair correlation functions and angular connectivities) of the magnetorheological (MR) fluids before the onset of flow. A more abrupt transition is observed for polydisperse MR fluids because interparticle links are weaker in this case if compared to monodisperse suspensions in spite of the fact that polydisperse MR fluids exhibit a larger connectivity.

8.1. INTRODUCTION

Conventional magnetorheological (MR) fluids are colloidal systems essentially formulated by dispersion of micron-sized carbonyl iron (magnetizable) particles in a non magnetic carrier. They have the ability to change from a liquid-like to a solid-like state upon the application of an external magnetic field (so-called MR effect). On the other hand, electrorheological (ER) suspensions are the electric analog of MR suspensions, whose rheological properties are enhanced by the application of an electric field. Both MR and ER fluids are characterized by the appearance of a yield stress for sufficiently large particle loadings and field strengths [Parthasarathy and Klingenberg (1996); Bossis *et al.* (2002); Gonzalves *et al.* (2006); Park *et al.* (2010); de Vicente *et al.* (2011); Segovia-Gutiérrez *et al.* (2012)].

Carbonyl iron particles employed in the formulation of commercial MR fluids are obtained by thermal decomposition of pentacarbonyl iron, and this process typically results in a very polydisperse powder with polydispersity $\nu \geq 0.20$ [Phule (1998)]. Here ν stands for the ratio between the standard deviation and the average diameter of the particles. For instance, $\nu = 0.38$ for a fine carbonyl iron grade (HS grade) commercialized by BASF SE and can be even larger for other grades ($\nu = 0.42$ for HQ grade and $\nu = 0.52$ for OM grade). Currently, to the

best of our knowledge, there is not a chemical route available in the literature to obtain monodisperse ($\nu = 0$) carbonyl iron particles of micrometric size. Separation and fractionation approaches seem to be the only possibilities to get less polydisperse powders but these methods are costly and time-consuming [e.g. Chiriac and Stonian (2009)]. As a result, all experiments reported up to now in the MR literature on conventional MR fluids having commercial applications, concern inherent polydisperse suspensions and therefore a question arises: would ideal monodisperse MR fluids have better MR performance than their polydisperse counterparts for the same mean particle diameter? In our opinion, particle-level simulations can help to answer this question.

Despite the fact that in practice MR fluids are highly polydisperse in particle size, in most particle-level simulations reported in the literature the MR fluid is treated as a suspension of neutrally buoyant monodisperse spherical particles dispersed in a Newtonian carrier liquid. As the typical experimental mean particle sizes are of the order of microns, thermal motion and inertial effects are discarded in the simulations [Klingenberg *et al.* (1989); Klingenberg *et al.* (1991); See and Doi (1992); Klingenberg *et al.* (1993); Liu *et al.* (2013)].

If compared to particle-level simulations on monodisperse systems, simulation studies on MR fluids containing dispersed particles with different sizes are very scarce. Furthermore, most of them focus on bidisperse MR fluids where particles having only two different sizes coexist in suspension [Kittipoomwong *et al.* (2002); Kittipoomwong *et al.* (2005); Ekwebelam and See (2009)]. Kittipoomwong *et al.* (2002) reported simulation data on bidisperse MR fluids under shearing flows. They demonstrated that the yield stress of bidisperse suspensions was larger than that of monodisperse suspensions at the same overall particle

volume fraction. In a follow-up paper by the same authors [Kittipoomwong *et al.* (2005)], a more comprehensive simulation was carried out to demonstrate that the enhanced stress transfer in bidisperse suspensions is not associated with an increase in particle packing. Actually, the smaller particles cause the larger particles to form more chainlike aggregates than those formed in monodisperse suspensions. These results were confirmed later by simulations carried out by See and coworkers [Ekwebelam and See (2009)]. Their simulations revealed that bidisperse suspensions have a higher tendency to form straight or close-to-aligned structures than the monodisperse suspensions. The stress enhancement in bidisperse suspensions was anticipated to be due to the population and orientation of interacting large particles in the bidisperse suspensions.

The number of simulation papers on MR fluids involving a continuous particle size distribution is even smaller. To the best of our knowledge, only two papers, the papers by Wang and coworkers [Wang *et al.* (1997)] and Wereley and coworkers [Sherman and Wereley (2013)] address this issue. A pioneering paper by Wang *et al.* (1997) used 2D molecular dynamic simulation methods to demonstrate that the shear stress of ER fluids decreases with increasing the standard deviation of a Gaussian distribution of the particle size and then reaches a steady value at high polydispersity levels. In their simulations, they adopt a local-field approximation to consider mutual polarization effects between particles. The standard deviation of the distribution changed from 0.0 to 3.0. The reduction of the yield stress when increasing the polydispersity level was ascribed to the imperfection and weakness of the chain-like disordered structures. Thermal forces were not included in the simulations and only two Mason numbers were investigated. More recently, Sherman and Wereley (2013) carried out a large-scale (high particle count) simulation

study on polydisperse MR fluids with log-normal distribution at a particle volume concentration of $\phi = 0.30$. In their study, the mean particle diameter was fixed at 8 microns and the carrier fluid viscosity was 0.1 Pa·s. They investigated the structure formation and shear rheology for a wide range in standard deviation of the distribution from 0.001 to 0.3. Their results demonstrate that: i) as the particle distribution size parameter increases, particles tend to form more irregular structures; ii) increasingly irregular structures manifest as a 25 % reduction in the shear stress at low Mason numbers; iii) wide particle size distributions correspond to a reduction in particle cluster size, and a small increase in connectivity. Again, thermal motion was neglected.

In an attempt to better understand the effect of particle size polydispersity, in this manuscript we carry out a comprehensive 3D simulation study to compare the behavior of perfectly monodisperse MR fluids and polydisperse suspensions having the same average diameter but different standard deviation, in the absence and presence of shearing flows. Bearing in mind the success of the classical particle-level simulation methodology developed by Klingenberg and coworkers in the 90's [e.g. Parthasarathy and Klingenberg (1996)], in this manuscript we extend, for the first time, this methodology to include a continuous polydispersity in particle size and thermal motion to capture the different time scales and Brownian diffusion of the particles (due to the difference in particle size). Particle concentrations and size distributions explored here are chosen to be similar to those employed in the formulation of commercial MR fluids. In particular, we study concentrated MR fluids (up to 20 vol%, $\phi = 0.20$) with particle sizes that follow a skewed distribution as frequently observed in experiments (in this case a Schultz distribution with standard deviation $\nu = 0.2$ and polydispersity index $PDI = 1.12$). Also, for the first time, the range of Mason numbers simulated will span from the

"solid-like" to the "liquid-like" regimes. The effect of polydispersity in particle size is studied here during field driven structuration at rest, under stress growth (also known as start-up tests) and unsteady dynamic oscillatory shear tests.

8.2. SIMULATION TECHNIQUE

Brownian dynamics simulations were used to model mono- and polydisperse MR fluids in a confined geometry between parallel plates. The MR fluid was composed by $N = 1000$ neutrally buoyant hard spheres of diameter σ_i in a Newtonian continuous phase with a viscosity η_c . The particles were initially distributed randomly in a box with dimensions L_x , L_y , and L_z with $L_x = L_y = L$. The box height was $L_z = 15\sigma_m$ for all the simulation results shown in this work. This is a typical box height used in this kind of simulations for the monodisperse case. We also carried out simulations at $L_z = 20\sigma_m$ but did not find any significant differences. Here, σ_m is the mean value of the particle

diameter. $L = \sqrt{\frac{\pi}{6\phi L_z} \sum_{i=1}^N \sigma_i^3}$ changes according to the total volume

fraction, ϕ , of the MR fluid and the diameter distribution $\{\sigma_i\}$. Periodic boundary conditions were imposed in the x and y directions. The shearing flow was created in the x direction.

8.2.1 Particle size distribution

Polydispersity is included in the form of a Schultz particle diameter distribution with the following normalized probability [Schultz (1939)]:

$$P(\sigma) = \left(\frac{z+1}{\sigma_m} \right)^{z+1} \frac{\sigma^z}{\Gamma(z+1)} \exp\left(-\frac{z+1}{\sigma_m} \sigma \right) \quad (8.1)$$

where $\Gamma(x)$ is the gamma function and the z parameter is a measure of the width of the distribution through the quadratic dispersion of the distribution:

$$\nu^2 = \frac{1}{\sigma_m^2} \int (\sigma - \sigma_m)^2 P(\sigma) d\sigma = \frac{1}{z+1} \quad (8.2)$$

The polydispersity index (*PDI*), defined as the fourth moment of the distribution divided by the third moment and the average diameter, is in this case given by the following equation $PDI = 3\nu^2 + 1$. In Figure 8.1 we show the histogram of the particle size distribution used in this work together with the Schultz distribution for $\nu = 0.2$ (i.e. $PDI = 1.12$). For completeness, in Figure 8.1 we also include another distribution that is frequently used in particle size characterization: the log-normal distribution. As observed, both distributions are very similar. In this work, we will stay with the Schultz distribution.

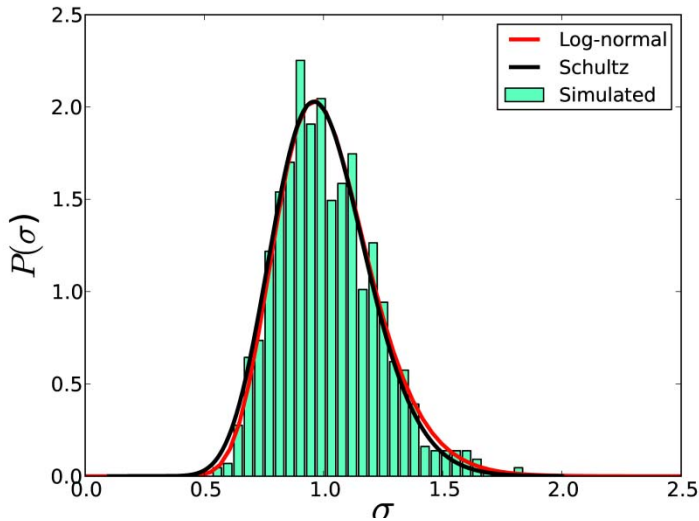


Figure 8.1.- Particle size distribution for the polydisperse MR fluid investigated in this work. The lines correspond to the Schultz and Log-normal ($\sigma_m = 1$ and $\nu = 0.2$) distributions.

8.2.2. Equation of movement

The time evolution of the system is described by the Langevin equation:

$$M_i \frac{d^2 \vec{r}_i(t)}{dt^2} = -\zeta_i \left(\frac{d\vec{r}_i(t)}{dt} - \vec{u}_i^\infty \right) + \vec{F}_i + \vec{f}_B(t) \quad (8.3)$$

where M_i is the mass of particle i , $\zeta_i = 3\pi\eta_c\sigma_i$ is the friction coefficient, \vec{u}_i^∞ is the ambient fluid velocity at the center of particle i , and $\vec{f}_B(t)$ is a random force introduced to model the Brownian motion of the particles $f_B \propto \sqrt{\kappa_B T \zeta_i / \Delta t}$. Here, κ_B is the Boltzmann constant, T is the absolute temperature and Δt is the time step. In this way, Langevin dynamics allows controlling the temperature like a thermostat. The force acting on particle i , \vec{F}_i , includes induced magnetostatic forces coming

from interparticle interactions \vec{F}_i^{mag} , short range repulsive forces between spheres \vec{F}_i^{HS} , and between spheres and walls \vec{F}_i^{wall} .

$$\vec{F}_i(\vec{r}_i) = \vec{F}_i^{mag}(\vec{r}_i) + \vec{F}_i^{HS}(\vec{r}_i) + \vec{F}_i^{wall}(\vec{r}_i) \quad (8.4)$$

This simple model neglects the hydrodynamic interactions between the particles. Despite this assumption, it is found that the macroscopic dynamics is predicted rather accurately by this model and avoiding the calculation of hydrodynamic force, makes this method the fastest. Moreover, it has been reported that the inclusion of hydrodynamic interactions has quantitative but no qualitative importance in the dynamic response of ER suspensions [Parthasarathy *et al.* (1999)]. More sophisticated numerical schemes based on the Stokesian Dynamics [Brady and Bossis (1988)] are capable of treating multi-body hydrodynamic interactions. This technique has valuable properties when small-scale phenomena are investigated, but still computationally too demanding.

8.2.3. Interactions

As frequently done in the simulation of MR fluids, the magnetostatic force between spheres is treated in the dipole-dipole limit [Klingenberg *et al.* (1989, 1991)]. This dipolar approximation is known to underestimate the magnetostatic interaction between closely-spaced particles. Accordingly, the application of an external magnetic field $\vec{H} = H_0 \hat{z}$ induces a magnetic moment in each particle:

$$\vec{m}_i = m_i \hat{z} = \frac{\pi \sigma_i^3 \beta H_0}{2} \hat{z} = \sigma_i^{*3} m_m \hat{z} = \sigma_i^{*3} \vec{m}_m \quad (8.5)$$

where $m_m = \pi \sigma_m^3 \beta H_0 / 2$ is the magnetic moment for a mean particle size, $\sigma_i^* = \sigma_i / \sigma_m$ is the reduced diameter of the particle i (see below),

$\beta = (\mu_{pr} - \mu_{cr}) / (\mu_{pr} + 2\mu_{cr})$ is the contrast factor, $\mu_{pr} = \mu_p / \mu_0$ is the relative magnetic permeability of the particles, $\mu_{cr} = \mu_c / \mu_0$ is the relative magnetic permeability of the carrier fluid, and μ_0 is the permeability of vacuum. Under this frame, multibody interactions are neglected, and H_0 represents the internal magnetic field within the suspension. With this, the force on sphere i due to sphere j is given by:

$$\vec{F}_{ij}^{mag}(\vec{r}_{ij}) = F_0^{ij} \left(\frac{\sigma_m}{r_{ij}} \right)^4 \left[(3 \cos^2 \theta_{ij} - 1) \hat{e}_r + \sin 2\theta_{ij} \hat{e}_\theta \right] \quad (8.6)$$

where r_{ij} is the center-to-center distance between spheres i and j , θ_{ij} is the angle between the line-of-centers and the \hat{z} direction, and \hat{e}_r and \hat{e}_θ are unit vectors in the r and θ_{ij} direction respectively.

The factor F_0^{ij} is defined as follows:

$$F_0^{ij} = \frac{3\mu_0\mu_{cr}m_im_j}{4\pi\sigma_m^4} = F_m\sigma_i^{*3}\sigma_j^{*3} \quad (8.7)$$

where $F_m = \frac{3\mu_0\mu_{cr}m_m^2}{4\pi\sigma_m^4}$. Here, F_0^{ij} is defined in terms of the average diameter due to the continuous particle size distribution. It is a generalization of the parameter $r_{\min} = (\sigma_i + \sigma_j) / 2$ used by Kittipoomwong *et al.* (2002) for bidisperse particles to a continuous distribution of particle diameters.

Short range repulsive forces between particles are modeled as an exponential interaction similarly to the Klingenberg approach [Klingenberg *et al.* (1989, 1991, 1993)]:

$$\vec{F}_{ij}^{rep}(\vec{r}_{ij}) = F_0^{ij} \exp[-\kappa(r_{ij} - \sigma_{ij})] \hat{r}_{ij} \quad (8.8)$$

where $\sigma_{ij} = 0.5(\sigma_i + \sigma_j)$ and κ is chosen to be $\kappa = 100 / \sigma_m$.

Again, a quasi-hard sphere exponential model is used to mimic the short-range repulsive forces between particles and walls:

$$\vec{F}_i^{wall,bottom}(\vec{r}_i) = F_0 \exp[-\kappa(z_i - 0.5\sigma_i)] \hat{z} \quad (8.9)$$

$$\vec{F}_i^{wall,top}(\vec{r}_i) = -F_0 \exp[\kappa(z_i - (L_z - 0.5\sigma_i))] \hat{z} \quad (8.10)$$

The Brownian motion is also considered to satisfactorily describe the motion of the smallest particles in the distribution. The thermal force on an isolated i particle is random with zero mean $\langle f_B(t) \rangle = 0$, and uncorrelated with a strength described by:

$$\langle f_B(t) f_B(t + \Delta t) \rangle = 2\kappa_B T \zeta_i \quad (8.11)$$

The relative magnitude of magnetic to Brownian energy is given by the so-called λ parameter [de Vicente *et al.* (2011)]:

$$\lambda = \frac{\pi\mu_0\mu_{cr}\beta^2\sigma_m^3 H_0^2}{16\kappa_B T} \quad (8.12)$$

This parameter is usually high for typical experimental parameters and therefore Brownian motion is frequently neglected, in the monodisperse case [Klingenberg *et al.* (1989), Wang *et al.* (1997), Kittipoomwong *et al.* (2002), Sherman and Wereley (2013)]. Although this consideration does not affect significantly the structure of the particles for high enough λ values [Segovia-Gutiérrez *et al.* (2013)], experiments are usually performed at a constant temperature and the Brownian motion could affect

to the diffusion of the smallest particles in the polydisperse MR fluid when a shear flow field is applied.

8.2.4. Flow kinematics

In this work we consider two shearing flows. On the one hand we perform stress growth tests (start-up tests) where the ambient fluid velocity $\vec{u}^\infty(\vec{r}_i)$ is given by:

$$\vec{u}_i^\infty = \begin{cases} 0 & t \leq 0 \\ \dot{\gamma} z_i \hat{x} & t > 0 \end{cases} \quad (8.13)$$

Here, $\dot{\gamma}$ is the magnitude of the shear rate tensor. On the other hand we also explore unsteady oscillatory shear tests. In this case, a local shear strain $\gamma(t) = \gamma_0 \sin(\omega t)$ is imposed on the top wall, while the lower wall keeps stationary. Here, the ambient fluid velocity is given by:

$$\vec{u}_i^\infty = \gamma_0 \omega z_i \cos \omega t \hat{x} \quad (8.14)$$

where γ_0 and ω are the amplitude and the angular frequency of the shear strain, respectively.

In order to use the Langevin thermostat for simulations under external flow, we switch-off the thermostat in the direction in which non-conservative external forces are applied. In this way, momentum conservation in the shear direction is recovered.

8.2.5. Stress tensor calculations

The microscopic derivation of the stress tensor is due to Irving and Kirkwood [Irving *et al.* (1950)]:

$$\tau_{\alpha\beta} = -\frac{1}{V} \left(\sum_{i=1}^N \frac{p_i^\alpha p_i^\beta}{M_i} + \sum_{i \neq j} r_{ij}^\alpha F_{ij}^\beta \right) \quad (8.15)$$

The first term in Equation 8.15 is the summation of the kinetic contribution to the stress tensor; here p_i^α is the α component of the momentum of the particle i . The second term represents the contribution of the potential to the stress tensor; here r_{ij}^α is the α component of the center-to-center distance connecting particles i and j , and F_{ij}^β is the β component of the total pairwise interaction between particles i and j (magnetostatic plus short range repulsive interactions). The contribution of the momentum, \vec{p}_i , to the stress tensor will be neglected for the shear rates considered in this work, and therefore the shear stress will be approximated by:

$$\tau_{\alpha\beta} \approx -\frac{1}{V} \sum_{i \neq j} r_{ij}^\alpha F_{ij}^\beta \quad (8.16)$$

8.2.6. Reduced units

It is important to choose appropriate reduced units to solve the equations of motion. In this manuscript we choose three natural scales: $\sigma_s = \sigma_m$, $M_s = M_m$ and $F_s = F_b$ for the length, mass and force, respectively. Here, σ_m stands for the mean diameter, M_m represents the mean particle mass, and finally F_b corresponds to a typical force of the order of the thermal force. With these natural scales one can define dimensionless variables. For instance, the reduced diameter is $\sigma_i^* = \sigma_i / \sigma_m$ and the reduced mass can be written as:

$$M_i^* = \frac{\pi\sigma_i^3\rho}{6M_m} = \frac{\pi\sigma_m^3\rho}{6M_m} \frac{\sigma_i^3}{\sigma_m^3} = \sigma_i^{*3} \quad (8.17)$$

where ρ is the density of the particle.

The origin of the force F_B can be explained as follows. The magnetic force contribution is orders of magnitude larger than the Brownian force for typical magnetic field strengths. In order to equilibrate the magnetic and Brownian contribution to the total force, we choose as a moment unit:

$$m_B = \frac{\pi\sigma_m^3\beta H_B}{2} \quad (8.18)$$

Here H_B is a relative low external magnetic field ($H_B = 200 A/m$), where the magnetic and Brownian contribution to the total force are similar. We select H_B and m_B as units of magnetic field strength and magnetic moment, respectively. With this, the moment of each particle can be expressed as follows:

$$m_i = m_B \left(\frac{\sigma_i}{\sigma_m} \right)^3 \frac{\beta(H_0)H_0}{\beta(H_B)H_B} = m_B \sigma_i^{*3} H_0^* \quad (8.19)$$

where the magnetic field parameter H_0^* is defined as $H_0^* = \frac{\beta(H_0)H_0}{\beta(H_B)H_B}$.

This normalization of the magnetic field differs from the normalization in Klingenberg *et al.* (1989), using the magnetic field strength, and Kittipoomwong *et al.* (2002), using the saturation magnetization as the normalization factor of the magnetic field. This normalization comes from numerical reasons for the inclusion of the thermal force.

For the reduced forces we use F_B as the force unit and as a result:

$$F_0^{*ij} = \frac{F_0^{ij}}{F_B} = \frac{3\mu_0\mu_{cr}m_i m_j}{4\pi\sigma_m^4 F_B} = \frac{3\mu_0\mu_{cr}m_B^2}{4\pi\sigma_m^4 F_B} \sigma_i^{*3} \sigma_j^{*3} H_0^{*2} = \sigma_i^{*3} \sigma_j^{*3} H_0^{*2} \quad (8.20)$$

On the other hand, the friction coefficient of particle i is given by:

$$\zeta_i = 3\pi\eta_c \sigma_i = 3\pi\eta_c \sigma_m \frac{\sigma_i}{\sigma_m} = 3\pi\eta_c \sigma_m \sigma_i^* \equiv \zeta_m \sigma_i^* \quad (8.21)$$

where $\zeta_m \equiv 3\pi\eta_c \sigma_m$ is the friction coefficient of the mean size particle.

With this, the reduced friction coefficient, can be obtained dividing Equation 8.21 by the scaling factor $\zeta_S = (M_m F_B / \sigma_m)^{1/2}$:

$$\zeta_i^* = \frac{\zeta_i}{\zeta_S} = \left(\frac{\sigma_m}{M_m F_B} \right)^{1/2} \zeta_m \sigma_i^* = \zeta_m^* \sigma_i^* \quad (8.22)$$

$$\text{where } \zeta_m^* \equiv \frac{3\pi\eta_c \sigma_m^{3/2}}{M_m^{1/2} F_B^{1/2}}.$$

Next step is to write the main dimensionless numbers employed in magnetorheology in reduced form. On the one hand, the ratio between magnetostatic to thermal energies (i.e. Lambda ratio, Equation 8.12) can be written as $\lambda = H_0^{*2} / (3T^*)$ where $T^* = k_B T / (F_B \sigma_m)$ is the reduced temperature. On the other hand, the ratio between hydrodynamic to magnetostatic energy (i.e. Mason number) can be written as $Mn = 8\eta\dot{\gamma} / (\mu_0\mu_{cr}\beta^2 H_0^2) = \dot{\gamma}^* \zeta_m^* / (2H_0^{*2})$ where $\dot{\gamma}^*$ is the reduced magnitude of the shear rate tensor. In this work, the scaling factor for the shear rate, $\dot{\gamma}$, is given by $\dot{\gamma}_S = \sqrt{F_B / (\sigma_m M_m)}$. At this point we would like to remark that different definitions for the dimensionless numbers can be found in the literature, all differing in a constant factor. For instance, the Mason number defined in Klingenberg *et al.* (2007) is sixteen times larger than the Mason number used in this manuscript and the normalized

shear rate employed by Klingenberg *et al.* (1991), $\dot{\gamma}_K^*$, is related to our Mason number through the following expression: $\dot{\gamma}_K^* = \dot{\gamma}^* \zeta_m^* / (4H_0^{*2})$.

Finally, using reduced units, the equation of movement for the polydisperse MR fluid is given by:

$$\sigma_i^{*3} \frac{d^2 \vec{r}_i^*(t^*)}{dt^{*2}} = -\zeta_m^* \sigma_i^* \left(\frac{d\vec{r}_i^*(t^*)}{dt^*} - \vec{u}^{*\infty} \right) + \vec{F}_i^*(t^*) + \vec{f}_B^*(t^*) \quad (8.23)$$

In the simulations reported in this manuscript we consider that the MR fluid is composed of iron particles ($\rho = 7.8 \times 10^3 \text{ kg/m}^3$) of diameter $\sigma_m = 10^{-6} \text{ m}$ suspended in a Newtonian fluid ($\eta_c = 1 \times 10^{-3} \text{ Pa}\cdot\text{s}$). This results in $F_B = 4.17 \times 10^{-14} \text{ N}$ and $\zeta_m^* = 722.09$. Three values for the magnetic field parameter H_0^* have been investigated: $H_0^* = 5, 25$ and 50 . These field strength values correspond to $\lambda = 85, 339$ and 8541 , respectively. As a summary, the real and reduced parameters used in the simulations are shown in Table 8.1. As shown in Table 8.1, the reduced parameters used in this work are different from the reduced parameters used in the MR simulation literature [e.g. Klingenberg *et al.* (1989), Kittipoomwong *et al.* (2002)]. σ_m , M_m and F_B are chosen here as fundamental normalization factors of length, mass and force, respectively, due to the inclusion of Brownian motion in the simulation code.

Magnitude	Simulation Parameter	Real Unit	Scale	Reduced Unit
Length	σ_m	$10^{-6} m$	σ_m	1.0
Friction Coefficient	ζ_m	$9.43 \cdot 10^{-9} N \cdot s / m$	$\sqrt{M_m F_B / \sigma_m}$	722.09
Magnetic Field	H_0	$1kA/m, 5.04kA/m, 10.2kA/m$	$\beta(H_B)H_B / \beta(H_0)$	5.0, 25.0, 50.0
Temperature	T	300 K	$F_B \sigma_m / k_B$	0.099
Time step	Δt	$10^{-9} s$	$\sqrt{M_m \sigma_m / F_B}$	$3.2 \cdot 10^{-4}$

Table 8.1. Reduced units and natural scales employed in the simulation code.

8.2.7. Solving the equations

Introducing thermal noise and inertia into the simulation model has to be done with especial care. The drawback of introducing Brownian forces in strongly interacting large-size particle dispersions is that the magnetic forces are huge in comparison and this is computationally inconvenient. From Equation 8.3 we can identify three different time scales: the inertial time, $\tau_M = M_i / \zeta_i$; the diffusive time, $\tau_D = 3\pi\eta\sigma_m^3 / k_B T$; and the characteristic relaxation time, $\tau_R = 8\eta / \mu_0 \mu_{cr} \beta^2 H_0^2$ [Dhont (1996)]. From the parameters used in the simulations (see Table 8.1) we can obtain the order of magnitude of the different time scales: $\tau_M \sim 10^{-7} s$, $\tau_D \sim 1s$ and $\tau_R \sim 10^{-4} s$. This scaling analysis reveals that the relaxation processes are separated by at least 7 orders of magnitude in time. As a result, in order for the simulation to faithfully represent all associated relaxation processes, the time step should be lower than

$\sim 10^{-7} s$ and the total simulation time should be higher than ~ 1 (i.e. number of integration steps higher than $\sim 10^7$).

Equation 8.23 was solved using the standard Velocity-Verlet-like algorithm with neighbors list [Allen and Tildesley (1991)]. The particles with the selected diameter distribution $\{\sigma_i\}$ were randomly distributed in the simulation box. Then, a magnetic field was applied and the suspension was left to reach a steady state under rest. In particular we looked to the long time plateau in the energy of the system. Initially we performed simulations using a time step of $\Delta t = 10^{-7} s$ and no change in the energy neither in the structural parameters was observed after 10^8 simulation steps (10 seconds in real units) for all the simulations performed. Two different routes were followed in order to analyze the influence of the time step on the simulations' results. In the first route, we restarted the simulations with a shorter time step $\Delta t = 10^{-9} s$ for another 10^8 simulation steps. Here, the total energy value remained constant and there was not variation in the final structure of the system. In the second route, new simulations were performed starting from fresh/new randomly distributed particles with a time step of $\Delta t = 10^{-9} s$ for 10^8 simulation steps (0.1 seconds in real time). Computed total energies and structural parameters were found to be identical to those obtained for the $\Delta t = 10^{-7} s$ simulations. Therefore, we conclude that the results are independent on the selected time step. Mean Square Displacement (MSD) calculations (not shown here for brevity) revealed that the simulated structures are in "quasi-equilibrium" with $\text{MSD} \sim t^{0.27}$ at long times. As a way of example, after 2 seconds the mean movement of the particles is negligible, around 0.01 the diameter size.

In the second stage, a shear flow field was imposed to the structured suspensions and the stress evolution was monitored as a function of time. In the case of start-up tests, the time step of the simulation was tuned $\Delta t \in [10^{-9}, 10^{-4}]$ to ensure that the results were independent of the selected time step and each simulation run was carried out up to a total strain of $\gamma = 10$. The steady shear stress was calculated by averaging the large-strain value of the stress tensor in 500 configurations over the strain of $\gamma = 2$ to $\gamma = 10$. For the oscillatory sweep tests, the simulation was stopped after 10 cycles. This was a long enough time to overcome the initial transients. In all cases, when the flow field was applied, we considered a no-slip condition for the particles in contact with the wall boundaries. Particles within a distance $\delta_i = 0.05\sigma_i$ of a bounding surface are considered stuck and as a result, their velocity components are given by $(v_x, v_y) = (0, 0)$ and $(v_x, v_y) = (V_0, 0)$ for particles close to the bottom and top wall, respectively. Here, V_0 is the velocity of the top wall. The sticking condition is based on many experimental observations and more important, it is required to observe a yield stress within the frame of this simulation model [for a detailed discussion we refer to Klingenberg (1993)].

The connectivity of the system was monitored by considering the following interparticle bounding criteria; two particles i and j are considered bonded when the distance between their centers is smaller than $1.05(\sigma_i + \sigma_j)/2$. The connectivity $C(\theta)$ is defined here as the mean number of particles in contact to a central one with an orientation between angles θ and $\theta + d\theta$ with respect to the z axis:

$$C(\theta) = \frac{N(\theta)}{N-1} \quad (8.24)$$

Here, $N(\theta)$ is the number of connected particles oriented between angles θ and $\theta + d\theta$, and N is the total number of particles in the system.

8.3. RESULTS AND DISCUSSION

8.3.1. Aggregation kinetics at rest

The aggregation kinetics was studied in terms of magnetostatic energy, nearest neighbours (mean number of particles located at a distance $d \leq 1.05\sigma$ to a central one), mean cluster size (average number of monomers within the clusters), radii of gyration [see for instance Dhont (1996)] and angular connections evolution as a function of time. With the exception of the energy and angular connectivities (to be discussed further below), all magnitudes increase with time and eventually reach a final plateau that is associated to the stationary state and/or to the fact that the structures fully connect the gap in z -direction. For all the magnetic fields investigated ($H_0^* = 5, H_0^* = 25$ and $H_0^* = 50$), the energy of monodisperse systems is smaller, in absolute value, than the case of polydisperse MR fluids independently of the size of the simulation box. This is expected because of the cubic dependence of the magnetostatic interaction force with particle size (see Equation 8.7). However, the number of nearest neighbours is slightly sensitive to the box size because of confining effects. During structuration, the mean cluster size is a power-law function of time at small times and the exponent increases with particle concentration. At a certain time the curves deviate from the power-law behavior and approach an asymptotic plateau value. This is due to the clusters coming into contact with the boundary walls. Actually, simulations for $\phi = 0.20$ predict the formation of only one percolating cluster. Generally speaking, the growing kinetics of the clusters is slightly

increased for the polydisperse system than for the monodisperse case, but one does not observe a significant difference in the final mean cluster size at equilibrium as also corroborated with calculations of radii of gyration of the clusters.

Undoubtedly, during structuration, the most relevant information was given by the evolution with time of the angular connections. Figure 8.2 shows the time dependent connection evolution $C(\theta)$ for $\phi = 0.10$ and $H_0^* = 50$. The aggregation kinetics in the case of monodisperse MR fluids (see Figure 8.2a) is driven by the evolution of the connections at $\theta \in [0^\circ, 10^\circ]$ and $\theta \in [50^\circ, 70^\circ]$. Connections at other angles remain constant at a very low value (below 0.05) during the equilibration which suggests a crystal-like structure (to be discussed further below). First, $\theta \in [0^\circ, 10^\circ]$ connections form (vertical connections). This is a very fast process that is limited by the size of the box (L_z); in only $t^* = 20.0$ all connections are formed. Once, vertical connections are formed, lateral connections start to appear with angles $\theta \in [50^\circ, 70^\circ]$ while the rest of angular connections remain constant. At this stage, the system is composed basically as linear chains with few lateral interconnections - BCT packing- that increase with the magnetic field strength. Qualitatively similar results are obtained in the case of larger particle loadings, $\phi = 0.20$. However, here the number of horizontal connections overcomes the number of vertical connections as time passes because of the formation of thicker aggregates.

A more complex scenario appears for the polydisperse MR fluids (see Figure 8.2b). As expected, the first connections to form correspond again to $\theta \in [0^\circ, 10^\circ]$, but now these connections decrease during the

equilibration due to the increase of the $\theta \in [10^\circ, 30^\circ]$ connections in stark contrast to what happened for monodisperse case. This means, that the first clusters to form are linear at the beginning but the particle rearrangements provokes the lost of linearity of the clusters as a consequence of the polydisperse nature of the samples. If compared to the monodisperse case, at short times the total number of vertical connections is significantly smaller for polydisperse systems. This is the result of the fact that the connectivity of the system is much larger. It is remarkable that the majority of the lateral interconnections of the clusters for the polydisperse case are due to $\theta \in [30^\circ, 40^\circ]$, instead of the connection $\theta \in [50^\circ, 70^\circ]$ which is the typical for the monodisperse system where a BCT structure has been predicted using theoretical arguments [Parthasarathy and Klingenberg (1996)]. Moreover, pure horizontal connections ($\theta \in [80^\circ, 90^\circ]$) are not negligible for the polydisperse case and could be even larger than the horizontal connections of the monodisperse system.

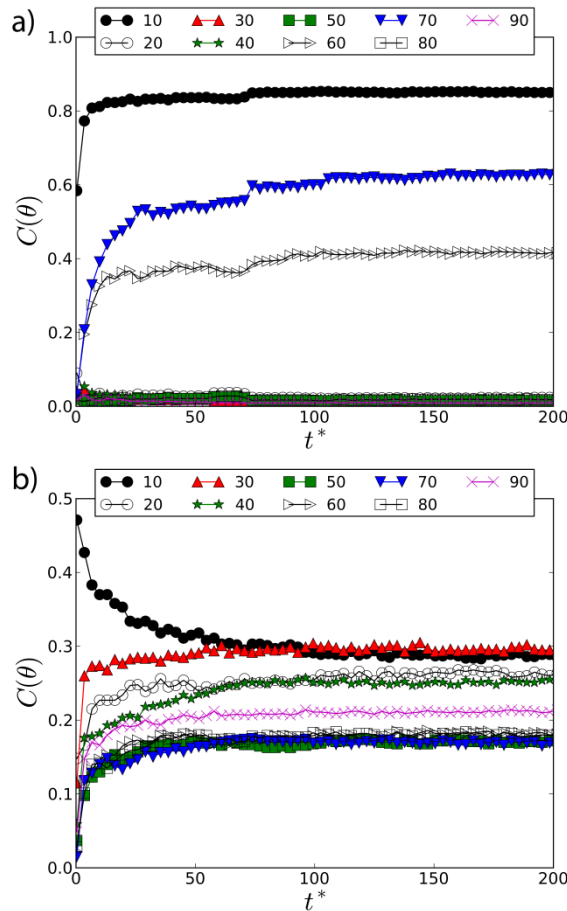


Figure 8.2 Time-dependent connection evolution for monodisperse (a) and polydisperse (b) MR fluids. $\phi = 0.10$. $H_0^* = 50$. $d\theta = 10^\circ$. Each point corresponds to an average of 20 configurations time-separated by 500 time steps.

8.3.2. Quasi-equilibrated structures

After the "equilibration" time, the final typical structures obtained are depicted in Figure 8.3 for two particle concentrations ($\phi = 0.10$ and $\phi = 0.20$) both in the case of monodisperse and polydisperse systems. As observed, the clusters formed in monodisperse simulations at equilibrium are elongated highly ordered structures spanning in the direction of the

magnetic field while polydispersity in particle size frustrates order. In an attempt to quantify the crystalline character of the field-induced structures, we calculated the radial distribution functions in 3D space $g(r)$, in the xy plane $g_{XY}(r)$, and along the z axis $g_Z(r)$. Additionally we also calculated the pair correlation function in the XY plane of the clusters mass center, g_{CM} . Briefly, very well defined peaks were observed for monodisperse MR fluids in the three different representations of the radial distribution function revealing a crystalline structure of the field-induced clusters. The MR fluid becomes more ordered at the highest fields explored as a consequence of the fact that the peaks in the radial distribution functions, $g(r)$ and $g_{XY}(r)$, grow as the magnetic field increases. Only $g_Z(r)$ remains unaltered under the increase of the magnetic field strength as a result of an arrested structure in the field direction. A similar observation was recently reported in Segovia-Gutiérrez *et al.* (2013). When including polydispersity in the MR fluids crystal formation is prevented and the radial distribution functions resemble that of a liquid-like structure. The most concentrated, monodispersed, MR fluids investigated ($\phi = 0.20$) also exhibited pronounced peaks in the radial distribution functions that are placed at the same positions as in less concentrated MR fluids. The main difference is that for MR fluids containing a particle concentration of $\phi = 0.20$ there exists only one percolating cluster independently of the magnetic field strength. Again, including polydispersity results in a disordered structure manifested by the disappearance of the peaks in the radial distribution functions.

To further quantify the field-induced structure in the MR fluid, in Figure 8.4 we show the angular connectivities $C(\theta)$ for the MR fluids under study. As expected, monodisperse systems exhibit two peaks at angles

$\theta_v \approx 0^\circ$ (vertical connections) and $\theta_h \approx 60^\circ$ (lateral connections). In the case of monodisperse MR fluids at $\phi = 0.10$, different structures appear depending on the strength of the magnetic field. The vertical angle θ_v becomes closer to zero when the magnetic field strength increases. This is a result of better aligned structures under stronger fields. On the other hand, the lateral angle θ_h remains essentially constant at the same value $\theta_h \approx 60^\circ$ independently of the magnetic field strength and is the result of a crystal-like packing of the particles within the aggregates. However, it grows with the field as a consequence of a more efficient particle packing in the structure under stronger fields. For monodisperse MR fluids at $\phi = 0.20$, the angular connectivity does not depend on the magnetic field strengths explored due to the large packing fraction. For the polydisperse case, the angular connectivity is one order of magnitude lower and remains flatter if compared to the monodisperse case. This is the result of a non-crystalline structure.

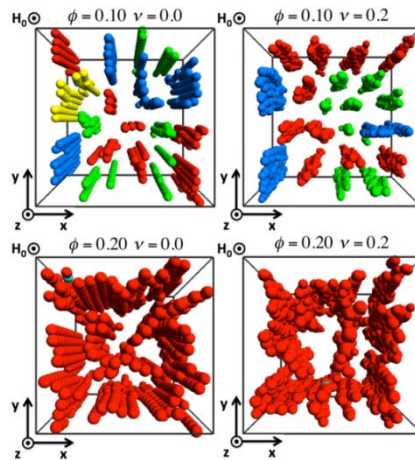


Figure 8.3 Quasi-equilibrium configurations for $H_0^* = 50$ and two packing fractions $\phi = 0.10$ and $\phi = 0.20$ in monodisperse (left column) and polydisperse (right column) cases. The colors have been introduced to distinguish between different clusters.

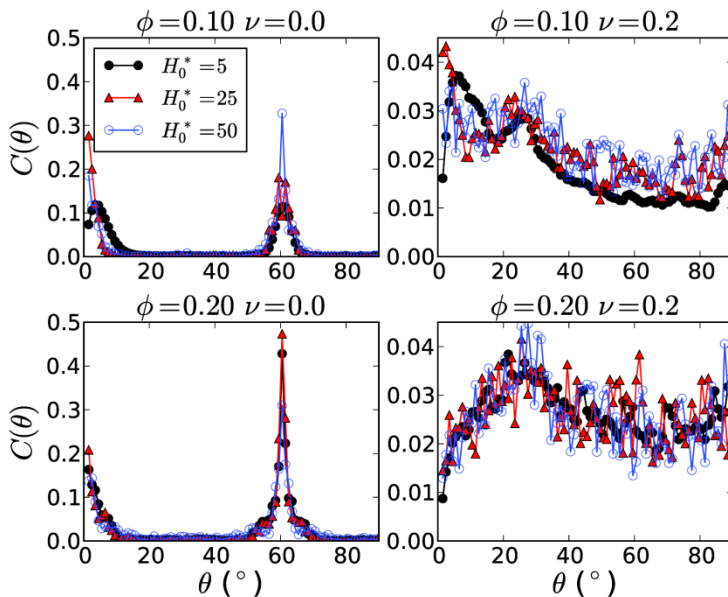


Figure 8.4 Angular connectivity $C(\theta)$ for three different values of the reduced magnetic field H_0^* . Left: monodisperse MR fluid. Right: polydisperse MR fluid. The connectivities are averaged over more than 10000 configurations separated by 100 time steps.

8.3.3. Stress growth simulations: yield stress

Start-up simulations were carried out for shear rates in the range $\dot{\gamma}^* \in [10^{-3}, 10]$ ($\dot{\gamma} \in [3.2s^{-1}, 3.2 \times 10^4 s^{-1}]$ in real units). It is worth to remark here that the minimum shear rate investigated in simulations is already large from an experimental point of view. However, as will be seen below, this shear rate value is well within the simulated low shear rate plateau region for the stress in conventional rheograms (stress versus shear rate representations). Figure 8.5a is a typical example where we show the results for the \mathcal{XZ} component of the microscopic stress evolution calculated through the Equation 8.16 under continuous shear. Therefore, the stress component represented in Figure 8.5a does not include the hydrodynamic contribution under shear. Below a certain strain level, the

stress versus time (or shear strain) response consists of an initially linear portion indicating quasielastic solid behavior, followed by a nonlinear region, a stress overshoot, a stress decay region and a high-strain plateau. There is no consensus in the rheology literature on the actual critical strain associated to the yielding point. In fact, some workers defend that yielding actually starts where the stress-time curve ceases to be linear [e.g. Mewis and Meire (1984)]. On the contrary, others defend that the peak in shear stress corresponds to the complete breakdown of the structure [e.g. Papenhuijzen (1972)]. In practice, the peak is easier to detect and therefore, as a first approximation, the magnitude of this critical stress value could be considered a good measure of the static yield value as soon as the shear rate is sufficiently low to discard the viscous contribution [Vinogradov and Malkin (1980)]. On the other hand, the plateau stress for large strains in the limit of small shear rates is identified as the dynamic yield stress. Because direct simulations at very small shear rates are computationally expensive, *stress relaxation simulation* experiments are generally preferred instead [Klingenberg *et al.* (1991)]. However, in this contribution, because the box size is not too large, direct simulations are not overly computationally expensive and this is the reason why direct simulations are run instead of stress relaxation tests.

For convenience, the peak value is determined by fitting a Gaussian function in the exit of the linear region (see Figure 8.5b) and represents the so-called static yield stress when the shear rate is exceedingly small. The critical strain above which the structure becomes unstable for a given shear rate, although not exactly the same, is rather close to the strain corresponding to the overshoot (maximum) in the start-up test [Parthasarathy and Klingenberg (1995a)]. Simulations performed here demonstrated that the effect of polydispersity is negligible in the critical strain associated to the maximum in the stress; it remains essentially

constant within the range 0.1-0.5 for shear rates $\dot{\gamma}^* \in [10^{-3}, 10]$. Simulations on monodispersed suspensions by Parthasarathy and Klingenberg (1995b), and micromechanical model predictions by Martin and Anderson (1996) and de Gans *et al.* (1999) give a critical strain of 0.1 and 0.34, respectively, in good agreement with our simulations results. Finally, the steady response is obtained by averaging the stress values in the high strain plateau for strain values between $\gamma = 2$ and $\gamma = 10$. Figure 8.5c represents the distribution of the stress values in the steady region, i.e., the region where the stress values are statistical independent on the strain. From the steady response it is possible to calculate the so-called dynamic yield stress in the limit of small shear rates. The effect of particle size polydispersity in the steady response is discussed further below.

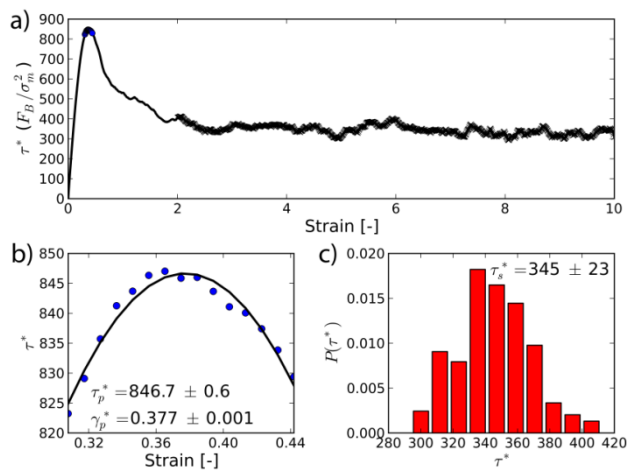


Figure 8.5.- a) Microscopic stress tensor (xz component) as obtained from Equation 8.16 (i.e. without hydrodynamic interactions) versus the shear strain. Simulation parameters: $\phi = 0.10$, $\nu = 0.0$, $H_0^* = 50$, $\dot{\gamma}^* = 1$. b) Calculation of the peak stress: Fitting from 20 to 100 points of the stress peak (depending on the strain rate) using a Gaussian of mean γ_p^* and value at the peak of τ_p^* . c) Calculation of the steady stress: Distribution of the stress value in the steady region (strain higher than 2 in subplot a). The mean steady stress value τ_s^* has been calculated using more than 1000 stress values.

Next we aimed to explore the occurrence of structural changes in the MR fluid under the application of a constant shear rate. In particular, we focused on the change of the angular connectivities $C(\theta)$ upon increasing the strain value. Color maps on top of Figure 8.6 represent the connectivity evolution under the flow application. Horizontal axis represents the strain while the vertical axis corresponds to the bond angle with respect the magnetic field vector. The connectivities $C(\theta)$ are represented in a color scale where warmer colors are associated to a larger number of interparticle connections. Below the color map figures we also include the corresponding XZ component of the stress tensor versus the strain curves in an attempt to correlate the stress evolution with particle-level microstructural changes. The results for mono- and polydisperse cases included in Figure 8.6 correspond to $\phi = 0.20$, $\dot{\gamma}^* = 1.0$ and $H_0^* = 25$. For the monodisperse case (see Figure 8.6a), the initial structure has predominant angles at $\theta = 0^\circ$ and $\theta = 60^\circ$. During the flow application, vertical ($\theta = 0^\circ$) and horizontal ($\theta = 60^\circ$) connections start to break. Some of vertical connections evolve to $\theta = 20^\circ$, and the horizontal connections evolve to $\theta = 20^\circ$ and $\theta = 80^\circ$ connections. An explanation for this may come from the tilting of the columns and particle aggregates. At steady shear rate, a balance between hydrodynamic and magnetostatic torques must be reached and a maximum angle is predicted by micromechanical models [Martin and Anderson (1996)]. The predicted critical angle is $\theta_c = 39.23^\circ$ for the linear chain model and $\theta_c = 35.26^\circ$ for rigid chains. These simplified models overestimate the critical angle obtained in simulations as expected because lateral interconnections between primary structures aligned with the field are not considered in micromechanical models. The stress peaks seem to be related with the total rupture of the $\theta = 60^\circ$ connections. As expected, the polydisperse

MR fluids (see Figure 8.6b) have not as pronounced peaks as in the monodisperse cases. Here, the main connections remain at $\theta = 20^\circ$ and $\theta = 80^\circ$. The mean peak appears when the $\theta = 80^\circ$ connections disappear and the relaxation after the peak can be explained as the reduction of the $\theta = 20^\circ$ connections.

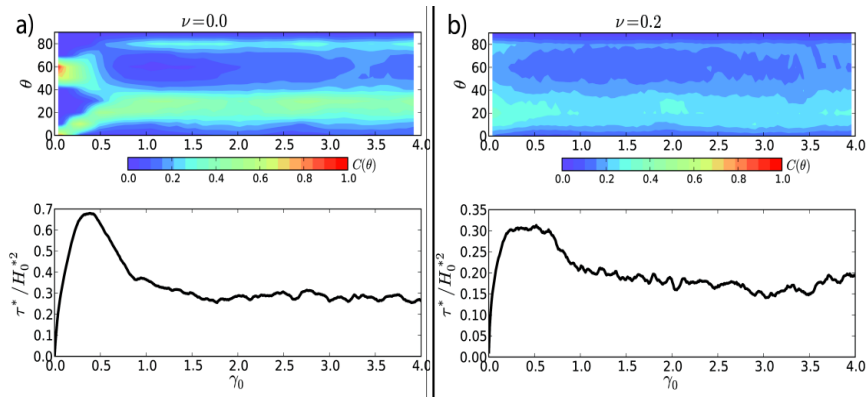


Figure 8.6 Bond angle (top) and stress (bottom) evolution during a start-up test simulations. $\phi = 0.20$. $\dot{\gamma}^* = 1.0$. $H_0^* = 25$. a) $\nu = 0.0$, b) $\nu = 0.20$. The stress tensor and the connectivities have been averaged over 20 configurations separated by 500 time steps.

Then we studied the shear rate dependence of the total stress. The total stress is estimated here by simply adding the pairwise interaction contribution (Equation 8.16) to the hydrodynamic (Newtonian fluid) contribution (i.e. carrier viscosity times the apparent shear rate). First we checked that the total stress obtained for different magnetic fields overlapped in a single curve when normalized by the magnetic field strength squared. This was expected from the simplifications of the simulation model, in good agreement with the particle magnetization model. Then, in order to quantify the accuracy of the simulations performed and to improve the statistics of the simulations, in the following we will carry out simulations for three different magnetic field strengths and then dimensionless curves will be averaged. Figure 8.7

shows the peak (a) and high strain plateau (b) values for the total stress as a function of the shear rate. As observed in Figure 8.7 the shear stress decreases and levels off as the shear rate is decreased. The low shear plateau occurs when hydrodynamic forces become negligible and the field-induced structure slowly evolves due to the movement of the particles stuck at the moving plate. This low shear plateau value of the stress is identified as the static or dynamic yield stress when the peak or high strain plateaus are considered, respectively [Klingenberg *et al.* (1991)]. The yield stress results are included in Table 8.2. As expected, we observe a clear increase in the static and dynamic yield stresses with increasing the packing fraction. Importantly, no significant differences have been observed in the static and dynamic yield stress between monodisperse and polydisperse simulations in spite of their different structural characteristics. In other words, the yield stress is not affected by the polydispersity level that typically exists in experimental MR fluid formulations. At the other extreme, at high shear rates, it is the hydrodynamic contribution that dominates magnetostatic interactions and therefore a power-law behavior is observed with exponent 1. The effect of polydispersity is not relevant in this high shear rate region either and only the particle volume fraction plays a role. In summary, the fact that both monodisperse and polydisperse curves collapse at very low and very high shear rate (i.e. Mason numbers), suggests that the effect of polydispersity is negligible at these two extremes, well within the solid-like and fluid-like regimes, respectively. These two regions are solely governed by the particle loading and are in good agreement with analytical theories and micromechanical models available in the literature that anticipate a plastic behavior. However, from the inspection of Figure 8.7, particle size polydispersity does clearly influence the yielding region; i.e. the transition region from magnetostatic (low shear rate) to hydrodynamic (high shear rate) control. Actually, a more abrupt transition is observed in the case of

polydisperse systems as a result of the fact that the bonds between polydisperse particles are more susceptible to break under shear than for the monodisperse case.

Steady shear stress data versus shear rate curves reported in Figure 8.7b are traditionally plotted in the MR literature in terms of shear viscosity versus Mason number curves. And, in its turn, these viscosity curves can be contrasted with dimensionless plastic-like constitutive equations such as the Bingham equation [de Vicente *et al.* (2011) and references therein]

$$\eta/\eta_\infty = 1 + (Mn/Mn^*)^{-1} \quad (8.25)$$

or the Casson plastic equation [Berli and de Vicente (2012)]:

$$\eta/\eta_\infty = 1 + (Mn/Mn^*)^{-1} + 2(Mn/Mn^*)^{-1/2} \quad (8.26)$$

Here Mn^* is the critical Mason number that determines the transition from magnetization to hydrodynamic control of the suspension structure. Linear regression fittings to the Bingham and Casson equations were carried out and best fitting parameters are included in Table 8.3. Both models give a good fitting to the simulation data. In general, polydisperse MR fluids are better fitted with the Bingham model and the critical Mason number as obtained from the regression fitting is always smaller than the monodisperse case as anticipated from Figure 8.7.

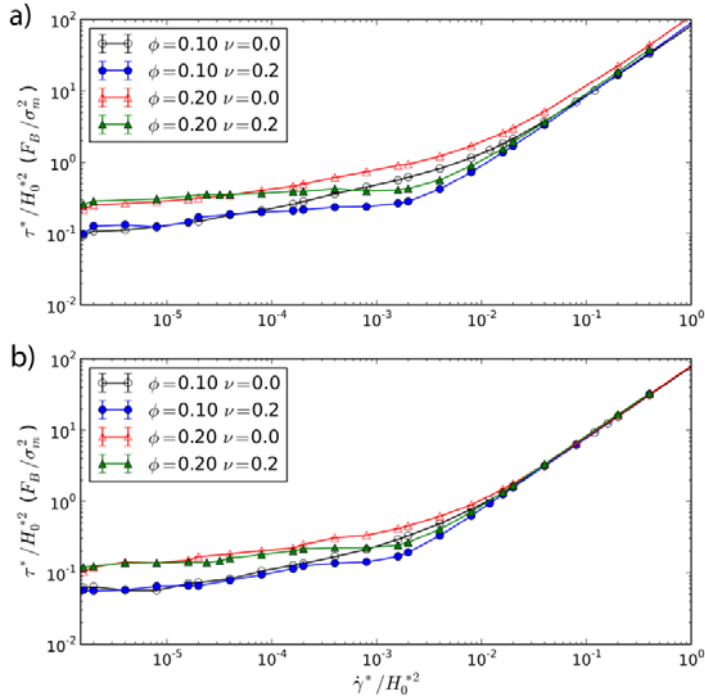


Figure 8.7. Total stress as a function of the shear rate: a) Constructed by using the peak values for the stress tensor. b) Constructed from the steady shear stress at long γ . Each curve has been averaged over the three magnetic field strengths used in this work. For better clarity, error bars are not shown because they are smaller than the symbol size.

8.3.4. Dynamic oscillatory strain amplitude sweep tests

Strain amplitude sweep simulations were also carried out, at two packing fractions ($\phi = 0.10$ and $\phi = 0.20$) and for the mono ($\nu = 0.0$) and polydisperse ($\nu = 0.2$) MR fluids. In these particular tests, the choice of the excitation frequency deserved careful attention because previous simulation works demonstrate a relaxation mechanism from the competition between magnetostatic and hydrodynamic forces acting on the particles, resulting in a transition in the dynamic structure and rheological response between small and large frequency limits. At small frequencies (large times), the deformation is completely determined by the

particles attached to the plates, hydrodynamic resistance to the particle motion is negligible and magnetostatic interactions dominate. As a result, motion is not affine. On the other hand, at large frequencies (short times), hydrodynamic forces dominate the motion of the dispersed particles and particles do not have sufficient time to move to lower energy positions. In this case the motion is affine. Bearing this in mind, in this work we worked at a constant excitation frequency. The selected reduced frequency of excitation was $\omega^* = 0.2$, which corresponds to a real frequency of 100 Hz -that is easily accessible experimentally with torsional rheometry-. This frequency is approximately two orders of magnitude lower than the transition frequency reported in Klingenberg (1993) ($\omega_K^* = 0.057\omega^*$) and therefore, strain amplitude sweep tests presumably only explore the low frequency regime. Knowing the shear strain and the resulting shear stress, one can easily calculate two materials functions: storage modulus (G') and loss modulus (G'') which respectively characterize the solid-like and fluid-like contributions to the measured stress response. In the linear regime, the strain amplitude is sufficiently small that both viscoelastic moduli are independent of strain amplitude, the oscillatory stress response is sinusoidal, and the results can be discussed within the frame of linear viscoelasticity theory. In the non-linear regime, the stress response to a sinusoidal excitation contains higher harmonic contributions, the storage and loss moduli are functions of the strain amplitude (not material functions anymore), and the periodic stress waveform deviates from a sinusoidal wave. Figure 8.8 depicts the strain amplitude dependence of G' and G'' for these simulations.

The simulated viscoelastic moduli curves shown in Figure 8.8 are in very good qualitative agreement with previously reported dynamic oscillatory shear experiments [Brooks *et al.* (1986); de Vicente *et al.* (2005);

McLeish *et al.* (1991)]. At very low strain values both G' and G'' remain constant within the linear viscoelastic region and, as expected from the field-induced structures, G' overcomes G'' . For slightly larger strain amplitudes both moduli start to decrease but the field-induced columnar structures do not break. Only above the flow point (i.e. when $G' = G''$), there is a massive reorganization and the formation of layered structures aligned in the flow direction (see inset in Figure 8.8) in agreement with previous experimental results by Bossis and coworkers [Cutillas *et al.* (1998)].

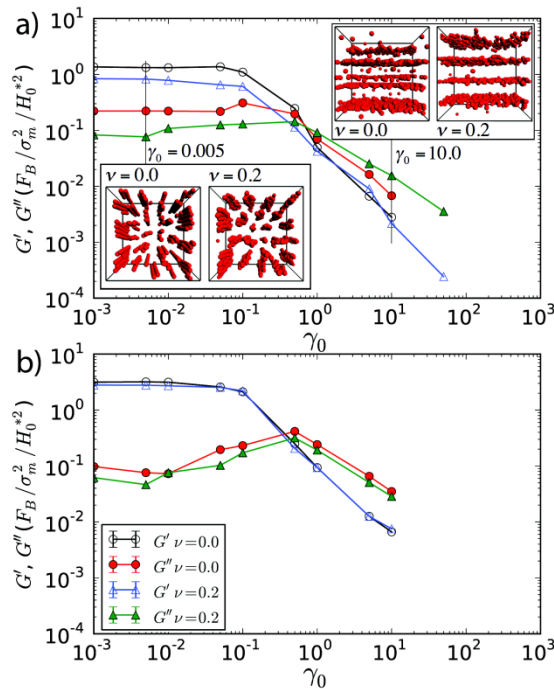


Figure 8.8.- Strain amplitude sweep curves in dynamic oscillatory shear rheology at a constant frequency of $\omega^* = 0.2$. This dimensionless frequency corresponds to a real frequency of 100 Hz. $H_0^* = 50$. a) $\phi = 0.10$, b) $\phi = 0.20$. The snapshots inside panel a) represent the steady structure observed for mono- and polydisperse simulations at $\phi = 0.10$: left) $\gamma_0 = 0.005$ and right) $\gamma_0 = 10.0$. For better clarity, error bars are not shown because they are smaller than the symbol size.

Generally speaking, the viscoelastic moduli within the linear viscoelastic regime clearly increase with increasing particle content and monodispersity in size. However, the larger the particle loading, the lesser the effect of particle polydispersity in the rheological response. These results are in agreement with experimental data by Ahn and Klingenberg (1994). In their paper, they demonstrated that polydispersity does not significantly alter the response observed for concentrated monodisperse suspensions under linear deformation regime. In agreement with previous results on steady shear, polydisperse MR fluids do more abruptly break, at slightly smaller strain values, if compared to monodisperse suspensions.

The evolution of the connectivities under oscillatory shear is presented in Figure 8.9 at different strain values. For the monodisperse simulations, no variation in the connectivities is observed for $\gamma_0 = 0.1$. At this strain value the MR fluid behaves in the linear viscoelastic regime. However, when the strain gets closer to the flow point ($\gamma_0 = 0.5$), oscillations come up for $\theta \in [0^\circ, 20^\circ]$ and $\theta \in [40^\circ, 70^\circ]$. If the strain is further increased to $\gamma_0 = 1.0$, almost all connectivities at $\theta = 0^\circ$ disappear and now the connectivities oscillate in the range $\theta \in [20^\circ, 80^\circ]$. This corresponds to the formation of the layers in the direction of the flow. Finally, at $\gamma_0 = 10.0$, the connectivities are located at $\theta = 20^\circ$ and $\theta = 80^\circ$. These connectivity values closely correspond to those dominating the steady shear response in Figure 8.6a.

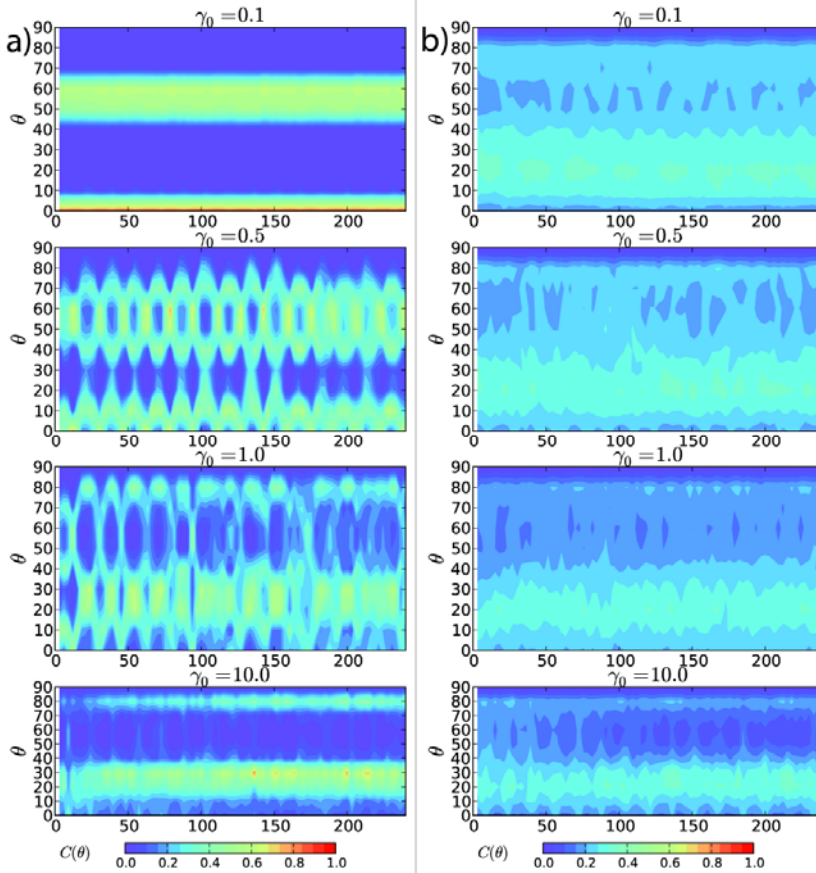


Figure 8.9 Connectivities evolution for the oscillatory strain simulations for $\phi = 0.10$ for different strain values (see Figure 8.8). a) Monodisperse and b) Polydisperse. Each plot is obtained from the average of 10 configuration separated by 1000 time steps.

Next we discuss the evolution of the connectivity for the polydisperse MR fluids. For very low strain values, $\gamma_0 = 0.1$, we observed both the fragmentation and formation of interparticle bonds at $\theta = 20^\circ$ and $\theta = 60^\circ$. However, in contrast to the monodisperse case, for polydisperse MR fluids we do not observe a clear transition between well defined angles. This is because the polydisperse particles can rearrange at more different angles than the monodisperse particles. When the strain amplitude is increased, the connectivities between $\theta = 30^\circ$ and $\theta = 70^\circ$

progressively disappear and the layers come up. Finally, at $\gamma_0 = 10.0$ the remaining connectivities are $\theta = 20^\circ$ and $\theta = 80^\circ$ similarly to the monodisperse case. Results on the evolution of the connectivity for MR fluids at $\phi = 0.20$ are qualitatively similar.

8.4. CONCLUSIONS

Starting from the well-known particle-level simulation methodology developed by Klingenberg in the 90's, a 3D particle-level dynamic simulation method is developed here to investigate the importance of particle size polydispersity on the kinetics of aggregation at rest and the rheological behavior under start-up and dynamic oscillation in magnetorheology. For the first time, two particle size distributions are compared both having the same mean diameter. One of them corresponds to a perfectly monodisperse MR fluid. The other corresponds to a skewed Shultz-like distribution with $\nu = 0.2$ (Polydispersity Index $PDI = 1.12$) as this is the typical polydispersity level encountered in commercial MR fluid formulations. In addition to the forces typically employed in these particle-level simulations (field-induced magnetic, hydrodynamic drag and short-range repulsive forces) the simulation approach used here also considers Brownian motion, which is particularly important for the smallest particles in the size distribution. Similar to previous papers in this research field, the simulation code employed here does ignore multipolar and multibody contributions, as well as hydrodynamic interactions between particles and between spheres and walls. As a consequence, the conclusions are valid at a qualitative level.

The growing kinetics of the clusters is slightly faster for polydisperse systems. Not much difference is observed in the final mean cluster size at equilibrium when comparing mono- and polydisperse cases. The

aggregation kinetics in monodisperse systems is determined by 0° and 60° connections while 30° connections dominate in the case of polydisperse systems. Equilibrated structures were characterized in terms of radial distribution, pair correlation functions and angular connectivities. A perfect crystal is formed in the case of monodisperse MR fluids. Polydispersity is demonstrated to frustrate order.

Direct simulations are employed to calculate the stress during start-up tests. Simulations demonstrate a stress overshoot that is attributed to structural breakdown; initially there is a stress build-up, then the stress reaches a peak value and finally reaches an asymptotic plateau. In the particular case of concentrated suspensions, the stress build-up comes from the crowding of particles and the collisions between them, the stress peak corresponds to the maximum stress required to cause rotation of the adventitious aggregates, and finally, for large enough strains aggregates break and particles tend to align along the direction of flow and to move in rafts. In the case of the MR fluids simulated in this work, as the strain level increases in the monodisperse case, vertical ($\theta = 0^\circ$) and horizontal ($\theta = 60^\circ$) connections start to break. Some of vertical connections evolve to $\theta = 20^\circ$, and the horizontal connections evolve to $\theta = 20^\circ$ and $\theta = 80^\circ$ connections. The stress peaks seems to be related with the total rupture of the $\theta = 60^\circ$ connections. In the case of polydisperse systems, the main angular connections remain at $\theta = 20^\circ$ and $\theta = 80^\circ$ during the shearing process. The mean peak occurs when the $\theta = 80^\circ$ connections completely disappear and the relaxation after the stress overshoot is explained as the reduction of the $\theta = 20^\circ$ connections. The critical strain associated to the peak stress occurs at approximately 0.1-0.5, in good agreement with micromechanical models and particle-level simulations on monodisperse MR fluids, and is not affected by the polydispersity level.

From (shear) stress growth curves, static and dynamic yield stresses are determined and rheograms are constructed. Static yield stresses are inferred from the low shear rate limit of the stress peak at low strain values while steady shear flow behavior of the MR fluids is obtained by taking long time (i.e. long strain) stress values. Importantly, introducing polydispersity does not affect the yield value and classical theories and models for monodisperse systems still apply. On the contrary, the effect of polydispersity is remarkable in the yielding region (i.e. in the frontier between the solid-like and fluid-like regimes). In fact, a clearly more abrupt transition (a lower critical Mason number Mn^*) is observed in the case of polydisperse systems. This result is a consequence of the very different structural properties of the field-induced aggregates at the beginning of the shearing process. In polydisperse MR fluids the number of connections is larger than in the monodisperse case, but as an average interparticle links are much weaker because of the topological limitations.

Dynamic oscillatory shear tests were also carried out. In agreement with start-up tests, for the less concentrated MR fluids ($\phi = 0.10$), a slightly more drastic drop in the viscoelastic moduli is obtained for polydisperse MR fluids if compared to monodisperse counterparts. Both mono- and polydisperse MR fluids initially exhibit a linear viscoelastic regime associated to nearly constant neighbors and connectivities. When strain amplitude increases, a layered structure appears for both mono- and polydisperse MR fluids. Future work should involve a more detailed study on other excitation frequencies to explore if particle size polydispersity actually broadens the frequency dispersion.

Overall, this work suggests that using monodisperse particles in the formulation of conventional MR fluids would not have any major effect in the yield stress nor the high shear behavior. Using monodisperse MR

fluids would solely affect the yielding region by delaying the rupture of the field-induced structure to higher shear rates and hence increasing the critical Mason number Mn^* .

ACKNOWLEDGEMENTS

This work was supported by MINECO (MAT 2010-15101 and MAT 2013-44429-R) and by Junta de Andalucía (P10-FQM-5977, P10-RNM-6630 and P11-FQM-7074) projects. This research has been partially funded by the Interuniversity Attraction Poles Programme (IAP 7/38 MicroMAST) from the Belgian Science Policy Office. J. A. R. -L. acknowledges financial support by the “Ministerio de Educación: Becas del Programa de Formación del Profesorado Universitario (FPU)” (AP2010-2144).

References

- Ahn, K. H., and D. J. Klingenberg, “Relaxation of polydisperse electrorheological suspensions,” *J. Rheol.* **38**(3), 713-741 (1994).
- Allen, M. P., and D. J. Tildesley, “Computer simulations of liquids,” (Clarendon Press Oxford, New York, 1991).
- Berli, C. L. A., and J. de Vicente, "A structural viscosity model for magnetorheology," *Appl. Phys. Lett.* **101**, 021903 (2012).
- Bossis, G., O. Volkova, S. Lacis, and A. Meunier, “Magnetorheology: fluids, structure and rheology,” in *Ferrofluids: Magnetically Controllable Fluids and Their Applications*, Lectures Notes in Physics Vol. 594, edited by S. Odenbach, (Springer-Verlag, Berlin, 2002), 202-230.
- Brady, J., and G. Bossis, "Stokesian Dynamics," *Ann. Rev. Fluid Mech.* **20**, 111–157 (1988).

- Brooks, D., J. Goodwin, C. Hjelm, L. Marshall, and C. Zukoski, "Visco-Elastic Studies on an Electro-Rheological Fluid," *Colloids Surf.* **18**, 293-312 (1986).
- Chiriac, H., and G. Stonian, "Influence of particle size distributions on magnetorheological fluid performances," *Journal of Physics: Conference Series* **200**, 072095 (2009).
- Cutillas, S., G. Bossis, and A. Cebers, "Flow-induced transition from cylindrical to layered patterns in magnetorheological suspensions," *Phys. Rev. E* **57(1)**, 804-811 (1998).
- de Gans, B. J., H. Hoekstra, and J. Mellema, "Non-linear magnetorheological behavior of an inverse ferrofluid," *Faraday Discuss.* **112**, 209-224 (1999).
- de Vicente, J., D. J. Klingenberg and R. Hidalgo-Álvarez, "Magnetorheological Fluids: A Review," *Soft Matter* **7**, 3701-3710 (2011).
- de Vicente, J., M. T. Lopez-Lopez, J. D. G. Duran, and G. Bossis, "A slender-body micromechanical model for viscoelasticity of magnetic colloids: comparison with preliminary experimental data," *J. Colloid. Interface Sci.* **282**, 193-201 (2005).
- Dhont J. K. G., "An Introduction to Dynamics of Colloids," (Elsevier, New York, 1996).
- Ekwebelam, C., and H. See, "Microstructural investigations of the yielding behavior of bidisperse magnetorheological fluids," *Rheol. Acta* **48**, 19-32 (2009).
- Gonzalves, F. D., J. -H- Koo, and M. Ahmadian, "A review of the state of the art in magnetorheological fluid technologies - Part I: MR fluid and MR fluid models," *The Shock and Vibration Digest* **38(3)**, 203-219 (2006).

-
- Irving, J. H., and J.G. Kirkwood, "The statistical theory of transport processes IV. The equations of hydrodynamics," *J. Chem. Phys.* **18**, 817-829 (1950).
- Kittipoomwong, D, D. J. Klingenberg and J. C. Ulicny, "Dynamic yield stress enhancement in bidisperse magnetorheological fluids," *J. Rheol.* **49**(6), 1521-1538 (2005).
- Kittipoomwong, D, D. J. Klingenberg and J. C. Ulicny, "Simulation of bidisperse magnetorheological fluids," *Int. J. Mod. Phys. B* **16**, 2732-2738 (2002).
- Klingenberg, D. J., "Simulation of the dynamic oscillatory response of electrorheological suspensions: demonstration of a relaxation mechanism," *J. Rheol.* **37**(2), 199-214 (1993).
- Klingenberg, D. J., C. F. Zukoski and J. C. Hill, "Kinetic of structure formation in electrorheological suspensions," *J. Appl. Phys.* **73**(9), 4644-4648 (1993).
- Klingenberg, D. J., F. van Swol, and C. F. Zukoski, "Dynamic simulation of electrorheological suspensions," *J. Chem. Phys.* **94**, 7888-7895 (1989).
- Klingenberg, D. J., F. van Swol, and C. F. Zukoski, "The small shear rate response of electrorheological suspensions. I. Simulation in the point-dipole limit," *J. Chem. Phys.* **94**, 6160-6169 (1991).
- Klingenberg, D. J., J. C. Ulicny, and M. A. Golden, "Mason numbers for magnetorheology," *J. Rheol.* **51**, 883-893 (2007).
- Liu, T., X. Gong, Y. Xu, S. Xuan, W. Jiang, "Simulations of magneto-induced rearrangeable microstructures of magnetorheological plastomers," *Soft Matter* **9**, 10069-10080 (2013).
- Martin, J.E., and R. A. Anderson, "Chain model of electrorheology," *J. Chem. Phys.* **104**(12), 4814-4827 (1996).

- McLeish, T.C.B., T. Jordan, and M.T. Shaw, "Viscoelastic response of electrorheological fluids. I. Frequency dependence," *J. Rheol.* **35**, 427 (1991).
- Mewis, J. and C. Meire, "Yielding in weakly flocculated systems," in *Advances in Rheology 2*, edited by B. Mena, A. García-Rejón, C. Rangel-Nagaile, (Univ. Nac. Auton. Mex., Mexico City, 1984), 591-98.
- Papenhuijzen, J. M. P., "The role of particle interactions in the rheology of dispersed systems," *Rheol. Acta* **11**, 73-88 (1972).
- Park, B. J., F. F. Fang, and H. J. Choi, "Magnetorheology: Materials and application," *Soft Matter* **6**, 5246-5253 (2010).
- Parthasarathy, M. and D. J. Klingenberg, "Electrorheology: Mechanisms and models," *Mater. Sci. Eng. R.* **17**, 57-103 (1996).
- Parthasarathy, M., and D. J. Klingenberg, "A microstructural investigation of the nonlinear response of electrorheological suspensions: I. Start-up of steady shear," *Rheol. Acta* **34**, 417-429 (1995a)
- Parthasarathy, M., and D. J. Klingenberg, "A microstructural investigation of the nonlinear response of electrorheological suspensions: II. Oscillatory shear flow," *Rheol. Acta* **34**, 430-439 (1995b).
- Parthasarthy, M. and D. J. Klingenberg, "Large amplitude oscillatory shear of ER suspensions," *J. Non Newtonian Fluid Mech.* **81**, 83 - 104 (1999).
- Phule, P. P., "Synthesis of novel magnetorheological fluids," *MRS Bulletin*, **23**(8), 23-25 (1998).
- Schultz, G. V. Z., "The Kinetics of Chain Polymerization. V. The Effect of Various Reaction Species on the Polymolecularity," *Z. Phys. Chem.* **25**(B43), 25-87 (1939).
- See, H. and M. Doi, "Shear resistance of electrorheological fluids under time-varying electric fields," *J. Rheol.* **36**(6), 1143-1163 (1992).

- Segovia-Gutiérrez, J. P., C. L. A. Berli, and J. de Vicente, "Nonlinear viscoelasticity and two-step yielding in magnetorheology: A colloidal gel approach to understand the effect of particle concentration," *J. Rheol.* **56(6)**, 1429-1448 (2012).
- Segovia-Gutiérrez, J. P., J. de Vicente, R. Hidalgo-Álvarez, and A. M. Puertas, "Brownian dynamics simulations in magnetorheology and comparison with experiments," *Soft Matter* **9**, 6970-6977 (2013).
- Sherman, S. G. and N. M. Wereley, "Effect of particle size distribution on chain structures in magnetorheological fluids," *IEEE Transactions on Magnetics* **49(7)**, 3430-3433 (2013).
- Vinogradov, G. V. and A. Ya. Malkin, "Rheology of polymers: viscoelastic and flow of polymers," (Springer-Verlag, Berlin, 1980).
- Wang, Z., Z. Lin, and R. Tao, "Influence of the size distribution of particles on the viscous property of an electrorheological fluid," *Chin. Phys. Lett.* **14(2)**, 151-154 (1997).

Chapter 9.

Start-up rheometry of highly polydisperse magnetorheological fluids: experiments and simulations

José Antonio Ruiz-López, Zuowei Wang, Juan Carlos Fernández-Toledano, Roque Hidalgo-Álvarez and Juan de Vicente.

This article is under review

Abstract

An extensive experimental and simulation study is carried out in conventional magnetorheological fluids formulated by dispersion of mixtures of carbonyl iron particles having different sizes in Newtonian carriers. Apparent yield stress data are reported for a wide range of polydispersity indexes (PDI) from PDI = 1.63 to PDI = 3.31, which for a log-normal distribution corresponds to the standard deviation ranging from $\nu = 0.38$ to $\nu = 0.76$. These results demonstrate that the effect of polydispersity is negligible in this range in spite of exhibiting very different microstructures. Experimental data in the magnetic saturation regime are in

quantitative good agreement with particle-level simulations under the assumption of dipolar magnetostatic forces. The insensitivity of the yield stresses to the polydispersity can be understood from the interplay between the particle cluster size distribution and the packing density of particles inside the clusters.

9.1. INTRODUCTION

Conventional magnetorheological (MR) fluids are dispersions of carbonyl iron microparticles in non-magnetic carriers. In the absence of magnetic fields, the dispersions exhibit a liquid-like behavior. However, upon the application of a large enough magnetic field (≥ 10 kA/m), the particles are magnetized and interact with each other to form elongated structures in the direction of the magnetic field. This results in a field-controllable increase in the viscosity and the eventual appearance of an apparent yield stress at appropriate particle loadings and field strengths (so-called MR effect).¹⁻⁵

Enhancing the yield stress under external fields is a priority for commercial applications. In this sense, it is well known that increasing the particle concentration results in an increase of the yield stress under the field (on-state) (e.g. Segovia-Gutierrez *et al.*⁶), but it also gives place to a large off-state (no field) viscosity⁷ and eventually leads to a reduction in the MR effect⁸. One way to increase the particle volume fraction without increasing the off-state shear viscosity is by using polydisperse MR fluids (i.e., dispersions of magnetizable particles with different sizes). In fact, polydisperse MR fluids inherently exhibit a lower off-state viscosity than monodisperse MR fluids due to the different particle packing characteristics; larger packing fractions are achieved with polydisperse systems. This means that using polydisperse MR fluids, the particle

volume fraction can be increased, without increasing the off-state viscosity, hence developing a larger MR effect.

The effect of particle size in the case of monodisperse systems has been largely reported in the literature for MR fluids, ER fluids and inverse ferrofluids,⁹⁻¹² in general, larger particles exhibit a larger yield stress under the presence of magnetic fields (e.g. Lemaire *et al.*⁹, Foister⁸, Trendler and Bose¹²). On the contrary, the understanding of polydisperse MR fluids is still not complete. As a first approximation towards the full understanding of the effect of particle size polydispersity, in recent years, a number of studies have focused on bimodal distributions (i.e. mixtures of particles having only two different sizes).¹³⁻¹⁸ Experiments and simulations demonstrate that it is possible to substantially increase the yield stress of an initially monodisperse MR fluid with the addition of a small amount of smaller particles (at the same total particle concentration), while simultaneously reducing the viscosity of the suspension.^{8,14} In most cases, particle packing arguments are employed to explain such an increase (e.g. Weiss *et al.*¹⁵ for MR fluids; e.g. See *et al.*¹⁹ for ER fluids). However, more recently, Kittipoomwong *et al.*²⁰ proposed an alternative mechanism for the enhanced yield stress in bidisperse suspensions by using particle level simulations. Interestingly, microstructure analysis revealed that the enhanced stress transfer in bidisperse suspensions was not associated with an increase in particle packing. Instead, the enhanced yield stress was associated with the presence of more highly anisotropic clusters of large particles than observed in monodisperse suspensions.

A complete understanding of the effect of particle size distribution in the MR effect of sphere-based suspensions is still missing in the literature. Actually, there are very few papers involving a *continuous* size

distribution. To the best of our knowledge, there are only three papers addressing this issue from the simulation side. Wang *et al.*²¹ reported a two-dimensional (2D) simulation study of ER fluids under the assumption of Gaussian distribution of particle sizes and negligible thermal and inertial terms. They introduced a local-field approximation to take into account the mutual polarization effects between the particles. Shear stresses were simulated for a constant shear rate value at different standard deviations of the Gaussian distribution (from $s = 0$ to 3). It was found that the stresses first dropped quickly with increasing polydispersity and then gradually saturate as $s > 0.5$ (corresponding to $\text{PDI} > 1.07$, considering that the particle sizes were limited in a range of within 50% from the mean size). The decrease in the shear stress was interpreted as a result of the formation of imperfect chain-like structures by particles of different sizes that are easier to break under shear than those formed by particles of uniform size. Recently, Sherman and Wereley²² carried out a comprehensive 3D simulation study under the assumption of log-normal distribution, again neglecting thermal and inertial terms. Their results demonstrate that as the particle distribution size parameter increases, particles tend to form more irregular structures and a 25 % reduction in the shear stress at low Mason numbers is observed. More recently, Fernández-Toledano *et al.*²³ carried out 3D Brownian dynamic simulations of MR fluids with $\text{PDI} = 1.12$ (i.e., the standard deviation of log-normal distribution $\nu = 0.2$). The results obtained were compared with purely monodisperse systems. The effect of polydispersity was very small and basically only noticeable in the yielding region: a slightly more abrupt decrease in viscosity was found in viscosity curves for polydisperse suspensions.

Also, very few papers have been published on the effect of a *continuous* size distribution in the MR performance from the experimental point of

view. The reason for this is that generally polydispersity is achieved by mixing *only* two populations having different particle sizes at different proportions (e.g. See *et al.*¹⁹ for ER fluids; e.g. Bombard *et al.*¹⁶ for MR fluids) and in most cases the particle size ratio is either large or extremely large.^{18,24} To the best of our knowledge, there is only one paper in the scientific literature that addresses a continuous distribution by mixing more than two systems.²⁵ In their paper, Chiriac and Stonian²⁵ carried out an experimental investigation to elucidate the effect of particle size distribution on MR effect. Distributions were obtained first by sieving commercial micrometric iron particles (Sigma-Aldrich) to obtain narrow distribution powders and then mixing the finer powders in order to obtain three batches with tailored size distributions. MR fluids investigated were formulated at a 10 vol% by mixing the powders in mineral oil. Unfortunately, although some changes were detected when measuring the MR response, the mean particle size changed among the batches prepared and this complicated the interpretation of their results.

In this work we carry out an extensive experimental study on the effect of particle size polydispersity in conventional MR fluids prepared by dispersion of mixtures of three varieties of carbonyl iron microparticles that only differ in size and having all other physical properties essentially the same (chemical composition and magnetic properties). Particle concentrations and size distributions explored are within the range of those of interest in commercial applications (clearly larger than that reported by Fernández-Toledano *et al.*²³). Special care is taken for the mean particle size of the distributions to remain constant (variations less than 5 %). Also, experimental results are compared to particle-level simulation data.

9.2. EXPERIMENTAL

Three types of carbonyl iron particles were obtained from BASF SE and used without further purification (grades HQ, HS and OM). These three powders were conveniently mixed to further produce mixed particle systems with different particle size distribution and polydispersity but similar mean size and magnetic properties. MR fluids were prepared by dispersion of the carbonyl iron powders in a silicone (PDMS) oil of viscosity 20 mPa·s (Sigma-Aldrich). The particle concentration was fixed at 10 vol%. Table 9.1 summarizes relevant information on the polydispersity and magnetic properties of the iron grades and mixtures used in this manuscript. Magnetic properties of carbonyl iron powders were modelled using the Fröhlich-Kenelly law.²⁶ Figure 9.1 contains the particle size distributions for the different MR suspensions investigated.

MR fluid	Fraction in mixed suspensions (wt%)			σ_m (μm)	PDI	V	M_s (kA/m)
	HQ	HS	OM				
S	100	0	0	1.26	1.64	0.42	1691
M	0	100	0	2.20	1.63	0.38	1703
L	0	0	100	4.30	1.85	0.52	1550
P1	13	80	7	2.22	2.48	0.52	1691
P2	20	70	10	2.22	2.71	0.58	1685
P3	25	60	15	2.28	2.88	0.64	1677
P4	33	50	17	2.25	3.02	0.68	1673
P5	40	40	20	2.24	3.13	0.72	1668
P6	50	30	20	2.15	3.31	0.76	1666

Table 9.1 Physical characteristics of the MR fluids used in this work. σ_m stands for the mean particle diameter, PDI is the polydispersity index and v the standard deviation of log-normal distribution. M_s is the saturation magnetization of the suspensions using a mixing rule.

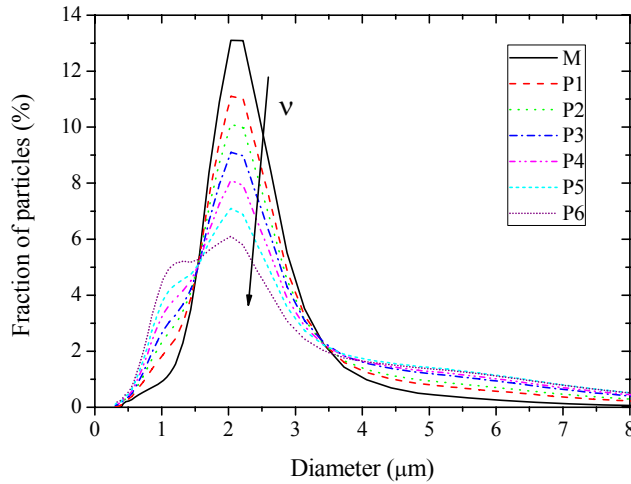


Figure 9.1 Particle size distributions for the polydisperse MR fluids investigated in experiments.

A MCR302 magnetorheometer (Anton Paar, MRD70/1T) was used in plate-plate configuration (20 mm diameter and 300 microns gap thickness). The magnetic field applied was always perpendicular to the plates and the temperature was maintained at 25 °C during the test. Experiments were carried out in saturation ($H_0 = 885 \text{ kA/m}$) for better comparison with the simulation results where the dipolar approximation is assumed.

The rheological protocol was as follows. First the sample was preconditioned at a high constant shear rate (100 s^{-1}) for a duration of 30 s to remove history effects. Next, the suspension was left to equilibrate at rest for 60 s under the presence of a magnetic field. Finally, the rheological test started. It consisted of a logarithmic stress ramp from 1000 Pa to 10000 Pa. The logarithmic increase of the stress was done at a rate of 50 points/decade and the acquisition time was 5s. The static yield stress was obtained from the stress corresponding to a sudden change in

shear rate in log-log stress versus shear rate representations. For the dynamic yield stress, a regression fit was carried out in lin-lin representation for the data points measured at the largest shear rates. All experimental data reported in this work were averages of at least three independent measurements with fresh new samples. As an example, the calculation of the static and dynamic yield stress is shown in the Supporting material (Figure S9.1).

9.3. SIMULATION TECHNIQUES

Molecular dynamic simulations were carried out in order to understand the microscopic mechanisms behind the performance of polydisperse MR fluids under shearing flow. The simulation method was an extension of the methodology developed by Klingenberg and coworkers^{1,13,20} for polydisperse particles taking the expressions for the forces from a previous work by Fernandez-Toledano *et al.*²³ The method concerns non-Brownian inertialess simulations. In general, this restriction can be easily accepted in the case of conventional MR fluids, since the so-called Lambda ratio (i.e. the ratio between the magnetostatic energy and the thermal energy) is generally large enough to safely neglect the thermal motion. MR fluids were thus modeled as $N=1000$ neutral buoyant particles in a continuous Newtonian medium. Hydrodynamic interactions were also neglected and the Stokes' law approximated the drag force. This approximation is generally adopted because of computational reasons. Also, a recent study by Lagger *et al.*²⁷ demonstrated that hydrodynamic interactions can be safely neglected if the hydrodynamic stress is not the main contribution to the total stress. Considering these approximations, the equation of motion of a particle i , can be expressed as follows:

$$\zeta_i \left(\frac{d\vec{r}_i}{dt} - \vec{u}_i^\infty \right) = \vec{F}_i \quad (9.1)$$

where $\zeta_i = 3\pi\eta_c\sigma_i$ is the friction coefficient of the particle with η_c the Newtonian medium viscosity and σ_i the diameter of the particle, respectively. \vec{r}_i is the position vector of the particle. $\vec{u}_i^\infty = \dot{\gamma} z_i \hat{e}_x$ is the ambient fluid velocity at the particle center with $\dot{\gamma}$ the magnitude of the shear rate tensor, z_i the z-coordinate of the particle and \hat{e}_x the unit vector in the x-direction in Cartesian coordinates. Finally, \vec{F}_i is the total force acting on the particle.

In Equation 9.1, the term \vec{F}_i includes the pair-wise magnetostatic forces exerted by all other particles on particle i , $\vec{F}_i^{mag} = \sum_{j \neq i} \vec{F}_{ij}^{mag}$.

Magnetostatic interaction force between two particles was modeled in the dipolar approximation as follows:

$$\vec{F}_{ij}^{mag} = F_0 \frac{\sigma_i^3 \sigma_j^3}{\sigma_m^2 r_{ij}^4} [(3 \cos^2 \theta_{ij} - 1) \hat{e}_r + \sin 2\theta_{ij} \hat{e}_\theta] \quad (9.2)$$

Here, $F_0 = 3\pi\mu_0\mu_{cr}\beta^2 H_0^2 \sigma_m^2 / 16$ stands for the typical magnetic interaction force between two particles with sizes of the average diameter σ_m . μ_0 is the magnetic permeability of the vacuum, μ_{cr} is the relative permeability of the continuous medium, $\beta = (\mu_{pr} - \mu_{cr}) / (\mu_{pr} + 2\mu_{cr})$ is the so-called contrast factor (or coupling parameter), μ_{pr} is the magnetic permeability of the particles, H_0 is the external magnetic field strength, r_{ij} is the center-to-center distance between two particles i and j , θ_{ij} is the angle between the line joining the centers of the two particles and the

magnetic field direction, and \hat{e}_r and \hat{e}_θ are the unit vectors in the directions r and θ using a spherical coordinate system.

Exponential short-range repulsive forces were included to avoid overlapping between particles, \vec{F}_{ij}^{rep} , and between each particle and the two confining walls, $\vec{F}_i^{wall,top}$ and $\vec{F}_i^{wall,bottom}$. Exponential forces are applied instead of stiff power law forces, since it was shown that exponential forces help the formation of thicker aggregates as already observed in experiments.^{28,29} Expressions for the exponential forces used in this manuscript for continuous particle size distributions can be found in the work of Fernández-Toledano *et al.*²³.

The equation of motion was made dimensionless using the following units: $l_s = \sigma_m, F_s = F_0$ and $t_s = 3\pi\eta_c\sigma_m^2 / F_0$. In simulations of continuously polydisperse systems we used a Log-normal distribution. The Log-normal distribution is a continuous probability distribution where the logarithm of the random variable is normally distributed. The Log-normal random variable was obtained, thus, by first calculating a normal variable of mean $\ln\sigma_m$ and standard deviation ν and then calculating the Log-normal random variable by taking the exponential of the normally distributed variable. Simulations also involved tri-disperse particle size distributions (i.e., mixtures of particles with three different sizes) to better understand the relationship between the field-induced microstructures and the rheological performance of the polydisperse MR fluids. Tri-disperse particle sizes, $\sigma_s < \sigma_a < \sigma_b$, for each given polydispersity index were obtained by taking three different average diameters from the Log-normal distribution with fixed probabilities of $P(\sigma_s) = P(\sigma_b) = 0.16$ and $P(\sigma_a) = 0.68$. Table 9.2 summarizes tri-disperse diameters as a function of

the standard deviation, ν , and so correspondingly the polydispersity index. From now on, we will also refer ν as the polydispersity index.

ν	σ_s^*	σ_a^*	σ_b^*
0.38	0.567	1.021	1.713
0.52	0.464	1.040	2.277
0.58	0.425	1.050	2.515
0.64	0.391	1.061	2.780
0.72	0.350	1.077	3.183
0.76	0.330	1.086	3.409

Table 9.2.- Dimensionless particle diameters, σ_s^* , σ_a^* , σ_b^* , as a function of the polydispersity index ν for tri-disperse molecular dynamic simulations. Probabilities for finding particles of different sizes were fixed at $P(\sigma_s) = P(\sigma_b) = 0.16$ and $P(\sigma_a) = 0.68$.

Once the total force acting on a particle was calculated, its equation of motion was solved using the Euler algorithm. Time variation was calculated at every step such that the maximum displacement of any particle, i , in one direction was no larger than $0.05\sigma_i$ in order to avoid particles to be ejected from the box due to the fact that big-small particle interactions can provoke the smallest particle to move outside the box. This condition typically reduced the time variation and the total simulation time increases specially for the highest polydispersity indexes.

Stress growth tests (start-up tests) were carried out at a small-normalized shear rate, $\dot{\gamma}^* = 10^{-3}$. This velocity was found to provide a stress value close to the yield stress.²³ Simulations were composed of three stages: (i) Particles were randomly distributed in the simulation box, (ii) Particles were allowed to move under the presence of the magnetic field in quiescent state until reaching a stationary state. The stationary state was

found to be established for all polydispersity indexes at a dimensionless time $t_{stat}^* = 3000$; (iii) Start-up test was properly initiated and steady shear flow was fully achieved when reaching a total strain of $\gamma=3$. The stress tensor was calculated at each time step as follows:

$$\tau_{\alpha\beta} = -\frac{1}{V} \sum_{i \neq j} r_{ij}^{\alpha} F_{ij}^{\beta} \quad (9.3)$$

where $\tau_{\alpha\beta}$ is the α - β -component of the stress tensor, V is the volume of the simulation box, r_{ij}^{α} is the α -component of the distance between particles i and j and F_{ij}^{β} is the β -component of the total pair-wise interaction between the two particles. Three regions were clearly identified in the stress versus time (or strain) curves: elastic, peak and steady regions.²³ The elastic region corresponds to the low-strain regime where the stress is found to be proportional to the shear strain. Then, a maximum in the stress (peak) is observed. Finally, for large enough strain values the stress levels off to a nearly constant value as a function of time in a steady region. As the shear rates imposed were very low, the static yield stress can be assimilated as the stress peak. Also, the dynamic yield stress was calculated as the shear stress averaged over 4000 configurations saved from strain $\gamma=2$ to $\gamma=3$. Simulation results were the average values of at least 3 different tests for each case. In order to obtain a better estimation of the static yield stress, more simulation runs (at least 10) were carried out up to a reduced total strain of $\gamma=1$.

To better understand the rheological performance of polydisperse MR fluids, we ran a microstructural analysis through the calculation of the particle pair distribution function. In the canonical ensemble, the

probability of finding a pair of particles at positions \vec{r}_1 and \vec{r}_2 respectively is given by the pair distribution function:

$$g_2(\vec{r}_1, \vec{r}_2) = \frac{N(N-1)}{\rho^2 Z_{NVT}} \int d\vec{r}_3 d\vec{r}_4 \dots d\vec{r}_N \exp[-U(\vec{r}_1, \vec{r}_2, \dots, \vec{r}_N) / k_B T] \quad (9.4)$$

where ρ is the number density of the particles, Z_{NVT} is the partition function, $U(\vec{r}_1, \vec{r}_2, \dots, \vec{r}_N)$ is the total interaction potential, k_B is the Boltzmann constant and T is the temperature of the system.

Due to the spherical and azimuthal symmetries in the pair dipolar magnetic interaction, Equation 9.4 could be reduced to a function of the radial distance between two particles, r , and the angle between the direction vector linking the centers of these two particles and the direction of the magnetic field, θ . Then the pair distribution function is converted to $g_2(r, \theta) \equiv g(r, \theta)$. In simulations, this function could be obtained simply by the following expression:³⁰

$$g(r, \theta) = \frac{V}{N^2} \left\langle \sum_i \sum_{j \neq i} \delta(r - r_{ij}) \delta(\theta - \theta_{ij}) \right\rangle \quad (9.5)$$

where the bracket refers to a volume average. Also, a radial distribution function could be easily obtained from the radial and angular distribution function by the integration of this function as a function of θ :

$$g(r) = \int_0^{\pi/2} d\theta \sin(\theta) g(r, \theta).$$

9.4. RESULTS AND DISCUSSION

9.4.1. Experimental yield stresses

In Figure 9.2 we show the rheograms (steady-state shear stress versus shear rate curves) corresponding to MR fluids having different polydispersity levels (from $\nu = 0.38$ to $\nu = 0.76$) at particle volume fraction $\phi = 0.10$. For low stress levels the shear rate remains below 10^{-3} s^{-1} suggesting that the sample is not flowing. However, for stresses above 6000-7000 Pa the shear rate dramatically increases in accordance to the initiation of flow. As observed, the curves essentially overlap suggesting that the effect of polydispersity is not important within the standard deviation of the data.

These results are in qualitative agreement with the simulation work of Fernández-Toledano *et al.*²³. In that work, a simulation study was carried out for both mono- and polydisperse (with $\nu = 0.2$) MR fluids. These two MR fluids exhibited very similar behavior, the only difference being in the transition region between the solid and liquid-like regimes. Actually, for polydisperse MR fluids a slightly sharper transition was found if compared to the monodisperse case.

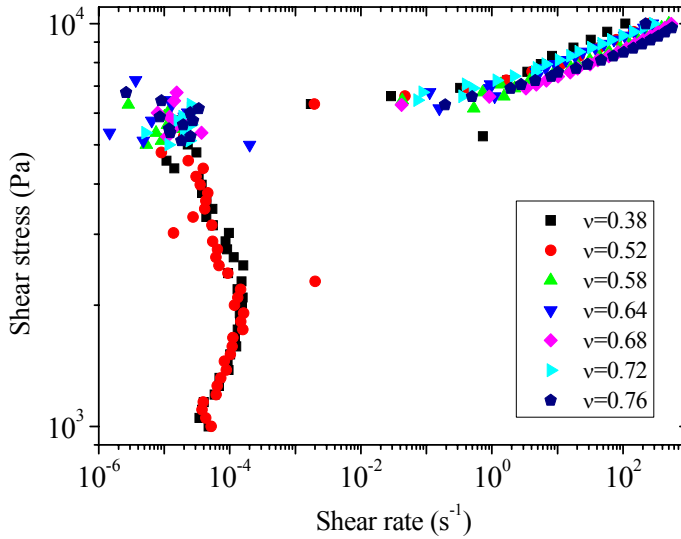


Figure 9.2 Experimental rheograms (shear stress versus shear rate) for different polydispersity levels in $\phi = 0.10$ MR fluids.

Figure 9.3 contains experimental (static and dynamic) yield stresses for a particle concentration of $\phi = 0.10$. As observed, the yield stresses do not depend much on the polydispersity index. They remain basically constant over the range of ν values we studied, with the dynamic yield stress being higher than the static one (see Figure S9.1 for the measurement of the two stresses). Only a very slight local maximum in the yield stress was measured for a polydispersity index of $\nu \approx 0.7$. Experiments were also carried out for other particle concentrations including $\phi = 0.01$, $\phi = 0.05$ and $\phi = 0.20$, all giving very similar results. These experiments are not shown for brevity. To get a better insight into the effect of polydispersity we pursued particle-level simulations.

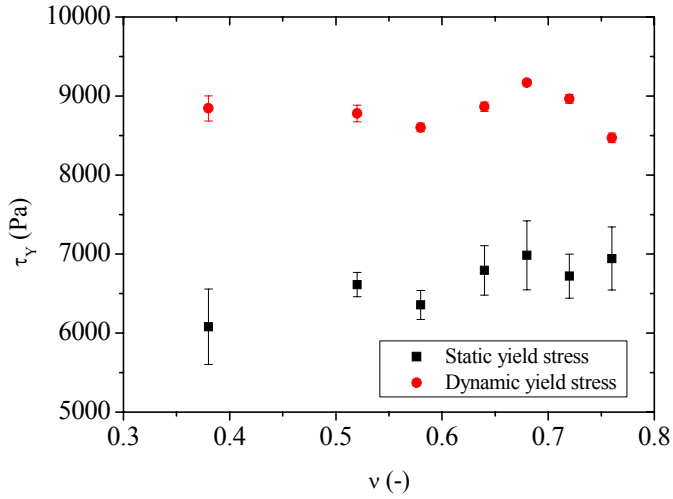
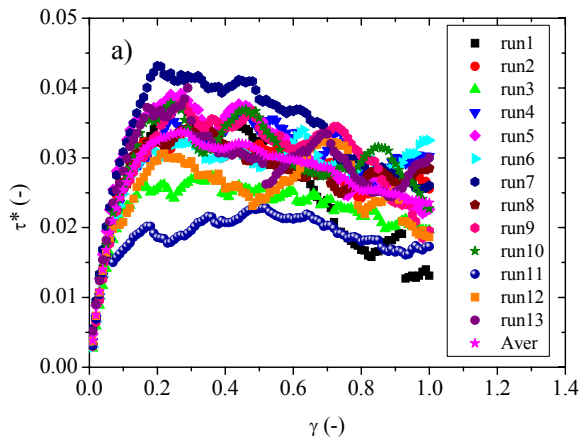


Figure 9.3 Experimental static and dynamic apparent yield stresses as a function of polydispersity index ν for $\phi=0.10$ MR fluids.

9.4.2. Simulated yield stresses for MR systems with continuous particle size distributions



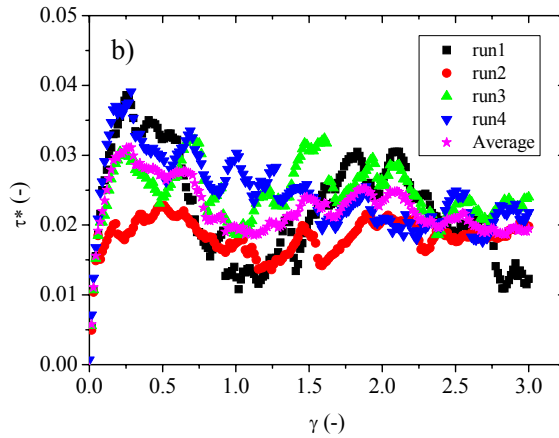


Figure 9.4 Typical example of the simulated shear stress-strain curves for $\phi=0.10$ and $\nu=0.64$. Every curve corresponds to an independent simulation run. a) Tests up to strain $\gamma=1$. b) Tests up to $\gamma=3$. Dimensionless shear rate is $\dot{\gamma}^* = 10^{-3}$.

The static and dynamic yield stresses of the MR systems with continuous particle size distributions were determined using particle-level simulations. The start-up tests were performed at a low shear rate ($\dot{\gamma}^* = 10^{-3}$) similar to that used by Fernández-Toledano *et al.*²³. As an example, typical stress-strain curves for $\phi = 0.10$ and $\nu = 0.64$ are presented in Figure 9.4 for a total of 13 independent runs for strains up to $\gamma=1$ (4 runs for strains up to $\gamma=3$) to appreciate the repeatability of the simulations. In general, three regions can be identified: a first elastic region where the stress grows linearly with strain, a maximum (peak) in the stress, and finally a monotonous decay of the stress towards a final steady region marked by the long-time plateau. On the one hand, the maximum of the stress in each stress-strain curve is taken here as an estimate for the static yield stress in the suspension. On the other hand, the long-time stress plateau is taken as the dynamic yield stress of the suspension. In this sense, the dynamic yield stress was obtained as the

average of the stress values from $\gamma=2$ to $\gamma=3$. It is worthwhile to note that the high number of repetitions was necessary to obtain a good estimation for the static yield stress (more than 10 independent runs). In the case of the dynamic yield stress, as it was already taken as a time average in each individual test, less (but at least 3) repetitions were needed to get a reasonably good estimation.

Simulated yield stresses are reported in Figure 9.5 for the particle concentration $\phi = 0.10$. In good agreement with the experimental observations (c.f. Figure 9.3), both the static and dynamic yield stresses exhibit very minor changes with the variation of the degree of polydispersity. Despite many simplifications made in the simulation model, the simulation data fall well into the same quantitative range as the yield stresses measured in experiments. It is useful to remark that the definitions of the static and dynamic yield stresses differ between the experimental and simulation cases, as described in the previous sections. This difference, however, has no qualitative effect on the observed behavior of the yield stresses with respect to the level of polydispersity.

The mechanical properties of the MR fluids are inherently correlated to the microstructures formed by the particles. For convenience of structural analysis, we have also decided to carry out simulations on tri-disperse MR systems.

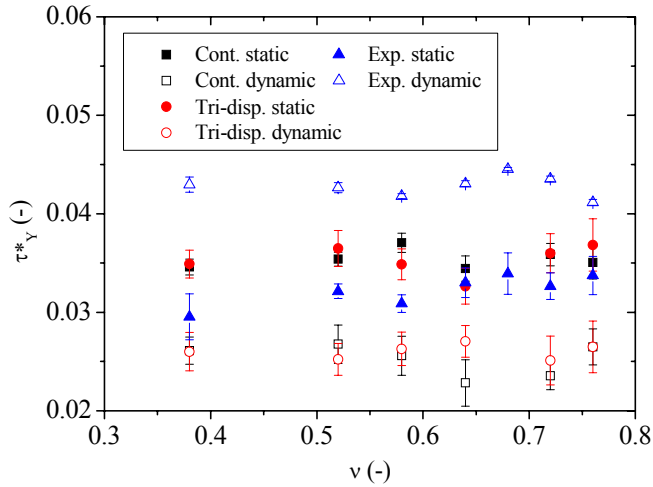


Figure 9.5 Experimental and simulation static and dynamic yield stresses as obtained from the maximum and long-time plateau in stress-strain curves reported in Figure 4 for different polydispersity indexes in the $\phi=0.10$ MR fluids. Squares correspond to continuous particle size distributions. Circles correspond to tri-disperse distributions. Triangles correspond to experimental data.

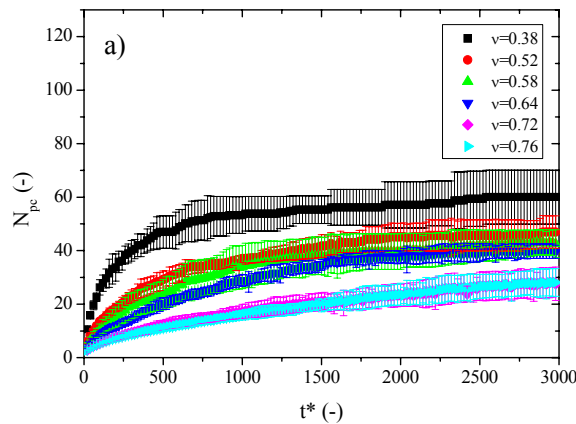
9.4.3. Simulated yield stresses for MR systems with tri-disperse particle size distributions

Simulation results on the static and dynamic yield stresses of the tri-disperse MR fluids are also contained in Figure 9.5. It can be seen that these stress values are very similar to those obtained from the MR systems with continuous size distributions, suggesting that the tri-disperse suspensions can closely capture the behavior of the experimental systems with continuous particle size distributions. Simulations of penta-disperse model systems have also performed. As expected, they provided consistent results (not shown for simplicity) with the case of tri-disperse suspensions, suggesting again that the tri-disperse model suspension is sufficient to represent the continuous size distribution. We can then analyze the structural properties of these model systems for getting

insights into the physical reasons of the negligible dependence of the yield stresses on the polydispersity.

9.4.4. Characterizing structural formation in simulated MR systems with continuous size distributions

To explore the structural characteristics of the particle aggregates formed in the MR systems, we calculated the average number of clusters N_c , the average number of particles in each cluster $N_{pc} = \sum_i n_i / N_c = N / N_c$ and the weight-averaged number of particles in each cluster $S_2 = \sum_i n_i^2 / \sum_i n_i = \sum_i n_i^2 / N$ for the cases both prior to and under shear. Here, n_i is the number of particles in the cluster i . The simulation results on N_{pc} are shown in Figure 9.6, while those for N_c and S_2 are given in Figures S9.2 and S9.3 in the Supporting Information. Note that there is a simple inverse relationship between N_c and N_{pc} because of the use of constant number of particles in the simulation box.



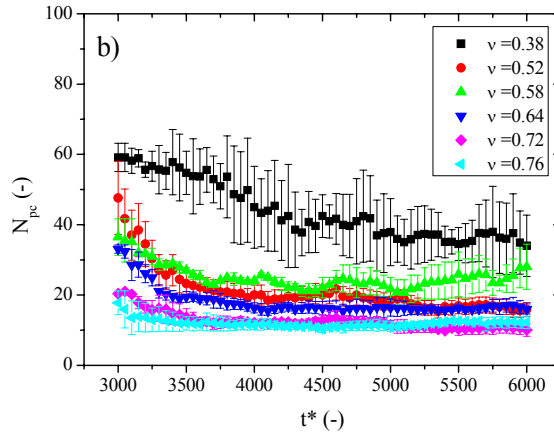
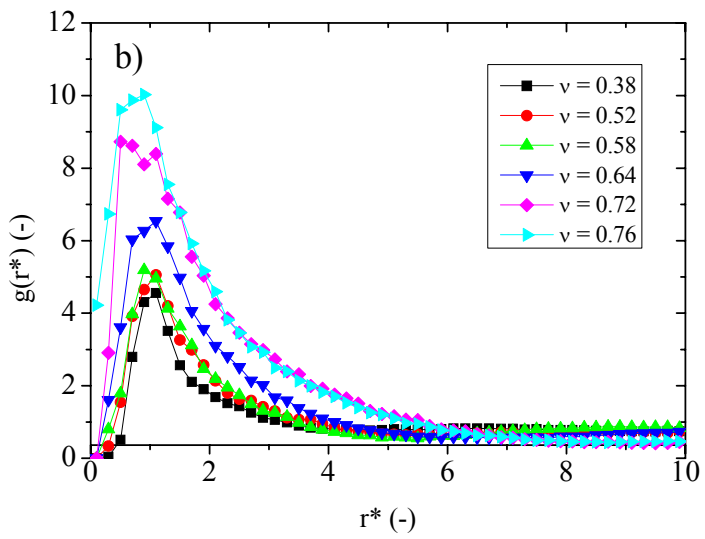
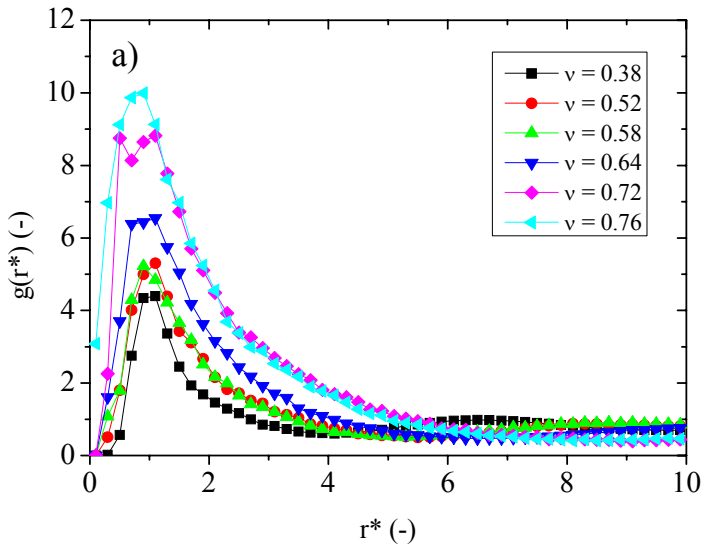


Figure 9.6 Simulation results on the average number of particles per cluster, N_{pc} , for MR fluids with continuous particle size distributions at fixed particle concentration $\phi = 0.10$. a) Prior to shear; b) Under shearing.

Simulation results in the absence of shear demonstrate a monotonic increase of N_c , and a concomitant decrease of N_{pc} and S_2 with the increased polydispersity. For the highest polydispersities, the stationary state is difficult to achieve but the number of clusters only varies in less than 1 for reduced times higher than 2700. Considering the insensitivity of the yield stresses to the polydispersity, these simulation results reveal the importance of the internal microstructure of the aggregates for understanding the experimentally observed trends in the yield stress. They indicate that the yield stress depends not only on the number and sizes of the aggregates, but also on their mechanical strength to deformation. This is further supported by the simulation data upon shear, which show qualitatively similar structural changes with respect to polydispersity.

9.4.5. Particle radial distribution function for MR systems with continuous particle size distributions

The particle radial distribution functions can provide more detailed information about the particle packing inside the clusters. The $g(r)$ curves obtained from the MR systems with continuous particle size distributions are shown in Figure 9.7. These functions are calculated at three different stages of the deformation process: at $\gamma = 0.1$ within the elastic region, at the stress peak, and in the steady regime from $\gamma = 2$ to $\gamma = 3$. As can be seen, all pair distribution functions exhibit a maximum (first peak) close to the average particle diameter. The width of the peak increases with increasing polydispersity, which is expected as a result of the connections between particles of a broader range of sizes. Interestingly, the height of this peak is also found to grow with the increased polydispersity. This means that on average each particle in the suspension with higher polydispersity finds more nearest neighbors than the particles in the less polydisperse suspensions. In other words, the particle packing density is higher in the former case. This phenomenon can be easily understood from the fact that small particles can get into the voids left by large particles in the clusters. The more heterogeneous packing of particles in the highly polydisperse systems leave only one peak in their $g(r)$ curves. On the contrary, the particle pair distribution functions of the less polydisperse systems possess a long-distance peak at reduced distance of $r^* \approx 5$ or 6. The long-distance peak is related to the mean distance between clusters since $g(r, \theta)$ is higher for angles from $[60^\circ, 90^\circ]$ than in angles from $[0^\circ, 30^\circ]$.



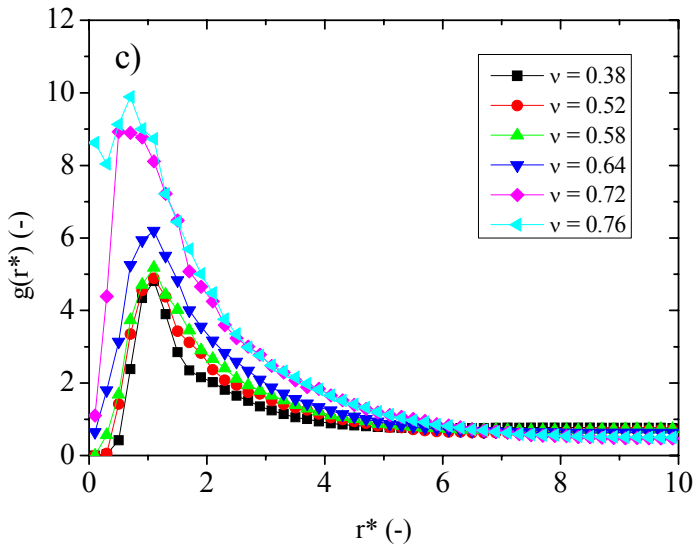


Figure 9.7 Particle radial distribution function in MR fluids with continuous particle size distributions and $\phi=0.10$ at three different stages of the deformation: a) elastic region (at $\gamma=0.1$), b) stress peak, c) steady region. The results in the steady region were calculated by averaging over 4000 configurations saved from $\gamma=2$ to $\gamma=3$.

Comparing the simulation results in Figures 9.6 and 9.7, it can be seen that although the aggregates or clusters formed in the more polydisperse systems are of smaller sizes, the packing density of particles in these clusters are higher. Since the higher packing density may allow the clusters to sustain stronger mechanical load or deformation, this contribution could effectively cancel out the stress reduction effect caused by the decrease in cluster sizes. It is the interplay between the two opposite effects that leads to the nearly invariant yield stress upon changes of polydispersity.

The particle packing effect on the yield stress can be further examined by analyzing the angle-dependent pair distribution function $g(r, \theta)$ (Equation 9.5). Figure 9.8 presents the polydispersity dependence of the maximum

(peak) value of the pair distribution function averaged within different angle limits, $g(r)_{\theta \in [\theta_1, \theta_2]} = \int_{\theta_1}^{\theta_2} d\theta \sin(\theta) g(r, \theta) / \int_{\theta_1}^{\theta_2} d\theta \sin(\theta)$. Two angle intervals are included. We show the simulation data for the (dipolar) energetic-favorable angles, $\theta \in [0, 30^\circ]$ and for the energetic-unfavorable angles, $\theta \in [60^\circ, 90^\circ]$. Although in both cases the peak values show a monotonic increase with increasing polydispersity, the corresponding increases in the packing densities at different angles contribute to the total interaction energy and consequently the yield stress of the system in very different ways. The increase in the peak value of the pair distribution function at the energetic-favorable angles ($\theta \in [0, 30^\circ]$) suggests the formation of well-arranged and so stronger structures along the magnetic field direction. But the increase of the pair distribution function at the energetic-unfavorable angles ($\theta \in [60^\circ, 90^\circ]$) implies that the structures also contain more bonds that are easier to break. As will be seen below, it is not only the average local density of particles what contributes to the yield stress, but also the direction-dependent microscopic arrangements of the particles inside the clusters. It is also important to remark that the maximum value of the pair distribution function for the smallest angles decreases in the steady region compared with the elastic region, suggesting the break-up of the column- or chain-like structures along the field direction.

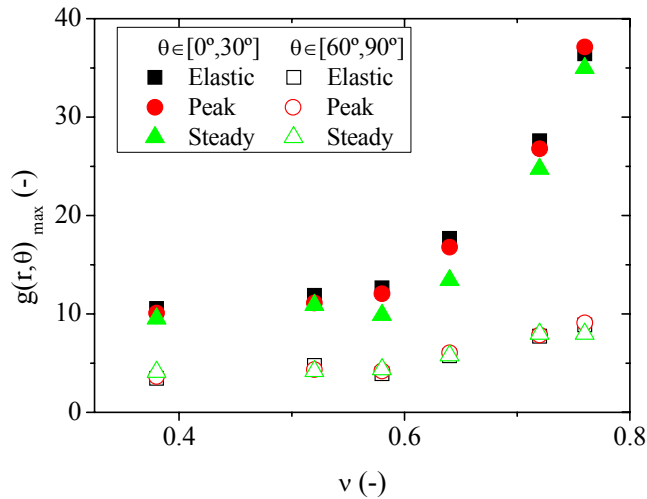


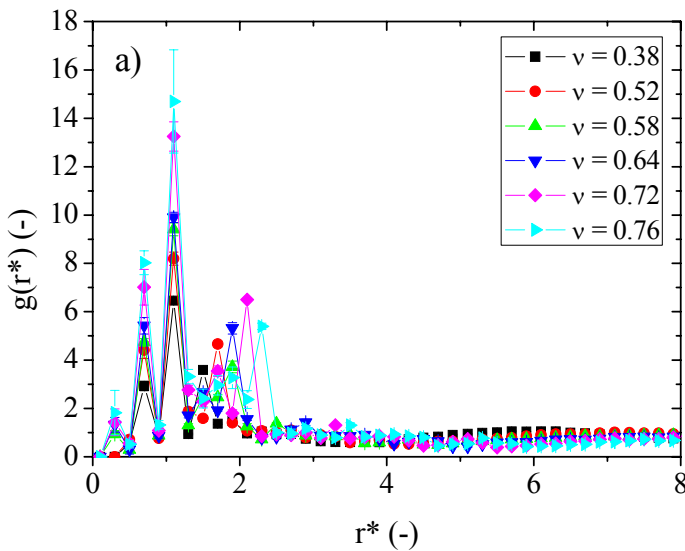
Figure 9.8 Polydispersity dependence of the maximum value of the pair distribution function, $g(r, \theta)$, averaged within different angle limits for the $\phi = 0.10$ MR fluids.

These results in Figure 9.8 are in agreement with the results from Fernandez-Toledano et al.²³ (see Figure 9.4 in that work) where the particle connectivities in the polydisperse system demonstrated a continuous distribution as a function of the connecting angle, instead of individual peaks marking the more favorable connections in the monodisperse system, for $\theta \in [0, 60^\circ]$. The dependence of particle connections on their sizes can be identified more easily for the tri-disperse systems, as shown below.

9.4.6. Radial distribution function for tri-disperse MR systems

In Figure 9.9 we show the radial distribution function curves for the tri-disperse MR suspensions. We observe that there are very reproducible peaks associated with the discrete particle sizes, namely the distances between particles of different sizes (small, average and big). In the case of the lowest polydispersity, another long-distance peak (at $r^* \approx 5 - 6$) is

found, which does not occur in the highly polydisperse systems. This peak cannot be associated to the three different sizes of the particles, but can be well understood from microstructural snapshots shown in Figure 9.10 for two different polydispersities, $\nu = 0.52$ and $\nu = 0.72$. These snapshots demonstrate that bunches of average-size particles serve as bridges connecting big particles to form chain-like structures. As in the continuous case, for larger polydispersities, the pair distribution function and the interparticle connections suggest a stronger cluster formation, which implies a higher yield stress. However, these microstructural differences are not enough to provide a significantly higher yield stress, and so only a slight enhancement can be observed in experiments and simulations.



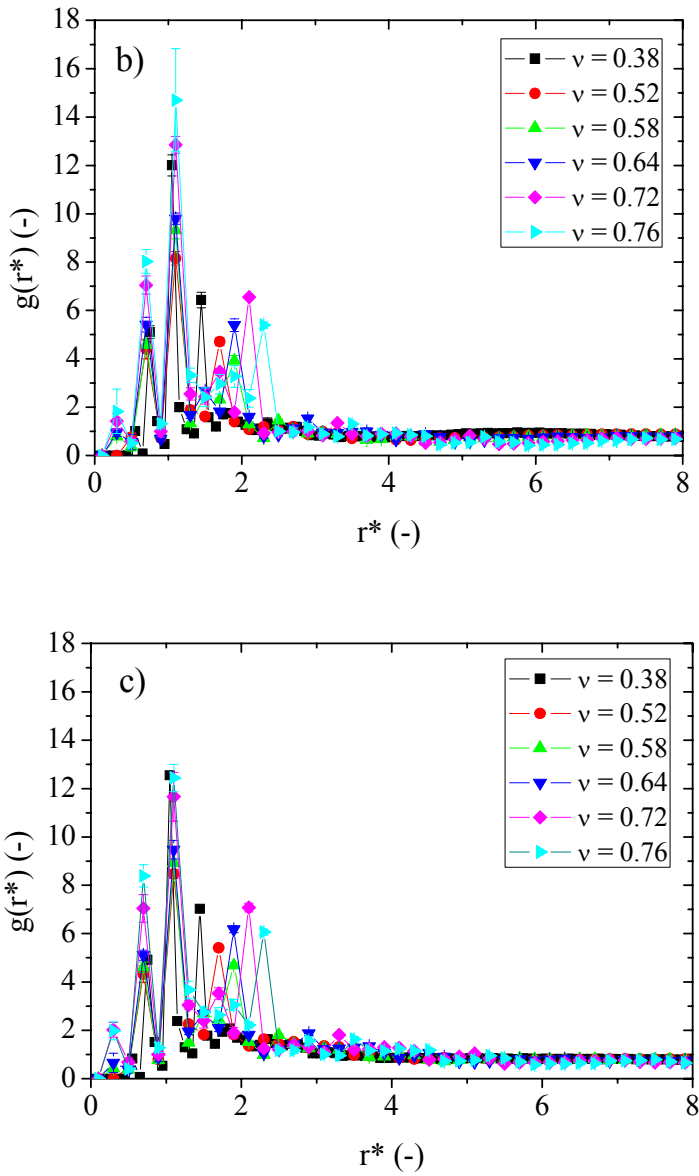
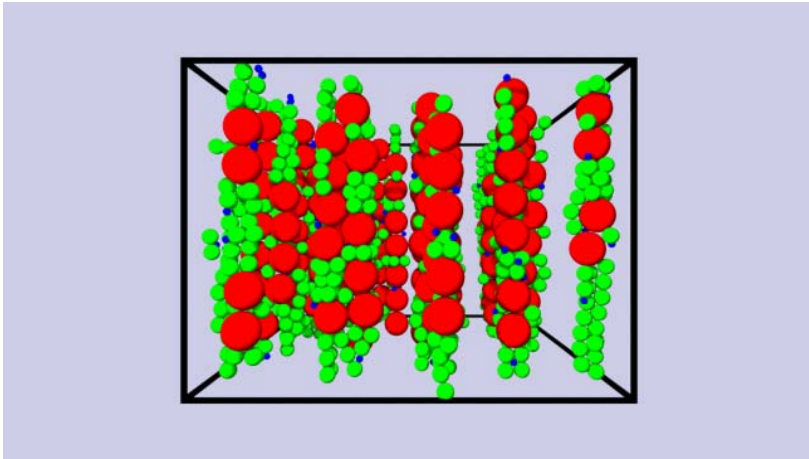


Figure 9.9 Radial distribution function for tri-disperse particle size distributions. $\phi = 0.10$. a) elastic region, b) stress peak, c) steady region. The steady region was calculated by averaging over 4000 configurations from $\gamma = 2$ to $\gamma = 3$.

a)



b)

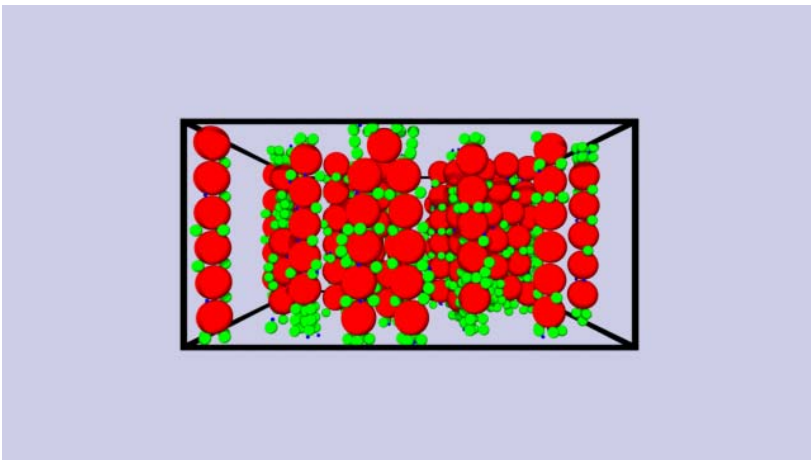
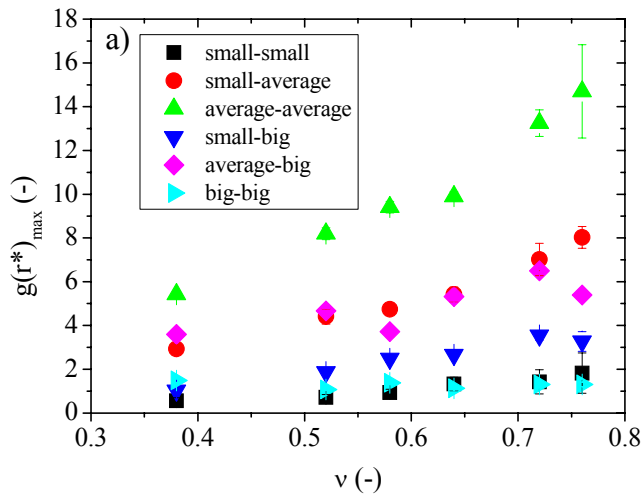
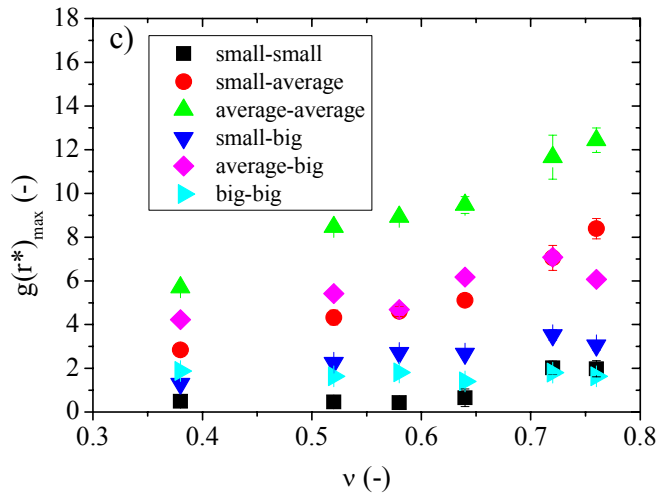
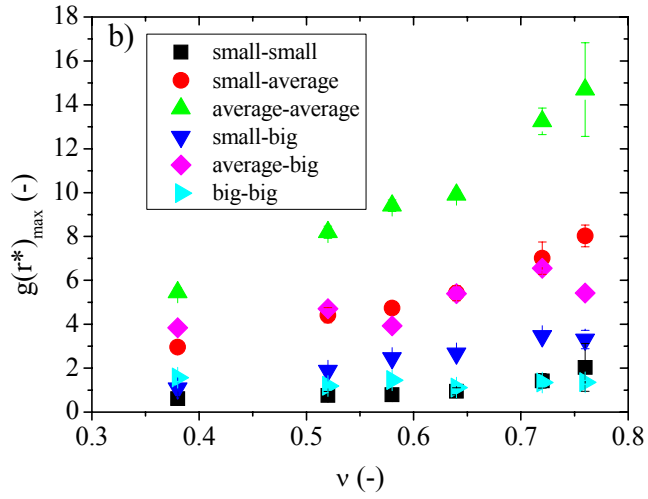


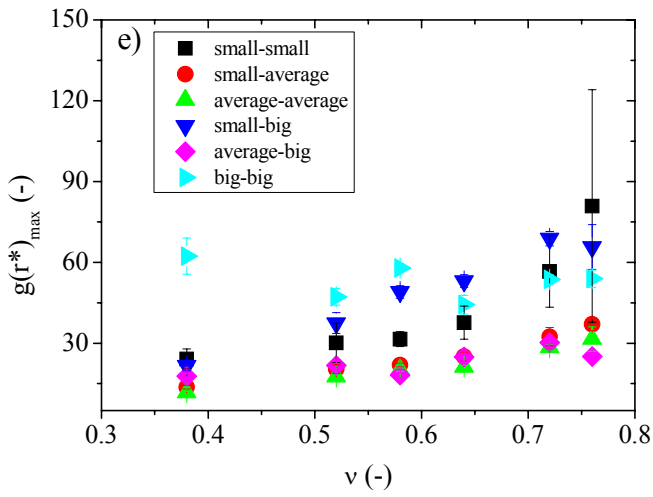
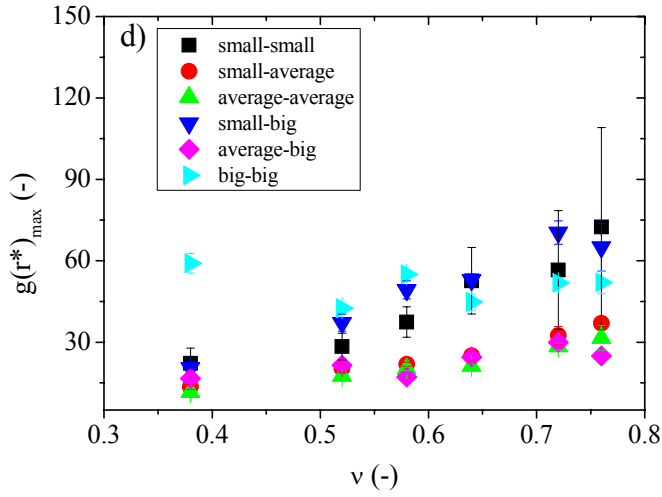
Figure 9.10 Snapshots of the microstructure prior to shear for $\phi=0.10$: a) $\nu=0.52$ and b) $\nu=0.72$.

First row in Figure 9.11 (from Figure 9.11a to Figure 9.11c) contains the maximum (peak) values in the radial distribution functions shown in Figure 9.9 for different polydispersity indexes, taking into account all possible connections between particles of different sizes. At first sight, these figures suggest that the average-average (a-a) particle connections dominate the response. However, this could be misleading, because the

probability of finding a big or small particle is much lower than the probability of finding an average-size particle. It is more helpful to obtain the relative importance of the connections among particles. In the simulations, we have 68.2 % of average-size particles and only 15.9 % of small-big particles, respectively. Hence, the results in the first row of Figure 9.11 were normalized by the probabilities of finding the different pairs of particles and presented in the second row of the figure. It then becomes evident that the small-small, small-big and big-big connections present a higher relative importance in determining the yield stress.







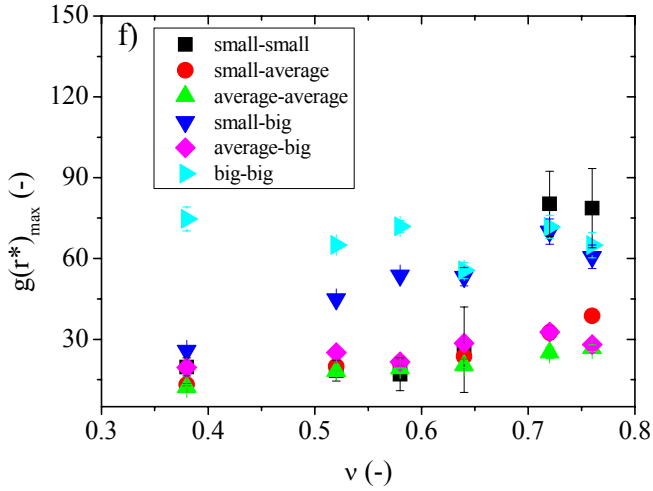


Figure 9.11 Peak heights of the radial distribution functions in tri-disperse simulations as a function of the polydispersity index. The particle concentration is $\phi=0.10$. a) elastic region, b) peak region and c) steady region. Normalization of the peak heights by the probabilities: d) elastic region, e) peak region and f) steady region.

Similar results have been found in the radial distribution functions in the peak and steady shear regions (these results are included in Figure 9.11). Interestingly, the long-distance peak observed in the elastic region of the lowest polydisperse systems is not observed now in the peak and steady shear regions due to the breakage of large columnar structure. The heights of the peaks are also lower in the steady region than those found in the elastic region.

9.5. CONCLUSIONS

In this work we investigate the role of the particle size polydispersity using experimental and simulation start-up tests. Polydispersity index was varied in a wide range containing typical experimental polydispersities, from PDI = 1.63 to PDI = 3.31. In this PDI range, the effect of the

polydispersity on the yield stress can be considered as negligible in experiments; only a very slight maximum can be observed in the experimental case for $PDI = 2.88$ ($\nu = 0.64$).

Two different particle size distributions were used in simulations: a continuous log-normal particle size distribution and a tri-disperse (i.e. three fixed different particle sizes) distribution. The results for the yield stress in both particle size distributions are in agreement with the experimental data and a slight but non-significant increase of the yield stress is found for the highest polydispersities.

Although variations in the yield stress were of minor importance, differences in the microscopic structures were found in simulations in the continuous and tri-disperse distributions. Analysis results on the particle cluster sizes and the particle radial distribution function show that increasing the level of polydispersity of the MR system leads to a smaller average number of particles per cluster but a higher packing density of the particles inside the clusters. Although the smaller cluster sizes may result in a reduction in the yield stress, the higher packing density can enhance the sustainability of the clusters to stronger mechanical load or deformation. It is the interplay between the two opposite effects that lead to the nearly negligible dependence of the yield stresses on the polydispersity.

Moreover detailed analysis of the angle-dependent pair distribution functions reveals that at high level of polydispersity particle connections are increased at all the angles with respect to the magnetic field direction (both energetic-favorable and energetic-unfavorable directions). This suggests another effect that, although the structure gets denser with increasing polydispersity, the bonds between particles can become

weaker. This also contributes to maintain nearly constant yield stress upon variation of polydispersity.

ACKNOWLEDGEMENTS

This work was supported by MAT 2013-44429-R project (Spain) and by Junta de Andalucía P10-RNM-6630, P10-FQM-5977 and P11-FQM-7074 projects (Spain). J.A.R.-L. acknowledges the financial support by the “Ministerio de Educación: Becas del Programa de Formación del Profesorado Universitario (FPU)” (AP2010-2144).

Supporting information

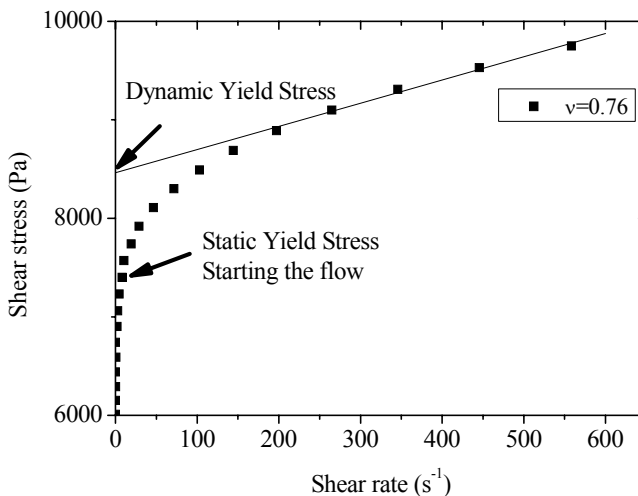


Figure S9.1 Calculation of the static yield stress and the dynamic yield stress for experimental results for the MR fluid with $\nu = 0.76$ and $\phi = 0.10$.

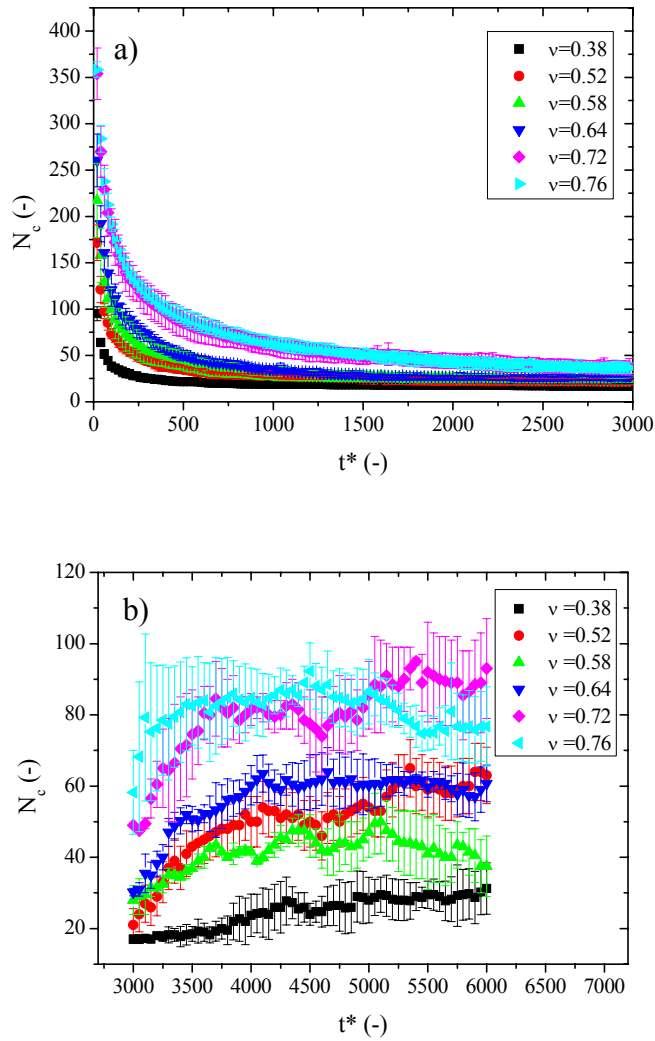


Figure S9.2 Simulation results on the average number of cluster, N_c for MR fluids with continuous particle size distributions at particle concentration $\phi = 0.10$. a) prior to shear, b) under shearing. The total number of particles in the simulation box is $N = 1000$.

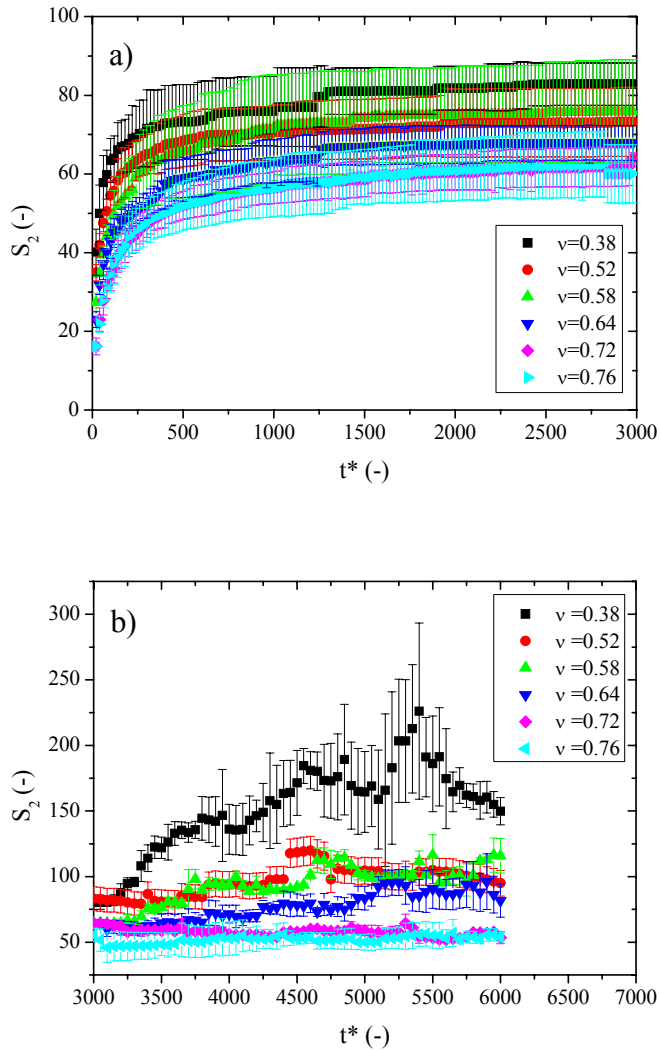


Figure S9.3 Simulation results on the weight-averaged number of particles in each cluster S_2 for MR fluids with continuous particle size distributions at fixed particle concentration $\phi=0.10$. a) prior to shear; b) under shearing.

References

- (1) Parthasarathy, M.; Klingenberg, D. J. Electrorheology: Mechanisms and models. *Mater. Sci. Eng.* **1996**, R. 17, 57-103.
- (2) Bossis, G.; Volkova, O.; Lacis, S.; Meunier, A. In *Ferrofluids*; Odenbach, S. Ed.; Springer, Berlin, 2002; pp 202-230.
- (3) Gonzalves, F. D.; Koo, J.-H.; Ahmadian, M. A review of the state of the art in magnetorheological fluid technologies-Part I: MR fluid and MR fluid models. *Shock Vib. Dig.* **2006**, 38(3), 203-219.
- (4) Park, B. J.; Fang, F. F.; Choi, H. J. Magnetorheology: Materials and application. *Soft Matter* **2010**, 6, 5246-5253.
- (5) de Vicente, J.; Klingenberg, D. J.; Hidalgo-Álvarez, R. Magnetorheological fluids: a review. *Soft Matter.* **2011**, 7, 3701-3710.
- (6) Segovia-Gutiérrez, J. P.; Berli, C. L. A.; de Vicente, J. Non-linear viscoelasticity and two-step yielding in magnetorheology: a colloidal gel approach to understand the effect of particle concentration. *J. Rheol.* **2012**, 56(6), 1429-1448.
- (7) Barnes, H. A.; Hutton, J. F.; Walters, K. *An Introduction to Rheology*; Elsevier: Amsterdam, 1989.
- (8) Foister, R. T. Magnetorheological fluids. *US Patent 5.667.715* **1997**.
- (9) Lemaire, E.; Meunier, A.; Bossis, G.; Liu, J.; Felt, D.; Bashtovoi, P.; Matoussevitch, N. Influence of particle size on the rheology of magnetorheological fluids. *J. Rheol.* **1995**, 39, 1011-1020.
- (10) Tan, Z. J.; Zou, X. W.; Zhang, W. B.; Jin, Z. Z. Influences of the size and dielectric properties of particles on electrorheological response. *Phys. Rev. E* **1999**, 59, 3177-3181.

-
- (11) de Gans, B. J.; Duin, N. J.; van den Ende, D.; Mellema, J. The influence of particle size on the magnetorheological properties of an inverse ferrofluid. *J. Chem. Phys.* **2000**, 113, 2032-2042.
 - (12) Trendler, A. M.; Bose, H. Influence of particle size on the rheological properties of magnetorheological suspensions. *Int. J. Mod. Phys. B* **2005**, 19, 1416-1422.
 - (13) Ahn, K. H.; Klingenberg, D. J. Relaxation of polydisperse electrorheological suspensions. *J. Rheol.* **1994**, 38(3), 713-741.
 - (14) Weiss, K. D.; Carlson, J. D.; Nixon, D. A. Method and magnetorheological fluid formulations for increasing the output of a magnetorheological fluid device. *US Patent 5.900.184* **1999**.
 - (15) Weiss, K. D.; Carlson, J. D.; Nixon, D. A. Method and magnetorheological fluid formulations for increasing the output of a magnetorheological fluid device. *US Patent 6.027.664* **2000**.
 - (16) Bombard, A. J. F.; Alcantara, M. R.; Knobel, M.; Volpe, P. L. O. Experimental study of MR suspensions of carbonyl iron powders with different particle sizes. *Int. J. Mod. Phys. B* **2005**, 19(07-09), 1332-1338.
 - (17) Golden, M. A.; Ulicny, J. C. Magnetorheological fluids. *US Patent 6.932.917 B2* **2005**.
 - (18) Song, K. H.; Park, B. J.; Choi, H. J. Effect of magnetic nanoparticle additive on characteristics of magnetorheological fluid. *IEEE Trans. Mag.* **2009**, 45(10), 4045-4048.
 - (19) See, H.; Kawai, A.; Ikazaki, F. The effect of mixing particles of different size on the electrorheological response under steady shear flow. *Rheol. Acta* **2002**, 41, 55-60.
 - (20) Kittipoomwong, D.; Klingenberg, D. J.; Ulicny, J. C. Dynamic yield stress enhancement in bidisperse magnetorheological fluids. *J. Rheol.* **2005**, 49(6), 1521-1538.

- (21) Wang, Z. W.; Lin, Z. F.; Tao, R. B. Influence of the size distribution of particles on the viscous property of an electrorheological fluid. *Chin. Phys. Lett.* **1997**, 14, 151-154.
- (22) Sherman, S. G.; Wereley, N. M. Effect of particle size distribution on chain structures in magnetorheological fluids. *IEEE Transactions on Magnetics* **2013**, 49(7), 3430-3433.
- (23) Fernández-Toledano, J. C.; Ruiz-López, J. A.; Hidalgo-Álvarez, R.; de Vicente, J. Simulations of Polydisperse Magnetorheological Fluids: a Structural and Kinetic Investigation. *J. Rheol.* **2015**, 59(2), 475-498.
- (24) Wu, C. W.; Conrad, H. Influence of mixed particle size on electrorheological response. *J. Appl. Phys.* **1998**, 83, 3880.
- (25) Chiriac, H.; Stonian, G. Influence of particle size distributions on magnetorheological fluid performances. *J. Phys. Conf. Ser.* **2009**, 200, 072095.
- (26) Jiles, D. C. *Introduction to magnetism and magnetic materials*; Chapman & Hall: London, 1991.
- (27) Lagger, H. G.; Breinlinger, T.; Korvink, J. G.; Moseler, M.; Di Renzo, A.; Di Maio, F.; Bierwisch, C. Influence of hydrodynamic drag model on shear stress in the simulation of magnetorheological fluids. *J. Non-Newtonian Fluid Mech.* **2015**, 218, 16-26.
- (28) Melrose, J. R.; Heyes, D. M. Simulations of electrorheological and particle mixture suspensions: agglomerate and layer structures. *J. Chem. Phys.* **1993**, 98(7), 5873-5886.
- (29) Segovia-Gutiérrez, J. P.; de Vicente, J.; Hidalgo-Alvarez, R.; Puertas, A. M. Brownian Dynamics Simulations in Magnetorheology and Comparison with Experiment. *Soft Matter* **2013**, 9, 6970-6977.
- (30) Allen, M. P.; Tildesley, D. J. *Computer Simulation of Liquids*; Oxford University Press: New York, 1987.

Conclusions

In this dissertation, both the squeeze flow behavior and the effects of the particle size distribution in the magnetorheological performance have been investigated. The main conclusions are summarized as follows:

Magnetorheology in squeeze flow mode

1. The normal force and the compressive stress increase under compression as a result of the reorganization of the particles within the aggregates.
2. The micromechanical model satisfactorily predicts the normal force and the compressive yield stress in a wide range of particle concentrations, magnetic field strengths, sample volumes and initial gap distances for small deformations. The model also explains deviations from continuous media theories.
3. Particle-level simulations predict the dependence of the normal force and the compressive yield stress on the particle concentration and the magnetic field strength but fail in the prediction of the normal force dependence on the compressive strain.
4. Including local field corrections in the micromechanical model and simulations is crucial for a satisfactory prediction at the lowest gap separations.
5. Continuous media theories predict reasonably well the normal force in the case of MR fluids in the constant volume regime at 5 vol%. However, deviations are observed for dilute MR fluids.

Model magnetorheology: inverse ferrofluids

1. The Structural Viscosity Model successfully explains the rheological behavior of inverse ferrofluids under shearing for a wide range of particle volume concentrations. It also provides a smoother transition from the magnetostatic to the hydrodynamic regime than the widely used Bingham model.
2. The Mean Magnetization approximation is applicable to inverse ferrofluids for a wide range of magnetic field strengths. However, it can only be applicable to conventional MR fluids for small magnetic field strengths and dilute suspensions.
3. Particle-level simulations successfully predict the rheological behavior of inverse ferrofluids under steady shear and large amplitude oscillatory shear tests. They also predict the critical Mason number and the storage modulus for all the concentration range investigated. However, simulations fail in the prediction of the loss modulus for the highest concentrations because hydrodynamic interactions are neglected in the model.

Effect of the polydispersity in particle size in magnetorheology

1. Experiments for highly polydisperse MR fluids show that the shear yield stress is not significantly dependent on the polydispersity index.
2. Brownian dynamic simulations for polydisperse MR fluids also show a non-dependent yield stress on the polydispersity.
3. Although the yield stress does not vary with the polydispersity, the microstructure of polydisperse MR fluids changes: there are more clusters but clusters have a higher particle density.

Conclusiones

En esta tesis, el comportamiento en compresión y los efectos de la distribución de tamaños en la respuesta magneto-reológica han sido investigados. Las principales conclusiones se resumen como sigue:

Magneto-reología en compresión

1. La fuerza normal y el esfuerzo de compresión se incrementan en compresión debido a la reorganización de partículas dentro de los agregados.
2. El modelo micro-mecánico predice satisfactoriamente la fuerza normal y el esfuerzo umbral de compresión en un intervalo amplio de concentraciones, campos magnéticos, volúmenes de la muestra y distancias iniciales de los platos para deformaciones pequeñas. El modelo también predice las desviaciones de las teorías para medios continuos.
3. Las simulaciones a nivel de partícula predicen la dependencia de la fuerza normal y el esfuerzo umbral de compresión con la concentración y el campo magnético pero fallan en la predicción de la dependencia de la fuerza normal con la deformación de compresión.
4. Incluyendo las correcciones de campo local en el modelo micro-mecánico y las simulaciones es crucial para unas predicciones satisfactorias sobre todo a distancias entre platos pequeñas.
5. Las teorías de medios continuos predicen razonablemente bien la fuerza normal en el caso de fluidos magneto-reológicos en

compresión a volumen constante para el 5% vol. Sin embargo, se observan desviaciones para fluidos magneto-reológicos diluidos.

Magneto-reología en sistemas modelo: ferrofluidos inversos

1. El modelo de viscosidad estructural explica satisfactoriamente el comportamiento reológico de ferrofluidos inversos en cizalla para un gran intervalo de concentraciones. Este modelo aporta una transición más suave desde el régimen magnetoestático al régimen hidrodinámico que el modelo de Bingham, usado comúnmente.
2. La aproximación de magnetización promedio es aplicable a ferrofluidos inversos en un gran intervalo de campos magnéticos. Sin embargo, sólo se puede aplicar a fluidos magneto-reológicos convencionales para campos magnéticos pequeños y suspensiones diluidas.
3. Las simulaciones a nivel de partícula predicen exitosamente el comportamiento de ferrofluidos inversos en cizalla simple y experimentos en cizalla oscilatoria de amplitud grande. También predicen el número de Mason crítico y el módulo de almacenamiento para todas las concentraciones investigadas. Sin embargo, las simulaciones fallan en la predicción del módulo de pérdidas debido a que se desprecian interacciones hidrodinámicas.

Efecto de la polidispersidad en tamaño en magneto-reología

1. Los experimentos para fluidos magneto-reológicos altamente polidispersos muestran que el esfuerzo umbral de cizalla no depende significativamente del índice de polidispersidad.

2. Simulaciones de dinámica browniana para fluidos magnetoreológicos polidispersos también muestran que el esfuerzo umbral no depende de la polidispersidad.
3. Aunque el esfuerzo umbral no varíe significativamente con la polidispersidad, la micro-estructura cambia: hay más agregados pero una mayor densidad de éstos al aumentar la polidispersidad.